

VT-Forschungsbericht 2018-01

Systematic Accuracy Assessment for Alternative Aviation Fuel Evaporation Models

Dipl.-Ing. Bastian Rauch

Deutsches Zentrum für Luft- und Raumfahrt
Institut für Verbrennungstechnik
Stuttgart



DLR

Deutsches Zentrum
für Luft- und Raumfahrt



Herausgeber

Deutsches Zentrum
für Luft- und Raumfahrt

**Institut für
Verbrennungstechnik**

Pfaffenwaldring 38-40
70569 Stuttgart

Telefon
Telefax

(0 7 11) 68 62 - 3 08
(0 7 11) 68 62 - 5 78

Als Manuskript gedruckt.
Abdruck oder sonstige Verwendung
nur nach Absprache mit dem Institut gestattet

D93, Stuttgart

Systematic Accuracy Assessment for Alternative Aviation Fuel Evaporation Models

A thesis accepted by the Faculty of Aerospace Engineering and Geodesy of the
University of Stuttgart in partial fulfillment of the requirements for the degree of
Doctor of Engineering Sciences (Dr.-Ing.)

by

Bastian Rauch

born in Bruchsal, Germany

Main Referee: Prof. Dr. Manfred Aigner

Co-Referee: Prof. Dr. Hans-Jörg Bauer

Date of Defence: 10.02.2017

Institute of Combustion Technology for Aerospace Engineering

University of Stuttgart

2018

Acknowledgement

Starting this PhD research topic, I had no idea how adventurous the journey would be. I was confronted with the well-known ups and downs one experiences in the search for a scientifically proven truth, together with the amazing power of diverse cultures / scientific approaches (German/Italian, experimental/numerical) intertwining in the process, notwithstanding the ensuing puzzlement. Sometimes the weight of the challenge felt more than I could bear - but then I was always reminded that I was not alone.

Firstly, I thank Prof. Dr.-Ing. Manfred Aigner for reviewing my work, as well as the opportunity to pursue research in the two research institutes, the DLR Institute of Combustion Technology in Stuttgart (DLR VT), Germany and the CNR Istituto Motori in Naples, Italy. Many thanks to him for the trust and support in pursuing this scientific adventure. I also thank Prof. Dr.-Ing. Hans-Jörg Bauer, chair of the Institute of Thermal Turbomachinery at the Karlsruhe Institute of Technology, for his prompt willingness to review this dissertation.

I extend my special thanks to Dr. Patrick Le Clercq and Dr. Patrizio Massoli for the mentoring and guiding inputs into different aspects of this work. I enjoyed the many in-depth and thought-provoking discussions we had, especially the ones where I came with answers but left with more questions that led me to a deeper truth. I owe them my warmest gratitude for their support during the clash of cultures / approaches - be it between the German and Italian cultures or between the experimental and numerical ways of perceiving reality.

I further thank all the colleagues at DLR VT and the CNR Istituto Motori for the fruitful cooperation with a friendly working environment. I owe special thanks to Dr. Raffaella Calabria for her guidance at work and life in Naples, and specially for the deep friendship, my colleagues and friends Dr. Bhavin Kapadia, Dr. Felix Grimm, Dr. Gregor Gebel, Dr. Uwe Bauder, Dr. Antonio Filosa, Andrea Tomasello, Yann Simsont, Alexander Steinbach, Fabio Chiariello, Dr. Markus Kindler, Markus Lempke and Martin Seidel - they always helped me to come back to „local normality“ and gave me the feeling that I had never truly left.

Finally, I want to express my deep personal gratitude to my parents, grandparents, brothers and sister. They have given me the possibility to hone the instruments I needed to pursue this adventure with open-mindedness and curiosity as well as a strong sense for passion for it. My deepest thanks and appreciation go to my beloved wife Irina. She has been my strongest supporter. During the different phases of my thesis, over the 6 years of traveling between the two worlds, she has been at my side in all the ups and downs - grazie infinitamente

Contents

List of Figures	ix
List of Tables	xv
List of Symbols	xvi
Abstract	xxi
Kurzfassung	xxiii
1 Introduction	1
1.1 Motivation.....	1
1.2 Literature Review	3
1.2.1 Multicomponent-Fuel Droplet Evaporation Models for Aviation Fuels	3
1.2.2 State-of-the-Art of validation for CTM evaporation models	6
1.2.3 Validation Standards	8
1.3 Objectives	14
1.4 Chapter Overview	16
2 Validation Domain for Alternative Aviation Fuel	17
2.1 Influencing Factors on the Development of Jet Fuels	17
2.1.1 Phases of Jet Fuel Development.....	18
2.1.2 Fuel Specifications and Alternative Fuel Approval Process	22
2.1.3 Fuel Processing Technology	25
2.1.4 Conclusions.....	28
2.2 Fuel Characterization	29
2.2.1 Fuel Composition	29
2.2.2 Distillation Curve	33
2.2.3 Variability of Jet Fuel Characteristics.....	34
2.3 Fuel Validation Domain	35
2.3.1 Fuel Formulation related Issues in the Fuel Approval Process	35
2.3.2 Validation Domain for Alternative Aviation Fuel Droplet Evaporation Models.....	36
2.4 Conclusions	37
3 Model Form Uncertainty of Droplet Evaporation Models	39
3.1 Spray Modeling	40
3.2 Discrete Component Evaporation Models	41
3.2.1 Conceptualization.....	42
3.2.2 Gas-Phase Analysis.....	43
3.2.3 Liquid Phase Analysis	47
3.3 Continuous Thermodynamics Model	48

3.3.1	Description of Liquid and Vapor Compositions by Γ -PDF	49
3.3.2	CTM Evaporation Equations.....	51
3.4	Thermodynamic Property Modeling.....	53
3.4.1	Basic Property Correlation for Fuel Families.....	55
3.4.2	Liquid Phase Property Correlations	55
3.4.3	Gas Phase Property Correlations	56
3.4.4	Phase Equilibrium for Non-Ideal Mixtures.....	57
3.5	SPRAYSIM: Framework for the Solution of Evaporation Equations.....	58
3.6	Conclusions	59
4	Validation Experiment	61
4.1	Experimental System	61
4.1.1	Diagnostics.....	63
4.1.2	Inlet System	63
4.2	Flow Field Characterization.....	65
4.2.1	Cold Flow	65
4.2.2	Hot Flow	66
4.2.3	Conclusions.....	67
4.3	Spray Characterization.....	68
4.3.1	Generalized Mie Scattering Imaging.....	68
4.3.2	Application of GSI.....	70
4.3.3	Spray Characterization	72
4.3.4	Data Reduction.....	73
4.3.5	Conclusions.....	76
4.4	Measurement Uncertainty	76
4.4.1	Measured Quantities	77
4.4.2	Derived Quantities.....	80
4.4.3	Additional Uncertainties.....	83
4.5	Conclusions	84
5	Modeling of the Validation Experiment and Uncertainty Quantification	85
5.1	Modeling of the Validation Experiment	85
5.1.1	Definition of the Computational Domain.....	86
5.1.2	Classification of Boundary Conditions	87
5.1.3	Numerical Model of the Flow Field.....	89
5.1.4	Simulation Strategy	90
5.2	Accuracy Assessment of the Flow Field Simulation.....	91
5.2.1	Parameter Estimation: Flow Field Boundary Conditions	91
5.2.2	Flow Field Validation	94

5.3	Accuracy Assessment of n-Decane Droplet Evaporation Models	98
5.3.1	Parameter Estimation: Spray Injection Conditions	98
5.3.2	Definition of the Validation Metrics.....	101
5.4	Evaluation of the Effect of Input Uncertainties	105
5.4.1	Identification and Characterization of Input Uncertainties	105
5.4.2	Estimation of Uncertainties in the SRQs.....	107
5.4.3	Analysis of the Effect of Injection Parameter Uncertainties.....	109
5.5	Conclusions	110
6	Accuracy Assessment of Alternative Aviation Fuel Droplet Evaporation Models ..	113
6.1	Validation Domain for Droplet Evaporation Models.....	114
6.1.1	Test Fuels	114
6.1.2	CTM Description of Multicomponent Fuels	115
6.2	Global Statement of Model Accuracy	116
6.2.1	Global Validation Metric for the Validation Domain	117
6.2.2	Analysis of the Maximum Error.....	119
6.3	Validation by the Evolution of the Mean Values.....	121
6.3.1	Single Component Fuels	121
6.3.2	Binary Mixtures.....	125
6.3.3	Non-Ideal Mixtures	126
6.3.4	Multicomponent Mixtures.....	127
6.4	Conclusions	128
7	Summary	131
7.1	Outlook.....	133
7.1.1	General	133
7.1.2	Validation and Uncertainty Quantification for Reacting Multiphase Flow Models	134
8	Bibliography.....	137
A	Validation of Single Component Fuel Property Models	151
B	Boundary Conditions.....	155
B.1	Cold flow Carrier Jet Inflow Conditions.....	155
B.2	Hot Flow Carrier Jet Inflow Conditions.....	155
C	Validation Results	157
C.1	Flow Field Validation	157
C.1.1	Cold Flow Velocity Field	157
C.1.2	Hot Flow Temperature Field	159
C.1.3	Heating Up Computations	160

C.2	Spray Validation Results	161
C.2.1	Single Component Fuels	161
C.2.2	Binary Mixtures.....	165
C.2.3	Non-Ideal Mixtures	167
C.2.4	Multicomponent Mixtures.....	169

List of Figures

Figure 1.1:	Scheme of a conventional combustion chamber showing the basic thermo-chemical processes.....	2
Figure 1.2:	Validation plan from end-to-end (adapted from (ASME 2006; Oberkampf and Trucano 2008).).....	11
Figure 1.3:	Relationship between validation and application domain (Oberkampf and Roy 2010).....	12
Figure 2.1:	Timeline with different phases of jet fuel development.....	18
Figure 2.2:	Effective fuel composition range to fulfill ASTM D1655 and DS91-91 fuel specifications, adapted from (de Klerk 2012).....	23
Figure 2.3:	Test program for the approval of new aviation turbine fuels (ASTM International 2014a).	24
Figure 2.4:	Alternative jet fuel pathways adapted from Blakey et al. (2011).....	25
Figure 2.5:	GC chromatograms for Jet A-1 (Zschocke, Scheuermann, and Ortner 2015).....	30
Figure 2.6:	Distribution of fuel components for the different fuel families present in Jet A-1 characterized in (Wahl 2003; Kick et al. 2012), (Le Clercq et al. 2010).....	30
Figure 2.7:	Jet A-1 composition: fuel components are grouped into fuel families, for each family the distribution (Wahl 2003).	30
Figure 2.8:	GC-MS chromatogram comparison of CH, F-T CTL, and HEFA with Jet A-1 (Zschocke, Scheuermann, and Ortner 2015).....	31
Figure 2.9:	GC-MS chromatogram comparison of DSHC and ATJ-SPK with Jet A-1 (Zschocke, Scheuermann, and Ortner 2015).....	31
Figure 2.10:	Distillation curve of Jet A-1 and HEFA in comparison with the min and max values of the CRC World Fuel Survey (Johnson and Hadaller 2006) values for Jet A-1 (Zschocke, Scheuermann, and Ortner 2015).....	34
Figure 2.11:	Aromatics content of Jet A-1 during the burnFAIR Jet A-1 sampling program (Zschocke, Scheuermann, and Ortner 2015).....	35
Figure 2.12:	Variation of the density at 15°C inferred during the burnFAIR Jet A-1 sampling program (Zschocke, Scheuermann, and Ortner 2015).....	35
Figure 2.13:	Fuel validation domain for alternative fuel droplet evaporation models.	37
Figure 3.1:	Schematic of different droplet flow configurations in dependency of different droplet Reynolds numbers Re_D : a) Re_D close to zero (quiescent conditions), b) low to intermediate Re_D condition with internal circulation in the droplet and c) high Re_D conditions with complex flow in the droplet and separation region in the droplet wake.	42
Figure 3.2:	Schematic of the spherical symmetric droplet vaporization with heat and mass fluxes.	43

Figure 3.3:	Description of the discrete n-alkane fuel family of Jet A-1 by a Γ -PDF.....	51
Figure 3.4:	Comparison of thermodynamic property models with experimental data for liquid density.	54
Figure 3.5:	Liquid density surrogate for the iso-C ₁₀ H ₂₂ component: the gray lines represent the different isomers; the black line is the surrogate component, which is used to compute the density of iso-C ₁₀ H ₂₂	55
Figure 4.1:	Schematic presentation of the experimental system.....	62
Figure 4.2:	Inlet system: flow conditioner and droplet generator.....	64
Figure 4.3:	Cold flow velocity and turbulence field.....	66
Figure 4.4:	Temperature field.....	67
Figure 4.5:	Schematic view of laser light scattering.....	69
Figure 4.6:	GSI measurement image with noise due to reflections in the quartz tube.....	71
Figure 4.7:	GSI calibration signals at different longitudinal positions, comparing the effect of the quartz tube on the calibration signal.	72
Figure 4.8:	Spray structure: Jet-A1, measurement volumes at a step width of 10 mm.....	73
Figure 4.9:	Spray structure: n-decane, measurement volumes at a step width of 20 mm.	73
Figure 4.10:	N-decane spray, velocity scatter plot and reduction to mean velocity and velocity fluctuations.....	74
Figure 4.11:	Diameter distribution and distribution limits identified by a filter at $z = 5$ mm.....	75
Figure 4.12:	Effect of averaging over the laser sheet (Rauch, Calabria, Chiariello, Le Clercq, Massoli, and Rachner 2011): (a) Sketch of the measurement volume; (b) Size distribution of n-nonane droplets at $z = 80$ mm measured in the upper half and lower half regions of the laser sheet.....	76
Figure 4.13:	Showing the effect of the lower detection limit on the diameter distribution in case of a) experimental measurements and b) numerical simulation.....	81
Figure 5.1:	Scheme of the computational domains with boundary conditions and coordinate system for a) the complete fluid domain and b) test section domain.....	87
Figure 5.2:	Centerplane view of the mesh used.....	90
Figure 5.3:	Comparison of centerline velocities u and velocity fluctuations u' of computations performed in the inlet nozzle domain and test section domain with experimental data.....	91
Figure 5.4:	Hot flow: measured wall temperature profile of the inlet nozzle.	94
Figure 5.5:	Hot flow: measured wall temperature profile of the test track.....	94
Figure 5.6:	Hot flow: measured inlet temperature profile of the co-flow.	94
Figure 5.7:	Hot flow: measured inlet temperature profile of the carrier jet.....	94

Figure 5.8:	Cold flow: comparison of measured and predicted velocity fields.	95
Figure 5.9:	Cold flow centerline velocity and velocity fluctuations, comparison of CFD with measured data.	96
Figure 5.10:	Hot flow: comparison of measured and predicted temperature fields.	97
Figure 5.11:	Hot flow centerline temperatures: Comparison of CFD with measured data.	98
Figure 5.12:	Initial diameter distribution for n-decane injection at $z = 5$ mm.	99
Figure 5.13:	Volume concentration profile for n-decane injection at $z = 5$ mm.	99
Figure 5.14:	Computed injection velocities as a function of the droplet spacing in comparison to experimental mean injection velocity of 2.6 m/s and the computed dilute spray injection velocity of 2.04 m/s at $z = 5$ mm.	101
Figure 5.15:	N-decane diameter validation.	102
Figure 5.16:	N-decane velocity validation.	102
Figure 5.17:	N-decane diameter validation metric.	103
Figure 5.18:	N-decane velocity validation metric.	103
Figure 5.19:	N-decane evaporated spray volume flow rate in comparison with mean diameter. Measurement errors are displayed as grey envelopes around the experimental data.	104
Figure 5.20:	N-decane evaporated spray volume flow metric in comparison with mean diameter metric. Measurement errors are displayed as grey envelopes of the experimental data.	104
Figure 5.21:	Uncertainty of initial temperature distribution for n-decane. Estimation was performed with numerical simulation of the spray heating in the carrier gas flow before the test section with dilute spray assumption and droplet interaction with a fitted droplet spacing $C = 11$	106
Figure 5.22:	Injection parameter combinations of diameter and droplet temperature inferred by Latin Hypercube Sampling.	108
Figure 5.23:	Non-deterministic simulation results of n-decane spray evaporation, each line represent the evolution of the mean diameter for one set of injection conditions.	108
Figure 5.24:	Uncertainty quantification of n-decane evaporation: comparison of experimental data with deterministic computations that are based on a best estimate as spray injection input parameter and non-deterministic computations that take the variations and uncertainties in the injection parameter into account.	108
Figure 5.25:	Main effect of the most dominant input uncertainties: initial mean diameter D_0 , initial droplet temperature T_0 , initial mean velocity u_0 , standard deviation of initial velocity $u_{RMS,0}$, volume concentration profile at injection $vol. flux_0$, and spray center position X_{center} on mean diameter evolution.	109
Figure 6.1:	Jet A-1 composition and CTM description with Γ -PDF.	116

Figure 6.2:	HEFA composition and CTM description with Γ -PDF.....	116
Figure 6.3:	Global accuracy assessment for each fuel for the mean diameter predictions, mean velocity, and volume flow rate predictions.....	119
Figure 6.4:	Ratio of maximum error and mean global error.	120
Figure 6.5:	Position of maximum error for mean diameter, mean velocity, and volume flow rate predictions in comparison to the spray penetration length.....	120
Figure 6.6:	Evolution of the estimated mean diameter and velocity metric.....	122
Figure 6.7:	Comparison of thermodynamic property models with experimental data from (Frenkel et al. 2005) for latent heat of vaporization L_v	123
Figure 6.8:	Comparison of thermodynamic property models with experimental data from (Frenkel et al. 2005) for vapor pressure p_{vap}	123
Figure 6.9:	Validation graphs for the evolution of the diameter distribution.....	124
Figure 6.10:	Comparison of experimental and predicted diameter histograms at $z = 125$ mm for: a) n-Heptane b) n-Decane c) Ethanol d) Hexanol.....	125
Figure 6.11:	Evolution of the estimated mean diameter and velocity.	126
Figure 6.12:	Evolution of the estimated mean diameter and velocity metric.....	127
Figure 6.13:	Evolution of the estimated mean diameter and velocity metric.....	128
Figure 7.1:	Phenomena and interactions in reacting multiphase flows, adopted from Jenny, Roekaerts, and Beishuizen (2012).	135
Figure A.1:	Comparison of thermodynamic property models with experimental data for liquid density.	151
Figure A.2:	Comparison of thermodynamic property models with experimental data for liquid heat capacity.....	151
Figure A.3:	Comparison of thermodynamic property models with experimental data for latent heat of vaporization.	152
Figure A.4:	Comparison of thermodynamic property models with experimental data for vapor pressure.	152
Figure A.5:	Comparison of thermodynamic property models with experimental data for liquid heat conductivity.	153
Figure A.6:	Comparison of thermodynamic property models with experimental data for liquid dynamic viscosity.	153
Figure B.1:	Cold flow, measured carrier jet velocity profile.....	155
Figure B.2:	Cold flow, measured carrier turbulence kinetic energy.....	155
Figure B.3:	Hot flow: velocity profile of the carrier jet, estimated by computations of the inlet nozzle system	155
Figure C.1:	Cross section velocity profiles: Comparison of CFD with measured data.....	158

Figure C.2:	Cross section velocity profiles: Comparison of CFD with measured data.....	159
Figure C.3:	Heating up simulation for carrier jet flow heating up computation, comparison with measured temperature profile at $z = 5$ mm.....	160
Figure C.4:	Diameter validation for n-heptane and n-decane. Left column: comparison of computed with experimental data for diameter evolution. Right column: corresponding validation metrics.	161
Figure C.5:	Diameter validation for ethanol and hexanol. Left column: comparison of computed with experimental data for diameter evolution. Right column: corresponding validation metrics.	162
Figure C.6:	Velocity validation for n-heptane and n-decane. Left column: comparison of computed with experimental data for velocity evolution. Right column: corresponding validation metrics.	163
Figure C.7:	Velocity validation for ethanol and hexanol. Left column: comparison of computed with experimental data for velocity evolution. Right column: corresponding validation metrics.	164
Figure C.8:	Diameter validation for the binary mixtures of n-heptane and n-decane. Left column: comparison of computed with experimental data for diameter evolution. Right column: corresponding validation metrics.....	165
Figure C.9:	Velocity validation for the binary mixtures of n-heptane and n-decane. Left column: comparison of computed with experimental data for velocity evolution. Right column: corresponding validation metrics.....	166
Figure C.10:	Diameter validation for the non-ideal mixtures of ethanol and n-heptane. Left column: comparison of computed with experimental data for diameter evolution. Right column: corresponding validation metrics.....	167
Figure C.11:	Velocity validation for the non-ideal mixtures of ethanol and n-heptane. Left column: comparison of computed with experimental data for diameter evolution. Right column: corresponding validation metrics.....	168
Figure C.12:	Diameter validation for Jet A-1 and HEFA. Left column: comparison of computed with experimental data for diameter evolution. Right column: corresponding validation metrics.	169
Figure C.13:	Validation validation for Jet A-1 and HEFA. Left column: comparison of computed with experimental data for diameter evolution. Right column: corresponding validation metrics.	170

List of Tables

Table 2.1	Distribution of fuel components in fuel families for Jet A-1 and alternative aviation fuels (Gupta, Roquemore, and Edwards 2014).....	32
Table 2.2	Structural representation of fuel families, which can constitute the composition of conventional and alternative aviation fuels.....	32
Table 4.1	Overview of the uncertainties of the measured quantities.....	77
Table 4.2	Uncertainty components of the GSI uncertainty equation.	78
Table 4.3	Uncertainty components for the vertical position y	79
Table 4.4	Droplet velocity uncertainties.....	80
Table 5.1	Classification of the flow field boundary conditions for the test section domain by type of method used to determine the values.....	88
Table 5.2	Classification of the spray injection conditions for the complete fluid domain and the test section domain by the method used to determine the values.	89
Table 5.3	Cold flow: flow field boundary conditions for the complete fluid and test section computational domains.	92
Table 5.4	Hot flow: flow field boundary conditions for the complete fluid and test section computational domains.....	93
Table 5.5	Spray injection conditions for the n-decane spray.....	99
Table 5.6	N-decane global validation metrics for diameter, velocity, and volume flow rate.....	104
Table 5.7	Summary of uncertainties in the spray injection conditions for the n-decane spray.	106
Table 6.1:	Validation domain: single component fuels.....	115
Table 6.2:	Validation domain: binary mixture fuels.	115
Table 6.3:	Validation domain: non-ideal mixture fuels.	115
Table 6.4:	Validation domain: fuels with a high number of components.	115
Table 6.5:	Parameter for the Γ -PDF representing Jet A-1 fuel families (mean Θ , standard deviation σ , origin γ).....	116
Table 6.6:	Parameter for the Γ -PDF representing HEFA fuel families (mean Θ , standard deviation σ , origin γ).....	116
Table 6.7	Comparison of global accuracy assessment results for the different fuel categories.....	118

List of Symbols

Latin Letter Symbols

A	[m ²]	area
B_M	[-]	Spalding mass transfer number, Eq. (3.13)
B_T	[-]	Spalding heat transfer number, Eq. (3.5)
C	[-]	spacing between droplets
$CCD_{\text{mm/px}}$	[mm]	physical dimension of a pixel on a CCD
C_D	[-]	drag coefficient
c_l	[moles/m ³]	liquid molar density
$C_{\text{px/rad}}$	[-]	GSI calibration constant
c_p	[J/(kg K)]	specific heat at constant pressure
D_{10}	[μm]	mean diameter of droplet diameter distribution
D_d	[m]	droplet diameter
D_g	[m ² /s]	diffusion coefficient in gas mixture
D_{RMS}	[μm]	standard deviation of diameter distribution
$f(I)$	[kg/kmol]	probability density function of the mole fraction
$F(B)$	[-]	Abramzon's function
\vec{F}_D	[N]	drag force
\vec{F}_g	[N]	gravitational force
F_i	[-]	correction Factor for non-ideal mixtures
\vec{g}	[g/mm ²]	standard acceleration of gravity
h	[J/kg]	specific enthalpy
I	[kg/kmol]	distribution variable
P	[Pa]	pressure

P_{ATM}	[Pa]	atmospheric pressure (= 101325 Pa)
P_{vap}	[Pa]	vapor pressure
r	[m]	radial coordinate
\dot{Q}_{vap}	[W]	droplet heating rate
Re	[-]	Reynolds number
Sc Sc	[-]	Schmidt number
Sh ₀	[-]	Sherwood number without Stefan flow
Sh _{eff}	[-]	effective Sherwood number
S_{H}	[J/s]	parcel energy source term
S_{K}	[J/s]	parcel turbulent kinetic energy source term
S_{M}	[kg/s]	parcel mass source term
S_{V}	[N]	parcel momentum source term
t	[s]	time
T	[K]	temperature
m	[-]	complex refractive index
\dot{m}	[kg/s]	vapour mass flow rate
M_{OoF}	[1]	out of focus magnification
m_{p}	[kg]	droplet mass
Nu ₀	[-]	Nusselt number without Stefan flow
Nu _{eff}	[1]	effective Nusselt number
\dot{N}_{P}	[real particles/s]	parcel loading
\vec{v}'_{gas}	[m/s]	gas velocity fluctuation
\vec{v}_{gas}	[m/s]	mean gas velocity
v_m	[m/s]	mean velocity of droplets in the spray
\vec{v}_{p}	[m/s]	droplet velocity

\vec{v}_{rel}	[m/s]	relative velocity between droplet and gas
Vol / Vol_0	[-]	normalized spray volume flow rate
Wt	[g/mol]	Molecular weight
x_p	[-]	mole fraction
y_p	[-]	mass fraction

Greek Letter Symbols

α	[kg/kmol]	distribution parameter
β	[-]	distribution parameter
γ	[kg/kmol]	distribution parameter
γ_{ac}	[-]	activity coefficient
$\Gamma(\alpha)$	[kg/kmol]	gamma function
δ	[m]	film thickness
Δh_{vap}	[J/kg]	specific enthalpy of vaporization
ΔI	[kg/kmol]	step of distribution variable
$\Delta\vartheta$	[rad]	fringe spacing
ζ_i	[kg i/s / kg/s]	ratio of vapor mass flow rate for the species i over the global vapor mass flow rate ($\zeta_i = \dot{m}_i / \dot{m}$)
ζ_j	[kg j/s / kg/s]	ratio of vapor mass flow rate for the group j over the global vapor mass flow rate ($\zeta_j = \dot{m}_j / \dot{m}$)
η	[-]	modification factor for vapor mass flow rate, taking into account the effect of nearby droplet by correlation with droplet spacing
θ	[kg/kmol]	mean distribution parameter
ϑ	[rad]	scattering angle
Λ	[-]	Wilson parameter
λ	[W/(m s)]	thermal conductivity

μ	[kg/m s]	dynamic viscosity
σ	[kg/kmol]	standard deviation of the distribution parameter
Ψ	[kg/kmol]	2 nd moment of the distribution parameter

Subscripts and superscripts

b	boiling conditions
c	critical conditions
d	droplet
g	gas
<i>i</i>	single fuel species
<i>j</i>	fuel family = group of fuel species
l	liquid
max	maximal value
min	minimal value
proj	projection perpendicular to the free stream velocity vector
prec	precision
ref	1/3-reference state in the gas boundary layer around the droplet
S	droplet surface
vap	vapor
∞	far-field conditions (state outside the gas boundary layer around the droplet)

Acronyms

ATJ	Alcohol to Jet
CFD	Computer Fluid Dynamics
CH	Catalytic Hydrothermolysis
CTM	Continuous Thermodynamics
DCM	Discrete Component Model
DNS	Direct Numerical Simulation
DSHC	Direct Sugar to HydroCarbon
FAE	Fatty Acid Esters
F-T	Fischer-Tropsch
GC-MS	Gas Chromatography-Mass Spectrometry
GMO	Genetically Modified Organisms
GSI	Generalized Scattering Imaging
HEFA	Hydroprocessed Esters and Fatty-Acids
LES	Large Eddy Simulation
LHS	Latin Hypercube Sampling
OEM	Original Equipment Manufacturers
PDF	Probability Density Function
SIP	Synthesized Iso-Paraffins
SKA	Synthetic Aromatics in the Kerosene boiling range
SPK	Synthetic Paraffinic Kerosene
SRQ	System Response Quantities
V&V	Verification & Validation

Abstract

Environmental and security of supply concerns cause an increasing demand for alternative fuels in aviation. Different fuel production pathways for alternative aviation fuels have been suggested and approved in recent years. In that respect, changes in fuel production can result in various fuel compositions and properties and thus impose a risk for the use in the aircraft and jet engine; the ASTM D4054 approval process was developed to warrant the safety of flight. Nevertheless, tests are expensive and time-consuming. Particularly for the combustion testing part, numerical simulations can be beneficially used to reduce costs and time. Furthermore, virtual prototyping and robust design methods might be essential in supporting the design of fuel flexible combustion chamber with reduced emissions. The use of simulation in the context of decision making in situations with risks related to humans and the environment raises the questions how reliable and accurate simulation results are.

In this work, new methods are applied that have been developed for scientific computing. The focus of these methods is on supporting simulation informed risk-related decision making as the final recipient of validation activities. Hereby, it is of essential importance that metrics describing the accuracy of the models over the domain of application are inferred systematically. Furthermore, by reporting the influence of uncertainties in input quantities on the response quantities, the reliability of the simulation results can be increased substantially.

Evaporation is an important sub-process of the fuel preparation in a combustion chamber and depends strongly on the fuel composition and properties. Conventional Jet A-1 and most alternative aviation fuels consist of several hundred of different species. Continuous Thermodynamic Models (CTM) have been successfully used in recent years to describe multicomponent-fuel droplet evaporation of real fuels. CTM capture the details of the fuel evaporation while preserving the information of the fuel composition over the evaporation process with low computational load. Up to the present, validation activities have been performed by comparing numerical simulation results with experimental data from suspended droplets experiments. These tests proved the functionality of the concepts successfully. However, the fuel composition was unknown, and the droplet suspension had a strong intrusive effect. Thus, the validations are limited to qualitative statements.

In this work, a validation domain was derived from the character of actual and future alternative aviation fuels to determine quantitative metrics for alternative aviation fuel evaporation models systematically. Experiments with different fuels from the validation domain were performed in a newly designed experiment. The validation experiment enables to study the evaporation of a wide range of fuels under controlled conditions in a non-intrusive way. Global and local metrics for the evaporation models were inferred. The effect of uncertainties in the

spray injection conditions on simulation results was determined by using Latin Hypercube Sampling to sample the input domain and to propagate the uncertainties through the governing equations. The resulting uncertainties in the simulation result can be interpreted as the precision of the validation approach. Validation metrics, as well as the precision, give future users (modeler, analyst and decision maker) all information required to assess the model adequacy for the intended use and, if necessary, to determine next actions to improve the model or the validation experiment.

Kurzfassung

Um die langfristige Versorgungssicherheit mit flüssigen Treibstoffen in der Luftfahrt sicherzustellen und die ökologischen Auswirkungen zu minimieren, wurden in den letzten Jahren verschiedene Herstellungspfade für alternative Treibstoffe entwickelt und zugelassen. Jede Änderung im Herstellungspfad hat jedoch einen Einfluss auf die Zusammensetzung des Treibstoffes und birgt somit ein Risiko bei der Nutzung des Treibstoffes in Flugzeug und Triebwerk. Die Zuverlässigkeit der Nutzung neuartiger Treibstoffe wird durch aufwendige und kostenintensive Tests nach dem ASTM D4054 Zulassungsverfahren sichergestellt. Numerische Simulationen haben das Potential, die Zeitdauer von Verbrennungstests beim Zulassungsverfahren maßgeblich zu verkürzen und Kosten einzusparen. Darüber hinaus können der virtuelle Entwurf und Methoden der Entwicklung von robusten Designs eine wesentliche Unterstützung beim Entwurf von neuen brennstoffflexiblen und schadstoffärmeren Brennkammern sein. Hier muss jedoch die Frage gestellt werden, wie zuverlässig und belastbar die aus numerischen Simulationen gewonnenen Informationen sind und inwieweit sie als Basis für Entscheidungen mit Konsequenzen für die Sicherheit von Mensch und Umwelt dienen können.

In dieser Arbeit werden neue Methoden für die Validierung von numerischen Modellen angewandt, die im Bereich des wissenschaftlichen Rechnens in den letzten Jahren entwickelt wurden. Das risiko-informierte Entscheiden, basierend auf aus Simulationen gewonnenen Daten, steht hier als Endprodukt im Fokus. Dabei ist es zum einen von wesentlicher Bedeutung, die Genauigkeit der verwendeten Modelle quantitativ und systematisch über den Anwendungsraum der Modelle zu erfassen. Zum anderen wird die Zuverlässigkeit der Modelle maßgeblich erhöht, indem die Auswirkung von Unsicherheiten in den Eingangsgrößen auf relevante Zielgrößen in die Untersuchung einbezogen wird.

Die Verdunstung ist ein wichtiger Teilprozess der Treibstoffaufbereitung in der Brennkammer, der unter anderem stark von den Treibstoffeigenschaften und somit der Treibstoffzusammensetzung abhängt. Konventionell hergestelltes Jet A-1 und ebenso die meisten alternativen Luftfahrttreibstoffe bestehen aus hunderten Einzelkomponenten. Um die Mehrkomponenten-Verdunstung realer Treibstoffe abbilden zu können, wurde in den letzten Jahren die Methode der kontinuierlichen Thermodynamik erfolgreich angewandt. Diese Methode ermöglicht es, Veränderungen in der Treibstoffzusammensetzung während der Verdunstung detailliert wiederzugeben und ist dabei sehr rechenzeiteffizient. Bisherige Validierungen wurden durch den Vergleich von Simulationsergebnissen mit Daten durchgeführt, die aus Experimenten an aufgehängten Tropfen gewonnen wurden. Durch diese Tests wurde die Funktionalität der Modelle erfolgreich nachgewiesen, jedoch war die Zusammensetzung der

Treibstoffe nicht bekannt und die Tropfenaufhängung hatte einen stark intrusiven Einfluss. Damit sind bisherige Validierungen des Modelles nur auf qualitative Aussagen beschränkt.

In dieser Arbeit wurde, basierend auf den Charakteristika aktueller sowie potentieller alternativer Treibstoffe, eine Validierungsdomain für Luftfahrttreibstoffe abgeleitet. Diese ermöglichte es, systematisch quantitative Metriken über die Genauigkeit von Verdunstungsmodellen für alternative Luftfahrttreibstoffe zu bestimmen. In einem neu entwickelten nicht intrusiven Validierungsexperiment wurde die Verdunstung verschiedener Treibstoffe aus der Validierungsdomain unter kontrollierten Bedingungen detailliert untersucht. Anhand der gewonnenen experimentellen Daten und Simulationsergebnisse konnten globale und lokale Validierungsmetriken abgeleitet werden. Der Einfluss von Unsicherheiten in den Spraystartbedingungen auf die Simulationsergebnisse wurde mittels Latin Hypercube Sampling bestimmt. Die resultierenden Unsicherheiten in den Simulationsergebnissen können als Präzision des Validierungsexperimentes interpretiert werden. Die Validierungsmetriken sowie die Information über die Präzision des Validierungsexperimentes ermöglichen dem zukünftigen Nutzer die Adäquatheit des Modells für den Einsatzbereich zu bewerten und gegebenenfalls Maßnahmen für die Verbesserung des Modells oder des Validierungsexperimentes vorzuschlagen.

1 Introduction

1.1 Motivation

Environmental (IPCC 2007) and supply security concerns cause an increased demand for alternative fuels in the transport and energy sectors. This is especially the case for aviation where the long-term dependency on liquid fuels is the strongest. This push for a change yielded in the development of different fuel production pathways to create aviation fuel from a variety of feedstock in recent years. However, resulting fuel products are different with respect to petroleum-based fuels. Although alternative fuels can consist of several hundreds of different hydrocarbon fuel components like it is for Jet A-1, the distribution of components in hydrocarbon fuel families differs remarkably. Furthermore, in some fuel production pathways, additional complexities can arise due to the addition of molecules of different nature than conventional hydrocarbons. Therefore, the properties of the fuel and thus the fuel-dependent processes in the jet engine might vary. Although such a change can be beneficial for the performance, the jet engine operability has to be guaranteed under all circumstances and for all engine types.

From a historical viewpoint, the development of jet engines and fuels was interdependent and strongly tied together. The first jet engine, the He S3A, was successfully developed and tested by Hans-Joachim Pabst von Ohain in 1937. He employed hydrogen as a fuel for the first run of the engine. Due to the low volumetric energy density of hydrogen and its effect on the design of the aircraft he then switched to gasoline (Edwards 2003). In the same year, the Whittle engine developed by Sir Frank Whittle first ran successfully on a test bench and used petroleum as fuel. In the following years, several different designs had been tested, finally resulting in basic design features of gas turbine combustors (Lefebvre and Ballal 2010) in the 1950s. At the same time, the definition of several fuel standards, like the Jet A-1 (DERD-2494) standard in England, as well as the Jet A (ASTM D-1655) and JP-4 (MIL-F-5624) standards in the United States, set the range of possible fuels for jet engines. The following period from 1960 to 2005 was characterized by an interdependent development of jet engines and fuel specifications to solve operational problems encountered like coking (Edwards 2003).

As described above, jet engines are complex systems that have been evolving iteratively over the years. The design methods usually applied were of empirical nature, based on experimental characterizations of different generations of jet engines, all utilizing conventional jet fuels. The introduction of new fuels changes the underlying assumption of using petroleum-based

1 Introduction

jet fuels and thus requires gaining a basic understanding of the effects of new fuel compositions on the major processes in a combustion chamber.

Figure 1.1 shows a conventional rich-burn-quench-lean-burn combustor with the main thermochemical processes. The primary air enters the combustion chamber through a diffuser to reduce the velocity and thus to minimize pressure loss in the combustion zone. The liquid fuel is injected into the primary zone of the combustor. Atomization of the liquid jet yields an increase of the total surface area by a large number of small droplets. The subsequent evaporation creates the fuel vapor required for ignition and contributes to sustaining combustion. Carefully designed air injection generates a toroidal flow reversal in the primary zone. The flow recirculation yields a low-velocity region to anchor the flame and to use the burned products as a hot air source to provide continuous ignition of the incoming fuel-air mixture. Through the liner wall, secondary air is injected to quench the primary region, which burns rich. In the final part of the combustion chamber, the dilution zone, air is used to dilute the combustion products and to design a temperature profile, which is beneficial for the downstream turbine.

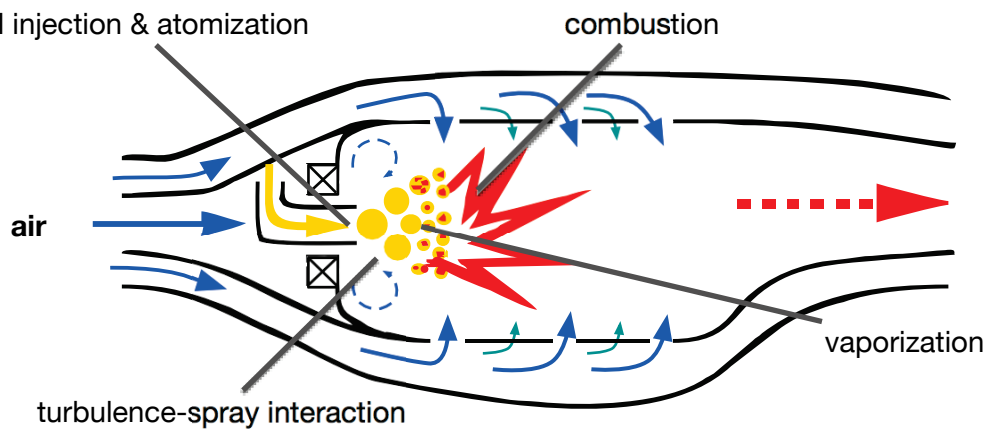


Figure 1.1: Scheme of a conventional combustion chamber showing the basic thermochemical processes.

To prioritize the fuel property which affects engine safety and operability, two priority levels of combustor performance issues have been introduced by a team of engine manufacturers (General Electric, Pratt & Whitney, Rolls Royce/LibertyWorks, Honeywell, and Williams) (Edwards, Moses, and Dryer 2010): Of highest priority are cold-day ignition limits, lean blowout limits, and altitude relight limits. The temperature field, combustion efficiency, emissions, as well as combustor coking were defined as of secondary importance. As the fundamental processes influencing the primary combustor performance issues, the atomization, evaporation, and flammability are named. Each of the processes are driven by a combination of fuel properties: liquid viscosity, liquid density, and surface tension in case of the atomization process, liquid specific heat, latent heat of vaporization, and vapor pressure in case of the evaporation process, flammability limits, ignition delay, flame speed, extinction strain rate, and flame temperature in the case of flammability (Lefebvre and Ballal 2010; Edwards, Moses, and Dryer 2010).

To quantify the fuel effects, extensive tests resulting in high costs have to be conducted. In this context, the time saving and cost effectiveness of robust design methods by virtual prototyping would be highly beneficial. Furthermore, combustor developments in future decades will be based on detailed knowledge of the processes occurring in combustion chambers, inferred by advanced diagnostic techniques and numerical simulation. As an example out of many, Edwards et al. (2010) and Law (2011) state that numerical simulation can be used as a beneficial tool to understand the effect of different fuel compositions on combustion performance. Nevertheless, they also indicate that advances in detailed sub-models and methodologies are required to build the necessary predictive capabilities.

However, the application of numerical simulation in the case of the approval process of new alternative fuels or simulation-based design of combustion chambers represent situations with possible effects on human safety or mission success. To be part in such risk-related decision-making, the reliability and fidelity of the models applied have to be expressed as objective, quantitative measures of how the model agrees with reality for the intended use. As shown before, the fuel preparation is one of the processes with a major influence on engine safety and operability. Subsequent processes to the evaporation like ignition or pollutants formation can strongly depend on the local composition of the gaseous mixture. Thus, evaporation models that shall be used in the robust design of combustion chambers need to be able to capture the multicomponent nature of the fuels. The focus of this study is to assess the accuracy of droplet evaporation models for alternative fuels. A rigorous and systematic model testing and the analysis of the influence of all the process-inherent uncertainties are required to define reliable quantitative measures of the model accuracy.

1.2 Literature Review

Several approaches to model the evaporation of multicomponent-fuel droplets have been developed in recent years, tailored to solve specific engineering problems. However, to be used for the robust design of combustors or simulation-informed decision-making, new standards in supporting the reliability and accuracy of the applied models must be reached. In recent years, the development of methods of verification and validation has been pushed forward as a response to the needs of simulation-informed decision-making in high consequence situations. In the following sections, the state-of-the-art in validation methods and the degree of validation of multicomponent-fuel droplet evaporation models are summarized. Based on this extensive review, the objectives of this study are defined.

1.2.1 Multicomponent-Fuel Droplet Evaporation Models for Aviation Fuels

In the case of multicomponent-fuel evaporation models, the first developments focused on modeling the phenomena of droplet interior mixing. This resulted in the formulation of six widely acknowledged types of models (Sirignano 1999): (i) constant droplet-temperature (or frozen-limit)

model (ii) infinite liquid-conductivity (or rapid mixing) model, (iii) spherically symmetric transient conduction-limit model, (iv) effective-conductivity model, (v) vortex model, and (vi) Navier-Stokes solution. Another phenomenon of interest were micro-explosions (Law 1982). Micro-explosions are due to violent internal gasification of fuel components and lead to a secondary atomization of the droplets, which can be beneficially used for heavy fuel oils or highly viscous fuels.

While the studies above have been limited to rather few-component mixtures (mainly binary mixtures), for the modeling of real fuel additional complexities are introduced. On the one hand, the number of components is too high to solve the conservation equations for each component in a computationally efficient way suitable for industrial applications. On the other hand, the characterization of such complex fuels is difficult, and often information is missing for the complete description of the fuels.

For aviation fuels, the number of components is in the range of hundreds and constitutes significantly to the complexity of the modeling problem. In the following, different multicomponent-fuel droplet evaporation models are summarized and discussed in their capability of modeling alternative aviation fuels.

Single Component Surrogates Models

To solve the issue of a vast number of fuel components, different simplifications, and models have been developed. In combustion environments, discrete component models using either iso-octane (C_8H_{18}) to represent gasoline, or n-decane ($C_{10}H_{22}$) to represent Jet A-1 or tetradecane ($C_{14}H_{30}$) to represent diesel fuel have often been used. An alternative approach is to define a single component surrogate fuel mimicking the properties of the real multicomponent-fuel like it was done for Jet A-1 by Rachner et al. (1996). Such single component surrogates are based on extensive literature reviews (Rachner 1998) and often yield good results on a global scale. However, single component surrogates are not able to capture important details, like the selective evaporation of components that influences the fuel/air mixture preparation significantly. Thus, they can have a relevant influence on ignition and emission processes (Lippert and Reitz 1997; Le Clercq and Bellan 2005a; Ra and Reitz 2009; Le Clercq et al. 2010).

Discrete Component Models

Discrete Component Models (DCM) represent the fuel with a finite number of compounds. Real fuels are very complex, and the composition is often unknown. Therefore, to model the fuel for DCM, additional information about the characteristics of the real complex fuels is utilized. Commonly, the distillation curve is employed to characterize the fuel and also to estimate the fuel properties with techniques common in petroleum refining (Pedersen, Fredenslund, and Thomassen 1989; Riazi 2005). One approach is to divide the distillation curve into different fractions building pseudocomponents (Riazi and Al-Sahhaf 1996), which are identified by their carbon number. Based on historical data each pseudocomponent has a corresponding PNA

composition (PNA: Paraffin's, Naphthenes, Aromatics), which is used to estimate the required properties. In Ochs (1999) and Ochs, Gass, and Reh (2001), this method was applied with very good results for evaporation of monodisperse sprays of light heating oil in a hot turbulent flow. However, since the method is based on historical data gained solely from conventional crude-derived fuels, it is not easily applicable to alternative fuels.

With recent advances in techniques for the detailed characterization of fuels, DCMs with carefully selected components of the real fuel mixture are being applied (Ra and Reitz 2009; Abianeh and Chen 2012). This was enabled especially by the developments of the advanced distillation curve method (Bruno 2006; Bruno and Smith 2006; Smith and Bruno 2007b; Smith and Bruno 2007a). This approach characterizes the fuel by its distillation curve and simultaneously measures selected thermophysical properties like for example density, viscosity, and vapor pressure. Based on the measurement data, combinations of components that best represent the measured fuel characteristics can be selected. This strategy aims explicitly at the representation of the physical behavior of the fuel, in contrast to surrogates, which model the chemical kinetic behaviors of the fuels (Bruno and Smith 2010; Bruno and Huber 2010). DCMs based on physical surrogates are very promising but require a complex apparatus for the fuel characterization. Furthermore, by reducing the number of components, information about the full fuel composition is lost during the process and thus ignoring the influence of neglected components in subsequent processes.

Distillation Curve Model

A model considering a large number of components is the distillation curve model (Bardon and Rao 1984; Bardon, Gauthier, and Rao 1990; Chin 1994; Burger et al. 2003). Instead of the composition, it utilizes the distillation curve to describe the progress of evaporation. The distillation curve model captures the multicomponent-fuel effects on the evaporation process by considering the volatility differences. It is computationally very efficient. However, the fuel composition is unknown and has to be assumed to allow a detailed description of the gas phase combustion processes.

Continuous Thermodynamics Models

Continuous Thermodynamics Models (CTM) use the information of the fuel composition to build a probabilistic description of the fuel. They had first been developed in petroleum refining industry (Katz and Brown 1933; Kehlen, Rätzsch, and Bergmann 1985) to describe the complex petroleum fraction by a statistical approach. Instead of taking into account each component, which is often unknown in petroleum processing, the fuel composition is described by distribution functions. CTM was first applied by Tamim and Hallett (1995) and Hallett (2000) for multicomponent-fuel droplet evaporation and extended to more complex compositions like non-ideal mixtures and pyrolysis oils or fatty acid ester fuels (Hallett and Clark 2006; Hallett and Beauchamp-Kiss 2010; Hallett and Legault 2011). The composition is commonly described by

using Gamma distribution functions coming along with restrictions due to the monomodal shape of the distribution function. This might cause problems in the specific case of condensation (Harstad, Bellan, and Le Clercq 2003) or can introduce model errors in regard to complex compositions. Doué et al. (2007) and Le Clercq et al. (2009) applied Fourier series to represent more complex shapes of fuel distributions and to improve robustness with regard to Gamma-PDFs. Recently, quasi-discrete components based on CTM have been developed. Arias-Zugasti and Rosner (2003) used truncated spectral expansions to approximate the PDF of the fuel composition and (Laurent et al. (2009; 2010) used a quadrature method of moments to represent the PDF by a variable set of quasi-discrete components based on Dirac delta peaks. This quasi-discrete component method was later on extended by Sazhin et al. (2011) and Elwardany and Sazhin (2012) to include the effective conductivity models and to model complex fuel composition by different fuel families (Sazhin, Qubeissi, Nasiri, et al. 2014).

CTM evaporation models are computationally very efficient and maintain the information about the evolution of the fuel composition in the liquid and gas phase. However, additional assumptions and simplifications are introduced concerning often-tested DCM models. For example, in CTM models simplified thermodynamic descriptions of the fuels are required, which cause uncertainties in the model simulation results.

1.2.2 State-of-the-Art of validation for CTM evaporation models

During the development of CTM evaporation models (Abdel-Qader and Hallett 2005; Hallett 2000; Tamim 1996), Hallett stated that rigorous experimental testing with well-characterized mixtures is required. He subsequently applied CTM to fuels of different complexities, pyrolysis oils (Hallett and Clark 2006), ethanol-fuel oil mixtures (Hallett and Beauchamp-Kiss 2010) and biodiesel (Hallett and Legault 2011). For these fuels, validation studies had been performed by comparing the CTM predictions with data from suspended droplet experiments carried out by the group of Hallett. Due to the lack of information about the fuel composition, the composition of the pyrolysis oils tested was estimated based on literature values. For the fuel oil and biodiesel, the composition of the fuel was also unknown and estimated by a parameter fitting based on continuous thermodynamics simulation of the ASTM D-86 distillation curve.

Reitz et al. applied CTM in internal combustion engines (Lippert and Reitz 1997; Lippert et al. 2000; Zhu and Reitz 2001; Zhu and Reitz 2002; Ra and Reitz 2005; S. Yang and Reitz 2009; S. Yang and Reitz 2010; S. Yang et al. 2010). For the validation, literature data of suspended droplets (Kadota and Hiroyasu 1976; Gökalp et al. 1994; Nomura et al. 1997) were used. Since no details about the fuel composition in the experiment were available, the composition was based on experience from literature.

Bellan et al. implemented CTM for Direct Numerical Simulation (DNS) and Large Eddy Simulations (LES) computation (Harstad, Le Clercq, and Bellan 2003; Harstad, Bellan, and Le

Clercq 2003; Harstad and Bellan 2004a; Le Clercq and Bellan 2004a; Harstad and Bellan 2004b; Le Clercq and Bellan 2004b; Le Clercq and Bellan 2005a; Le Clercq and Bellan 2005b; Selle and Bellan 2006; Selle and Bellan 2007a; Selle and Bellan 2007b; Selle and Bellan 2007c; Selle and Bellan 2008; Bellan and Selle 2009). In these studies, no validation activities were reported. Only Le Clercq and Bellan (2004b) stated that the new CTM model performs well compared with a model validated in Miller et al. (1998). The validation activities in Miller et al. (1998) were based on suspended droplet using single component fuels.

Le Clercq et al. applied CTM for aviation and alternative aviation fuels (Doué, Le Clercq, and Aigner 2006; Doué, Le Clercq, and Aigner 2007; Le Clercq et al. 2009; Le Clercq et al. 2010). Validation activities had been carried out based on measurements of the evaporation of a monodisperse spray of single component fuels (n-octane and n-tetradecane) and light heating oil droplets in preheated flow (Ochs 1999). Since no information about the fuel composition of the light heating oil was available, the strategy of Ochs was applied. Ochs estimated the fuel composition with single carbon number groups (Riazi and Al-Sahhaf 1996). The single carbon number pseudo-components were then described as a Gamma-PDF and Fourier series.

Kong and Zhang applied CTM for the use in internal combustion engines and alternative automotive fuel (Zhang and Kong 2009; Zhang and Kong 2010; Zhang and Kong 2011; Zhang and Kong 2012). Validation activities had been carried out for DCM, modeling biodiesel droplet evaporation on suspended droplets (Gökalp et al. 1994; Nomura et al. 1997; Morin, Chauveau, and Gökalp 2000). No validation activities for the CTM models were reported.

The quasi-discrete component model was developed for aviation (Laurent, Lavergne, and Villedieu 2010; Laurent, Lavergne, and Villedieu 2009), Sazhin et al. later on extended it for the use in internal combustion engine (Sazhin, Qubeissi, Nasiri, et al. 2014; Sazhin, Qubeissi, Kolodnytska, et al. 2014; Elwardany, Sazhin, and Farooq 2013; Elwardany and Sazhin 2012; Sazhin et al. 2011). No validation activities were reported in these studies.

As from now, validation activities to assess the accuracy of CTM models have been performed mainly by comparing the model with experimental data from suspended droplet experiments. Suspended droplet experiments are preferably used because there is a considerable amount of information available in the literature. They are easy to perform and to model. Additionally, they represent a unit case focusing on droplet evaporation (or combustion). For a quantitative assessment of the model accuracy, these kinds of experiments have some severe drawbacks. The major one is the intrusive effect due to the suspension of the droplet. It introduces a heat transfer from the fiber (J.-R. Yang and Wong 2001) into the droplet and modifies the mixing in the droplet (Shringi, Dwyer, and Shaw 2013). The suspension has a complex influence on the droplet vaporization rates, which varies with fiber diameter, droplet Reynolds number and ambient temperature (Shringi, Dwyer, and Shaw 2013). Furthermore, it

influences the droplet shape corrupting the spherical shape assumptions that many evaporation models are based on. Also, the diameter range of 0.5 mm to 1.5 mm is one order of magnitude higher than typical droplet diameters in combustion chambers, which are around [30 – 100] μm in size. This results in different phenomena and flow fields inside the droplet; a scaling to smaller sized droplets is questionable. In consequence, suspended droplet experiments introduce many uncertainties and undetermined parameters thus undermining a reliable quantitative accuracy assessment.

In addition, in the validation mentioned above activities, the composition of the fuel was unknown. It is thus a primary source of uncertainty in the model input variables. To reduce the uncertainty, distillation curve measurements are often used for the fuel characterization. Therefore, distillation curve measurements based on the ASTM D-86 standard (ASTM 2012) seem to be beneficial since they are widely accepted and used in industry. Furthermore, distillation measurements are included as a matter of course in the fuel specifications (Bruno 2006), thus making such measurements highly available. However, as pointed out in the work of Bruno (2006) and Satyro et al. (2009), significant uncertainties are inherent to ASTM D-86 measurements: Measured temperatures have only little theoretical significance because they are not corresponding with true thermodynamic state points. However true thermodynamic state points are required in the surrogate development to model the distillation curve. Distillation curves with true thermodynamic state points can be inferred by two methods (Satyro and Yarranton 2009), the advanced distillation curve method (Bruno 2006) or the vacuum potstill method (ASTM 2013). Consequently, the use of the ASTM D-86 for fuel characterization leads to uncertainties in the formulation of the fuel composition and thus in the fuel evaporation simulations.

1.2.3 Validation Standards

Validation in computer science is often used as a loose concept to show in some way that the modeling results correspond well with reality and are plausible. However, discussions about how to prove the truth of theories is one of the oldest philosophical questions. In the context of numerical simulations, the question is strictly speaking not about the absolute truth, but to use the words of George E. P. Box “All models are wrong, but some are still useful.” – It is about finding the useful models for the intended application. For virtual prototyping, a new emphasis is put on model reliability; validation metrics as a measure to state quantitatively how close the model reflects reality are of fundamental importance. In the last 40 years, verification and validation (V&V) standards have been developed to systematically increase the reliability of models and their use for high consequence situations.

In 1998, the American Institute of Aeronautics and Astronautics (AIAA) published a guide of V&V (AIAA 1998) focusing on the field of Computational Fluid Dynamics (CFD). The guide introduced concepts like that the accuracy assessment in validation must only be performed by

comparison of simulation results with experimental measurements since only experimental measurements represent the best measure of reality. Based on the AIAA Guide for CFD, the American Society of Mechanical Engineers (ASME) developed a guide for V&V in computational solid mechanics and published it in 2006 (ASME 2006). The guide was formulated in a general way and can be applied to other disciplines. It comprehensively links all V&V activities to form a V&V plan from end-to-end. The plan starts with the abstraction of reality to build the models and flows finally into a decision point about model adequacy assessment for the intended use of the model. Furthermore, the concept of uncertainty quantification for numerical simulation is introduced. Uncertainties in the numerical simulation results are due to variability in model parameters, lack of knowledge of the parameters, and errors due to the model form (assumptions and simplifications). In uncertainty quantification, the effect of uncertainties on response quantities is quantified and used in the evaluation of the validation metric. In 2009, the ASME published a standard for V&V in CFD and heat transfer (ASME 2009). This standard is formulated as a step-by-step guide to infer the validation metric under consideration of uncertainties in the experimental data and in the numerical simulation. In contrast to the more philosophical definitions of error and uncertainty in the two beforehand published guides from AIAA and ASME, the standard applies the ISO guide for the expression of uncertainties in measurements (ISO Guide 1995), which is a methodology to infer uncertainties in experimental and numerical solution results.

Between the two ASME standards, there are basic differences. The (ASME 2009) standard focuses on the application of the ISO guide for expressing uncertainty in measurements (ISO Guide 1995) to define a unique way of determining uncertainties for measurement and numerical simulation results. The (ASME 2006) guide instead, applies the concepts of irreducible uncertainty (also called aleatory uncertainty) and reducible uncertainty (also called epistemic uncertainty), which were defined in the risk assessment community. The definition of reducible uncertainty has the advantage of enabling strategies on how to decrease uncertainties in the system response quantities and thus to improve the accuracies of simulation results. The concepts presented in the following are based on the book of Oberkampf and Roy (2010), which represents the most extensive work. The book itself extends the standards as presented by ASME (2006).

There are even more V&V standards, their number, and their different application contexts result sometimes in conflicting definitions. The basic definitions of V&V used in this work are summarized as follows:

Verification: the process of determining that a computational model accurately represents the underlying mathematical model and its solution. (ASME 2006)

Validation: the process of determining the degree to which a model is an accurate representation of the real world from the perspective of the intended uses of the model. (DoD 1994)

Prediction: use of a computational model to foretell the state of a physical system under conditions for which the computational model has not been validated. (AIAA 1998)

Validation plan

The ASME (2006) validation plan from end-to-end will be applied for this study. It emphasizes that in a validation study, the validation experiment and the validation metric have to be defined in a way to be significant for the person, who decides if the model is adequate for the intended application. The decision maker is usually the analyst who has to choose which models to apply or the project leader who needs to decide how to proceed on the basis of simulation results.

Figure 1.2 shows the sequence of operations for a validation study from end-to-end. The starting point is the reality that has to be abstracted to build on the one hand the model and on the contrary the validation experiment. As mentioned before, it concludes with the assessment of the model adequacy for the intended use of the model by the decision maker. The concepts of validation as described in ASME (2006) can be categorized into three distinct aspects (Oberkampf and Trucano 2008):

- 1) Assessment of model accuracy by comparison with experimental data;
- 2) Interpolation or extrapolation of the model for the intended use;
- 3) Decision of model adequacy for intended use.

In aspect 1) the experimental results and simulation results are reduced to System Response Quantities (SRQ) that are useful in the context of intended applications. To give a measure of the reliability of the data, the uncertainties in the SRQ need to be quantified. Uncertainties considered are from measurement uncertainties but also from uncertainties in the simulation results. To finally infer the validation metric, different operators can be used. The choice of the operator depends mainly on the mathematical nature of the SRQ (deterministic or probabilistic).

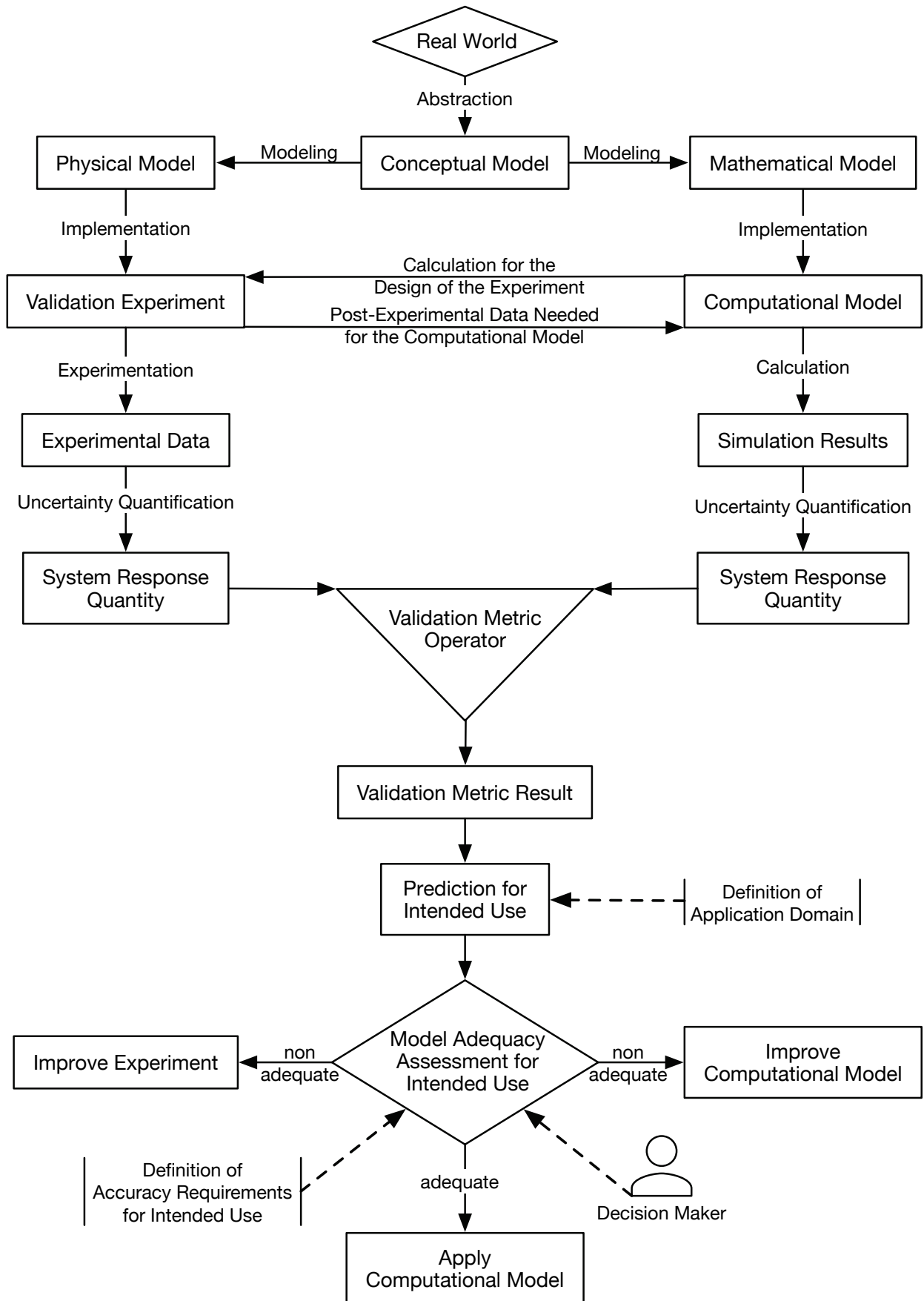


Figure 1.2: Validation plan from end-to-end (adapted from (ASME 2006; Oberkampf and Trucano 2008).)

The second aspect of the validation plan (Figure 1.2) is to perform simulations in the application domain. If the model is interpolated or extrapolated depends on the relation between validation and application domain, as depicted in Figure 1.3: model interpolation is given in the case of the intersection of validation domain and application domain. Thus the validation metric can be interpolated to the application conditions. When the validation domain does not cover the application domain, extrapolation of the validation metric is required. Since the validation metric is a measure of the uncertainties in the models, the ability to perform extrapolations depends on the nature of the models. In the case of models based on physical laws, the validation metric can be connected to uncertainties in the model form. Thus, mathematical models can be suggested to extrapolate the model form uncertainty to the application domain. However, with increasing distance between the validation and application point, the model form uncertainty estimation becomes highly erroneous.

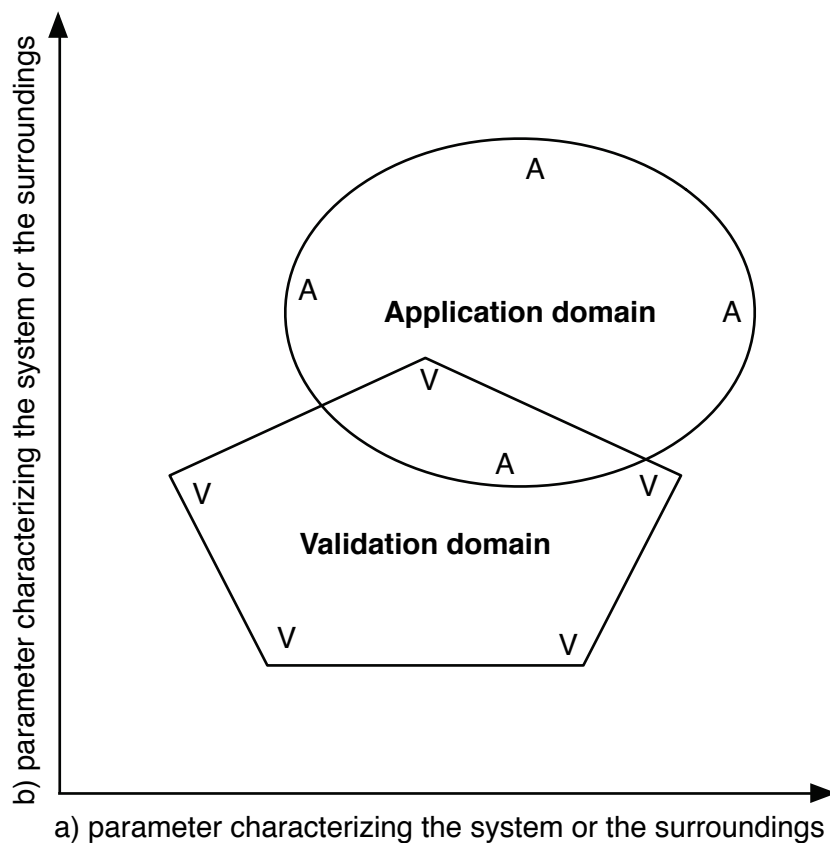


Figure 1.3: Relationship between validation and application domain (Oberkampf and Roy 2010).

The final step (aspect 3) in the end-to-end validation plan is to assess the model adequacy. It requires the information about the inter- or extrapolated validation metric and a quantitative definition of maximum allowable uncertainty over the parameter range of the intended use of the model (Oberkampf and Roy 2010). It should be mentioned, that the decision maker who evaluates the model adequacy should be the person responsible for using the information from the simulation and ideally not the person who developed the model or assessing the model

adequacy. So that the decision maker can define the next actions in the case that the model is inadequate for the intended application, it is important to track the influence of the origin of the uncertainties throughout the validation process. This requires some distinct difference from traditional validation concepts, which are summarized in the following.

Validation Experiments versus Traditional Experiments

In general, traditional experiments can be grouped into three categories (Oberkampf and Roy 2010): physical-discovery experiments, model development experiments, and qualification tests. Although the aim of these three types of experiments is different, they have a common emphasis on the characterization of processes in a controlled environment. The controlled environment is essential to ensure the repeatability of the experiment. For validation experiments instead, the emphasis is on inferring all the important characteristics of the experiment, which are required for the simulation. Repeatability is of second order importance, as long as the variability is characterized well. Since the purpose of a validation experiment lies in the assessment of the accuracy of the mathematical model (Oberkampf and Roy 2010), uncertainties due to undetermined experimental parameter should ideally be nonexistent.

The most prominent reason why traditional experiments fail as validation experiments is that relevant information for simulation input is not available or poorly characterized (Oberkampf and Roy 2010). In order to identify all-important characteristics that need to be measured, a strong interaction between the experimenter and modeler during the design phase is very beneficial and should be included in the validation plan as shown in Figure 1.2.

Model Form Uncertainty

To infer the validation metric, ideally simulation results without uncertainties and solution errors would be compared with measurement data without uncertainties. In such a hypothetical case, the validation metric would directly reflect the uncertainties in the model form. Model form uncertainties are created mainly in the process of abstraction and formulation of the mathematical models. They are due to the assumptions and simplifications made concerning the physical reality to derive the models and can be categorized into omission, aggregation, and substitution type (Pegden, Shannon, and Sadowski 1995; Oberkampf and Roy 2010). Omission means that certain physical characteristics or processes are ignored, aggregation means the combination, or lumping into similar characteristics and substitution denotes the replacement of complex characteristics by simpler characteristics. Thus, depending on the definition of the validation experiments, specific aspects of the model can be tested. The validation metric allows to evaluate the effect of the model form uncertainty for the given conditions and thus to improve the quality of physics modeling.

Uncertainty Quantification

In reality, uncertainties in the experiments and simulations complicate the validation and model development process. Experiments represent only the best measure of reality and exhibit uncertainties due to measurement errors or undetermined parameters. While it is now common to provide the uncertainty of measurement results to support the reliability of the measurements by well-recognized standards as the Guide to the Expression of Uncertainty in Measurement (ISO Guide 1995), uncertainties in numerical simulation results are often ignored.

Uncertainties in numerical simulation results can originate from numerical solution errors, uncertain inputs to the model, and model form uncertainties from the model including sub-models (Oberkampf and Roy 2010). Following the ASME (2006) guide, uncertainties in numerical simulations can be categorized into irreducible or reducible uncertainties. Irreducible uncertainties follow statistical distributions and can, for example, be due to variations in geometry or material properties. Reducible uncertainties originate from the model form uncertainty or a lack of complete information or knowledge (ASME 2006). They can be lowered by acquiring more knowledge. Since input parameters for numerical simulations are often determined from measurement data, the characterization of the model input parameters in the validation experiment and resulting uncertainties in the simulation are tightly connected.

Next actions for an inadequate model

When the model is assessed as inadequate for the intended use, two possible next steps as shown in Figure 1.2 can be undertaken: If the validation metric is dominated by uncertainties due to experimentally determined model input quantities or by uncertainties in the measured SRQ, the experiment has to be improved. If the validation metric is dominated by uncertainties of the model form, the computational model has to be improved.

1.3 Objectives

Developments in recent years are aiming at enabling the use of numerical simulation for virtual prototyping and robust design. Concerning the use of numerical simulation to facilitate the introduction of alternative fuels, it requires, on the one hand, detailed models capable of capturing the relevant details like the multicomponent nature of the fuels. On the other hand, the predictive capabilities of the models have to be supported by systematic validation activities focusing on inferring the model accuracy quantitatively over a range of relevant parameters. The objective of this study is the accuracy assessment of multicomponent-fuel droplet evaporation models for alternative aviation fuels. This requires:

- Definition of a validation domain covering conventional jet fuel, existing alternative aviation fuels, and potential alternative aviation fuels.

- Development of a validation experiment with very well characterized experimental parameters and capable of accurately characterizing the evaporation of a variety of different fuels.
- Experimental and numerical investigation of fuels sampling the validation domain. To minimize model input uncertainties, the composition of the fuel has to be well characterized.
- Quantification and identification of the uncertainties inherent in the overall validation approach.
- Definition and development of validation metrics appropriate for the evaluation of the model adequacy for future uses.
- Analysis of the validation metrics to identify potential model form uncertainties.

1.4 Chapter Overview

In this study, new and detailed data for the accuracy assessment of alternative fuel evaporation will be presented. In chapter 2, the validation domain consisting of fuels of different complexities is derived. The historical viewpoint on the interdependent historical evolution of fuels and jet engines builds a framework for estimating the direction of future development of alternative aviation fuels.

The origin of the model form uncertainties for multicomponent-fuel droplet evaporation models is outlined in chapter 3 by presenting the assumptions and simplifications made while formulating the spray evaporation models and included sub-models.

The validation experiment for freely falling monodisperse sprays under atmospheric conditions is shown and characterized in chapter 0. The abilities and constraints of the validation experiment, as well as the procedure to infer the validation data sets, are displayed to give relevant details for the interpretation of the data.

In chapter 0, the conceptualization of the validation experiment is discussed. The data set of n-decane is used as a benchmark case to assess the characteristics of the validation approach. Results of uncertainty quantification computations evaluating the influence of model input uncertainties on simulation results are presented and analyzed concerning their impact on the validation metric.

In chapter 6, the validation metrics for a variety of different fuels across the validation domain are inferred and discussed. Validation metrics are defined in a way that the user of the information (modeler, analyst or decision maker) can extract the relevant information in the context of future model applications. Although validation activities are performed in a unit case of evaporation, the focus in the analysis and interpretation of the data has to be on the intended use of the models: fuel preparation in gas turbine combustion chamber.

In chapter 7, implications of the model capabilities in modeling alternative fuel evaporation in technical relevant conditions are discussed, and next steps are suggested.

2 Validation Domain for Alternative Aviation Fuel

Being able to infer the model accuracy for all circumstances in which the model will be used represents the ideal case of model validation. Such an agreement of validation domain with the application domain allows a reliable interpolation of the quantitative model accuracy information to the given application conditions. However, alternative fuels for aviation are quite new, and developments are ongoing.

Only recently in 1998, the first synthetic fuel blend, the Sasol semi-synthetic jet fuel, was approved by the Ministry of Defence (MOD) in the UK. In turn, it was included in the Defense Standard 91-91 (DS91-91) (Great Britain Ministry of Defence 2008), which is the standard defining Jet A-1. In 2009, the F-T-SPK fuel specifications were fixed by ASTM International in the ASTM D7566 standard (ASTM International 2014b) in Appendix A in 2009. It was followed by the approval of Hydroprocessed Esters and Fatty Acids-SPK (HEFA) based fuel blends in 2011 and by the approval of Synthesized Iso-Paraffins (SIP) produced from Direct Sugar to HydroCarbon (DSHC) in 2014. Additional different pathways are in development and in the approval process.

To understand future developments that have the potential to shape the validation domain, a historical viewpoint is taken and the milestones, which led to the development of modern jet fuels, are discussed. The definition of the validation domain concluding this chapter is based on characteristics of existing and potential alternative aviation fuels. Particular attention is paid to include conditions that lead to concerns by Original Equipment Manufacturers (OEM) in the approval process due to missing experience bases.

2.1 Influencing Factors on the Development of Jet Fuels

Liquid fuels have been a source of energy for a long time. In the beginning, the main purpose of the fuels was lighting, but with the invention of engines, the demand for liquid fuels increased rapidly. In the 1870s, for safety reasons the kerosene cut was used for lighting purposes, the remaining gasoline cut was cheap and prone to be used for the newly developed engines. Several years later, facts changed, and with the broad application of electrical light, the kerosene cut became cheap and was a welcomed energy source for diesel engines.

As displayed in the previous example, technological evolutions had a significant impact on the usage of liquid fuels. Fuel as an energy storage is affecting our daily lives. As will be shown in the historical overview of the phases, which led to the definition of jet fuels, jet fuel definition is a

result of interdependent evolutions. Constraints and opportunities characterizing the design space are mainly determined by fuel specifications, the approval process to include new fuels into the standards, and the technical possibilities imposed by existing and emerging fuel processing technologies.

2.1.1 Phases of Jet Fuel Development

The evolution resulting in the actual definition of jet fuel can be categorized into five phases as exemplified in Figure 2.1. The pre-phase summarizes the historical understanding of liquid fuels from their first uses up to the first utilization in a combustion engine. In the early use of liquid fuels, fuels were applied to generate power in different kind of combustion engines. In the phase following the Second World War, experiences made during the war were formulated and standardized to fuel specifications to allow a worldwide and secure use of fuels in aviation. The efforts, which had been made, opened the doors for the world wide commercial aviation use. With the standards been set, the following phase was focusing on the refinement of fuel specification to minimize operational problems encountered. First attempts to use fuels produced from a different feedstock than crude oil in aviation gas turbines have been made in the US already in the 1980s. Starting from 2005, focused progress is being made to introduce fuels from alternative sources into jet fuel specifications and the phase of specification enlargement began and is still ongoing.

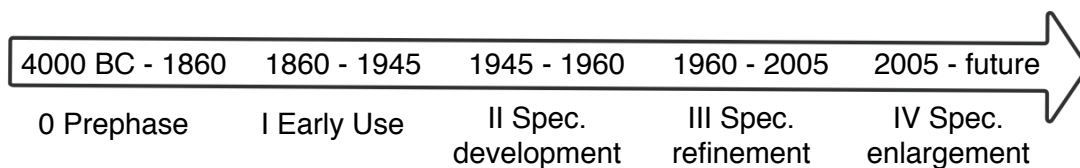


Figure 2.1: Timeline with different phases of jet fuel development.

Prephase: Before Combustion Engines (4000 BC – 1860)

The use of petroleum can be dated back long ago in history. It was used for different purposes, for the construction of buildings, as medicine, in warfare and as an energy source for heating or lighting. The name petroleum is derived from the Latin *petra* “rock” and *oleum* “oil.” It has always been a limited resource, limited by its occurrence and accessibility, sometimes occurring in oil springs, as shale oil, or tar sands.

The first refinement of crude oil for the use in lamps and heating home can be dated back to 2200 BC in China (Cleveland and Ayres 2004) but played a minor role. Normally beeswax, vegetable oils, animals fats like tallow or whale oil have been used for lighting purposes (Kovarik 1998; Knothe 2012). In the 16th century, the superior burning behavior of whale oil started industrial whaling. Due to lower prices, camphene, a mixture of 50-80% ethyl alcohol with turpentine (mainly from pines), was starting to replace whale oil as a lighting fuel in the 1830s. By

1860, distilleries in the US sold 30 to 80% of their alcohol production to the fuel market, which corresponds to 340 million liters a year.

Although petroleum products have been known and used through the history, the biggest breakthroughs have been in the middle of the 19th century, with Gesner extracting kerosene from coal in 1846 and 1853 the developments of Ignacy Lukasiewicz of distilling kerosene from petroleum oil. Initially, the kerosene had problems to compete with the cheaper camphene and was not well seen due to its strong odor. Further refinements and the invention of a safe and odorless kerosene lamp improved the kerosene's competitiveness remarkably (Lucier 2010).

Besides that the oil rush started in 1859, by Edwin Drakes first commercial oil well, petroleum-derived fuels had to still compete with the cheaper camphene. In 1859 the price of coal derived kerosene was 1.2\$ a gallon and thus twice as high as for camphene, which costs were around 50 cents a gallon (Lucier 2010). To raise money during the American Civil War (1861-65) a tax of 2.08\$ per gallon was imposed on alcohol. From one day to the other, the well-established ethanol industry could not compete anymore with the now strongly growing petroleum industry. (Kovarik 1998) reports that the evolution was quite different in Europe. In countries like France, Germany, and Great Britain concerns about the security of petroleum supply existed in the beginning, and thus the utilization of ethanol was promoted (Knothe 2012). However, improvements in the kerosene distillation process and the future utilization of internal combustion engines manifested the dominant use of petroleum worldwide.

Early Use in Combustion Engines (1860 – 1945)

At the beginning of the development of internal combustion engines, ethanol was often used as a fuel. This was the case for the engine developed and sold by Nikolaus Klaus Otto in 1862 (Kovarik 1998). At this time petroleum derived kerosene was beginning to be widely used as a lighting fuel. However, the gasoline cut from petroleum oil had little use, since due to its low flash points, it was too dangerous to be used as a lighting fuel. Thus it was cheap and highly available (Kovarik 1998). Already in 1876, the famous four-stroke version of the internal combustion engine developed by Otto was running mainly on gasoline but was adaptable to ethanol and benzene derived from coal (Kovarik 1998).

Even though ethanol showed a very satisfactory level of performance in Otto engines and in 1908 the alcohol tax in the US was abandoned, the ethanol industry could never establish again. One reason was that the petroleum industry had built up a strong lobby, and was telling that ethanol was an inferior fuel (Kovarik 1998). Despite this fact, in the 1920s and 1930s, gasoline-ethanol blends have been used worldwide (Kovarik 1998). In summary, one can say that the competition between crude oil derived and 'alternative' fuels based on renewable, domestic feedstock's is not a new concept (Knothe 2012).

Start of the aviation age

At the 14th December 1903, the brothers Wright started the aviation age. At this time, there was a high diversity of fuels available, coarsely divided by their distillation range. For their first flight the brothers Wright used a self-constructed gasoline powered engine (Edwards 2003).

In 1907 the first U.S. Government fuel specification was released, specifying the specific gravity of the fuel and “that it shall not be contaminated with material that would leave a residue after fuel evaporation” (Edwards 2007). In the following period, especially during the World War I, experiences about the effect of fuel differences were made. Subsequently, the autoignition phenomena and its effects (preignition, knocking, pinging) was related to the fuel characteristics (Edwards 2007) and regulated in the fuel specifications.

In the following decades, engines were improved yielding in new requirements for the fuels and the development of new fuel test methods (Edwards 2003). Performance property requirements, like the octane number, were introduced (1930) and resulted in a quest for reaching higher and higher performance levels, as in the case of the U.S. Army X3575 avgas specification with a 100/130-octane/performance number requirement. These developments challenged refiners and initiated the development of new fuel processing methods (Edwards 2003).

Jet engine development

During World War II the first jet engines had been developed. In 1939, the Heinkel 178 was the first aircraft powered by a turbojet engine, which had been developed by Dr. Hans von Ohain. Von Ohain first chose hydrogen as a fuel, “but due to vehicle considerations, he switched to gasoline” (Edwards 2003). In 1941, the first Whittle engine (developed by Sir Frank Whittle) was flying in a Gloster Meteor aircraft. Whittle considered diesel oil as a fuel, but freezing point requirements lead him to use illuminating kerosene (Edwards 2003).

Jet Fuel Specification Development (1945 – 1960)

Similar to the first development of avgas specifications, in the period after the World War II experiences made were used to develop fuel standards for the use in jet engines. Starting from knowledge based on the developments of avgas specifications, the jet fuel specifications had to be adapted to the “new boundary conditions” by the new technology: higher flight altitudes required a specified freezing point, and limitations were imposed on the vapor pressure to prevent “vapor lock” and loss of fuel (Maurice et al. 2001.)

However, the first jet fuel standards failed due to too restrictive performance property regulations and the neglect of the interdependence of fuel properties (Maurice et al. 2001). With piston engine powered aircrafts and avgas fuel specifications already well established, the potential use of jet engines instead was unclear for fuel refiners. The situation changed over the years when ongoing efforts were taken to develop new jet engines, thus supporting the

economic interest. Learning from precedent failures, fuel refiners were strongly involved in the successful definition of new jet fuels specifications.

The middle distillate fraction in the kerosene range proved to be an ideal compromise, being well suited for the use in jet engines (Maurice et al. 2001). It is nice to notice, how the economic relevance of petroleum fractions changed over the years. With electricity becoming the largest source of power for lighting and the strong growth of car transportation, the former leading force in fuel economy, the illuminating kerosene became an unused, cheap byproduct, ideally suited for the new emerging jet age. Two fuels emerged in this situation a naphtha/kerosene mixture called JP-4 in the United States (MIL-F-5624) and a kerosene fuel called Jet A-1 in England (DERD-2494) and Jet A (ASTM D-1655) in the U.S. (Edwards 2003).

Jet Fuel Specification Refinement (1960 – 2005)

The year following the initial definition of the JP-4 and Jet A-1 specifications were determined by adding refinements enabled by the evolution of test methods and additives to solve operational problems encountered (Edwards 2003). For example, to prevent coking, additives were developed, which increased the thermal stability of the fuels. During this time, the maxim was to find “the best compromise to balance the engine performance requirements technology needs, fuel cost economic factors, and fuel availability strategic factors” (Edwards 2007)

Also, the evolution of the refinery industry was firmly connected to the feedstock available, as reported by (Maurice et al. 2001). In the first years high-quality low sulfur crude oils enabled the production of fuels by straight atmospheric distillation. The ease of implementation resulted in a variety of small refineries producing fuels. By the years the high-quality crude oil depleted and had to be replaced with crude, high in sulfur and difficult to refine (Maurice et al. 2001). Finally, environmental regulations to phase out leaded gasoline take effect in the 1990s in U.S. and lead to the closing of the small independent refineries (Maurice et al. 2001).

Jet Fuel Specification Enlargement to Include Alternative Fuels (2005 – Future)

Starting with the energy crisis in the 1970s, different programs in the U.S. were started investigating the potential use of non-petroleum feedstocks. The research focused on synthetic jet fuels from coal, oil shale, or tar sands. The efforts concluded with successful engine tests and flight demonstrations for shale-derived fuels that “JP-4 specification was restrictive enough to provide adequate fuel, regardless of the hydrocarbon source” (Edwards 2007). However, such a synthetic fuel was found to be “too costly, both on economical and environmental grounds” (Maurice et al. 2001).

In the 1990s, the aviation sector in South Africa started growing fast. To meet the growing demand, Sasol (South African Synthetic Oil Limited) wanted to produce synthetic aviation fuels (Moses and Roets 2009). In 1991, Sasol started communication with the ASTM committee, requesting the approval of synthetic jet fuels. Finally in 1998, the semi-synthetic jet fuel was

included in UK Defense Standard 91-91, Issue 3 (Great Britain Ministry of Defence 2008) and after July 1999 the fuel was being delivered to Johannesburg Airport (Moses and Roets 2009).

Modification of the fuel standards due to changes in process technology was not new. As reported by Wilson et al. (2013) with advancing refining technology, hydroprocessed fuel components had been used to blend aviation fuels. Since these fuel components are prone to oxidation, the aviation fuel standards were modified to require a treatment of the hydroprocessed components with approved antioxidants (Wilson et al. 2013). However, the request of Sasol to produce synthetic hydrocarbons derived from non-petroleum feedstock (coal), by processing technology (Fischer-Tropsch (F-T)) differing much from conventional jet fuel production processes, was a significant departure from experience and required an extensive approval procedure (Wilson et al. 2013).

After their first success, Sasol went on, and in April 2008, the Sasol Fully Synthetic Jet Fuel was qualified and implemented in DS91-91 (Great Britain Ministry of Defence 2008). With the fuel crises and the growing awareness of human induced global warming in 2008, a tipping point was reached. Research and development activities started worldwide aiming to produce environmentally friendly fuels based on alternative feedstocks. The approvals of the two Sasol fuels had been performed on an individual and site-specific basis; a process not viable for the number of new fuel candidates coming up. With the experience made with the Sasol fuels and by testing a number of different fuels from various producers (all using the F-T processes), it was shown that such fuels are sufficiently similar to allow a general approval of F-T derived SPK (Synthetic Paraffinic Kerosene) as a blend (Moses 2007; Moses 2008).

2.1.2 Fuel Specifications and Alternative Fuel Approval Process

The two major jet fuel specifications for the aviation industry are the Defense Standard 91-91 (DS91-91) (Great Britain Ministry of Defence 2008) of the Ministry of Defence in the UK defining Jet A-1, and the ASTM D1655 (ASTM International 2013), defining Jet A. The fuel specifications are not explicitly defining the composition, but instead are a combination of minimum and maximum requirements on performance, material and manufacture properties. How this requirement results in an effective range of possible composition is displayed in Figure 2.2. The ternary diagram uses the n-alkanes, cycloalkanes, and aromatics to describe the fuel composition. For the sake of simplicity, iso-alkanes have been grouped with cycloalkanes by de Klerk (2012). One can see that a range of different compositions can fulfill the fuel requirements. However, the underlying assumption is the use of crude-oil derived fuels, which has implications on the fuel characteristics, as will be seen later on in section 2.2.

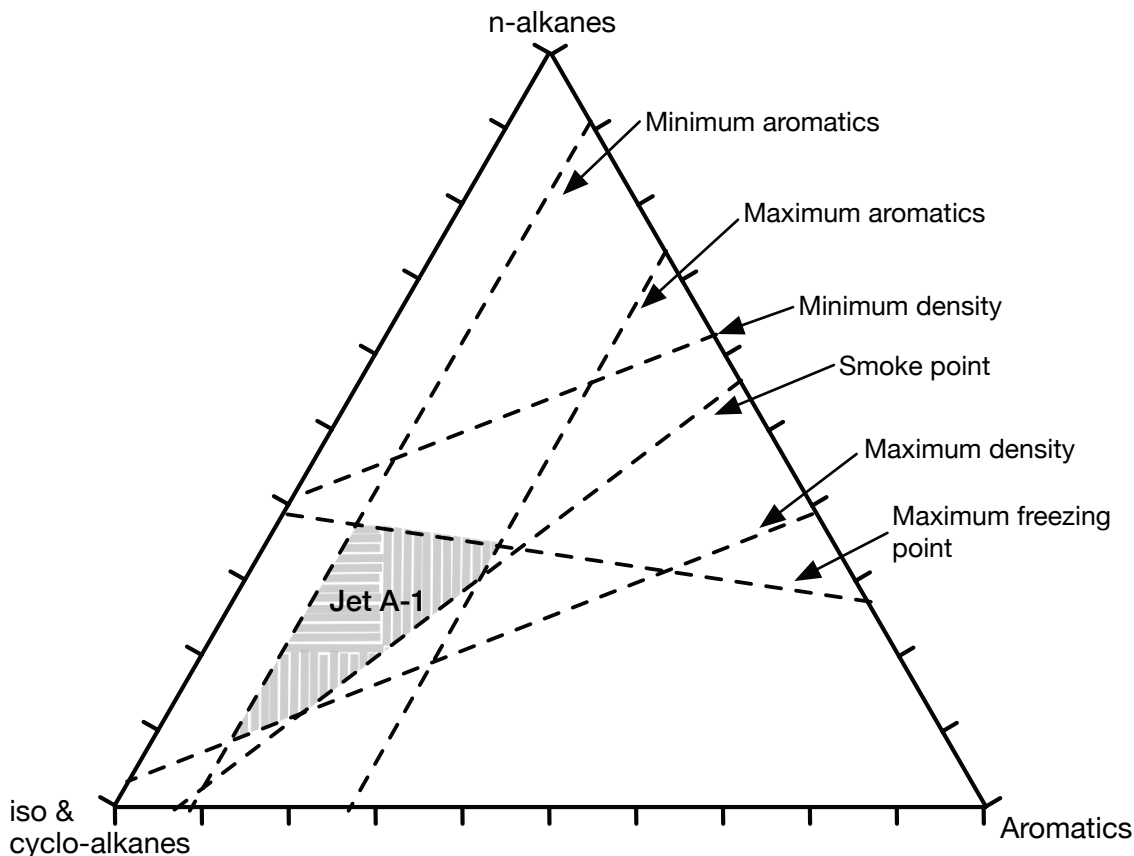


Figure 2.2: Effective fuel composition range to fulfill ASTM D1655 and DS91-91 fuel specifications, adapted from (de Klerk 2012).

In 2009, based on the experiences and processes developed for the certification of the Sasol Semi-Synthetic Jet Fuel, the ASTM D4054 standard was modified to include approval procedures of new aviation turbine fuels. Also, the ASTM D7566, the standard specification for aviation turbine fuels containing synthesized hydrocarbons, was released. With this fuel specification, the drop-in fuel concept was formalized, stating that a fuel certified to fulfill ASTM D7566 could be treated as a fuel certified by the ASTM D1655, the standard specification for aviation turbine fuels. In a subsequent step, the UK Ministry of Defence (MOD) linked the Defense Standard 91-91 to ASTM D7566, stating that any fuel approved by the ASTM D7566 is approved by the MOD Defense Standard 91-91.

Figure 2.3 shows the scheme of the ASTM D4054 approval process. In incremental steps with increasing complexity and amount of fuels required, fuel candidates are tested by (1) evaluation the specifications properties, (2) evaluation of fit-for-purpose properties, (3) turbine hot section testing, (4) component testing, and finally, if required, (5) engine testing and flight testing. Each step has to be reported in-depth, and each time the fuel properties are evaluated critically. If the fuel candidate passed all the tests successful, finally a committee of OEM's has to decide if the fuels can be used securely with their equipment.

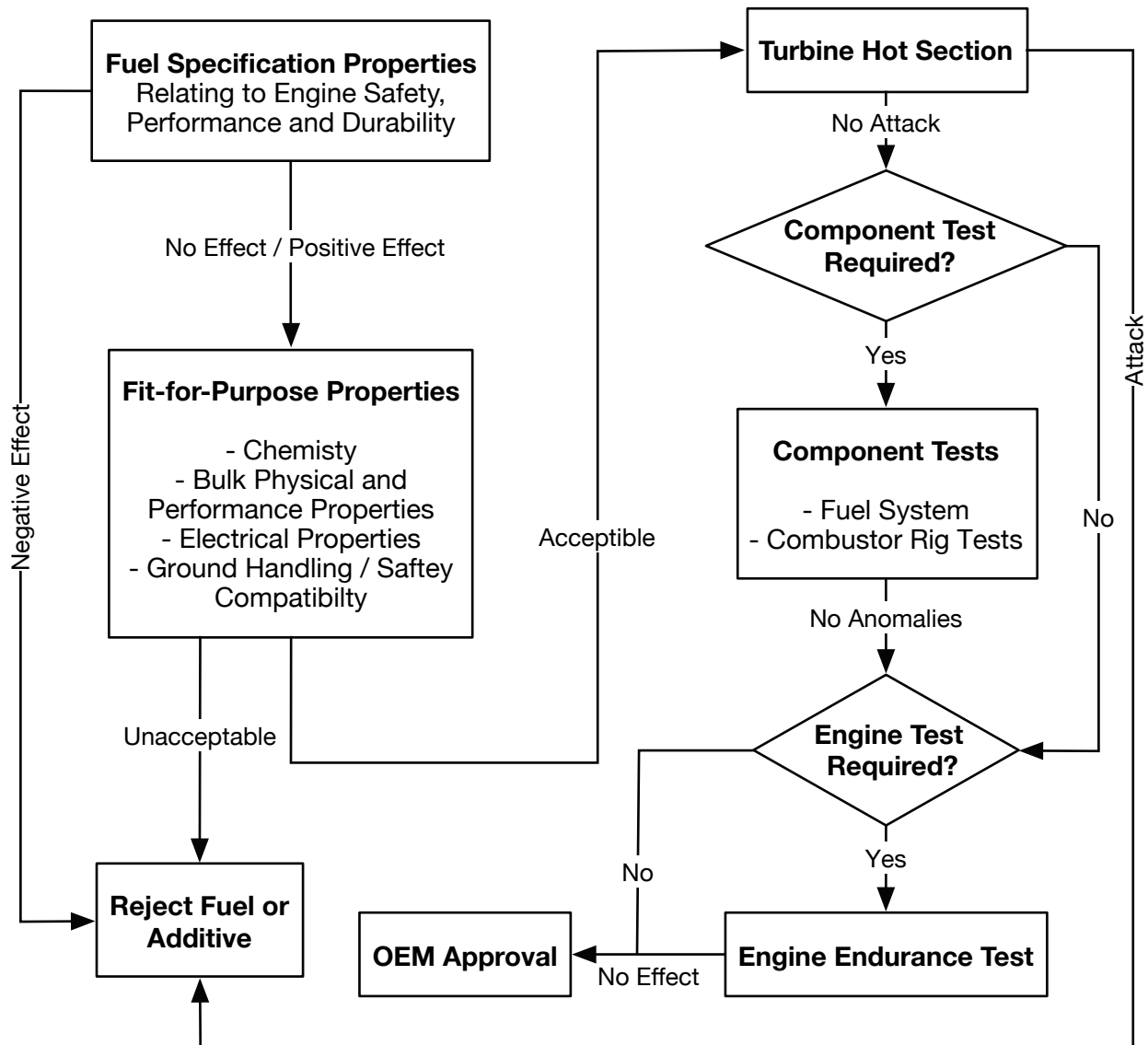


Figure 2.3: Test program for the approval of new aviation turbine fuels (ASTM International 2014a).

Since not all critical parameters can be tested, a combination of property tests and performance tests are performed. Not all properties have specified limits, but are compared to the range of properties based on former experiences with Jet A-1, mainly from the World Fuel Survey Program (Johnson and Hadaller 2006). Since the lifespan of jet engines is very long, fit-for-purpose tests have to cover several generations of jet engines. It is of utmost importance to understand the critical issues, relevant to the design and operation of an aircraft. New fuels/fuel blends have to prove very limited effects of the fuel difference concerning standard jet fuels as described by ASTM D1655 or DS91-91 under the various circumstances and operation conditions possible in aircraft operation. Such an approval process requires a strong collaboration of fuel producer, fuel certification facilities and organizations and Original Equipment Manufacturers (OEMs).

2.1.3 Fuel Processing Technology

The fundamental question of fuel processing is how to convert energy containing feedstocks into mixtures of higher-value molecules, which can be used in today's or future aircraft. An overview of the possible pathways for the production of jet fuel or jet fuel blends is given in Figure 2.4. In general, feedstocks can be divided into two groups; one based on fossil resources, the other from renewable biomass resources. From the processing point of view, the feedstocks are raw starting materials and need a pre-treatment. By removing undesirable constituents and by densification it is prepared for an efficient conversion. Depending on the feedstock, different key technological components can be used to convert the feedstock either on a thermochemical or biochemical route. The processes differ in flexibility and selectivity, namely the ability to convert the feedstock into the desired product with a proper overall conversion rate. After the principal processes, most pathways will finally use well-established methods, in common refineries, to upgrade their products to the desired liquid fuel or fuel-blending component.

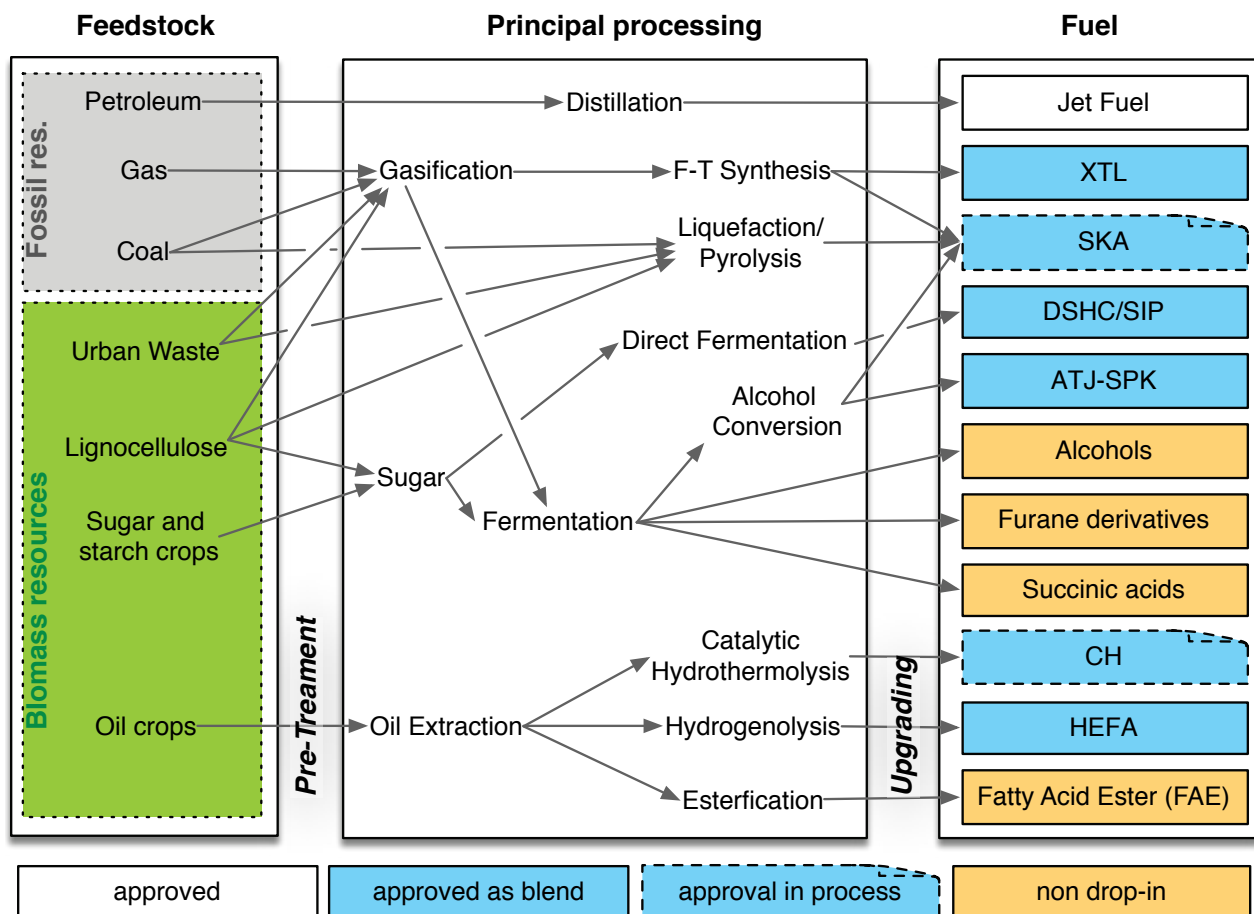


Figure 2.4: Alternative jet fuel pathways adapted from Blakey et al. (2011).

The resulting fuel products can be categorized by their applicability into three parts: a) approved jet fuel, b) drop-in jet fuel blends (approved or approval in progress) and c) non drop-in fuels or fuel blends. Furthermore, it can be thought of an additional category: near drop-in fuels. These fuels infringe the fuel specifications in minor parts, like using fuels with no or a very low

aromatic content, and thus increase the availability, reduce the manufacturing costs, or have specific advantages like reduced soot emission for no aromatic fuels. To unlock such a potential, the effect of such specification infringements on the aircraft system has to be understood so that appropriate counteraction with near term applicability can be undertaken.

Approved Fuels or Fuel Blends

In the simplest version of traditional jet fuel production, the jet fuel is extracted from the crude petroleum oil by fractional distillation. As described in Aitani (2004) the higher demand on specific oil products and growing market specifications, challenged oil companies and refineries; in response, new processes were developed to maximize the yield into highly specified products. In the 1920s thermal-cracking processes, like visbreaking and coking have been developed to convert also higher boiling point fractions into higher value fuel products. To maximize the yield and to produce high-performance fuels, catalytic processes have been developed in the early 1940s. In the 1960s, several catalytic and noncatalytic processes like catalytic cracking, alkylation, isomerization, hydrocracking, reforming have been developed to respond to stronger specification and increase gasoline yields. This development continued into high-conversion refineries existing nowadays with specialties practices.

The Fischer-Tropsch (F-T) process is a catalytic synthesis process that requires synthesis gas as an input. In general, there are two main F-T synthesis processes, which can be used to produce the fuel blend. The first is a low-temperature F-T synthesis utilizing a cobalt catalyst to produce a mixture of normal and iso-paraffins. Such F-T SPKs were approved by DoD for the DS91-91 in 1998 and by ASTM international in 2008. The second is a high-temperature F-T synthesis process with an iron-based catalyst to produce hydrocarbon mixtures containing n-, isocycloparaffins and single ring aromatic in the jet fuel boiling range. The Fully Synthetic Jet fuel was approved by DS91-91 in 2009, the approval from ASTM International is ongoing. The F-T process is very feedstock flexible, considering that the synthesis gas can be obtained from biomass or coal by gasification, directly from natural gas resources or energy conversion technologies like power-to-liquid or sun-to-liquid.

To produce a HEFA fuel blend, in the pretreatment, the triglycerides and fatty acids are extracted from oil plants and animal fats. In the subsequent hydrotreatment unit, the olefinic bonds and carbon-oxygen bonds are broken by catalytic hydrogenolysis reactions using hydrogen as a catalyst. The resulting HEFA crude consists of a mixture of highly paraffins, similar in this nature to the F-T crude. In subsequent steps, the crude is upgraded to the desired fuels. Due to this closeness to standard refinery processes, a hydrotreatment of oils and fats to produce fuels has been suggested several times in the past but was not viable due to higher production cost concerning conventional petroleum oil processing. However, the general interest remained due to both the high-quality fuels (no sulfur, no aromatics, high cetane number), which could be produced, and the well-known processes. In contrast to the F-T processing, the HEFA products

show a dependency on feedstock. The chain length of the HEFA crude depends on carbon number range of the original feedstock, which is for most vegetable oils in the range of diesel fuels. In consequence, this means, on the one hand, a process adaptation to local constraints. On the contrary, the production of jet fuels needs additional upgrading activities, thus decreasing the cost effectiveness of the jet fuel blend concerning a diesel fuel production.

Direct Sugar to HydroCarbons (DSHC) was approved in April 2014 as the third pathway to produce an alternative fuel blend. The process developed by Amyris is based on the utilization of genetically modified organisms (GMO) to convert sugar to farnesene directly. Farnesene is an unsaturated, branched hydrocarbon with four double bonds. In subsequent hydroprocessing and fractioning steps, the farnesene is converted into farnesane, which is approved as a jet fuel blend up to 10 % vol.

To produce SPK by Alcohol-To-Jet (ATJ) pathway, the feedstock is first converted to alcohol and then to hydrocarbons forming a fuel blend. The ATJ pathway is marked by high feedstock flexibility, since starches, biomass, and industrial gases via gas fermentation can be converted to alcohol intermediates. A broad range of alcohols can be produced as intermediates such as ethanol, butanol, and alcohol mixtures. Because butanol has the double amount of carbons per molecule concerning ethanol, it is the most commonly used intermediate (IATA 2012). In the subsequent processing steps, the alcohol intermediates are first dehydrated and then oligomerized into hydrocarbons. With an additional upgrading, the yield of hydrocarbons in the jet fuel-boiling range can be optimized. ATJ taps new feedstock resources and is also promising in the production costs, mainly due to the lower feedstock cost (IATA 2012). The very different nature and character of the fuel (it consists mainly of two iso-alkanes), questions some fundamental assumptions of common properties of jet fuels, like the shape of the distillation curve. ATJ was approved in April 2016 with a maximum blending ratio of 30%.

Drop-in Fuels or Blend with the Approval in Process

Major concerns in the utilization of drop-in jet fuel blends are blending issues to satisfy ASTM 7566 requirement, especially concerning the aromatics content. To satisfy the minimum limit of 8% aromatics in jet fuels, crude oil based jet fuels with a high amount of aromatics are required. Another class of pathways, which are under approval, is Synthetic Aromatics in the Kerosene boiling range (SKA). With the production of synthetic aromatics, blending effort shall be reduced, and it is a key step required to produce fully synthetic jet fuel. Sasol also pioneered in this sector; with their high-temperature F-T process, single ring aromatics can be generated and a small amount of di-aromatics (<0.2 %-mass). The Sasol fully synthetic jet fuel was approved in 2009 by DS91-91, the approval of a generic class of F-T derived SKA is in the ASTM approval process. Also, processes to produce aromatics based on sugars and alcohols ATJ-SKA or Catalytic Hydrothermolysis (CH) are under development (Gupta, Roquemore, and Edwards 2014). Liquefaction and pyrolysis yield a mixture of naphthenic compounds and aromatics, thus

representing also a possible pathway to SKA; furthermore, it can be used as synthetic crude for standard refinery upgrading. In direct liquefaction coal, hydrogen and, a catalyst are brought into a high pressure, high-temperature environment. This causes hydrocracking and yields the formation of naphthenes and aromatics liquid mixture (Höök and Aleklett 2009). In the pyrolysis process, the feedstock is heated in the absence of oxygen, yielding to a devolatilization and thermal decomposition breaking of the carbon bonds of the feedstock.

Non Drop-In Fuels

In the ASTM 7566 and DS91-91, only hydrocarbons are considered, as underlined by Wilson et al. (2013), which is of high importance to secure the safety of flight for short to mid-term alternative fuels. With pressing supply and environmental issues, it can be thought of non-drop-in fuels for to be used in the long-term. A non-drop-in fuel blend suggested in the Alfabird project (Allouche et al. 2012) could be blends with higher alcohols (like hexanol), showing advantageous soot emissions profiles and potential benefits in CO₂ reduction. The introduction of FAE (Fatty Acid Esters) blends are seen ambiguously, on the one hand, it is declared as non viable blending solution (Lewis 2011; Allouche et al. 2012; Wilson et al. 2013), on the other hands research efforts are ongoing (IATA 2012; Llamas et al. 2012)

The following fuels are oxygenated fuels and thus classified as non drop-in fuels. Longer chain alcohols, as hexanol, have the potential to be used as non drop-in fuel blend, as they could lower the production cost remarkably, (Allouche et al. 2012). A further possibility would be the addition of succinic acid to ethanol yielding to diethyl-succinate (DES). DES has similar properties to jet fuel and was identified as a potential (non drop-in) fuel in the long term by the SWAFEA project. Also identified as non drop-in fuel with potential application in the long run are furane derivatives. Furane derivatives can be produced by fermentation of glucose.

As an alternative pathway to HEFA processing, the triglycerides could first be converted into vegetable oils, then in combing them, alcohol transformed into a mixture of Fatty Acid Ester (FAE) by transesterification reactions. FAEs have beneficial production costs, but are seen as a contaminant in aviation (Wilson et al. 2013); their role as a non drop-in fuel is questionable.

2.1.4 Conclusions

Aviation fuels are an interdependent product, driven by technological advancements of jet engines, fuel-processing technology and influenced strongly by the political and the economic environment. From the viewpoint of the fuel processing industry weakly defined regulations, like done in the first fuel specification in the US in 1907, would be economically beneficial. In the first fuel specification, only the density range was fixed and that no particulate matter shall be left after evaporation of the fuel (Edwards 2003). Also for the brothers Wright the availability and handling of fuels as an energy source were the dominant factors. However, with the evolution of aircraft to higher performance other requirements for the fuels became important. For example, for high

altitude flights, a low freezing point limit of the fuel must be ensured to guarantee the safety of flights. With the successful commercialization of civil aviation, economic factors, like the costs of the fuels and an increased need for security, yielded the development of specialized fuel standards (Jet A-1 and Jet A). The ongoing evolution of aircraft and jet engines yielded to the situation that aviation fuels are the most highly regulated transportation fuels with the most extensive set of specifications in the industry (Wilson et al. 2013).

However, history has shown that specifications pushed technological development in the fuel processing technology. In response to the quest for high-performance aviation fuels in the 1930s, the development of new fuel processing methods like alkylation and catalytic cracking processes was initiated (Edwards 2003). With the danger of a future depletion of conventional oil sources and an increasingly critical evaluation of aviation effects on the environment new constraints are forming the evolution of the fuel and jet engines. In fact, several pathways to produce alternative aviation fuels are in the development. Synthetic paraffinic kerosene (SPK) blends produced by Fischer-Tropsch (F-T) synthesis or Hydroprocessed Esters and Fatty Acids (HEFA) as well as Synthesized Iso-Paraffins (SIP) by Direct Sugar to HydroCarbons (DSHC) process have been approved in recent years. Pathways like Alcohol-to-Jet (ATJ) or Catalytic Hydrothermolysis (CH) are in the approval process as drop-in fuel blend or drop-in fuels. Several options like long chain alcohols or new molecules like furane derivatives and succinic acids exist in the long-term as non drop-in fuels with the potential to increase availability and reduce economic costs remarkably.

Since there are too many critical parameters for the fuel, they cannot all be tested. Specification requirements are grouped in performance, material and manufacturer requirements. These specifications are expressed as combinations of minimum and maximum limitations on relevant aspects of chemical composition and performance parameters. Since specifications have been developed with the underlying assumption of using crude derived jet fuel, there is a potential that the detailed characteristics of the fuels can differ remarkably.

2.2 Fuel Characterization

Because of the fuel specifications and the fuel approval process, a variety of fuels can be considered as potential aviation fuels. To model the fuels and fuel related effects on the combustor, the fuel characteristics need to be captured in detail.

2.2.1 Fuel Composition

The most direct characterization is to infer the fuel composition. For a general overview of the fuel composition usually gas chromatography–mass spectrometry (GC-MS) is used. Figure 2.5 shows the chromatogram of Jet A-1. It depicts the width of the distribution with retention time and carbon number range covered. In this way, it gives an idea about the number of components existent in the fuel mixture.

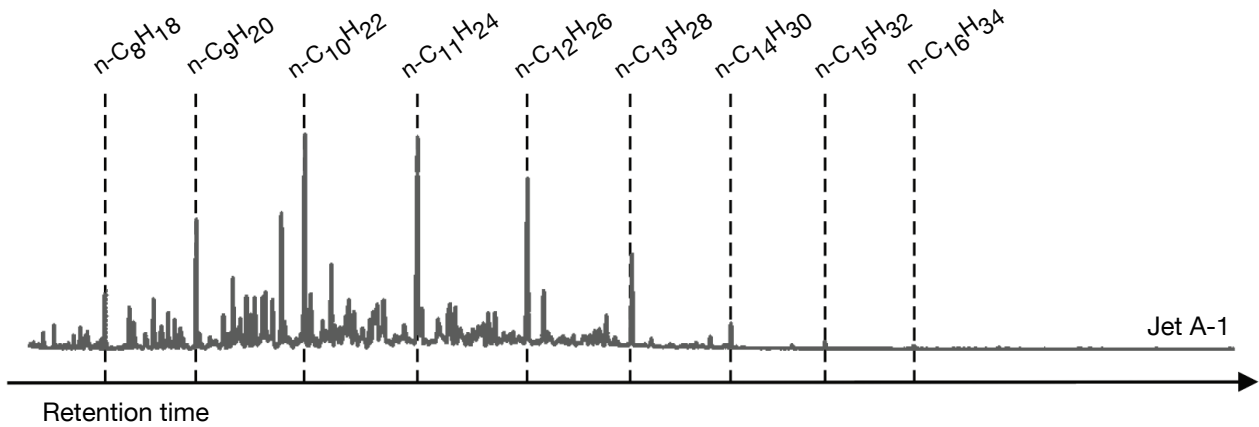


Figure 2.5: GC chromatograms for Jet A-1 (Zschocke, Scheuermann, and Ortner 2015).

Furthermore, the GC chromatogram can also be used to infer quantitative information about the fuel composition by coupling a mass spectrometer (MS). By using GC-MS (Wahl 2003) identified 410 different components present in the Jet A-1 under investigation. The composition of the fuel is displayed in Figure 2.6. To give an understanding of the nature of the fuel, the different components have been categorized into their corresponding fuel families: n-alkanes, iso-alkanes, cycloalkanes, mono-aromatics, di-aromatics, and olefins. To facilitate the interpretation, fuel components with the same carbon number are displayed as one component. It is common to furthermore group the mono-aromatics, di-aromatic and olefins into a general aromatics category, as shown in Figure 2.7. The volatility characteristics of fuel components are indicated by using the boiling points of the components as distribution parameter.

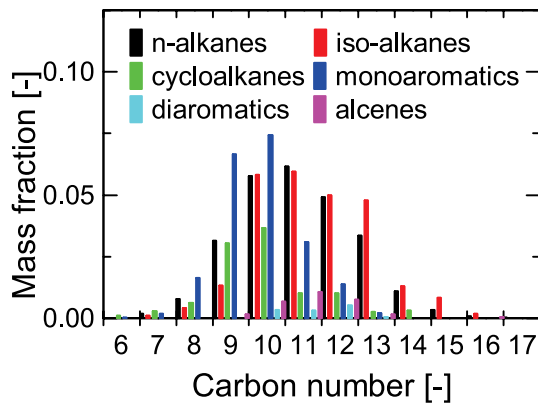


Figure 2.6: Distribution of fuel components for the different fuel families present in Jet A-1 characterized in (Wahl 2003; Kick et al. 2012), (Le Clercq et al. 2010).

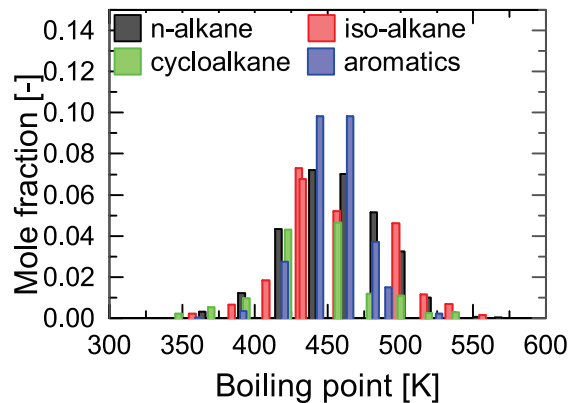


Figure 2.7: Jet A-1 composition: fuel components are grouped into fuel families, for each family the distribution (Wahl 2003).

GC-MS results of different alternative fuels are shown in Figure 2.8 and Figure 2.9 in comparison with Jet A-1. The F-T SPK, HEFA SPK, and DSHC have been certified to be used as drop-in fuel blends. Since the fuel processing of F-T and HEFA is close to petroleum based fuel

processing technology, in turn very similar, carbon number distributions can be seen. While all the alternative fuels displayed in the two graphs, are to be used as blends with conventional Jet A-1, the CH fuel is designed to be a fully synthetic jet fuel. Also having a wider distribution of components, it shows a high similarity with the Jet A-1 chromatogram.

The DSHC and ATJ-SPK instead differ strongly from compositional "experience base" (Edwards, Moses, and Dryer 2010), showing a very limited number of components. These unusual features of the fuels are reasons of concern for OEMs since there is no experience base of the impact of a limited number of chemical species on combustor performance (Edwards, Moses, and Dryer 2010).

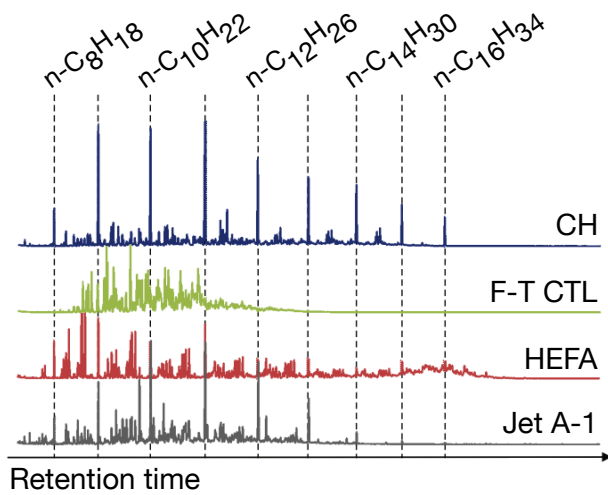


Figure 2.8: GC-MS chromatogram comparison of CH, F-T CTL, and HEFA with Jet A-1 (Zschocke, Scheuermann, and Ortner 2015).

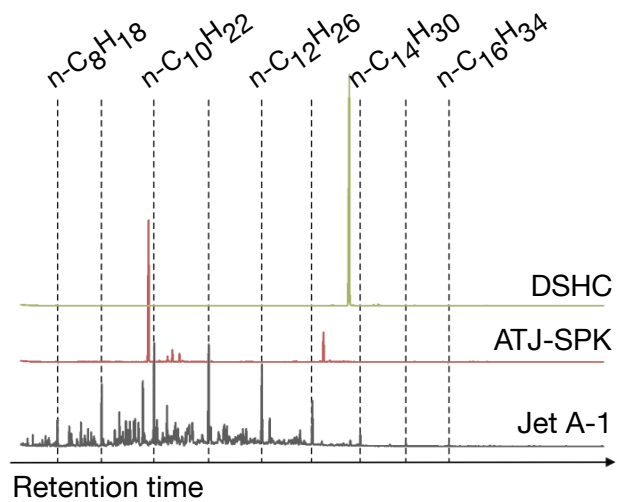


Figure 2.9: GC-MS chromatogram comparison of DSHC and ATJ-SPK with Jet A-1 (Zschocke, Scheuermann, and Ortner 2015).

The classification of the fuel components into fuel families is summarized in Table 2.1. Two remarkable differences with respect to conventional Jet fuel can be seen: first the FT-CTL, HEFA, DSHC, and ATJ-SPK are strongly paraffinic and free of aromatics, second, the CH has a much higher concentration of cycloalkanes with respect to all other fuels.

2 Validation Domain for Alternative Aviation Fuel

Fuel Name	N-Alkanes [%-vol]	Iso-Alkanes [%-vol]	Cycloalkanes [%-vol]	Aromatics [%-vol]
Jet A-1	25	33	22	20
F-T CtL	--	97	3	--
HEFA	9	91	--	--
DSHC	--	99	1	--
ATJ-SPK	--	97	2	1
CH	32	9	43	16

Table 2.1 Distribution of fuel components in fuel families for Jet A-1 and alternative aviation fuels (Gupta, Roquemore, and Edwards 2014).

The differences seen here can have implications on the performance of the fuel. In general, hydrocarbons consist of compounds of two elements, carbon and hydrogen, but varying in their molecular structure. However, macroscopic properties of molecules depend on the molecular structure and the bonds/intermolecular forces between atoms (Poling, Prausnitz, and O'Connell 2000). In consequence, the similarity in the molecular structure is used for the categorization of the fuel composition. Table 2.2 summarizes the structural representation of the four main fuel families present in aviation fuels; also, saturated straight-chain alcohols are listed as a potential non drop-in fuel candidate in the long term. Within each fuel family, the components are further distinguished by the number of carbon atoms n .




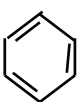

Fuel Family	General Formula	Structural representation
n-alkanes	C_nH_{2n+2}	
iso-alkanes	C_nH_{2n+2}	
cycloalkanes	$(CH_2)_n$	
aromatics	C_nH_{2n-6}	
saturated straight-chain alcohols	$C_nH_{2n+1}OH$	

Table 2.2 Structural representation of fuel families, which can constitute the composition of conventional and alternative aviation fuels.

N-alkanes and iso-alkanes have the same structural formula and are often grouped as paraffin. They have similar properties: each carbon atom is fully saturated with hydrogen, and thus they build a chemically stable structure. The high hydrogen/carbon ratio yields high specific

energy. Regarding the bulk properties of jet fuels, paraffins have a low density, a low freezing point, high thermal stability and do not tend to coke deposition and exhaust smoke formation during combustion (Lefebvre and Ballal 2010). N-alkanes are straight chains hydrocarbons and show a smooth graduation of physical properties like boiling point and density. Iso-alkanes are branched chained exhibiting a significant variation in chemical structure. With increasing branching, the volatility increases.

Cycloalkanes are also saturated hydrocarbons with the carbon atoms linked to form rings. The chemical stability is similar to n- and iso-alkanes. In general, they have a high gravimetric heat of combustion, low soot-forming tendencies a lower freezing point, and high density (Lefebvre and Ballal 2010).

Aromatics are ring compounds with one or more six-member rings, each with three double bonds. Aromatics have less hydrogen than cycloalkanes and are fully unsaturated. Thus they have a high chemical reactivity. They have lower specific energy than n-, iso- and cycloalkanes and are prone to form soot during combustion (Lefebvre and Ballal 2010).

Saturated straight chain alcohols are formed by a hydrocarbon component and one hydroxyl radical. Compared to hydrocarbon, they have a low calorific value, lower freeze point, high flash point, high latent heat of vaporization, and yield reductions in combustion particulates, CO and NO_x emissions. Disadvantages for application in aviation are the low vapor pressure, aldehyde emissions, lower specific energy, and energy density.

2.2.2 Distillation Curve

The distribution of components and the kind of fuel families affect the physical properties. To furthermore characterize the influence on evaporation, the distillation curve is commonly used as an indicator of fuel volatility. In ASTM D1655 (ASTM International 2013) the distillation curve is limited in two ways: by an upper limit of 478 K on the 10 % distilled temperatures to “ensure easy starting” and an upper limit of the final boiling point of 573 K to “exclude heavier fractions that would be difficult to vaporize”.

In Figure 2.10 the distillation curves of Jet A-1 and alternative fuels are compared with the minimum, and maximum values for Jet A-1 inferred in the CRC World Fuel Sampling Program (Johnson and Hadaller 2006). The CRC World Fuel Sampling data represent the limits of experience values. As expected, the Jet A-1 and the CH fully synthetic jet fuel are within the minimum and maximum values. The other fuels are partially outside of the experience domain but are used or intended to be used blend components with Jet A-1.

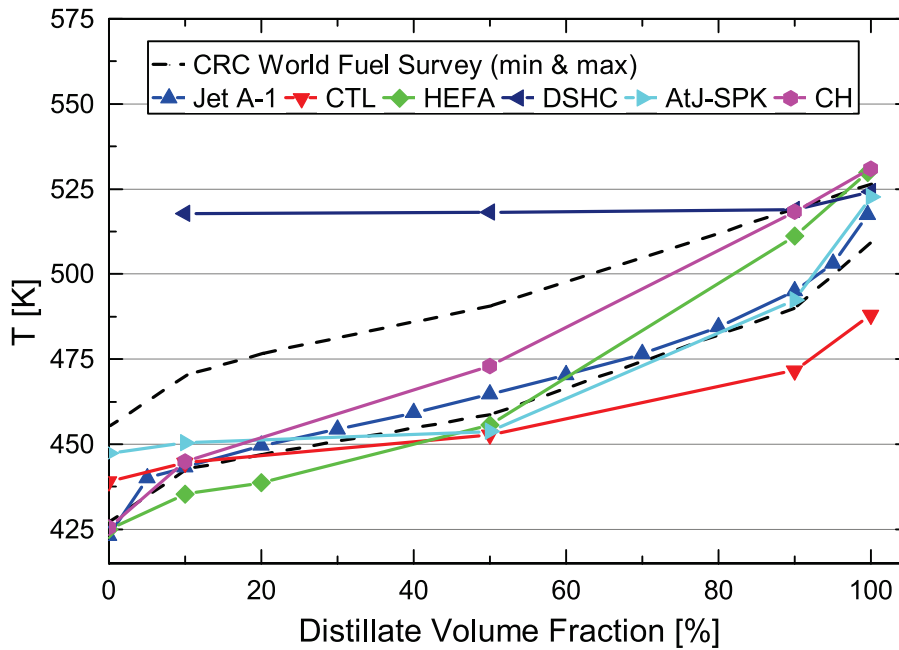


Figure 2.10: Distillation curve of Jet A-1 and HEFA in comparison with the min and max values of the CRC World Fuel Survey (Johnson and Hadaller 2006) values for Jet A-1 (Zschocke, Scheuermann, and Ortner 2015).

It has to be pointed out, that the CTL, the ATJ-SPK, and DSHC exhibit a region with a flat distillation curve compared to Jet A-1. The investigations of effects of such flat distillation curves or heavy concentrations of specific hydrocarbon families in a volatile fraction (Moses 2012) are part of ongoing research (ASTM International 2014b).

2.2.3 Variability of Jet Fuel Characteristics

As mentioned in the historical overview of jet fuel standard development, there are two counteracting forces in the design of fuel specifications. On the one hand, by tight specifications, high-performance fuels can be defined. In fact, this was the strategy in defining the fuel standard JP-2 and JP-3 after the second world war (Maurice et al. 2001). However, despite the advantages of high-performance fuels, too tight specifications cause very high costs in fuel production and strongly restrict the availability of the fuels. Consequently, fuel manufacturers are involved in the definition of the fuel standards and in finding compromises, allowing a limited variability of the fuels but ensuring the operational safety.

To control the fuel quality different sampling programs exist monitoring variations of jet fuels worldwide. As part of the burnFAIR project, the Lufthansa AG did an extensive sampling (2400 samples) of conventional Jet A-1 fuels from November 2010 to October 2011 in different locations in Germany (Zschocke 2013). Results depicting the variability of the aromatics content in jet fuels are shown in Figure 2.11. Specified in ASTM D1655 and DS91-91 is a max. aromatics content of 25 vol%. One can see a distribution ranging from 6 to 26% of aromatics. However, not only the composition varies, as shown in the case of liquid density variation in Figure 2.12.

Such variations can alter the jet engine emissions and performance observably but without affecting the operational safety. Similar variations can be expected for alternative fuels, depending on feedstock and process parameter.

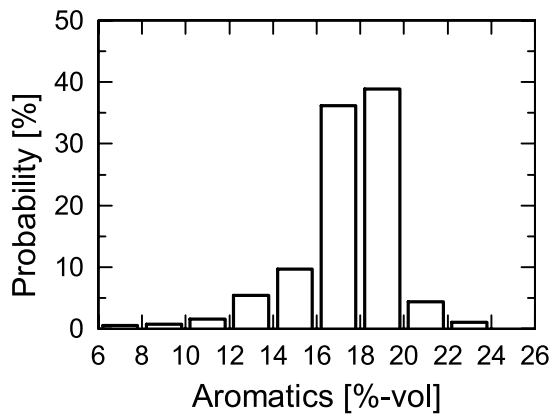


Figure 2.11: Aromatics content of Jet A-1 during the burnFAIR Jet A-1 sampling program (Zschocke, Scheuermann, and Ortner 2015).

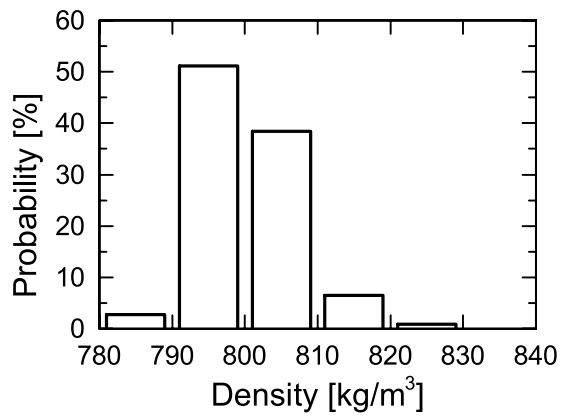


Figure 2.12: Variation of the density at 15°C inferred during the burnFAIR Jet A-1 sampling program (Zschocke, Scheuermann, and Ortner 2015).

2.3 Fuel Validation Domain

To optimize jet engines or to design fuel flexible jet engines, numerical models could beneficially be used to predict the effect of fuel composition on combustor performance for actual and future fuels reliably. However, the judgment of the model adequacy for the intended application is a critical step in the design process. The assessment of model adequacy is based on quantitative metrics of the model accuracy for the intended application conditions. In the context of this work, the capabilities of models to simulate and predict the evaporation of alternative aviation fuels is of fundamental interest. As seen before, different production pathways yield to changes in the fuel composition, which in turn can affect various properties - it changes the thermodynamic and chemical properties of the fuel - and subsequently the properties of different processes (atomization, evaporation, mixing, combustion...).

The validation domain needs to be constructed to adequately test evaporation models for their accuracy in simulating the evaporation of the variety of possible alternative aviation fuels. Of particular interest are the extreme cases of parameter combinations, which are related to potentially evaporation-caused combustor performance issues.

2.3.1 Fuel Formulation related Issues in the Fuel Approval Process

The fuel approval process involved a large variety of groups from academia, governmental organizations, Original Equipment Manufacturers (OEM), and fuel producers. To reduce costs and facilitate the approval process, the “Rules and Tools” program (Edwards, Moses, and Dryer

2 Validation Domain for Alternative Aviation Fuel

2010) was started by the US Air Force in 2009, which in 2014 was followed by the “National Jet Fuels Program” initiated under the Federal Aviation Administration (FAA) (Gupta, Roquemore, and Edwards 2014). Based on the experience made with already approved alternative aviation fuels, different categories of fuels to be investigated were defined (Edwards, Moses, and Dryer 2010) to challenge models and experiments:

- A) Fuels based on nominal and extreme cases of current jet fuel
- B) Alternative fuels that have already been tested (passed and/or failed)
- C) Surrogates with targeted physical properties and chemical compositions

Category A) addresses the possible variability of jet fuels. The fuels considered here are wide-boiling fuels, including all hydrocarbon fuel families with the components spread across boiling point ASTM D1655 specification limits. One limit is given by the worst-case fuel, a high viscosity Jet A with a high aromatic content and low derived cetane number. The best-case fuel is a low viscosity, low aromatic content and high derived cetane number Jet A fuel. In Category B) fuels are considered that are outside the experience base like single component fuels as the DSHC product farnesane or highly cycloparafinic fuels as the CH fuel. Category C fuels shall address special issues: related to evaporation, like the effects of a flat (narrow) boiling point distribution or the effect of bimodal boiling point distributions.

2.3.2 Validation Domain for Alternative Aviation Fuel Droplet Evaporation Models

As shown in section 1.2.3, in an ideal case, the validation domain is identical to the application domain. In the case of droplet evaporation, this means that the validation domain should comprise all evaporation-relevant property variations for existing and future aviation fuels.

Since the properties are a function of the composition and thermodynamic state points, the validation domain requires several dimensions. One category of dimensions describes the composition. As discussed in section 2.2.1, the composition can be described by a) grouping the molecules into fuel families and b) describing the distribution within the fuel families by an appropriate distribution parameter and the number of components. Furthermore, to address the concerns that arose during the approval of alternative fuels, the complexity of the distillation curve or in other words c) the complexity of the distribution of components over the boiling point has to be reflected. The fourth dimension is the thermodynamic state point, the temperature, and pressure range in which the fuels will be evaporating. These depend on the jet engine technology of existing and future engine. Regarding validation, these conditions are defined by the validation experiment.

The composition-related part of the validation domain for alternative fuel droplet evaporation models is depicted in Figure 2.13, utilizing the characteristics of Jet A-1, as well as the alternative fuels shown in chapter 2.2. The validation domain represents, on the one hand, the

complexity of alternative fuels and issues related to complex boiling point distributions. On the other hand it reflects different complexities for evaporation models, which have to deal with the whole range from single to multicomponent fuels. Varying the fuel families means to test the thermodynamic property models that are implemented in the evaporation model. The boiling point distribution is mainly an issue for practical usage of the fuels. Due to the non-ideal mixing behavior of alcohols with hydrocarbons, the alcohol-Jet A-1 case is rated as a distribution with high complexity. As shown earlier especially ATJ-SPK but also F-T and HEFA SPK have a flat distillation curve and impose a high complexity for the boiling point distribution.

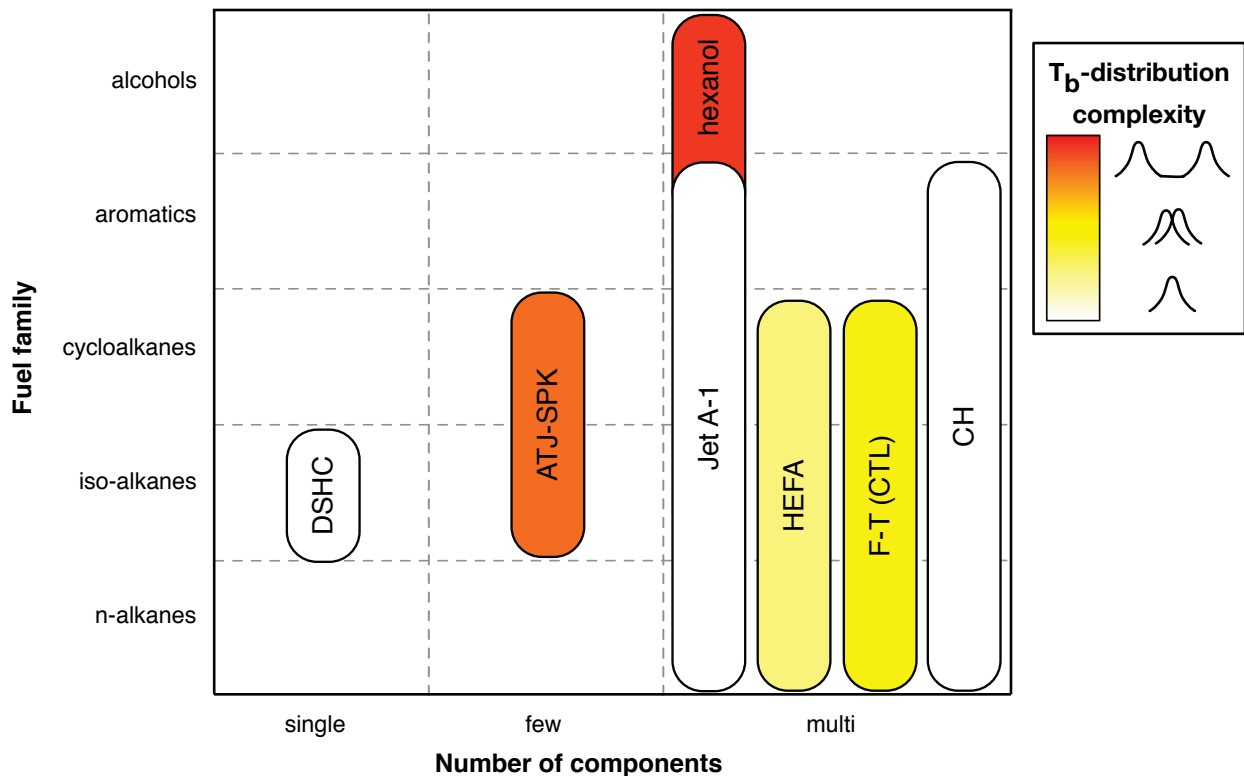


Figure 2.13: Fuel validation domain for alternative fuel droplet evaporation models.

2.4 Conclusions

Aviation fuel is a historical product and strongly influenced by the interdependence of jet engine technology, fuel processing technology, and political environment. Jet A-1 is a mixture of hundreds of hydrocarbon components from mainly four fuel families: n-, iso- and cycloalkanes as well as aromatics. While the first alternative aviation fuels F-T and HEFA fuels tried to copy the chemical composition of conventional Jet fuel, new pathways like DSHC yield different fuel composition. Such fuels can comprise only a few components like farnesane from direct fermentation or fuels from alcohol oligomerization. Alternatively, entirely new components for aviation like long-chain alcohols for future non-drop-in fuels.

To ensure the safety of flight, intensive testing programs, have been developed and fixed in the ASTM D4055 standard. During testing of new fuels concerns related to the number of

2 Validation Domain for Alternative Aviation Fuel

components and the boiling point distribution/slope of the distillation curve and their effect on combustor performance came up. The validation domain for fuel droplet evaporation models presented here covers all the issues mentioned above. It is characterized by three dimensions: a) kind of fuel family, b) number of components, and c) boiling point distribution complexity. Also, the fuel has to satisfy ASTM D7566 and ASTM D1655. Without unexpected radical changes in jet engine technology, the validation domain covers all possible evaporation-relevant characteristics of fuels, which could be used in the near and midterm in aviation engines.

3 Model Form Uncertainty of Droplet Evaporation Models

To model the evaporation of alternative fuels droplets means to mathematically describe the non-linearly coupled processes of motion, heat and mass transfer in a two-phase flow. Since these governing equations cannot be solved analytically, approximate solutions have to be found by simplifying the governing equations by assumptions and simplifications in a way that the governing equations can be solved numerically. High accuracy, numerical robustness and convenient computational time when solving the equations have to be assured to provide adequate tools.

Models covering future alternative aviation fuels need to capture the different nature of fuel composition with respect to conventional fuels. New molecules with different thermodynamic and chemical properties are introduced, and the number of components and properties can be very different from conventional hydrocarbon fuels. Also when mixing the fuels, the mixing behavior may vary sharply from the ideal behavior, due to the different nature/functional groups of the fuel components. Alternative fuel models used for design purposes have to be able to describe in detail the effect of the fuel complexity but without affecting the computational load too much.

The accuracy of the numerical solution with given boundary and initial conditions is composed by the numerical solution error and the model form uncertainty. The model form uncertainty is the error made by the simplifications and assumptions made when deriving the model governing equations from the exact mathematical models. The numerical solution errors are defined (Oberkampf and Roy 2010) as the sum of absolute values of the estimated iterative solution error, the estimated spatial discretization error, and the estimated time discretization error. The estimated solution error caused by adjustable parameters (relaxation factors, numerical damping parameters, limiters) in the numerical algorithms is already included in the aforementioned numerical error sources (Oberkampf and Roy 2010).

The focus of this chapter is to show the origin of the model form uncertainty for multicomponent-fuel droplet evaporation models and to display the main limiting parameters in the model and sub-models used. For this reason, the primary simplifications and assumptions made when deriving the modeling equations for discrete and continuous multicomponent-fuel droplet evaporation models are described.

3.1 Spray Modeling

An efficient conversion of the energy stored in liquid fuels is based on well-controlled fuel preparation. The liquid fuel is injected into the preheated flow in a gas turbine combustion chamber, and a dense spray is formed by primary atomization. With subsequent secondary atomization due to the high relative velocity between the droplets and the flow field, inertia effects dominate surface tension effects, and the size of the droplets is further reduced. The dominant phenomena in a spray can be classified by the liquid volume fraction. The first phase with a dense spray is a contact and collision-dominated flow. With further spreading of the spray and effects of turbulence dispersion, the number of collisions is decreased, down to dilute dispersed flow regimes with low liquid volume fractions. A dilute spray is characterized by only two-way coupling (exchange of mass, energy, and momentum) between the droplet and gas flow and no droplet-droplet interactions (Crowe 2005). In the following, the focus will be on dilute sprays.

There are different conceptual ways to model multiphase flows. Usually, the continuous flow is described with an Eulerian reference-frame methodology. For the dispersed phase depending on the situation, Eulerian, or Lagrangian reference frame are applied. One crucial argument in choosing the reference frame is the required resolution compared with spacing between droplets. If the resolution is smaller than the spacing, each droplet must be considered, and a Lagrangian reference frame has to be applied. If the resolution is larger than the droplet spacing, average droplets can be assumed, and Eulerian or Lagrangian reference frames can be considered. In the Eulerian reference frame, the spray is described as a continuum. The same discretization and similar numerical techniques as for dispersed continuous phase can be applied. Due to a significant reduction in computational costs, the Eulerian reference frame is most beneficial if two-way coupling effects are dominant (Crowe 2005). The Lagrangian representation yields to a decoupling of the continuous and dispersed phase. First, the continuous phase described by an Eulerian reference frame is solved. The resulting flow field forms the boundary conditions for the droplets in the spray. The droplets are being tracked, and the ordinary differential equations (ODEs) for the conservation of mass, energy, and momentum are solved in time steps along the droplet trajectories. Spray source terms give the feedback for the gas field for each integration time step. The Lagrangian reference frame reduces numerical error due to artificial diffusion and has a higher resolution, important for ignition and flame structure in combustion simulations (Sirignano 1999). Furthermore, the simulation methods can be distinguished by the discretization methods: mesh-based and meshfree methods. Mesh-based methods are computationally efficient and are widely used. In case of strong deformations of the liquid phase, meshfree methods like the Smoothed Particle Hydrodynamics Methods (Höfler 2013) are more accurate.

The droplets in the Lagrangian reference frame can be described as surface resolved or as a point source. In case of the surface resolved approach, the detailed flows around the droplet and

in the droplets have to be solved causing high computational costs. The point-source approximation assumes that the volume of droplets and surrounding gas films is small compared with the total gas volume. It is only exact in the case of a spherical symmetric transport field around the droplets and is otherwise approximative (Sirignano 1999). To be most accurate the droplet has to be much smaller than the numerical cells. The effects of the surrounding flow field on the droplets are considered by empirical correlations.

Due to the demand for high resolution and low computational costs the Euler-Lagrangian reference frame is used in this study. In the following, the droplet sub-grid models applied to describe the evaporation of alternative aviation fuels are described.

3.2 Discrete Component Evaporation Models

In Chiu (2000) the development of spray models are summarized in three distinct periods: In the first quarter of the twentieth century, activities focused on the spray characterization and on the derivation of suitable distribution functions describing the droplet size and velocities created by different atomizers. In the years from 1950 to 1970, fundamental models for the droplet behavior in spray combustion process (Spalding 1953; Godsave 1953) were derived. This was performed on the one hand by analytical and numerical studies and on the other hand by phenomenological empiricism, which provided the link between isolated droplets and dilute sprays like with the Ranz-Marshall correlations (Frössling 1938). In the following decades, activities focused on the relaxation of the classical droplet vaporization theory with its general assumptions of spherical-symmetry, quasi-steadiness, single component, and isolated droplets. The theory was fitted to non-linear phenomena considering the droplet heating, droplet interior circulation, droplet-turbulence interaction, and droplet-droplet interaction (Law 1982; Sirignano 1983; Sirignano 1999; Chiu 2000).

To infer the equations describing the exchange of mass, momentum, and energy between the gas and liquid phases the detailed solution of the exact Navier-Stokes equations are too costly for technical relevant applications. The definition of appropriate models in the sense of computational costs requires reasonable simplifications and assumptions but resulting in an increased model form uncertainty. The models have to be able to cover the different flow features present in a combustion chamber.

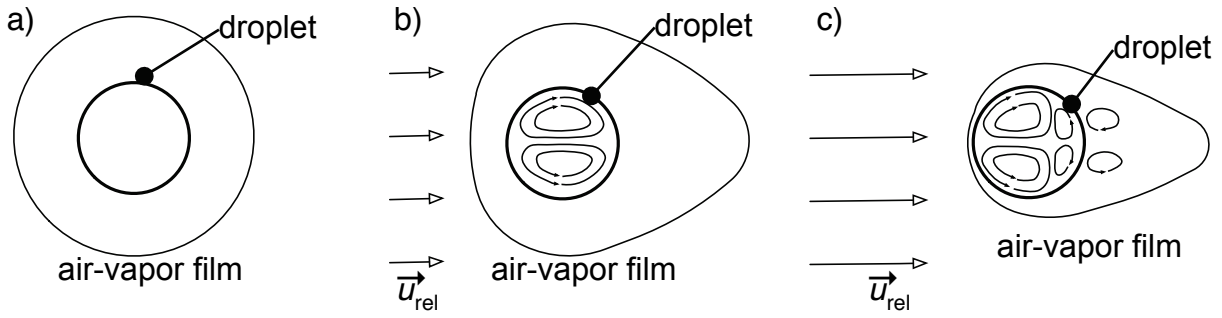


Figure 3.1: Schematic of different droplet flow configurations in dependency of different droplet Reynolds numbers Re_D : a) Re_D close to zero (quiescent conditions), b) low to intermediate Re_D condition with internal circulation in the droplet and c) high Re_D conditions with complex flow in the droplet and separation region in the droplet wake.

Figure 3.1 shows the dependency of the phenomena governing the energy, momentum and mass transfer from and to the droplet on the droplet Reynolds number Re_D . The droplet Reynolds number is defined by $Re_D = u_{rel} \rho_g D_d / \mu_g$, where u_{rel} is the magnitude of the gas-droplet relative velocity, ρ_g the gas phase density, μ_g is the gas phase dynamic viscosity, and D_d is the droplet diameter. The liquid droplet is surrounded by the air-vapor film that is formed during evaporation. The air-vapor film fundamentally influences the heat and mass transfer between the ambient and the droplet. Case a) shows a droplet with zero Reynolds number and spherical symmetric air-vapor film. With increasing Reynolds number, the air-vapor film is influenced by the ambient flow and a non-spherical shape of the air-vapor film is formed. The shear stress at the droplet surface causes a circulation in the droplet, which is influencing the heat and mass transfer processes in the droplet, see case b). In high Reynolds number situations (case c), complex flows in the droplet and a wake behind the droplet is formed with strong influences on heat and mass transfer processes. Models for droplet evaporation have to cover these different phenomena.

3.2.1 Conceptualization

In this study, the film theory as described in Abramzon and Sirignano (1989) and Sirignano (1999) is used to infer the governing equations for the heat and mass exchange between the phases. Figure 3.2 shows a schematic sketch of the spherical symmetric droplet evaporation. The liquid droplet is surrounded by an air-vapor diffusive film with thickness δ_m and a thermal film with the thickness δ_h . Since liquid heating is often rate controlling and gas phase transport processes are comparably fast, in the film-theory a quasi-steady gas film is assumed. It is further assumed that the heat and mass transfer takes place by heat conduction and molecular diffusion of the fuel vapor. To take the effects of convection (Figure 3.1 b), c)) into account, empirical correlations are used to correct the heat and mass transfer.

In general, the model is based on the assumptions (Sirignano 1999) that no droplet deformation (spherical droplets) takes place, radiation, Dufour energy flux and mass diffusion due

to pressure and temperature gradients are neglected. The gas phase is treated as an ideal gas, with no chemical reactions and ambient air is insoluble in the liquid

For the liquid phase, different models for heat and mass transfer can be applied, some requiring resolving the droplet interior. Due to its computational efficiency, the rapid mixing model, which assumes infinite conductivity and diffusivity in the droplet, is widely applied in practice and is used here. Effects of different modes of droplet internal mixing were not examined in this study.

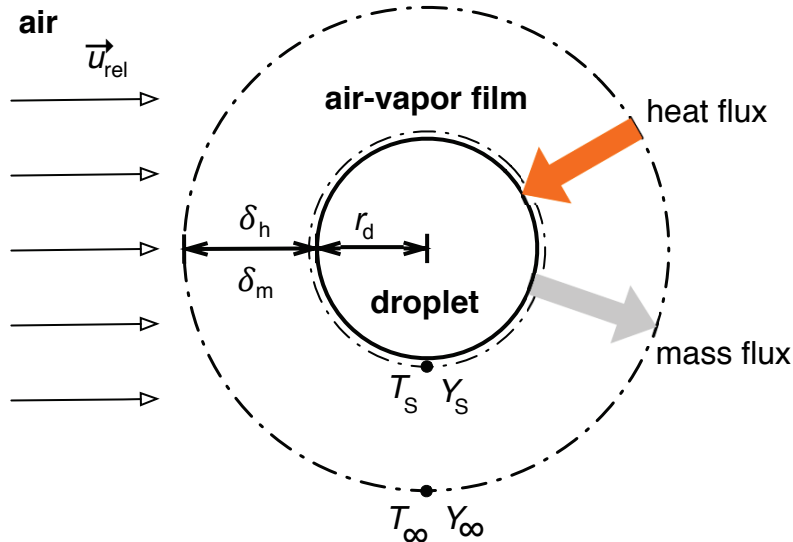


Figure 3.2: Schematic of the spherical symmetric droplet vaporization with heat and mass fluxes.

In the following, the main steps in the derivation of the governing equations will be shown. First, the heat and mass flux between the ambient and the droplet will be determined in the gas phase analysis. Then, liquid phase analysis will be performed yielding the equations for the evolution of droplet diameter, temperature, and composition in time.

3.2.2 Gas-Phase Analysis

Species Conservation

The conservation equation for the mass fraction of a single species i assuming the quasi-steady state, no chemical reactions and only Fickian diffusion (Sorret and Dufour fluxes are neglected) is

$$\frac{\partial}{\partial r}(\rho_g v r^2 y_{i,g}) - \frac{\partial}{\partial r} \left(\rho_g D_g r^2 \frac{\partial y_{i,g}}{\partial r} \right) = 0 \quad (3.1)$$

where ρ_g is the density of the gaseous mixture, v is the radial gas velocity induced by diffusion and is also called Stefan flow, $y_{i,g}$ is the mass fraction of species i in the gaseous mixture. D_g is the gas mixture diffusion coefficient, assuming the binary mass diffusion coefficients for all species are equal.

3 Model Form Uncertainty of Droplet Evaporation Models

To infer the species mass flow rate, the mass balance at the interface is performed:

$$\dot{m}y_{i,g}^S - 4\pi r_d^2 \rho_g D_g \left. \frac{dy_{i,g}}{dr} \right|_{r=r_d} = \dot{m}_i = \zeta_i \dot{m} \quad (3.2)$$

The first term describes the mass transport due to the Stefan flow; the second term is the mass transport due to diffusion from the droplet surface to the ambient. \dot{m}_i is the mass flow rate of the vapor species i . r_d the droplet radius, ζ_i is the ratio of vapor mass flow rate for the species i over the global vapor mass flow rate ($\zeta_i = \dot{m}_i / \dot{m}$).

To solve Eq. (3.2) for the mass flow rate, the equation can be integrated after a separation of variables. However, the diffusion coefficient D and the gas field density vary over the film. Hubbard et al. (1975) showed that the thermophysical properties might be treated as a constant provided they are evaluated at some reference conditions and recommended the use of the 1/3 rule:

$$T_{g,ref} = T_g^S + \frac{1}{3}(T_g^\infty - T_g^S) \quad (3.3)$$

$$\gamma_{g,ref} = \gamma_g^S + \frac{1}{3}(\gamma_g^\infty - \gamma_g^S) \quad (3.4)$$

With the introduction of the mass transfer number B_M :

$$B_M = \frac{y_{i,g}^S - y_{i,g}^\infty}{\zeta_i - y_{i,g}^S} \quad (3.5)$$

and applying the reference conditions for $\rho_g D_g|_S = \rho_{ref} D_{ref}$, the mass flow rate becomes:

$$\dot{m} = 2\pi r_d \rho_{g,ref} D_{g,ref} \text{Sh}_{eff} \ln(1 + B_M) \quad (3.6)$$

with the effective Sherwood number Sh_{eff} describing the non-dimensional mass transfer rate to the droplet:

$$\text{Sh}_{eff} = \frac{-2r_d}{\gamma_{i,g}^S - \gamma_{i,g}^\infty} \left. \frac{dy_{i,g}}{dr} \right|_{r=r_d} \quad (3.7)$$

The effective Sherwood number Sh_{eff} is unknown and has to be modeled. In case of small or negligible evaporation empirical Sh number correlation exists, which then have to be adapted for the case of strong evaporation.

Energy Conservation

The energy conservation equation assuming quasi-steady state and neglecting radiation and energy transport due to mass diffusion is:

$$\frac{\partial}{\partial r} \left(\sum_i \dot{m}_i h_{i,v} - 4\pi r^2 \lambda_g \frac{\partial T_g}{\partial r} \right) = 0 \quad (3.8)$$

The first term describes the convective energy transport by the Stefan flow, the second term the energy transport by heat conduction. $h_{i,v}$ denotes the species enthalpy, λ_g the gaseous heat conductivity, and T_g the gas phase temperature.

At the droplet surface the heat received by conduction is

$$\dot{Q}_{\text{vap}} = 4\pi r_d^2 \lambda_g \left. \frac{dT_g}{dr} \right|_{r=r_d} \quad (3.9)$$

With the definition of the effective Nusselt number

$$\text{Nu}_{\text{eff}} = \frac{2r_d}{T_g^\infty - T_g^S} \left. \frac{dT_g}{dr} \right|_{r=r_d} \quad (3.10)$$

the heat transfer rate through the film can be described with

$$\dot{Q}_{\text{vap}} = 2\pi r_d \lambda_{g,\text{ref}} \text{Nu}_{\text{eff}} (T_g^\infty - T_g^S) \quad (3.11)$$

Equation (3.11) can be used to infer the heat flow to the droplet, but the effective Nusselt number needs to be modeled. In the case of small or negligible evaporation, empirical Nu number correlations exist which have to be adapted for the case of strong evaporation.

With the integration of Equation (3.8) over the gas film and performing the energy balance at the interface, another relation for the mass flow rate can be derived

$$\dot{m} = 4\pi \frac{r_d r_T^\infty}{r_T^\infty - r_d} \frac{\lambda_g}{\sum_i \zeta_i c_{p,i,v}} \ln[1 + B_T] \quad (3.12)$$

with the radius of the thermal boundary layer r_T^∞ and the specific heat capacity of the vapor species i $c_{p,i,v}$ and the heat transfer number B_T

$$B_T = \frac{\sum_{k=1}^n \zeta_k \cdot c_{p,i,v} \cdot (T_{\text{amb}} - T_{\text{surf}})}{\dot{Q}_{\text{vap}}} \quad (3.13)$$

3 Model Form Uncertainty of Droplet Evaporation Models

To compute the heat transfer rate \dot{Q}_{vap} through the film, Equation (3.12) and Equation (3.6) are used to obtain the following relationship between B_T and B_M :

$$B_T = [1 + B_M]^\varphi - 1 \quad (3.14)$$

$$\text{with } \varphi = \frac{\text{Sh}_{\text{eff}} \rho_g D_g c_{pv}}{\text{Nu}_{\text{eff}} \lambda_g} \quad (3.15)$$

Since Nu_{eff} depends on B_T , there is no explicit solution for B_T and in consequence for \dot{Q}_{vap} . Abramzon and Sirignano (1989) suggest an iterative solution. First, we use B_T from the last timestep to compute Nu_{eff} , and then we use Nu_{eff} to compute a new value for B_T . It will be proceeded until the convergence of B_T is reached.

Vapor-Liquid Equilibrium

To calculate the vapor composition at the droplet surface Raoult's law is applied

$$x_{i,g}^S = \frac{x_{i,l} P_{\text{vap},i}(T^S)}{P^\infty} \quad (3.16)$$

where $x_{i,g}^S$ is the vapor mole fraction of the species at the droplet surface, $x_{i,l}$ is the vapor mole fraction of the species in the liquid, $P_{\text{vap},i}$ is the vapor pressure of species i and P^∞ is the far-field pressure. To determine $P_{\text{vap},i}$ thermodynamic property relations as described in section 3.4 are used.

Film Thickness Model

To determine the effect of convection on the heat and mass transfer in the gas film, experimental and theoretical correlations for the Sherwood and Nusselt number are applied. Sh_0 denotes the Sherwood and Nu_0 the Nusselt number in the case of small or negligible evaporation. The correlation of Clift et al (1978) are used in this study:

$$\text{Sh}_0 = 1 + \left(1 + (\text{ReSc})^{1/3}\right) \cdot f(\text{Re}) \quad (\text{Clift}) \quad (3.17)$$

$$\text{Nu}_0 = 1 + \left(1 + (\text{RePr})^{1/3}\right) \cdot f(\text{Re}) \quad (\text{Clift}) \quad (3.18)$$

with:

$$f(\text{Re}) = \max\left(1, \text{Re}^{0.077}\right) \quad \text{for } 0 < \text{Re} \leq 100 \quad (3.19)$$

$$f(\text{Re}) = 0.752 \cdot \text{Re}^{0.472 - 1/3} \quad \text{for } 100 < \text{Re} \leq 2000 \quad (3.20)$$

$$f(\text{Re}) = 0.44 \cdot \text{Re}^{1/2-1/3} + 0.034 \cdot \text{Re}^{0.71-1/3} \quad \text{for } 2000 < \text{Re} \quad (3.21)$$

Following Abramzon and Sirignano (1988) Eq. (3.19) has been extended to include $\text{Re} = 0$. The correlations are a fit of numerical studies; deviations from experimental data are reported to be below 3%.

In the case of strong evaporation, the Stefan flow leads to an enlargement of the film thickness and thus to decreasing heat and mass transfer through the film. Abramzon and Sirignano (1989) developed a model which takes into account the boundary layer blowing by introducing corrections factors F_M and F_H to take into account the relative change of the film thickness:

$$F_M = \frac{\delta_m}{\delta_{m,0}}, F_H = \frac{\delta_h}{\delta_{h,0}} \quad (3.22)$$

To infer the correction factors, the laminar boundary layer of the flow past a vaporizing wedge was modeled. The correlation of numerical results for the Falkner-Skan solutions by Abramzon and Sirignano (1989) show that

$$F(B) = (1 + B)^{0.7} \quad \text{for } 0 < B_T, B_M < 20; 1 < \text{Pr}, \text{Sc} < 3. \quad (3.23)$$

The effective Sherwood number Sh_{eff} and Nusselt number Nu_{eff} when taking into account the enlargement of the film thickness become (Ochs 1999):

$$\text{Sh}_{\text{eff}} = 2 + \frac{\text{Sh}_0 - 2}{F(B_M)} \quad (3.24)$$

$$\text{Nu}_{\text{eff}} = 2 + \frac{\text{Nu}_0 - 2}{F(B_T)} \quad (3.25)$$

3.2.3 Liquid Phase Analysis

The mass balance for the liquid droplet is

$$\dot{m} = \frac{d}{dt} \left(\frac{\pi}{6} D_d^3 \rho_1 \right) \quad (3.26)$$

The droplet diameter varies with time, and the density depends on temperature and composition of the liquid

$$\dot{m} = \frac{\pi}{2} D_d^2 \cdot \left(\rho_1 \frac{dD_d}{dt} + \frac{D_d}{3} \frac{d\rho_1}{dt} \right) \quad (3.27)$$

Resolving (3.27) for dD_d/dt gives the equation for the change in the droplet diameter:

$$\frac{dD_d}{dt} = -\frac{1}{\rho_l} \cdot \left(\frac{\dot{m}}{\pi/2 D_d^2} + \frac{D_d}{3} \cdot \frac{d\rho_l}{dt} \right) \quad (3.28)$$

The energy balance at the liquid droplet surface states that all the energy transferred to the droplet is used for heating the droplet and vaporization

$$\dot{Q}_{\text{vap}} = \sum_i \dot{m}_i \Delta h_{\text{vap } i} + \dot{Q}_l \quad (3.29)$$

with $\Delta h_{\text{vap } i}$ being the latent heat of vaporization for species i . In case of the rapid mixing model applied here, the droplet heating rate \dot{Q}_l is used to heat the droplet:

$$\dot{Q}_{\text{vap}} = \dot{m} \sum_i \zeta_i \Delta h_{\text{vap } i} + c_{p,l} \rho_l \frac{\pi}{6} D_d^3 \frac{dT_l}{dt} \quad (3.30)$$

Resolving equation (3.30) for the droplet temperature variation yields

$$\frac{dT_l}{dt} = -\frac{1}{c_{p,l} \rho_l} \frac{1}{\frac{\pi}{6} D_d^3} \cdot \left[\dot{m} \sum_i \zeta_i \Delta h_{i,v}(T_l) - \dot{Q}_{\text{vap}} \right] \quad (3.31)$$

The variation of the liquid composition is described by the species conservation equation

$$\frac{d}{dt} \left(\frac{\pi}{6} D_d^3 y_{i,l} \rho_l \right) = -\dot{m}_i = -\dot{m} \cdot \zeta_i \quad (3.32)$$

Using (3.28) one can write

$$\frac{\pi}{6} D_d^3 \rho_l \cdot \frac{dy_{i,l}}{dt} - y_{i,l} \dot{m} = -\dot{m} \cdot \zeta_i \quad (3.33)$$

resolving for liquid mass fraction yields to

$$\frac{dy_{i,l}}{dt} = \frac{\dot{m}}{\rho_l \cdot \frac{\pi}{6} D_d^3} \cdot (y_{i,l} - \zeta_i) \quad (3.34)$$

3.3 Continuous Thermodynamics Model

For real fuels with hundreds of different components solving the discrete component model equations would require solving the species conservation equation for each component. A cost-efficient alternative solution is the use of the continuous thermodynamics model. These have been developed and used in chemical process design since the 1930s for distillation calculations, dew, and bubble point calculations and flash calculations (Katz and Brown 1933; Bowman 1949; Edmister 1955; Kehlen, Rätzsch, and Bergmann 1985; Cotterman, Bender, and Prausnitz 1985).

The application of continuous thermodynamic models to transport processes was developed by Tamim and Hallett (1995) and with further simplification using steady state assumption for the gas phase yielded a droplet evaporation model using continuous thermodynamics (Hallett 2000). To derive the CTM equations, the discrete component droplet evaporation model reported in section 3.2 has to be extended for using continuous distribution functions. The main aspects therefore are:

- the selection of a distribution function to represent the fuel mixture,
- the selection of an appropriate characterizing variable for the distribution,
- the extension of the governing equations of the discrete component droplet evaporation for continuous mixtures and,
- the development of correlation equations for thermodynamic properties in terms of distributions characterizing variable, and temperature.

In the following, the distribution function will be described first, and then the extended governing equations for the droplet evaporation will be presented. Particular focus is on additional model form uncertainties, which might be introduced in the process.

3.3.1 Description of Liquid and Vapor Compositions by Γ -PDF

To describe the composition of the fuel in a continuous way, distribution functions are used for modeling groups of components with similar structure. In this study, the fuel components i will be grouped into fuel families (like n-alkane, iso-alkane, cycloalkane, mono-aromatics,...) denoted with the subscript j :

$$y_j = \sum_{i \in j} y_i; \quad x_j = \sum_{i \in j} x_i \quad (3.35)$$

The mole fractions x_i for component i of fuel family j in the range of the distribution ΔI can be described as

$$x_i = x_j f_j(I) \Delta I \quad (3.36)$$

with the distribution function $f_j(I)$ and distribution parameter I . For the distribution parameter I the molar mass, normal boiling temperature, the carbon number or any other suitable properties characterizing the fuel can be used.

The distribution function needs to approximate the fuel with sufficient accuracy, and at the same time, it must be versatile, with a discrete number of parameter that can be easily determined. As suggested by Cotterman et al. (1985) for petroleum fractions the gamma function (Γ -PDF) is used most often and will be applied in this study:

$$f_j(I) = \frac{(I - \gamma_j)^{\alpha_j - 1}}{\beta_j^{\alpha_j} \Gamma(\alpha_j)} \exp\left(-\frac{I - \gamma_j}{\beta_j}\right) \quad (3.37)$$

where α_j and β_j are the parameters determining the shape of the distribution function, γ_j the origin of the distribution and with Gamma function $\Gamma(\alpha_j)$:

$$\Gamma(\alpha_j) = \int_0^{\infty} t^{\alpha_j - 1} \exp(-t) dt \quad (3.38)$$

The normalization condition is:

$$\int_{\gamma}^{\infty} f_j(I) dI = 1 \quad (3.39)$$

By weighing the distribution parameter I with the distribution function and integrating, the first moment is obtained:

$$\int_{\gamma}^{\infty} f_j(I) I dI = \theta_j \quad (3.40)$$

the second moment is obtained by weighing the square of the distribution parameter with the distribution function and integrating again:

$$\int_{\gamma}^{\infty} f_j(I) I^2 dI = \Psi_j \quad (3.41)$$

Finally using the gamma distribution function Eq. (3.37) in Eqs. (3.40) and (3.41) one can obtain the following relations to relate the distribution parameter γ_j , α_j and β_j with the distribution mean θ_j and standard deviation σ_j :

$$\theta_j = \alpha_j \beta_j + \gamma_j \quad (3.42)$$

$$\sigma_j^2 = \Psi_j - \theta_j^2 = \alpha_j \beta_j^2 \quad (3.43)$$

Figure 3.3 shows the approximation of the n-alkane fuel family within a Jet A-1 fuel by the least square fitting of Γ -PDF parameter. The molar weight is chosen to be the distribution parameter.

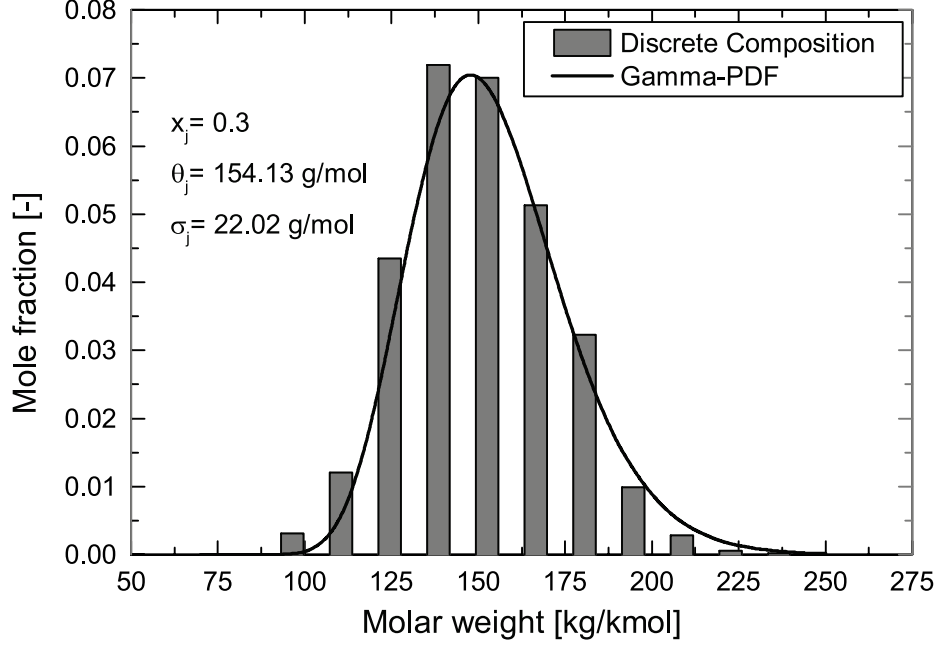


Figure 3.3: Description of the discrete n-alkane fuel family of Jet A-1 by a Γ -PDF.

3.3.2 CTM Evaporation Equations

To convert the discrete component evaporation model into the continuous thermodynamics form, the discrete mole fractions are described as their PDF-equivalent by Eq. (3.36) $x_i = x_j f_j(I) \Delta I \approx x_j f_j(I) dI$ and then integrated over the distribution $I \in [\gamma, \infty]$.

Gas Phase Analysis

The transport equations for the gas phase have the same form as for the discrete component model

$$\dot{m} = 2\pi r_d \rho_{g,\text{ref}} D_{g,\text{ref}} \text{Sh}_{\text{eff}} \ln(1 + B_M)$$

$$\dot{Q}_{\text{vap}} = 2\pi r_d \lambda_{g,\text{ref}} \text{Nu}_{\text{eff}} (T_g^\infty - T_g^S)$$

with the coefficient i for the discrete species replaced by coefficient j for the fuel group

$$B_M = \frac{\sum_j y_{v,j}^S - \sum_j y_{v,j}^\infty}{1 - \sum_j y_{v,j}^S} \quad (3.44)$$

and a relation to determine the mass fraction from the mole fraction

$$y_{j,g} = \frac{x_{j,g} \bar{W}_{t,j,g}}{\bar{W}_{t,g}} \quad (3.45)$$

with linear correlations for the molar weight

$$Wt_i = Wt_j(I) = Wt_{a_j} + Wt_{b_j}I + Wt_{c_j}I^2 \quad (3.46)$$

and fuel family mean molar weight

$$\bar{W}t_{j,g} = (Wt_{a_j} + Wt_{b_j}\theta_{j,g} + Wt_{c_j}\Psi_{j,g}) \quad (3.47)$$

Vapor-Liquid Equilibrium

To relate the vapor phase composition to the liquid composition at the droplet surface vapor-liquid equilibrium and ideal mixture are assumed as for the discrete components and the Raoult's law is applied. For the vapor pressure the correlation suggested by Doué et al. (2006) is used:

$$P_{\text{vap},j}(T^S, I) = P_{\text{ATM}} \exp\left(\frac{P1_j + P2_j I}{T^S}\right) \quad (3.48)$$

where $P_{\text{ATM}} = 1.01325 \cdot 10^5 \text{Pa}$ is the atmospheric pressure and $P1_j$ and $P2_j$ are quadratic functions of the temperature at the droplet surface and have been determined from Ambrose's correlation (Doué, Le Clercq, and Aigner 2006). This equation has been shown to be more accurate than the Clausius-Clapeyron equation with Trouton's rule for the entropy of vaporization. The expression for gas phase composition can be derived by using the equation (3.48) in Raoult's law and integration of the distribution with I^n ($n = 0, 1$ and 2) as shown in Doué (2005):

$$x_{j,g}^S = x_{j,l} \frac{P_{\text{ATM}} \exp\left(\frac{(P1_j + P2_j \gamma_j)/T^S}{1 - P2_j \beta_{j,l}/T^S}\right)}{P^\infty} \quad (3.49)$$

$$\theta_{j,g}^S = \gamma_j + \frac{\theta_{j,l}^S - \gamma_j}{1 - P2_j \beta_{j,l}/T^S} \quad (3.50)$$

$$\Psi_{j,g}^S = \theta_{j,g}^S{}^2 + \left[\sigma_{j,l} \frac{\theta_{j,v}^S - \gamma_j}{\theta_{j,l} - \gamma_j} \right]^2 \quad (3.51)$$

Liquid Phase Analysis

The governing equations describing the evolution of droplet diameter and temperature in the continuous space become (Doué 2005):

$$\frac{dD_d}{dt} = -\frac{1}{\rho_l} \cdot \left(\frac{\dot{m}}{\pi/2 D_d^2} + \frac{D_d}{3} \cdot \frac{d\rho_l}{dt} \right) \quad (3.52)$$

$$\frac{dT_1}{dt} = -\frac{1}{c_{p1} \rho_1 (\pi/6) D_d^3} \sum_j \left[\Delta \hat{h}_{\text{vap},j} - \frac{\hat{c}_{pv,j} (T_\infty - T_1)}{B_T} \right] \quad (3.53)$$

where $\Delta \hat{h}_{\text{vap},j}$ and $\hat{c}_{pv,j}$ are the specific enthalpy of vaporization and the specific vapor heat capacity-weighted by the vapor mass flow ratios of the component family.

$$\Delta \hat{h}_{\text{vap},j} = \zeta_j \Delta h_{\text{vap},j} \quad (3.54)$$

$$\hat{c}_{pv,j} = \zeta_j c_{pv,j} \quad (3.55)$$

$$\zeta_j \equiv \frac{\dot{m}_d}{\dot{m}_{d,j}} = \frac{y_{v,j}^s (1 + B_M) - y_{v,j}^\infty}{B_M} \quad (3.56)$$

The composition of the liquid is described by

$$\frac{dy_{j,l}}{dt} = \frac{\dot{m}}{\rho_1 \cdot \frac{\pi}{6} D_d^3} \cdot (y_{j,l} - \zeta_j) \quad (3.57)$$

$$\frac{d\Phi_{j,l}}{dt} = \frac{\dot{m}}{\rho_1 \cdot \frac{\pi}{6} D_d^3} \cdot \frac{\bar{W}t_{j,l}}{y_{j,l} B_M} \cdot \left[\frac{y_{j,g}^\infty \cdot (\Phi_{j,g}^\infty - \Phi_{j,l})}{\bar{W}t_{j,g}^\infty} - \frac{y_{j,g}^s \cdot (\Phi_{j,g}^s - \Phi_{j,l})}{\bar{W}t_{j,g}^s} (1 + B_M) \right] \quad (3.58)$$

where Φ can equal one of the two moments θ or Ψ .

3.4 Thermodynamic Property Modeling

To solve the governing equations of the evaporation models, the following thermodynamic properties are required: density (liquid and gaseous), viscosity (liquid and gaseous), heat capacity (liquid and gaseous), thermal heat conductivity (liquid and gaseous), diffusion coefficient (liquid and gaseous), latent heat of vaporization and vapor pressure. To model mixture properties appropriate mixing rules are chosen.

For discrete components properties equations have been taken from high-quality databases like REFPROP (Lemmon, Huber, and Mc Linden 2007) and NIST ThermoData Engine 103a database (Frenkel et al. 2005). If no data was available, suitable property relations have been chosen from Poling, Prausnitz, and O'Connell (2000). Figure 3.4 shows the comparison of the implemented discrete component density property with experimental data in the case of n-heptane, n-decane, ethanol, and hexanol fuel. Comparisons for the other property equations can be found in Appendix A.

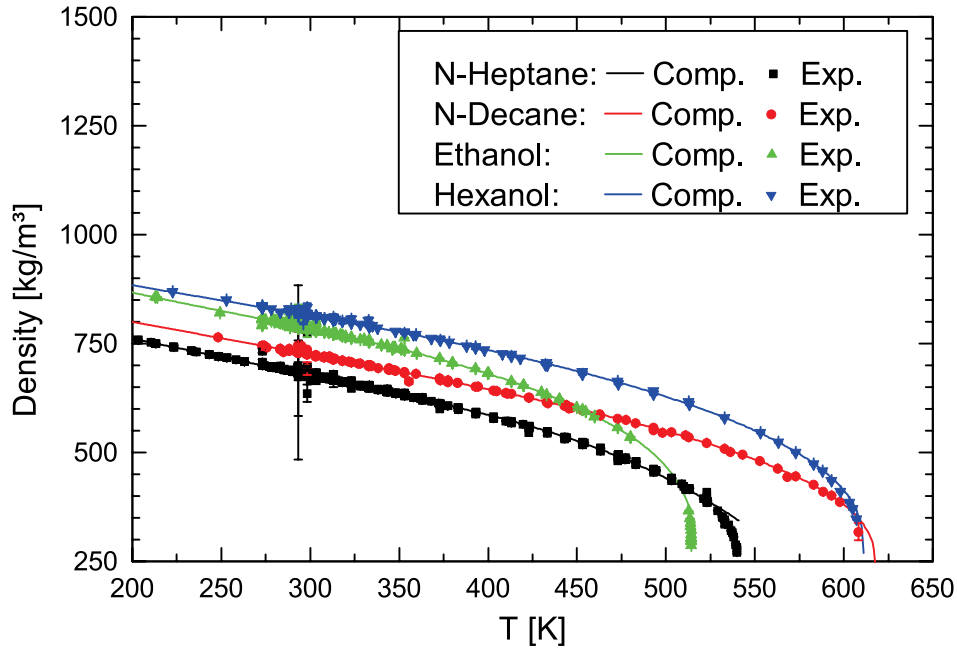


Figure 3.4: Comparison of thermodynamic property models with experimental data for liquid density.

For CTM evaporation models correlations of the thermodynamic properties with the distribution variable I and temperature are required. In this study, the equations developed in the work of Doué (2005) have been used. To develop the CTM property relations, the property of each component in a carbon number range from 4 to 20 have been computed. If there are multiple molecules for a certain carbon number, the properties are lumped together by linear mixing rules and formed a surrogated component. This procedure is exemplified in the case of iso-C₁₀H₂₂ in Figure 3.5. One can see how the simplification introduces a certain model form uncertainty for the thermodynamic sub-model, which can affect the evaporation model result.

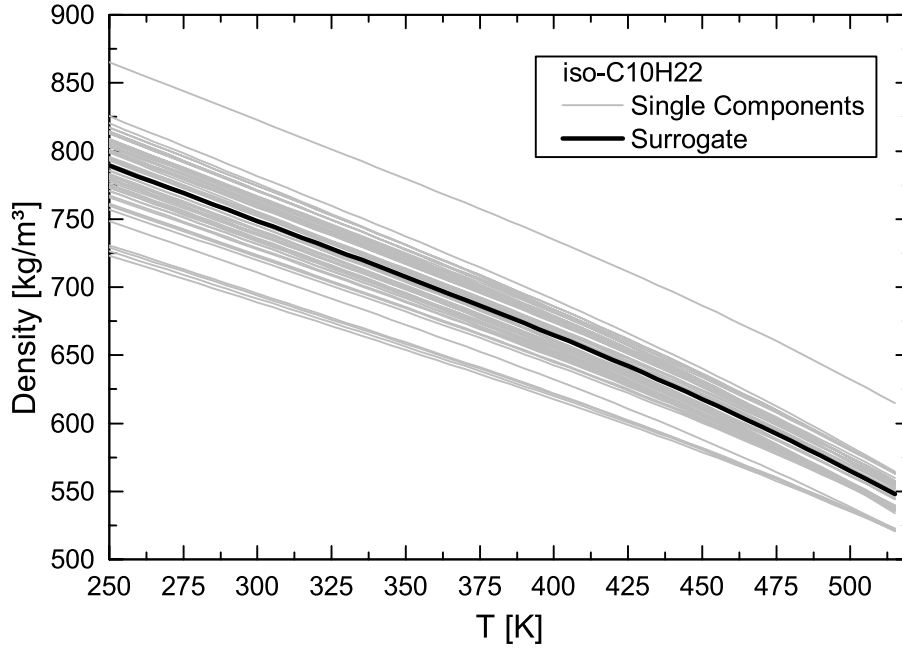


Figure 3.5: Liquid density surrogate for the iso-C10H22 component: the gray lines represent the different isomers; the black line is the surrogate component, which is used to compute the density of iso-C10H22.

3.4.1 Basic Property Correlation for Fuel Families

The correlation for the molar weight is in the general form

$$Wt = Wt_a + Wt_b I + Wt_c I^2 \quad (3.59)$$

with the coefficient $Wt_a, Wt_c = 0$ and $Wt_b = 1$ for the molar weight as distribution variable. The correlation for the normal boiling point is T_{nb} :

$$T_{nb} = T_{nb a} + T_{nb b} I + T_{nb c} I^2 \quad (3.60)$$

and for the critical temperature T_c

$$T_c = T_{c a} + T_{c b} I + T_{c c} I^2 \quad (3.61)$$

3.4.2 Liquid Phase Property Correlations

Enthalpy of vaporization

The temperature dependency is accounted for through the model of Watson and the fuel mixture latent heat of vaporization at the normal boiling point is given by the model of Vetere Poling, Prausnitz, and O'Connell (2000).

$$\Delta H_{\text{vap}} = \left(\Delta H_{\text{vap A}} + \Delta H_{\text{vap B}} I + \Delta H_{\text{vap C}} I^2 \right) \left(\frac{T_c - T}{T_c - T_{\text{nb}}} \right)^{0.38} \quad (3.62)$$

Liquid molar density

The correlation of Yamada and Gunn for pure species molar volume Poling, Prausnitz, and O'Connell (2000) is used together with a linear mixing rule. Then, using the molar mass, the results are fitted to define the liquid mole density of CTM mixtures

$$c_1 = (c_{1A1} + c_{1A2} T) + (c_{1B1} + c_{1B2} T) I + (c_{1C1} + c_{1C2} T) I^2 \quad (3.63)$$

Liquid heat capacity

The corresponding state method of Rowlinson Poling, Prausnitz, and O'Connell (2000) is used for pure components. Fitting discrete components results in the following correlation for CTM mixtures

$$C_{p1} = (C_{p1,A1} + C_{p1,A2} T) + (C_{p1,B1} + C_{p1,B2} T) I + (C_{p1,C1} + C_{p1,C2} T) I^2 \quad (3.64)$$

3.4.3 Gas Phase Property Correlations

Vapor pressure

The correlation follows Antoine's law and Antoine's coefficients for the mixture Poling, Prausnitz, and O'Connell (2000) are derived from a fit of the discrete component mixture

$$P_{\text{sat}}(T, I) = P_{\text{ATM}} \exp \left(\frac{A(T) + B(T) I}{T} \right) \quad (3.65)$$

$$A(T) = a_{\text{pv}0} + a_{\text{pv}1} T + a_{\text{pv}2} T^2 \quad \text{and} \quad B(T) = b_{\text{pv}0} + b_{\text{pv}1} T + b_{\text{pv}2} T^2$$

Vapor heat capacity

When available, the NASA polynomials (Goos, Burcat, and Ruscic, n.d.) are used to determine the molar heat capacity of pure species. For the remaining components, the group contribution method of Benson is used. Then, a linear mixing rule gives the mixture property. The fitting procedure using the values provided by this approach gives the following correlation:

$$C_{pv} = (C_{pv,A1} + C_{pv,A2} T + C_{pv,A3} T^2) + (C_{pv,B1} + C_{pv,B2} T + C_{pv,B3} T^2) I \quad (3.66)$$

Vapor dynamic viscosity

Single component viscosities were computed using the model of Reichenberg, and then Wilke's mixing rule based on simplified kinetic theory was used to derive the dynamic viscosity of gas mixture at atmospheric pressure. Finally, that pure component modeling technique was used to derive the following correlation for multicomponent-fuel vapor mixtures:

$$\log_{10}(\mu_1) = \left(Visb_1 + Visb_2 I + Visb_3 I^2 \right) \left(\frac{1}{T} - \frac{1}{Vis0_1 + Vis0_2 I + Vis0_3 I^2} \right) \quad (3.67)$$

Vapor thermal conductivity

The model of Roy and Todos Poling, Prausnitz, and O'Connell (2000) was used to derive discrete component thermal conductivity, and then the mixing rule of Wassiljewa was used to derive the thermal conductivity of the gas mixture.

$$\lambda_v = \left(\lambda_{vA1} + \lambda_{vA2} T + \lambda_{vA3} T^2 \right) + \left(\lambda_{vB1} + \lambda_{vB2} T + \lambda_{vB3} T^2 \right) I \quad (3.68)$$

Atomic diffusion volume for diffusion coefficient in the gas phase

Binary diffusion coefficients were derived from Fuller et al's method Poling, Prausnitz, and O'Connell (2000). Then, the mixing rule of Blanc Poling, Prausnitz, and O'Connell (2000) was used to derive the mass diffusion coefficient of species *i* within a gaseous mixture. In this procedure, the atomic diffusion volume *v* is a component-specific parameter, which can be correlated for CTM mixtures as follows

$$\sum v = v_A + v_B I \quad (3.69)$$

3.4.4 Phase Equilibrium for Non-Ideal Mixtures

For mixtures of high polar with non-polar components, the assumption of an ideal mixture is not valid. Following (Hallett and Beauchamp-Kiss 2010) a correction for the non-ideal mixture behavior based on activity coefficients for the phase equilibrium is introduced. The vapor pressure is most sensitive to the non-ideal mixing behavior, for the other thermodynamic properties an ideal mixing behavior is assumed. The following correlations are given by Poling et al. (2000). The corrected vapor pressure $P_{vap,i,nm}$ of a component in a non-ideal mixture is given by:

$$P_{vap,i,nm} = \gamma_{ac,i} x_{i,l} P_{vap,i} F_i \quad (3.70)$$

with the activity coefficient γ_i of species *i* and correction factor F_i which is near to unity for low total pressures.

The Wilson equation is used to describe the variation of the activity coefficients with mixture composition:

$$\ln \gamma_{ac,i} = -\ln \left(\sum_j^N x_j \Lambda_{ij} \right) + 1 - \sum_k^N \frac{x_k \Lambda_{ki}}{\sum_j^N x_j \Lambda_{kj}} \quad (3.71)$$

with Wilson parameter Λ , which can be determined with given experimental activity coefficients at infinite dilution $\gamma_{i/2}^\infty$ by solving:

$$\ln \gamma_{ac,1}^\infty = -\ln \Lambda_{12} - \Lambda_{21} + 1 \quad (3.72)$$

and

$$\ln \gamma_{ac,2}^\infty = -\ln \Lambda_{21} - \Lambda_{12} + 1 \quad (3.73)$$

Fuel fractions are treated as single components (Hallett and Beauchamp-Kiss 2010) with the activity coefficient equal to a representative component for the fuel fraction.

3.5 SPRAYSIM: Framework for the Solution of Evaporation Equations

The aforementioned droplet evaporation equations are part of the DLR in-house code SPRAYSIM. SPRAYSIM is written in Fortran 95 and is independent of a particular CFD-gasfield-code. It can be run standalone or coupled with various CFD codes (FLUENT, CFX, DLR theta, DLR Tascom). In standalone or one-way coupling, no source terms are exchanged with the gas field code. Two-way coupling happens in a spray-gas iteration process: spray feedback source terms are supplied to the gasfield code via file coupling or subroutine calls. In turn, the modified gasfield solution is returned to SPRAYSIM.

SPRAYSIM consists of three programs SPRAYPRE, SPRAYCORE, and SPRAYPOST and has the following features (Rachner 2014): In SPRAYPRE the particle initial conditions for the computational spray particles are generated. These initial conditions can be based on measurements, empirical correlations, or estimations. SPRAYCORE is the spray code for Lagrangian particle tracking. The Lagrangian particle tracking happens by solving the ordinary differential equations (ODEs) by Adams predictor-corrector scheme with the automatically adaption of order and step size (Brandt, Rachner, and Schmitz 1998) in time steps along the trajectories of many computational particles. Particle tracking is implemented for unstructured primary grids consisting of hexahedral, tetrahedral, prismatic and pyramidal elements. Tracked particles are registered in registration planes to enable the post-processing. SPRAYCORE has been augmented by a stripping atomization model for the plain-liquid jet in crossflow at high Weber numbers (Rachner et al. 1996; Rachner et al. 2002) and has different secondary break-up models as the TAB, ETAB and the CAB model (Tanner 2004). To model the particle dispersion Blümcke's spectral dispersion model (Bluemcke et al. 1991) or variants of the Gosman-Ioannides-

type dispersion model can be used. SPRAYPOST is a spray post-processing program, which has functions to analyze various aspects of the spray behavior, like diameter distributions, characteristic diameters (e.g., arithmetic mean diameter, Sauter mean diameter,) particle flows and fluxes, mean particle temperatures, and velocities.

3.6 Conclusions

Models for the numerical simulation of jet engine combustion chambers need to be computationally efficient but also capturing the details of evaporation of complex aviation fuels. To be able to solve the governing equations, simplifications and assumptions (like spherical symmetry, quasi-steady state in the gas film surrounding the droplet, and much more) are introduced. Furthermore, the heat and mass transfer processes through the film surrounding the droplet are described by empirical correlations (Nusselt and Sherwood number correlations). The sum of these builds up the model form uncertainty of discrete species droplet evaporation models. Furthermore, sub-models as those used for describing the thermodynamic properties introduce additional errors.

For the CTM model, the governing equations for discrete component models are transformed into the continuous space. The CTM presented here is based on Γ -PDF to describe the composition. Additional input errors are introduced by the initial fitting of the Γ -PDF to the discrete composition. Furthermore, it is required to develop simplified thermodynamic property correlations, which add to the models form error of CTM evaporation models.

In chapter 6, the model form uncertainties are quantified by comparing simulation results to measurement data. The knowledge of the nature and structure of the modeling equations becomes more critical when one wants to determine the predictive capability of the models. This often means the extrapolation of the inferred model accuracy (model form uncertainty) into conditions in which no model accuracy has been performed beforehand.

4 Validation Experiment

While traditional experiments focus on the characterization of the phenomena, validation experiments have an additional emphasis on inferring all the boundary and initial conditions required for numerical simulations. This means that the measurement access must not only include spray quantities of interest, but also all boundary conditions for the flow field and the initial conditions for the spray.

Alternative fuels for aero engines consist of hundreds of different species. During the evaporation, the composition of fuel is changing and thus its chemical-physical properties. In particular, the refractive index is one of the leading concerns in laser diagnostics of droplets and sprays in non-stationary conditions. Measurement techniques able to deal with alternative fuels need to be robust with respect to the variation of the fuel composition and accurate in resolving the diameter range of interest, as the diameter evolution in time and/or space is a measure of the evaporation rate.

In this chapter, the experimental system designed to study the evaporation of alternative fuel sprays under atmospheric pressure will be presented. The system will be characterized in detail to provide the information required for the modeling of the spray evaporation. The general features of the flow field and the data reduction of the spray measurements are described to give background information essential for the conceptualization of the system. The chapter will be concluded with a discussion about the spray measurement uncertainties.

4.1 Experimental System

The experimental system presented here has been developed based on earlier setups where the evaporation and combustion of fuel sprays have been studied with different kind of optical measurement techniques (Massoli, Beretta, and D'Alessio 1990; Massoli et al. 1993; Calabria and Massoli 2000; Calabria and Massoli 2004; Calabria, Casaburi, and Massoli 2003). The system has been redesigned to infer data for the validation of numerical droplet evaporation models. The focus was to maximize the measurement access to the spray and to create simple and well-defined boundary and initial conditions for the modeling.

Figure 4.1 is a schematic representation of the experimental system. The spray is generated at the top of the system and then transported into the test section by a cold quasi-laminar carrier gas flow. In the test section, the spray and carrier gas jet coincide with a preheated co-flow. The spray starts heating and then evaporates. The test section consists of a circular

4 Validation Experiment

quartz tube to enable the use of different scattering techniques at various scattering angles. It provides full optical access thereby allowing different kinds of measurement techniques to be applied (Rauch et al. 2010). The test section is mounted on a traversing unit and can be finely adjusted to new positions, in this way the whole spray can be characterized, and the diameter evolution can be inferred. When leaving the test section, the exhaust gases are cleaned by activated carbon filters.

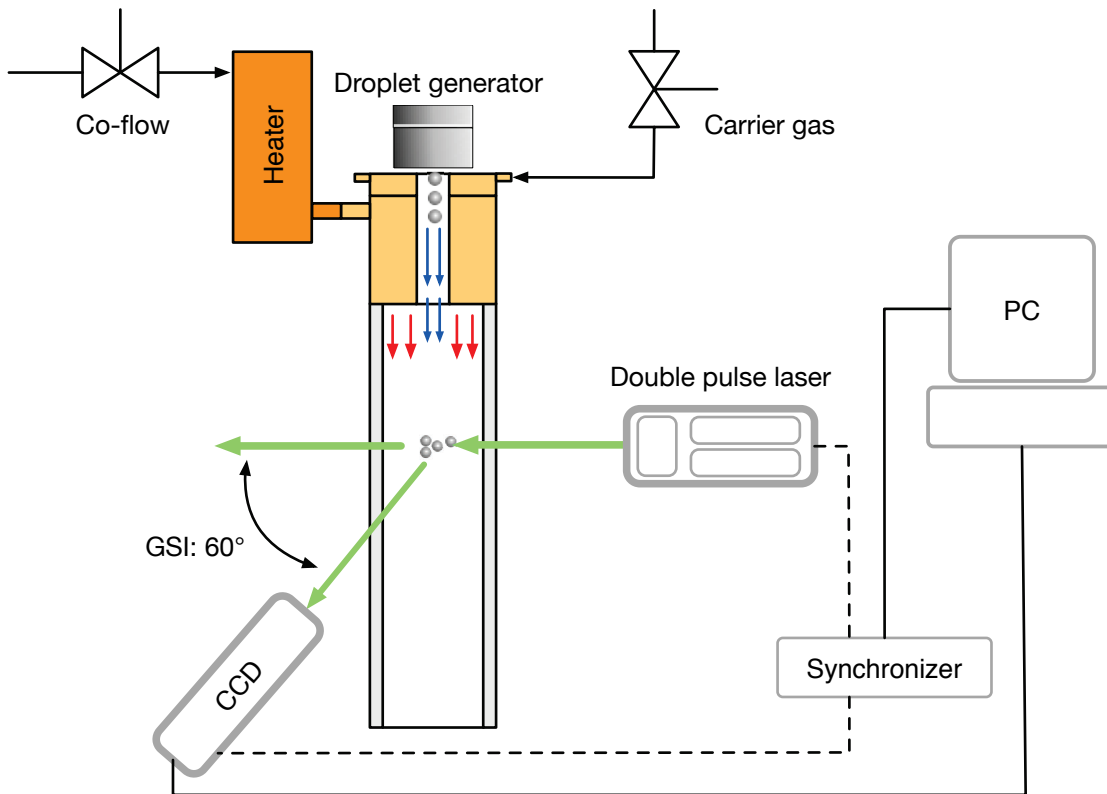


Figure 4.1: Schematic presentation of the experimental system.

For the spray generation, a monodisperse droplet generator is utilized. In this way, the effects of the different fuels on the evaporation can be distinguished more clearly. The spray is generated by the vibrating orifice aerosol generator (VOAG), Model 3450 of the TSI Corporation, MN, USA. It generates a monodisperse stream of droplets by applying an oscillating voltage to the piezoelectric crystal that induces regular instabilities on the liquid jet exiting the orifice. The generated stream of droplets is forced through a cone-shaped hole to disperse the droplets, and a monodisperse spray is generated. Interchangeable orifices allow varying droplets initial diameter from 21 μm to a maximum of about 400 μm . The droplet generator is suitable for alternative fuels and was used successfully in precedent studies with highly complex fuels like pyrolysis oil diluted with acetone (J. D'Alessio et al. 1998).

The co-flow is controlled by a thermal mass flow controller (Brooks Smart Series 5850S) and heated by a Sylvania Inline Heater 1.6 kW. To regulate the droplet carrier flow a Swagelok

Low-Pressure Valve M in combination with a high precision pressure valve SMC IR2020 is used. In the present configuration, for a mass flow rate of 3.54 kg/h, a maximum inlet temperature of 800 K can be reached. If required, two Sylvania inline heaters can be connected in series to reach a maximum temperature of 1000 K at the inlet.

To ensure always the same operating conditions, thermocouples have been installed at relevant positions. The temperature at the top of the flow conditioner is monitored to identify when the system reaches equilibrium temperature conditions. A thermocouple is installed centered at the outlet of the test section to monitor the temperature evolution of the flow field over time and to detect instabilities. Finally, a thermocouple is installed at the droplet generator head to measure the liquid injection temperature of the droplets.

4.1.1 Diagnostics

To characterize the spray, the generalized scattering imaging (GSI) is applied. In GSI configuration the CCD camera is placed at a scattering angle $\vartheta = 60^\circ$, where droplets size measurements exhibit the minimum sensitivity to the refractive index (Calabria and Massoli 2000). GSI is a robust measurement technique and has been used for a variety of fuels, from single component fuels like isopropyl alcohol, n-heptane, n-tetradecane as well as commercial fuels for heating and transportation, and complex fuels like emulsions or blends of heavy mineral oils, vegetable oils and pyrolysis oils (Stengele 1997, Massoli and Calabria 1999; Calabria and Massoli 2000; Calabria, Casaburi, and Massoli 2003; Calabria and Massoli 2004; Pan et al. 2006; Calabria and Massoli 2007).

The laser is a CFR200 Pulsed Nd:YAG Laser from the company Big Sky Laser Technologies Inc. It has a wavelength of 532 nm, a pulse duration of 8 ns, and a repetition rate of 15-30 Hz. The images are taken with the TSI Power View 4MP. The camera has a high resolution with 4 million pixels (resolution 2048 x 2048 px); it has a 12-bit intensity dynamic range and an image-capturing rate of 16 frames per second.

4.1.2 Inlet System

Of central importance for the quality of the experiment is the flow conditioner. In Figure 4.2 the details of the flow conditioning system and the position of the droplet generator are given. The flow conditioner has two primary tasks: first, to carry the spray from the injection point into the test section and, second, to condition the two inflows in order to create reproducible and stable experimental conditions. Limiting conditions for the development of the flow conditioning system are on the one hand the needs to minimize spray heating up in the distance from the spray generation to the test section and, on the other hand, to maximize the settling length that is required for the flow conditioners to create a homogeneous inflow.

4 Validation Experiment

To prevent vaporization of the spray before the test section, the carrier gas flow (see Figure 4.2) is entering the system at ambient temperature. The cone-shaped nozzle supports the development of flow with minimized turbulence levels (Martin et al. 2006). By this way, the dispersion of the spray and thus the number of droplets touching the walls before entering the test section is significantly reduced. The nozzle design yields low velocities at the porous media flow conditioner. This allows the use of small pore sizes (35 μm) to create small-scale turbulence without introducing a high-pressure drop at the flow conditioner.

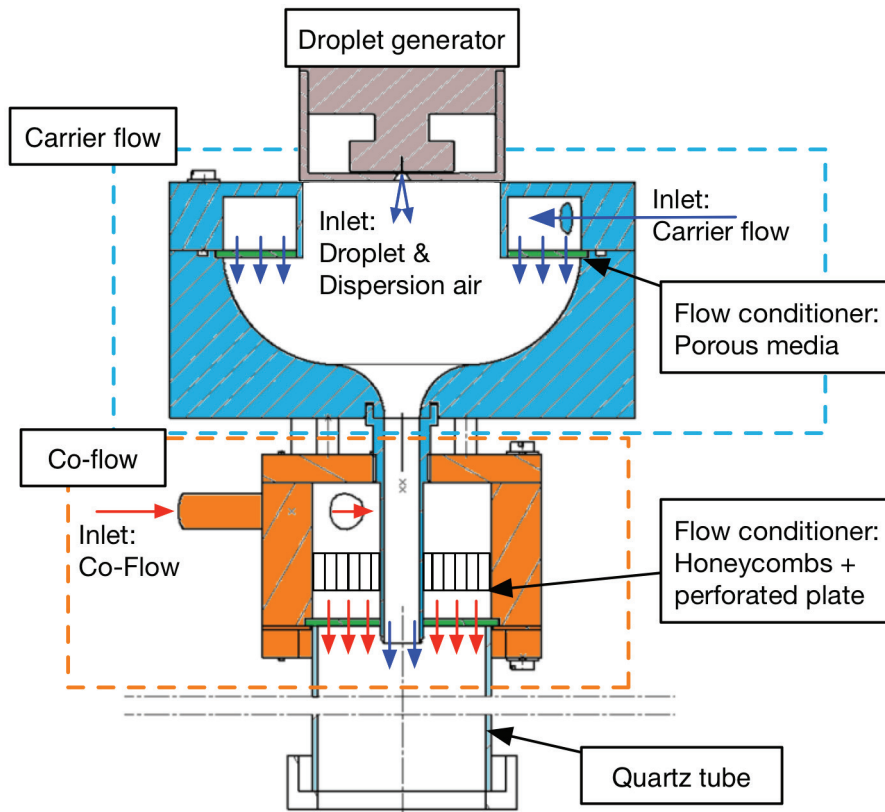


Figure 4.2: Inlet system: flow conditioner and droplet generator.

For the conditioning of the co-flow, a combination of honeycombs and perforated plate (hole diameter 1.5 mm, open surface factor 21%) are used. First, the honeycombs remove the swirling velocity component, then the pressure loss of the perforated plate yields to a homogenization of the air in the settling chamber. The turbulence structures at the test section inlet are created by interaction and decay of the jets leaving the perforated plate. For studies of the effect of turbulence on the spray evaporation, the flow conditioners can be changed.

The experimental system presented here is designed to study the spray evaporation of different kinds of fuels under well-controlled and monitored conditions. Ideally, the flow conditioner should yield simple and well-defined inlet conditions. The characterization of the flow field will be discussed in the following chapter.

4.2 Flow Field Characterization

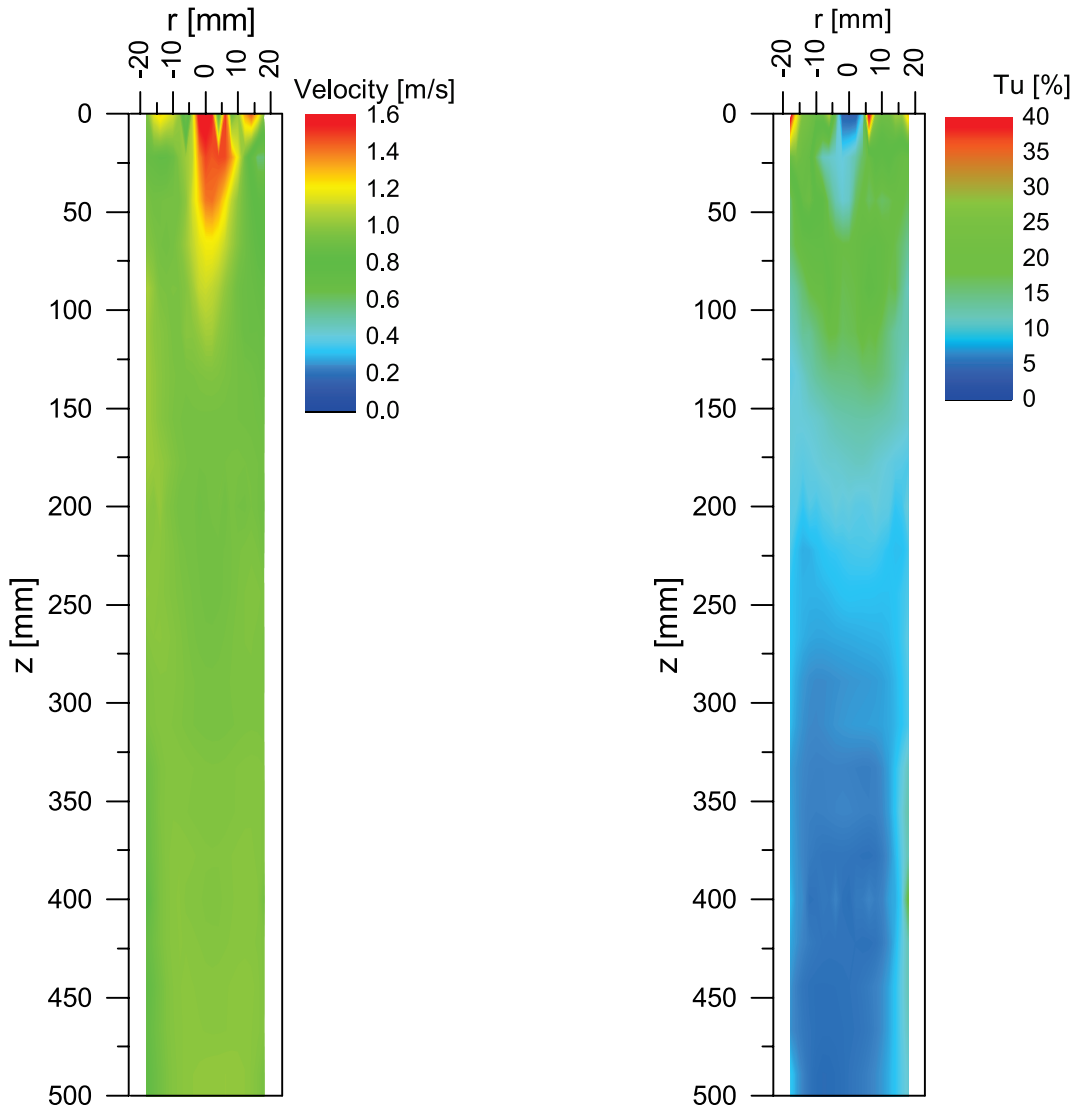
The aim in the development of the flow conditioner was to create simple and well-defined boundary conditions. Two flow fields are used in the study: one with a cold co-flow (at ambient temperature) and the other one with a preheated co-flow (average co-flow inlet temperature: 700 K). In the cold flow case, the velocity field was characterized by a hot wire anemometer. The hot flow temperature field was characterized with thermocouple measurements. Since the hot wire anemometer is not suitable for flows with non-uniform temperature fields with temperature fluctuations, no velocity field information is available for the hot flow case.

To characterize the flow fields, the probes have been mounted on a horizontal traversing unit. Measurements have been performed every 2 mm to infer the radial profiles. By moving the test section, different profiles along the axis have been taken. Close to the inlet, every 2 mm a radial profile was inferred to characterize in detail the inhomogeneity. From $z = 50$ to 200 mm a profile every 25 mm was taken, after 200 mm the step size was increased to 50 mm.

4.2.1 Cold Flow

For the characterization of the mean velocity, the velocity fluctuations and the turbulence spectrum a constant-temperature anemometer from Dantec Dynamics was utilized. The probe used was the single sensor miniature wire 55P11 probe with a length of 1.25 mm and a diameter of 5 μm .

Figure 4.3 shows the mean flow velocity field and the turbulence intensity field. In the picture $z = 0$ mm corresponds to the beginning of the test section. When entering the test section, the carrier gas is forming a jet with an initial diameter of 10 mm. It can be seen that the inflow of the co-flow is not homogeneously distributed. Small jets are forming at $r = -15$, 6, and 14 mm, their direction is towards the carrier gas jet. The jets show strong velocity fluctuations causing high turbulence intensity at the inlet. The carrier gas flow has to transport the droplets into the test section; by the higher velocity with respect to the co-flow, the imperfections resulting from the co-flow flow conditioning are overcome. After $z = 50$ mm the co-flow shows a homogeneous distribution and the carrier gas transporting the droplets is still aligned with the centerline thus preventing the droplets from leaving the measurement volume. After $z = 100$ mm the jet is completely mixed and a homogeneous velocity condition is reached.



a) Velocity field

b) Turbulence intensity field

Figure 4.3: Cold flow velocity and turbulence field.

Figure 4.3b) shows very low turbulence intensity of the carrier flow jet at the injection into the measurement section. The co-flow injection turbulence intensity, which is of the order of 20% and the shear stresses due to the velocity difference of carrier jet and co-flow cause a rapid increase in the turbulence intensity of the carrier gas jet.

4.2.2 Hot Flow

For the hot flow case, a similar ratio of carrier and co-flow was chosen so that the carrier jet transports the spray into the test section by overcoming initial asymmetries in the co-flow system. To measure the temperature of the flow field a J-type thermocouple was used. Measurements were taken radially each 1 mm for $-18 < r < 18\text{mm}$ and then moving down 5 mm for $0 < z < 50\text{mm}$) 25 mm for $50 < z < 100\text{mm}$, 50 mm for $100 < z < 200\text{mm}$ and 100 mm for $200 < z < 600\text{mm}$. Figure 4.4 shows the temperature distribution in the test section.

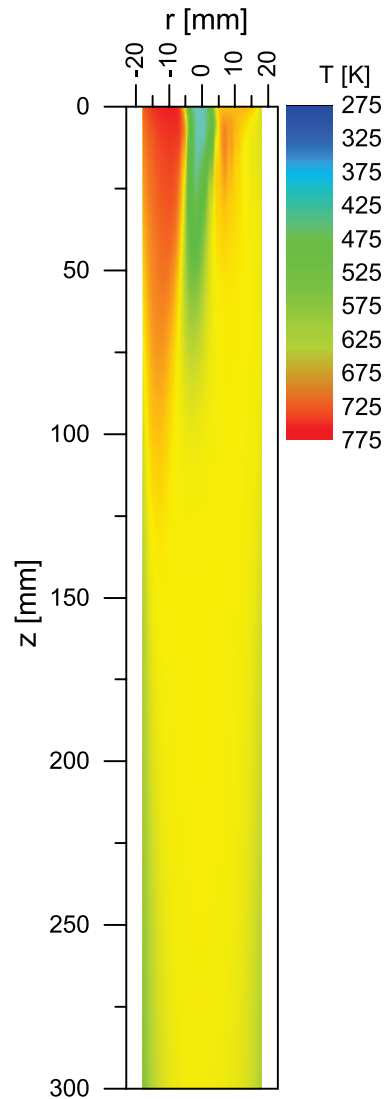


Figure 4.4: Temperature field.

It can be seen that the carrier gas, which started at 300 K at the droplet generator, was heated up to around 400 K when entering the test section. The preheated co-flow enters the test track with a radially averaged temperature of 700 K. The inlet temperature distribution is asymmetric with a difference of 50 K. As for the cold flow, the carrier jet remains centered in the test section and is only slightly distorted to the left. At $z = 100$ mm the jet is mixed with the co-flow. The asymmetry in the co-flow field diminished nearly entirely until $z = 125$ mm.

4.2.3 Conclusions

The velocity and temperature fields of the validation experiment have been characterized with hot-wire anemometry and thermocouple measurements. The co-flow inflow showed a certain degree of asymmetry and irregularities: in the cold flow velocity field, jets can be seen leaving the flow conditioner and their direction is towards the carrier gas jet, in addition in the hot flow field the inflow is hotter by 50 K on the left-hand side. The carrier gas jet remained aligned with the centerline in both cases, which is essential to ensure that the evolution of the spray along the

centerline is captured by the measurement volume. For the carrier gas jet, an immediate transition to turbulence has been detected when entering the test section. The turbulence intensity was characterized to be in the range of 5 to 10% along the spray evaporation axis while showing higher degrees (25 % to the maximum value of 40%) of turbulence intensity for the primary inflow.

The effect of the asymmetry in the inflow conditions on the spray evaporation will be evaluated in chapter 0. It determines if the data analysis can be simplified by assuming a symmetric flow field and if the spray droplets can be reduced to one characteristic value for each measurement position. Furthermore, the need to model the inflow asymmetry will be evaluated as part of the discussion when evaluating the conceptualization of the validation experiment in chapter 0.

4.3 Spray Characterization

The experimental system is designed to study a large variety of fuels with different properties. Information about the evolution of the spatial distribution of droplet diameter and velocities along the test section is inferred to provide information for the validation of fuel droplet evaporation models. The best settings of the measurement technique have been determined to resolve the phenomena of interest in detail with maximized accuracy. To describe the spray evaporation and to be able to confront simulation results with experimental data, the measurement data has to be reduced to meaningful and significant System Response Quantities (SRQ's).

4.3.1 Generalized Mie Scattering Imaging

To characterize the spray evaporation, the Generalized Scattering Imaging (GSI) technique (Calabria and Massoli 2000) was applied to simultaneously determine the size, velocity, and spatial location of the evaporating droplets. GSI uses the Mie scattering of laser light at the spray droplets to infer in the out-of-focus condition the planar characteristics of the spray.

Figure 4.5 shows a schematic view of laser scattered by a droplet. The laser light is scattered by the droplet with the scattering angle ϑ . In out-of-focus position, an oscillatory pattern is shown with a characteristic $\Delta\vartheta$. α represents the Mie scattering parameter.

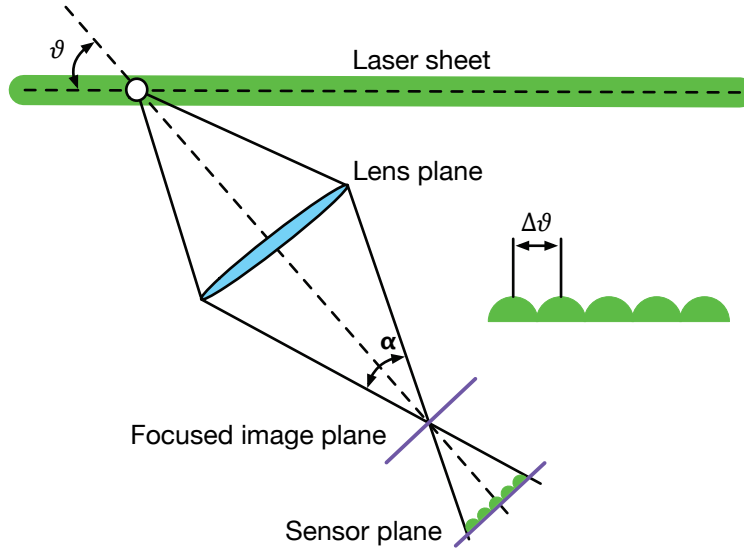


Figure 4.5: Schematic view of laser light scattering.

The technique routes in the early developments of Bartholdi et al. (1980 and König et al. (1986). (Hesselbacher et al. (1991) related the fringe spacing $\Delta\vartheta$ to the droplet diameter D by using the formula of Glantschnig and Chen (1981), which was derived under geometrical optics assumptions:

$$\Delta\vartheta \cong \frac{2\pi}{\alpha} \left(\cos(\vartheta/2) + \frac{m \sin(\vartheta/2)}{\sqrt{1 + m^2 - 2m \cos(\vartheta/2)}} \right)^{-1} \quad (4.1)$$

and with the relation of the Mie scattering parameter α with the droplet diameter D and laser wavelength λ as defined in Kerker (1969):

$$\alpha = \pi D / \lambda \quad (4.2)$$

m denotes the complex refractive index and ϑ the scattering angle (the angle between the incident light beam and the detection optics). First approaches were using an array of photodiodes applied on single droplets in laboratory environments. To extend the technique to sprays (Ragucci, Cavaliere, and Massoli 1990) used a digital camera in out-of-focus conditions, thus enabling planar measurements. To determine the droplet diameter, they compared the measured signal with light scattering calculations based on the Lorentz Mie theory. Being based on the Mie theory, the group later called the technique Generalized Scattering Imaging (GSI). (Glover et al. (1995) applied the approach introduced by Ragucci, Cavaliere, and Massoli (1990) to characterize a sparse spray. For the evaluation of the droplet diameter, they use a simplified form of Eq. (4.1), as first suggested by König, Anders, and Frohn (1986). They called the technique Interferometric Laser Imaging for Droplet Sizing (ILIDS). Maeda, Kawaguchi, and Hishida (2000) applied the approach of Ragucci, Cavaliere, and Massoli (1990) and introduced

4 Validation Experiment

an optical compression to reduce the oscillation pattern overlap and thus to increase the maximum limit in measurable number density.

In the aforementioned developments, the diameter measurements depend on the refractive index as can be seen in Eq. (4.1). In technical relevant conditions the refractive index changes due to heating and selective evaporation causing nonnegligible errors in the diameter measurement (Glover, Skippon, and Boyle 1995; Massoli 1998). Massoli and Calabria (1999) and Calabria and Massoli (2000) theoretically studied the light scattering on droplets with a variety of refractive indexes and considering the radial distribution of refractive index inside the droplet. They found that at $\vartheta = 60^\circ$ the influence of the refractive index on the sizing is at a minimum. Neglecting the refractive index the droplet diameter can be inferred with an uncertainty below 4% with

$$\Delta\vartheta_{\text{rad}}(\vartheta, m(r), D) = 1.129(180^\circ / \alpha) \quad (4.3)$$

and with

$$D = 1.129 \left(\frac{\lambda}{\Delta\vartheta_{\text{rad}}} \right) \quad (4.4)$$

where 1.129 is a fitting parameter, which has been inferred in Massoli and Calabria (1999) and Calabria and Massoli (2000). The parameter can be adapted with knowledge of the refractive index to reduce the measurement uncertainty further. The fringe spacing in radians $\Delta\vartheta_{\text{rad}}$ is inferred from the fringe spacing in pixel $\Delta\vartheta_{\text{px}}$ by experimental calibration

$$\Delta\vartheta_{\text{rad}} = \Delta\vartheta_{\text{px}} * C_{\text{rad/px}}(x) \quad (4.5)$$

with the calibration constant $C_{\text{px/rad}}(x)$ as a function of the axial position.

4.3.2 Application of GSI

The test section is a quartz tube of non-optical quality with a diameter of 50 mm. The quartz tube transmits most of the laser light; however, noisy luminous spots were generated on the tube wall due to multiple reflections of the laser beam at the quartz/air interphases, caused by the roughness of the tube surfaces and small misalignments. Figure 4.6 shows a typical measurement image. The signal pattern of the droplets can be seen in the center. At the border, reflections of the laser light in the quartz tube can be observed. The positions of the reflections depend on the optical setup and are at the same position during a measurement campaign. Data in these regions could not be analyzed and was masked for the signal analysis. By changing the magnification and the relative aperture of the CCD, the dimensions of the noisy region can be controlled within certain limits. An optimum value was iteratively determined to be able to resolve the diameter range of interest and to minimize the noisy region. Only in the later part of the spray evaporation,

the dispersion of the spray leads to an overlapping of the noisy region and spray measurement signals, but the effect was very limited in most cases.

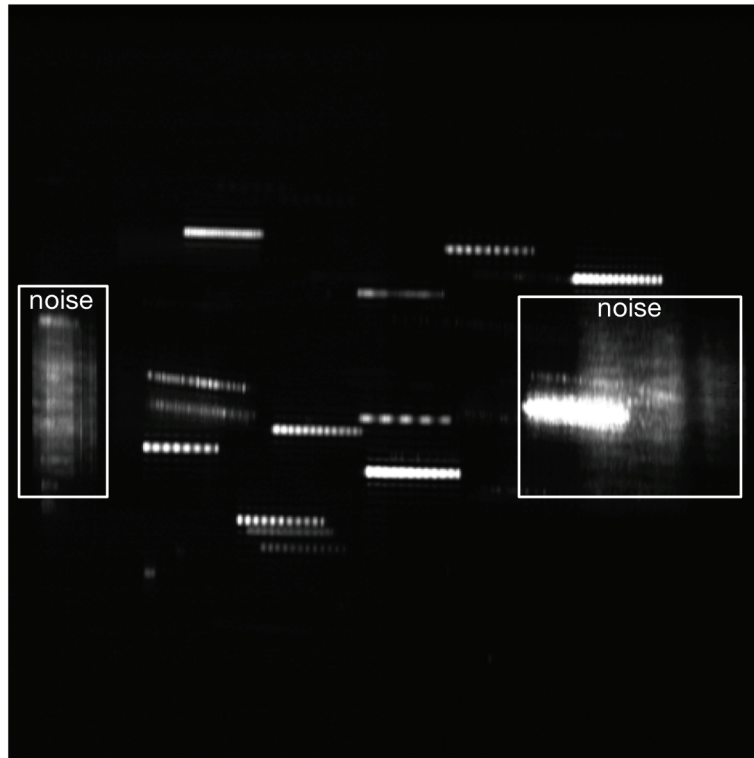


Figure 4.6: GSI measurement image with noise due to reflections in the quartz tube.

To verify that the quartz tube does not lead to a distortion of the measurement signal, the scattering signal of the calibration target was inferred at various longitudinal positions. In Figure 4.7 the comparison of two calibrations measurements is shown. To infer the influence of the quartz tube on the calibration, one calibration has been inferred without the quartz tube and the other at the same configuration but inside the quartz tube. Besides some random scatter of the signal, which can be seen for both calibration signals, there is only a negligible difference. In consequence, calibrations have been performed without the quartz tube.

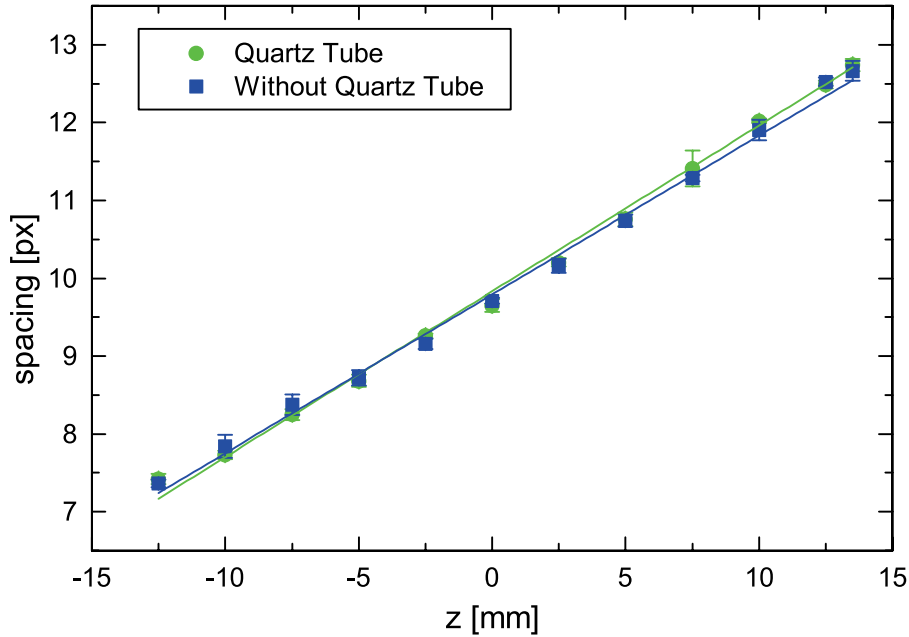


Figure 4.7: GSI calibration signals at different longitudinal positions, comparing the effect of the quartz tube on the calibration signal.

As mentioned before, the optical settings (magnification and defocus shift) have been determined iteratively to optimize the ratio of the size of the measurement plane and noise. The resulting theoretical limitations of the measurable diameter range are given by two conditions: The lower diameter limit is determined by the condition that at minimum one oscillation has to be covered by the aperture (width of oscillation pattern). The upper limit is determined by the Nyquist criterion, which specifies that one oscillation must cover at least two pixels. The width of the oscillation pattern can be inferred from the calibration measurements. Applying these two extreme conditions to Equation (4.4) results in a measurable diameter range of 8 to 250 μm , for the chosen optical configuration.

In addition, since the intensity of the scattered light is proportional to the square of the diameter, the dynamic range of the light intensity is limiting the measurable diameter range. For the measurement this means, bigger droplets can yield a saturation of the signal, while smallest droplets end up with a too low signal to noise ratio. In practice, for the chosen beam fluence the measurable diameter range was in between 20 to 200 μm . The influence of the measurable diameter range on the characterization of the spray evaporation is part of the measurement uncertainty discussion in section 4.4.2.

4.3.3 Spray Characterization

The overall spatial distribution of the spray and its variation along the path are analyzed to depict the spray evaporation process. To this aim, the size and position of each droplet in the spray at different axial positions were inferred using the GSI technique. Figure 4.8 and Figure 4.9 show the reconstruction of the spatial spray distribution for Jet A-1 and n-decane. The analysis of the

raw GSI data was performed by means of a post-processing software, which was developed during this study. Measurements were performed with a 10 mm or 20 mm step along the z-axis, with the initial location centered at $z = 5$ mm, then going down the axis all the way to $z = 240$ mm. Each captured droplet is represented by a circle, the diameter of which is proportional to its actual size. The height of the spray section in every location is limited by the laser sheet width and is equal to 10 mm. This post-processing method and associated graphical representation allow verifying the centering and the tilting of the spray with respect to the quartz tube axis. During the tests, the maximum off-center position and tilting were limited to 2 mm and 0.5° , respectively.

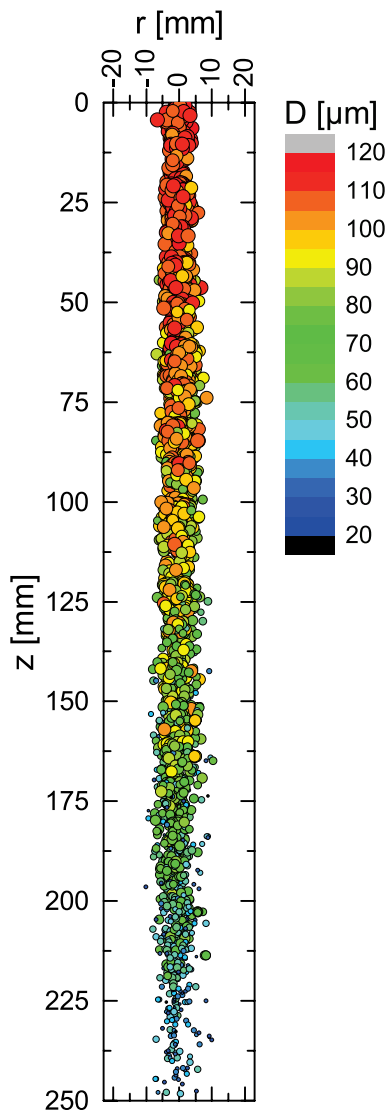


Figure 4.8: Spray structure: Jet-A1, measurement volumes at a step width of 10 mm.

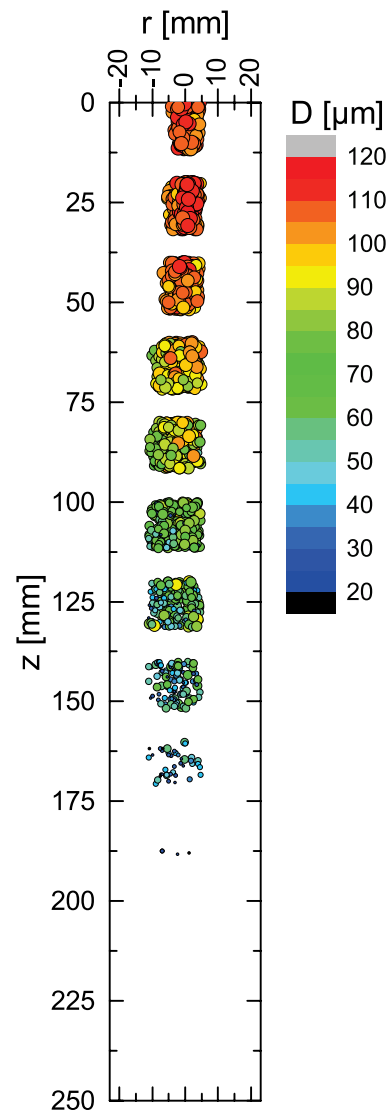


Figure 4.9: Spray structure: n-decane, measurement volumes at a step width of 20 mm.

4.3.4 Data Reduction

To be able to compare the effect of different fuels compositions on the evaporation, the spatially distributed single droplet diameter and velocity data points have to be reduced to significant

4 Validation Experiment

values describing the evaporation characteristics of the spray. From the repeated instantaneous measurements at different axial positions, one can derive statistics about the droplet size distribution. On average, 500 droplets have been processed in each measurement position. The spatial evolution of the droplet diameter ensemble average (mean of the distribution) and its standard deviation are given in Figure 4.10. At $z = 5$ mm the spray is injected with a normal distribution, a mean diameter of $109 \mu\text{m}$ and a standard deviation of around $3.5 \mu\text{m}$. The distribution is becoming wider and the mean diameter is reduced with proceeding heat and evaporation of the spray. After $z = 100$ mm the smallest droplets are below the detection limit and are not captured anymore. The influence on the measurement uncertainty is evaluated in section 4.4.2. Due to the velocity profile of the carrier gas before the test section, the spray is injected with a velocity distribution (mean velocity of 2.6 m/s and standard deviation of 0.26 m/s). After injection, the standard deviation of the spray velocities is diminishing with the decay of the carrier gas jet and turbulence levels of the flow and reaching their minimum values after $z = 120$ mm. These qualitative features are similar for all the fuels characterized in this study.

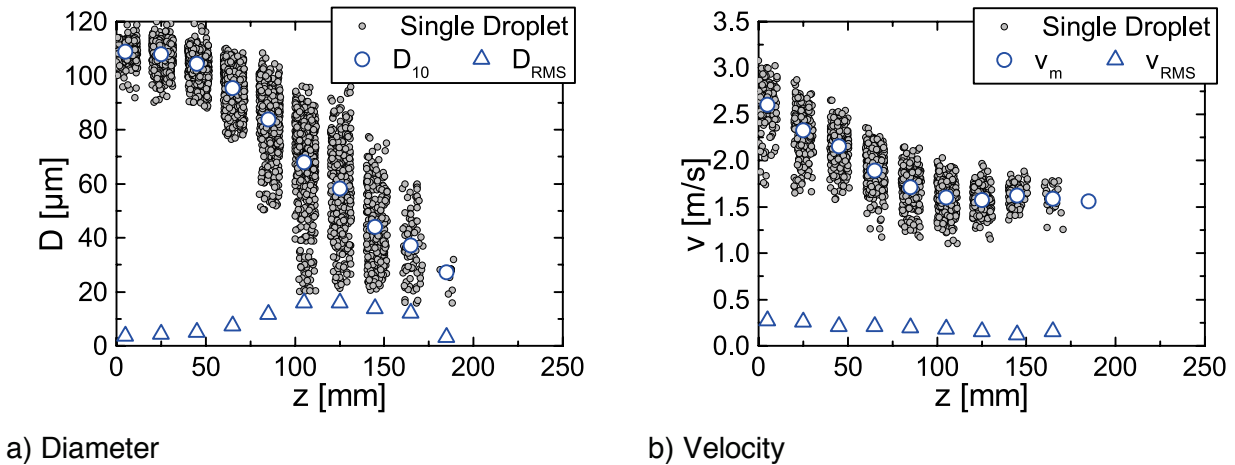


Figure 4.10: N-decane spray, velocity scatter plot and reduction to mean velocity and velocity fluctuations.

To describe the evaporation characteristics of the spray, the arithmetic mean of the diameter and velocities was chosen. It was found to be the most robust with errors and required the lowest number of samples per position (see also Panão and Moreira (2008)). In the actual configuration, the measurement time available was limited by the capacity of the fuel reservoir and determined the number of samples per position. In addition the droplet generator produced a monodisperse spray, resulting in very similar values for the Sauter mean diameter and the arithmetic mean diameter in the beginning, but to higher uncertainties for the Sauter mean diameter after $z = 100$ mm.

The data reduction requires different assumptions and simplifications to be made. Some smaller and bigger droplets outside the normal range of droplet diameters can be observed for all discrete distributions as shown in Figure 4.11. These can be due to single random effects such as

droplet coalescence, to droplet flight paths in the secondary flow that are closer to the near wall hot region, or to droplet generator instabilities which can result in the production of satellite droplets. For the comparison with the numerical simulation, these droplets have been filtered out since they are seldom, of random nature and cannot be reproduced. To filter the data the main peak of the distribution function is identified. Starting from this point the two minimum values in the distribution function, one for the smaller diameters and one for the bigger diameters are identified. Droplets outside this range are removed for further data analysis.

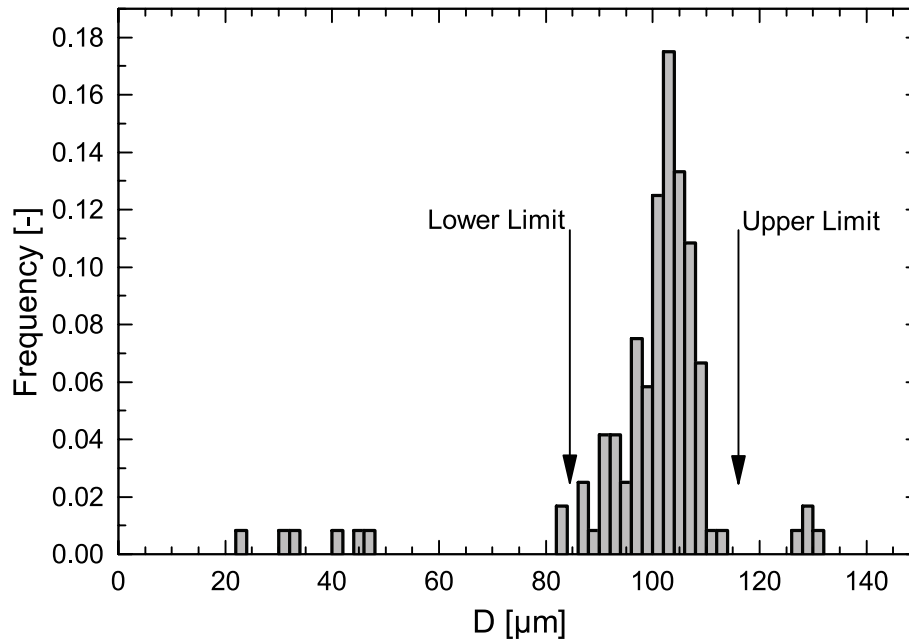


Figure 4.11: Diameter distribution and distribution limits identified by a filter at $z = 5$ mm.

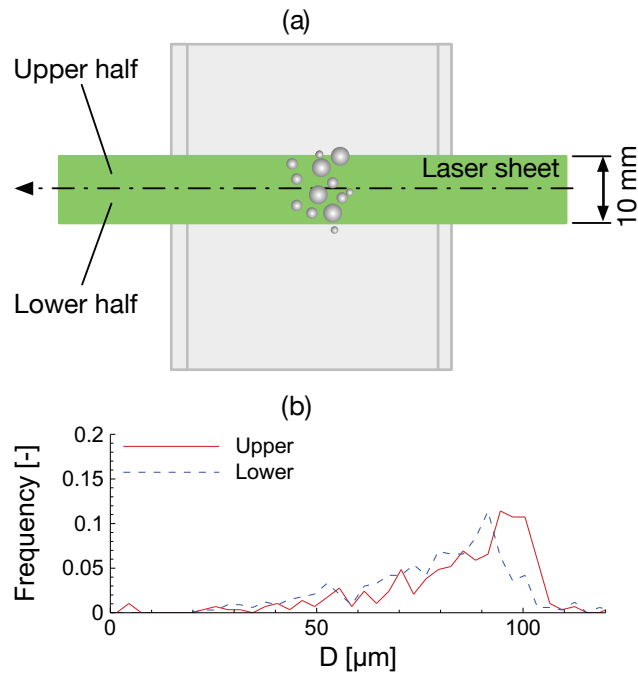


Figure 4.12: Effect of averaging over the laser sheet (Rauch, Calabria, Chiariello, Le Clercq, Massoli, and Rachner 2011): (a) Sketch of the measurement volume; (b) Size distribution of n-nonane droplets at $z = 80$ mm measured in the upper half and lower half regions of the laser sheet.

Moreover, it should be emphasized that the laser sheet width, which is equal to 10 mm in the axial direction, adds substantially to the size distribution deviation about the mean. Actually, Figure 4.12 (a) gives the relevant details concerning the droplet size distributions within the upper and lower halves of the laser sheet separately. As can be seen in Figure 4.12 (b) the n-nonane droplet size distribution in the upper half of the sheet (i.e.: earlier in the droplet lifetime with respect to the middle of the sheet width) has a bigger mean value than the distribution in the lower half (i.e.: later in the droplet lifetime). This effect is more pronounced for droplets that vaporize rapidly.

4.3.5 Conclusions

In this section, the application of the GSI measurement technique to the experiment was described. The full measurement access in the test section enables to capture the complete spray in the test section. Since the spray is quasi-monodisperse, the evolution of the arithmetic mean droplet diameter over each measurement position is taken to characterize the spray evaporation. In the following section, the measurement uncertainties for the measured quantities and the mean values are derived and discussed.

4.4 Measurement Uncertainty

Since measurement data represent only the best estimate but not the true value, for the interpretation of the measured quantities and for the comparison with simulation results, it is crucial to estimate the range in which the true value lies. In this section, the measurement

uncertainties for the measured quantities of the spray are determined and summarized. For all measurement uncertainties, a confidence interval of 95% is used.

4.4.1 Measured Quantities

Table 4.1 summarizes the results of the uncertainty evaluation of the quantities characterizing the spray. The uncertainties are deduced from parameter uncertainties; details are given in the following sections.

Quantity	Method	Uncertainty
Droplet diameter	GSI	$ \delta D/D _{\text{single}} = \pm 4.77\%$
Droplet position x y	GSI	$\delta x_{\text{mm}} = \pm 0.09 \text{ mm}$ $\delta y_{\text{mm}}/y_{\text{mm}} = \pm 0.86\%$
Droplet velocity	GSI	$\delta u_y/u_y = \pm 1.13\%$

Table 4.1 Overview of the uncertainties of the measured quantities.

Droplet Diameter

The uncertainty in the droplet diameter measurement $|\delta D/D|_{\text{single}}$ is constituted of three uncorrelated parts, the model uncertainty due to neglecting the refractive index $|\delta D/D|_{\text{GSI}}$, the uncertainty due to the finite laser beam thickness $|\delta D/D|_{\text{beam}}$, and the uncertainty due to the propagation of the parameters uncertainties of the GSI sizing equation (4.4) $|\delta D/D|_{\text{exp}}$.

$$\left| \frac{\delta D}{D} \right|_{\text{single}} = \sqrt{\left| \frac{\delta D}{D} \right|_{\text{GSI}}^2 + \left| \frac{\delta D}{D} \right|_{\text{beam}}^2 + \left| \frac{\delta D}{D} \right|_{\text{exp}}^2} \quad (4.6)$$

As discussed in section 4.3.1 GSI theory, by neglecting the refractive index a maximum uncertainty of $|\delta D/D|_{\text{GSI}} = \pm 4\%$ is created. This uncertainty is systematic, and it can be reduced by numerically evaluating the influence of the expected variations of the refractive index on the sizing measurements and deriving a new fitting parameter for the limited variation of the refractive index (Calabria and Massoli 2000).

In the present configuration, the defocus distance was equal 25 mm. However, droplets traversing the beam in different locations will be subjected to different magnifications. The laser sheet thickness was 500 μm to allow high droplet detection rate. According to Hesselbacher et al. (1991), the expected uncertainty in the size determination $|\delta D/D|_{\text{beam}}$ due to the Gaussian beam is about $\pm 2\%$.

To describe the uncertainty in the GSI sizing equation, the law of error propagation is applied to Equation (4.4), where the angular fringe spacing was replaced by Equation (4.5).

$$\left| \frac{\delta D}{D} \right|_{\text{exp}} = \sqrt{\left(\frac{\delta \lambda}{\lambda} \right)^2 + \left(\frac{\delta \Delta \vartheta_{\text{px}}}{\Delta \vartheta_{\text{px}}} \right)^2 + \left(\frac{\delta C_{\text{rad/px}}}{C_{\text{rad/px}}} \right)^2} \quad (4.7)$$

The uncertainty in the wavelength is small, and the maximum deviation is estimated to be ± 0.5 nm. To evaluate the uncertainty in the detection of the oscillation spacing $\delta \Delta \vartheta_{\text{px}} / \Delta \vartheta_{\text{px}}$, the work of Dehaeck and van Beeck (2007) is followed, they state that the primary uncertainty derives from noise in the signal. The Cramer–Rao Lower Bound as described in Albrecht et al. (2002) is used to “determine the minimum variation on the estimated spacing that an unbiased estimator can obtain in the presence of white Gaussian noise.” The calibration with the optical fiber contributes with a relative uncertainty $\delta C_{\text{rad/px}} / C_{\text{rad/px}}$ of $\pm 1.2\%$. The computed uncertainty components are summarized in Table 4.2.

Term	Uncertainty	Error source
$\frac{\delta \lambda}{\lambda}$	$\pm 0.09\%$	$\delta \lambda = \pm 0.5 \text{ nm}$
$\frac{\delta \Delta \vartheta_{\text{px}}}{\Delta \vartheta_{\text{px}}}$	$\pm 1.13\%$	Noise, Cramer-Rao Lower Bound estimation
$\frac{\delta C_{\text{rad/px}}}{C_{\text{rad/px}}}$	$\pm 1.2\%$	From calibration

Table 4.2 Uncertainty components of the GSI uncertainty equation.

In addition to the aforementioned uncertainties, other factors like the effect of non-spherical particles, particle overlapping and the influence of the finite duration of the laser pulse influence the diameter measurement. Non-spherical particles and the overlapping of particles result in a distorted signal with multiple spacing information. This can be detected during the signal analysis, and such signals are not considered for the further analysis.

Finally, the influence of the droplet motion during the image acquisition (exposure time) on the measurement accuracy has been also evaluated. In the present case, the images were frozen by the short duration of the laser pulse. By considering the laser pulse duration, 8 ns, and the maximum droplet velocity, 3 m/s, the maximum droplet’s shift during the image acquisition is equal to 24 nm. Therefore, the maximum deformation of the droplet image is well within the one-pixel resolution of the digital system where 1px corresponds to approximately 10 μm . Thus, the finite duration of the laser pulse had negligible influence on the size determination.

Droplet Position

As described in section 4.3.2 the longitudinal position of the droplet is determined by a calibration correlation inferred by moving the calibration target to different longitudinal positions. The uncertainties of the lateral position is composed of two correlated parts,

$$\delta x_{\text{mm}} = \delta x_{\text{mm,calib}} + \delta x_{\text{mm,detec}} \quad (4.8)$$

with the calibration uncertainty $\delta x_{\text{mm,calib}} = \pm 0.13\text{mm}$ and detection uncertainty $\delta x_{\text{mm,detec}} = 10\text{px} \hat{=} 0.15\text{mm}$. The detection uncertainty is mainly due to partial overlapping from droplet signals and difficulties in defining the lateral limitations of the droplet signals.

The vertical position of the droplet is determined by an equation derived from geometrical optics:

$$y_{\text{mm}} = \frac{y_{\text{px}} \text{CCD}_{\text{mm/px}}}{M_{\text{OoF}}} \quad (4.9)$$

The uncertainty in the physical dimensions of a pixel on the CCD, $\text{CCD}_{\text{mm/px}}$, can be neglected. Thus, the uncertainty of the vertical position is determined by the detection uncertainty δy_{px} and the uncertainty in determining the out of focus magnification δM_{OoF} :

$$\frac{\delta y_{\text{mm}}}{y_{\text{mm}}} = \sqrt{\left(\frac{\delta y_{\text{px}}}{y_{\text{px}}}\right)^2 + \left(\frac{\delta M_{\text{OoF}}}{M_{\text{OoF}}}\right)^2} \quad (4.10)$$

In Table 4.3 the contributing uncertainties are summarized. In contrary to the difficulties in the longitudinal detection, the center of the vertical droplet position can be clearly defined, and an overlapping of scattering signal is minimized by the use of a slit in front of the camera.

Term	Uncertainty	Error source
$\frac{\delta y_{\text{px}}}{y_{\text{px}}}$	0.056%	$\delta y_{\text{px}} = \pm 1_{\text{px}}$
$\frac{\delta M_{\text{OoF}}}{M_{\text{OoF}}}$	0.844%	$\delta M_{\text{OoF}} = 0.0051$, uncertainties from calibration

Table 4.3 Uncertainty components for the vertical position y.

Droplet Velocity

The uncertainty in the velocity vector is mainly due to the propagation of the uncertainty in determining the droplet position. The uncertainties in the droplet velocity are summarized in Table 4.4. Since the horizontal droplet velocity component u_x is very small with respect to the vertical droplet velocity, its contribution to the uncertainty of the velocity magnitude is very limited.

Term	Uncertainty	Error source
$\delta \vec{u} $	± 0.04 m/s	Error propagation of velocity components ($\delta u_x, \delta u_y$)
δu_x	± 0.45 m/s	Position measurement δx_{mm} and laser pulse delay $\delta \Delta t \approx 1\mu\text{s}$
$\frac{\delta u_y}{u_y}$	$\pm 1.72\%$	Position measurement δy_{mm} and laser pulse delay $\delta \Delta t \approx 1\mu\text{s}$

Table 4.4 Droplet velocity uncertainties.

The uncertainty in the velocity components is determined by

$$\delta u_x = \frac{\Delta x_{\text{mm}}}{\Delta t} \sqrt{\left(\frac{\delta \Delta x_{\text{mm}}}{\Delta x_{\text{mm}}}\right)^2 + \left(\frac{\delta \Delta t}{\Delta t}\right)^2} \quad (4.11)$$

and

$$\frac{\delta u_y}{u_y} = \sqrt{\left(\frac{\delta \Delta y_{\text{mm}}}{\Delta y}\right)^2 + \left(\frac{\delta \Delta t}{\Delta t}\right)^2} \quad (4.12)$$

The maximum deviation of the laser pulse delay was estimated to be around 1 μs . To compute the standard uncertainty a Gaussian distribution of the deviations is assumed. With a value of 400 μs for the pulse delay, its contribution to the uncertainty is negligible.

The uncertainty of the total velocity magnitude is determined by the law of error propagation of the velocity components. To evaluate the velocity magnitude uncertainty, average magnitudes of the velocity components ($u_x = 0.1\text{m/s}$ and $u_y = 2\text{m/s}$) have been taken:

$$\delta|\vec{u}| = \sqrt{\frac{1}{u_x^2 + u_y^2} \left((u_x \cdot \delta u_x)^2 + (u_y \cdot \delta u_y)^2 \right)} \quad (4.13)$$

4.4.2 Derived Quantities

The spray characteristics are described by the mean and standard deviation about the mean of the droplet diameter and velocity distributions at the different measurement positions. One part of the uncertainties of these derived quantities is due to uncertainty propagation of the measured quantities. In addition, the limitations of the measurement range and the influence of the number of measurements on the precision have to be taken into account. These uncertainties depend in particular on the spray characteristics at each measurement position and have to be evaluated for each case.

Mean Diameter

The uncertainty of the mean diameter measurement consists of three parts: The uncertainty due to the propagation of the single droplet measurements $|\delta D / D|_{\text{single}}$ the uncertainty of the measurement range $|\delta D / D|_{\text{range}}$ and the precision uncertainty $|\delta D / D|_{\text{prec}}$ which is due to the limited numbers of droplets. The uncertainty components of the droplet mean diameter are uncorrelated, and the total droplet mean diameter uncertainty can be computed by:

$$\left| \frac{\delta D_{10}}{D} \right| = \sqrt{\left| \frac{\delta D}{D} \right|_{\text{single}}^2 + \left| \frac{\delta D}{D} \right|_{\text{range}}^2 + \left| \frac{\delta D}{D} \right|_{\text{prec}}^2} \quad (4.14)$$

The uncertainty due to the propagation of the single droplet measurements $|\delta D / D|_{\text{single}}$ is dominant at the beginning of the spray evaporation. With proceeding evaporation, part of the droplet diameter distribution is becoming smaller than the minimum detectable diameter of 20 μm , and the uncertainty of the measurement range $|\delta D / D|_{\text{range}}$ is becoming increasingly dominant. Finally, at the end of the spray lifetime, the diminishing numbers of droplets lower the precision $|\delta D / D|_{\text{prec}}$ of the mean diameter significantly.

To estimate the measurement range uncertainty δD_{range} simulation results are utilized. The lower detection limit of 20 μm can be seen in the experimental diameter distribution displayed in Figure 4.13 a). Simulation results as shown in Figure 4.13 b) are utilized to compute the truncated mean diameter and thus to infer the deviation from the complete distribution. Finally, a functional dependence of the deviation on the truncated mean droplet diameter is inferred to compute the range uncertainty of the measured mean diameter. Because this procedure inherits uncertainties, instead of using the computed deviation to correct the measurement data, the deviation is taken into account as an additional uncertainty component to the mean diameter.

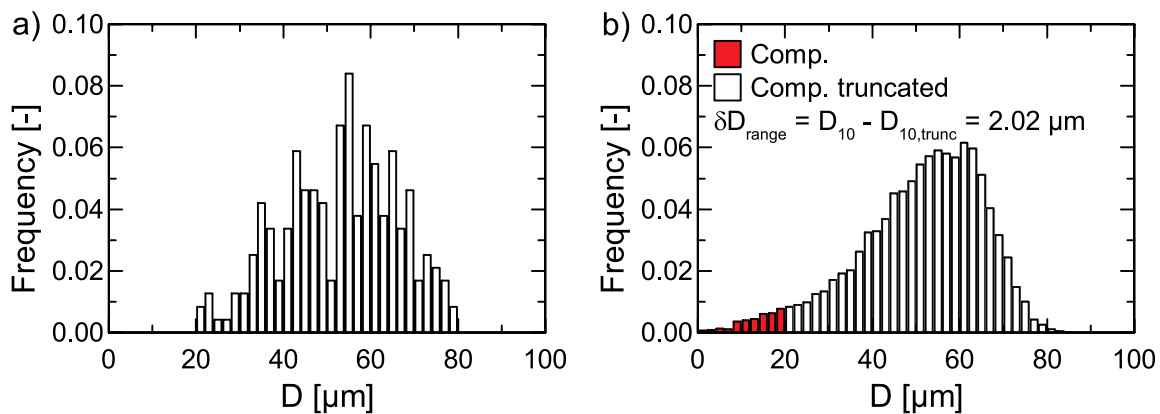


Figure 4.13: Showing the effect of the lower detection limit on the diameter distribution in case of a) experimental measurements and b) numerical simulation.

The precision is evaluated by computing the average of one measurement image and evaluating the standard uncertainty of the mean of all measurement images for the given

4 Validation Experiment

measurement position with $|\delta D / D|_{\text{prec}}$. To infer the influence of the limited number of measurements the Student t-distribution was used:

$$\left| \frac{\delta D}{D} \right|_{\text{prec}} = t \frac{S_m}{\sqrt{n}} \quad (4.15)$$

t is the Student t-distribution parameter for a two-tailed t-distribution of a confidence interval of 95%, S_m is the standard deviation of the mean, and n is the number of images.

Since the mean of each measurement image is independent of each other, the precision computed with Equation (4.15) gives a measure of the short-term variability of the droplet diameter. For wider droplet diameter distributions (at the end of the spray lifetime), a higher number of measurements are required to state precisely the droplet mean diameter.

Additionally, to detect systematic changes of the injection conditions due to droplet generator instabilities, each measurement position was measured twice. The first half of measurements have been taken characterizing the spray evaporation sequentially downwards the axis; the second half of measurements have been taken backward at the same measurement positions. Then, changes in the injection conditions have been detected by comparing the evolution of the mean for the downward and upward measurement. In case of significant differences, the measurement campaign was repeated.

Mean Velocity

The evaluation of the mean velocity uncertainty mainly follows the procedure explained for the mean diameter uncertainty evaluation. Since all droplet velocities existing in the spray could be resolved, the procedure to evaluate the uncertainty of the measurement range was changed slightly.

$$\left| \frac{\delta v_{10}}{v} \right| = \sqrt{\left| \frac{\delta v}{v} \right|_{\text{single}}^2 + \left| \frac{\delta v}{v} \right|_{\text{prec}}^2} \quad (4.16)$$

The choice of the laser pulse delay was determined iteratively. On the one hand, a short laser pulse delay yields high uncertainties in the single droplet velocity measurement (see Eqs. (4.11) and (4.12).) On the other hand when increasing the laser pulse delay the probability that the droplet leaves the measurement volume is high, resulting in reduced detection rates and thus in increasing the precision uncertainty by a high Student t-distribution parameter:

$$\left| \frac{\delta v}{v} \right|_{\text{prec}} = t \frac{S_m}{\sqrt{n}} \quad (4.17)$$

4.4.3 Additional Uncertainties

The primary focus of the developed system was on yielding a high precision and accuracy in the measurements so that the effect of different fuel composition on the evaporation can be clearly distinguished. In the preceding section, the uncertainties deduced from the use of the measurement techniques and induced by stochastic variations during a measurement campaign have been evaluated. Furthermore, the measurement uncertainty is influenced by environmental conditions including the experimental facilities. Optimally, the same experiments should be performed in different labs and with different groups of experimenters to evaluate the measurement uncertainties and systematic errors with high accuracy. Such a comprehensive uncertainty assessment was not part of this study, and the presented uncertainty evaluation is based on a single experimenter performing experiments in the same facility over the course of two years. Measurements of n-decane evaporation have been used as a reference to evaluate the repeatability.

The time between different measurement campaigns was from few minutes to several months. During such a time, ambient conditions changed and also reassembling the test track after maintenance (quartz tube deposits) could bring variations to the experimental boundary conditions. By monitoring the flow field temperature at the outlet and repeated studies of n-decane evaporation, systematic errors could be identified, and it was ensured that changes had a limited effect below the precision limit of a measurement run.

The primary source of uncertainty influencing the precision was the droplet generator. The evaporation of the spray is very sensitive to the injection conditions. These are determined by the history of the spray before entering the test section.

The flow before the test section is a Hagen–Poiseuille like flow. Thus temperature and velocity fields are non-homogeneous and determined by the wall boundary layer flows. This means that small distortions in the spray velocity vector from the centerline axis at the droplet generator exit yields a different flow path in the secondary flow section and subsequently to different conditions at the test section injection point. Such distortions could be caused by a partial clogging of the droplet generator orifice by impurities or dissolved gas bubbles.

In addition, for each orifice, some frequency band exists where a stable monodisperse droplet stream is formed. These frequency bands depend on ambient conditions and the fuels used. They have to be determined iteratively by adjusting the frequency to the actual conditions. Changes in the ambient conditions and changes by refueling the fuel vessel yield different stable frequency bands for the droplet generation and thus different initial diameter distributions.

This means that for each measurement campaign different injection conditions are created. These variations lower the precision of the experimental system when comparing the experimental results with each other. Therefore, for the comparison of simulation results with

experimental data the injection conditions for the simulation have to be inferred from experimental measurements for each measurement campaign.

4.5 Conclusions

The experimental system presented in this chapter was designed to study the evaporation of complex fuels sprays under simplified but realistic conditions. To study the evaporation, first, the spray is transported by a cold carrier-flow into the test section. In the test section, the spray and carrier gas jet coincide with a preheated co-flow. The spray starts heating and evaporates. The co-flow has well-controlled turbulence levels and can be preheated up to 800 K.

The generalized scattering imaging technique (GSI) was applied to simultaneously determine the size, velocity and, the spatial location of the evaporating droplets. This technique has the advantage that it is weakly dependent on the refractive index; neglecting the refractive index at all, the measurement uncertainty is smaller than 4% for the droplet sizing. Thus, it is possible to characterize fuels with unknown composition and thermophysical properties, and hence it is especially suitable for alternative fuel studies.

As the characteristic parameter describing the spray evaporation, the evolution of the mean diameter and standard deviation of the mean in the flow direction was chosen. Due to the nearly monozised injection diameter, differences between the Sauter mean diameter or area-averaged diameter to the arithmetic mean value have been found to be negligible. The mean diameter evolution will be used to compare the evaporation of the different fuels with simulation results in chapter 6.

The measurement uncertainties of the boundary, initial conditions, and spray parameter have been determined precisely. These uncertainties are of fundamental importance on the one hand when comparing the prediction results with the experimental data and on the other hand, when the boundary and initial conditions for the computations have to be set. In addition, to the best of the author's knowledge, all possible systematic errors of relevance have been summarized. The measurement uncertainties will be used for the evaluation of the validation experiment approach in chapter 5 and the accuracy assessment of the alternative fuel models in chapter 6.

For the conceptualization of the validation experiment, all the details about the flow conditioning system, the geometry, and the features of the system are given. To be able to choose the best representation of the boundary conditions and the right model to represent the physical nature of the phenomena to be modeled, the nature and character of the physical processes in the test section but also before the modeling domain have been characterized. How the models are applied, and the characterization of the computational uncertainty will be presented in chapter 5.

5 Modeling of the Validation Experiment and Uncertainty Quantification

Ideally, the validation metric is a measure of the uncertainties and errors of the specific model. To achieve such an ideal case, simulation results would be compared with reality or measurement data with no measurement errors and no intrusive influence. Furthermore, such simulations would be based on exactly known input parameters. Simulations would have no numerical solution errors and uncertainties from sub-models.

In practice, uncertainties are propagated to the validation metric and “blur” the results. In case of droplet evaporation simulations, these uncertainties come from inaccuracies in the simulation of the gas field, uncertainties in the spray injection conditions, numerical solution errors, and measurement uncertainties. Depending on the tendency of the respective uncertainties, they can lower or higher the validation metric. Consequently, the aim is to identify all significant uncertainties and, if possible, minimize them.

In this chapter, n-decane is used as a benchmark to assess the characteristics of the validation approach. The basic concepts and decisions for modeling the validation experiment are described. To be useful for the adequacy assessment in future applications, meaningful System Response Quantities (SRQ) are identified. These SRQs have to be significant for (combustor) design issues like the total evaporation time that contributes to the definition of the combustor dimensions and fuel placement strategies. In addition, for the adequacy assessment of coupled multi-physics simulations, it is vital that SRQs of the spray evaporation model represent input quantities for subsequent models. Details on how the validation metric for selected SRQs is computed are reported in this study, exposing the underlying assumptions and simplifications. Finally, the uncertainties in the validation metrics are quantified and discussed concerning their meaning for this study.

5.1 Modeling of the Validation Experiment

The modeling of validation experiments includes several design decisions that have an influence on the accuracy of the simulation results. It starts with the definition of the computational domain, which determines the phenomena that need to be modeled and the interphase (boundary and initial conditions) with the surroundings. Usually, this decision is a trade-off between the accuracy of the models available for the representation of the phenomena in the computational domain and the accuracy that can be reached in modeling the boundary and initial conditions.

Additionally, the choice of the model is constrained by the computational resources available, and the characterization of the boundary conditions is constrained by the available experimental resources.

5.1.1 Definition of the Computational Domain

In the qualitative characterization of the experiment in chapter 4, the phenomena that have to be modeled appropriately were identified. Specifically, the complexities arising from the laminar-turbulent transition of the carrier jet challenge existing CFD models. There are two practical approaches to define the computational domain: one is to model the complete fluid domain as presented in Figure 5.1 a), including the inlet nozzle flow and the test section. The other approach is to model the test section only, as shown in Figure 5.1 b). Modeling the complete fluid domain has the advantage that the inlet conditions of the carrier flow and especially the spray injection conditions are well defined. In contrary, by including only the test section in the computational domain, the modeling of the laminar-turbulent transition can be avoided. Besides the phenomena that have to be modeled, the choice of the validation domain determines the boundary and initial conditions and influences the accuracy but also trustworthiness of the simulations. This will be explained in the following.

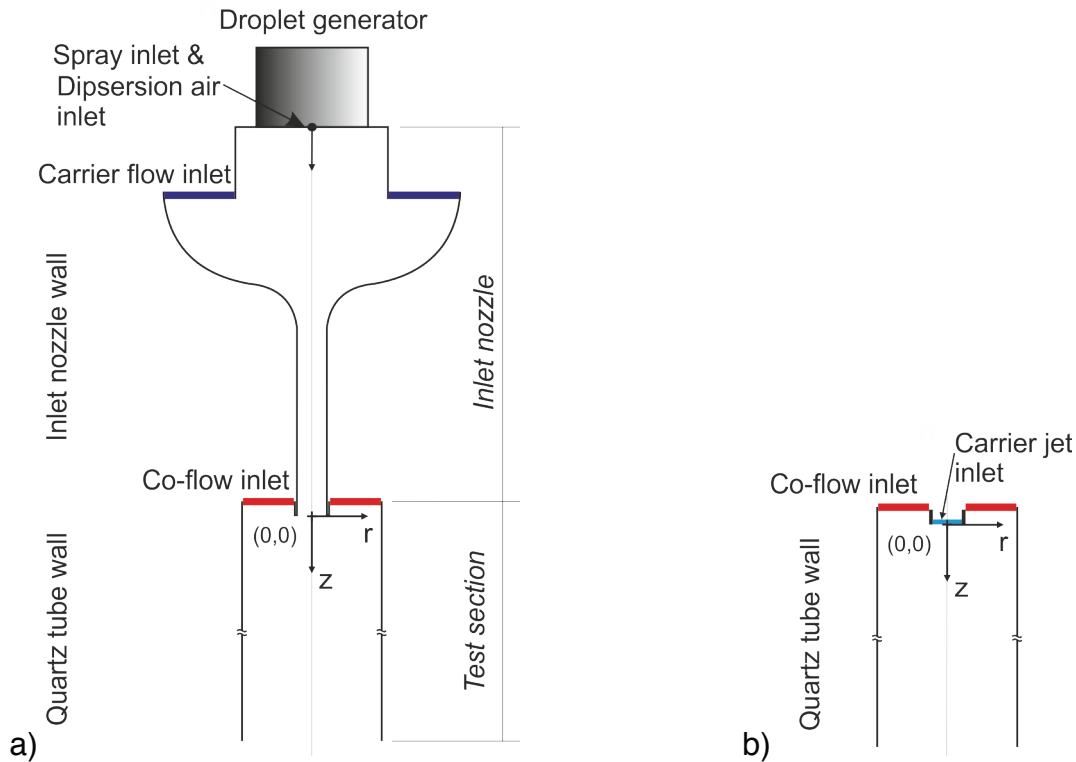


Figure 5.1: Scheme of the computational domains with boundary conditions and coordinate system for a) the complete fluid domain and b) test section domain.

5.1.2 Classification of Boundary Conditions

The boundary conditions for the flow field are shown in Figure 5.1, in blue the inlet for the carrier flow, in red the inlet for the preheated co-flow. The reference coordinate system is located on the centerline at the beginning of the test section. This is the first position where spray measurements could be performed. Both domains have the quartz tube wall and co-flow inlet condition in common but differ in the boundary condition for the spray and carrier flow.

In practice, there are basically three different possibilities to determine the boundary and initial conditions, or generally speaking model input parameters. Each of them has an effect on the trustworthiness of the simulation (Oberkampf and Roy 2010): The most reliable approach is the measurement of the required parameters. However, if experimental data is limited, the parameters have to be estimated. For this purpose, physics-based models, empirical correlations, or literature values can be used. If none of them is available, the parameters might be estimated by experts. In the third case, if the parameter is left adjustable, the determination is classified as parameter calibration. Such calibration parameters can be used to tune the simulation results in a way that they agree with measurement data. However, at the same time errors in the models or other model input parameters are possibly compensated.

Boundary condition	Complete fluid domain	Test section domain
<u>Test section wall</u> Temperature	Measurement data	
<u>Co-flow inlet</u> Mass flow rate Turbulence Intensity Temperature	Measurement data Measurement data Measurement data	
<u>Carrier gas inlet</u> Mass flow rate Turbulence Intensity Temperature	Measurement data Expert opinion Measurement data	-- -- --
<u>Dispersion air droplet generator</u> Mass flow rate Turbulence Intensity Temperature	Measurement data Expert opinion Measurement data	-- -- --
<u>Carrier jet inlet</u> Velocity Turbulence Intensity Temperature	-- -- --	Measurement data (cold)/ Estimated by num. (hot) Measurement data Measurement data

Table 5.1 Classification of the flow field boundary conditions for the test section domain by type of method used to determine the values.

The boundary conditions for the flow field and the respective determination methods are summarized in Table 5.1 for both domains. Temperatures, mass flow rates, and velocities can be determined for all inlets from measurement data. Except for the velocity inlet condition at the carrier jet inlet in the hot flow case, the velocity inlet profile was estimated by extracting the velocity profile from the complete fluid domain. The turbulence intensity could only be determined from experimental data in the case of co-flow inlet and the carrier jet inlet condition for the test section domain. For the complete fluid domain, there is no measurement access to characterize the turbulence intensity of the carrier gas inlet and the dispersion air inlet. However, sensitivity studies show a negligible influence on the flow field, and the turbulence intensity was therefore set to 1%.

Table 5.2 shows how the injection conditions for the spray can be determined in case of the complete fluid domain and the test section domain. As mentioned before, the advantage of taking the complete fluid domain is that the droplet temperatures are known. Although the droplet composition cannot be measured, it can be determined accurately. From the fuel container of the droplet generator down to the injector, the fuel does not experience any processes that can alter the fuel composition. Thus, it can be assumed, that the fuel composition corresponds to the initial composition of the fuel. The droplet diameter distribution, the magnitude of the spray velocity and the volume concentration profiles can be determined from empirical correlations that have been verified by experimental measurements to be very accurate. The radial component of the

spray injection velocity is assumed zero on average. In case of the test section domain, the diameter distribution, velocity distribution, the volume concentration profile, and the spray center can be determined from measurement data. Since the possibilities for measuring the droplet temperature and composition are limited and prone to high measurement uncertainties, these values are estimated by computing the spray heating in the carrier gas nozzle prior to the test section, while using the complete fluid domain.

Injection condition	Complete fluid domain	Test section domain
Diameter distribution	Estimation by empirical correlations	Measurement data
Spray velocity distribution Axial component Radial component	Estimation by emp. correlation Expert opinion	Measurement data Measurement data
Volume concentration profile	Estimation by emp. correlation	Measurement data
Spray center	Measurement data	Measurement data
Droplet temperatures	Measurement data	Estimation by num. sim.
Droplet composition	Expert opinion	Estimation by num. sim.

Table 5.2 Classification of the spray injection conditions for the complete fluid domain and the test section domain by the method used to determine the values.

5.1.3 Numerical Model of the Flow Field

The gas field was computed with the commercial CFD code ANSYS® CFX-13.0. It solves the Reynolds-averaged Navier–Stokes (RANS) equations in their conservative form augmented with a transport equation for the specific enthalpy. Additional transport equations for the gaseous species including fuel vapor, for the turbulent kinetic energy and for the turbulent frequency are also solved. In this context, the $k-\omega$ shear–stress transport (SST) model in the formulation of Menter (1994) is used to close the Reynolds stress tensor based on the eddy dissipation concept. In case of the complete fluid domain, the gamma-theta transition model (Langtry and Menter 2005) is used.

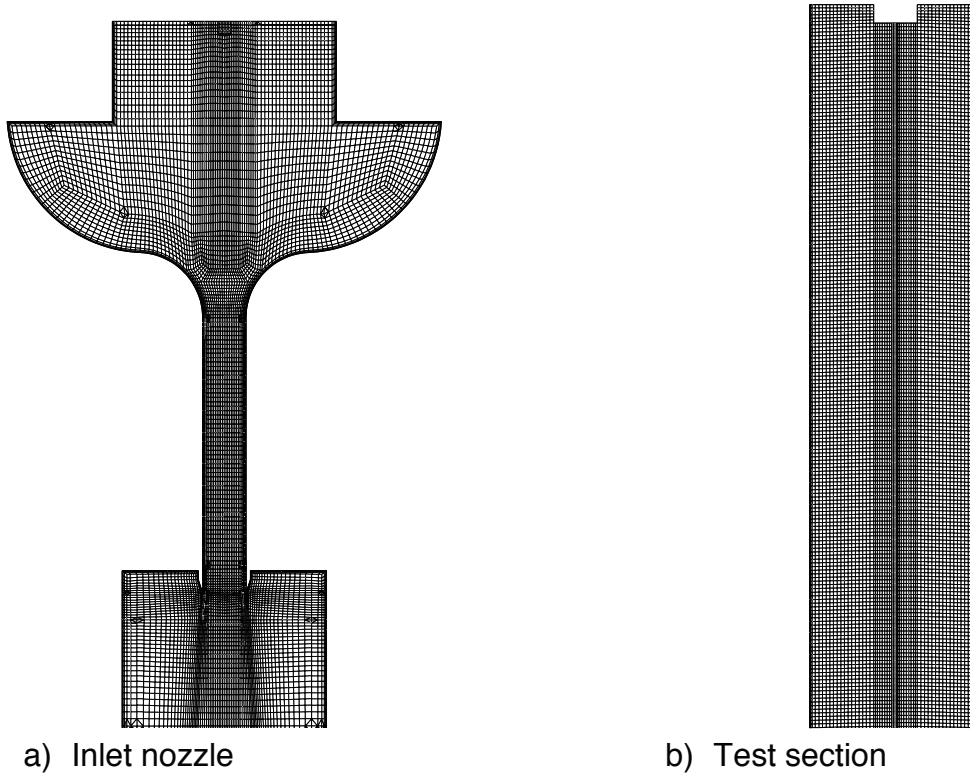


Figure 5.2: Centerplane view of the mesh used.

The computational domain consists of hexahedral elements. The nozzle grid shown in Figure 5.2 a) comprises $5.7 \cdot 10^5$ points and the test section mesh $5.1 \cdot 10^5$ points, Figure 5.2 b). Both meshes have a high resolution of near-wall regions and a minimum cell spacing of $250 \mu\text{m}$ in the spray region.

5.1.4 Simulation Strategy

To determine the simulation strategy, studies utilizing different RANS turbulence models have been used in both computational domains (Miranda 2011). The $k-\omega$ SST model exhibited the best performance and is used here to discuss the effect when using the two different computational domains. Figure 5.3 shows the velocity at the centerline of the test section. Simulation results for the complete fluid domain and the test section domain are compared with experimental data. The velocity fluctuations u' are computed by assuming isotropic turbulence on the basis of the turbulent energy k with:

$$k = \frac{3}{2} \overline{u'^2} \tag{4.18}$$

The mean velocity at the centerline of the complete fluid domain shows a delayed transition to turbulence in comparison to the experimental data (Rauch et al. 2010; Rauch, Calabria, Chiariello, Le Clercq, Massoli, and Rachner 2011). A better agreement could be reached by resolving smaller scales with a large-eddy simulation, which is not part of this study. The

centerline velocity of the test section domain instead, shows a much better agreement with experimental data.

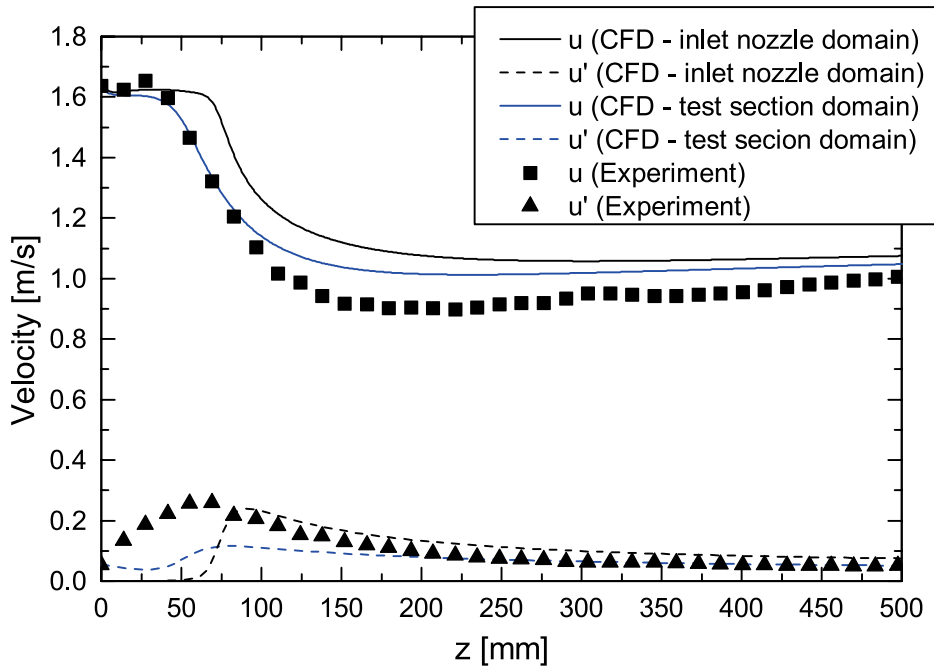


Figure 5.3: Comparison of centerline velocities u and velocity fluctuations u' of computations performed in the inlet nozzle domain and test section domain with experimental data.

Due to the better representation of the velocity field, the test section domain is used for further studies. Computations in the complete fluid domain are used to estimate the droplet temperatures and the droplet composition at the injection into the test section domain.

5.2 Accuracy Assessment of the Flow Field Simulation

The flow field defines the boundaries for the evaporating spray. Hence, uncertainties in the flow field are propagated to the spray simulation results and are added to the validation metrics of the spray evaporation. The magnitude depends on the sensitivity of the spray behavior on the flow field. Due to time and budget constraints, no flow velocity field for the hot flow was inferred. To assess if the main velocity field phenomena are captured well, the velocity field in the cold flow case is used. In case of the hot flow, the flow field temperatures are used to assess the accuracy of the flow field simulation.

5.2.1 Parameter Estimation: Flow Field Boundary Conditions

The flow field boundary conditions have been inferred from experimental measurements whenever possible. However, no velocity and turbulence information is available in the hot flow case. To determine the carrier jet inlet conditions, the complete fluid domain is used to estimate the parameters. The boundary conditions were kept constant for all computations.

Cold flow boundary conditions

The flow field boundary conditions for the cold flow case are summarized in Table 5.3. The boundary conditions of the test section wall and the co-flow inlet are common for both computational domains. In the cold flow case, all boundary conditions of the test section can be taken from measurements. The complete fluid domain is required for the estimation of the droplet injection temperature.

Boundary conditions for both domains		
Test section wall	Temperature	295 K
Co-flow inlet	Mass flow rate	1.475×10^{-3} kg/s
	Turbulence intensity	20%
	Temperature	295 K
Boundary conditions for the complete fluid domain		
Inlet system wall	Temperature	295 K
Carrier gas inlet	Mass flow rate	6.45×10^{-5} kg/s
	Turbulence intensity	1%
	Temperature	295 K
Dispersion air droplet generator	Mass flow rate	2.95×10^{-5} kg/s
	Turbulence intensity	1%
	Temperature	295 K
Boundary conditions for the test section domain		
Carrier jet inlet (Carrier gas + dispersion air droplet generator)	Velocity	Figure B.1
	Turbulence intensity	Figure B.2
	Temperature	295 K

Table 5.3 Cold flow: flow field boundary conditions for the complete fluid and test section computational domains.

Although measurement data for the co-flow inlet velocity distributions have been used as inflow condition, simulations showed a better agreement with experimental data, with the application of a mass flow rate inlet condition (Miranda 2011). A higher resolution of measurement points over the co-flow inlet is required to characterize and model the inflow conditions appropriately and to capture the imposed 3D effects. For the same reason, averaged turbulence intensity was taken from measurements, and the turbulence length scale was therefore estimated in the CFD software. As will be seen in section 5.2.2, these settings lead to a satisfactory agreement between simulation and flow field measurements.

Hot flow boundary conditions

In Table 5.4, the flow field boundary conditions are summarized. For the hot flow field, the complete fluid domain is used for the estimation of the carrier jet inlet velocity profile. The value for the turbulence intensity of the co-flow is assumed equal to the value of the cold flow

simulation. The turbulence intensity at the carrier jet inlet was adapted so that the difference between the computed temperature field and the measurement data was at a minimum.

Boundary conditions for both domains		
Test section wall	Temperature	Figure 5.4
Co-flow inlet	Mass flow rate Turbulence intensity Temperature	0.98333×10^{-3} kg/s 20% Figure 5.6
Boundary conditions for the complete fluid domain		
Inlet system wall	Temperature	Figure 5.5
Carrier gas inlet	Mass flow rate Turbulence intensity Temperature	8.74×10^{-5} kg/s 1% 383 K
Dispersion air droplet generator	Mass flow rate Turbulence intensity Temperature	2.95×10^{-5} kg/s 1% 295 K
Boundary conditions for the test section domain		
Carrier jet inlet (Carrier gas + dispersion air droplet generator)	Velocity Turbulence Intensity Temperature	Figure B.3 15% Figure 5.7

Table 5.4 Hot flow: flow field boundary conditions for the complete fluid and test section computational domains.

The measurement values of the wall temperature distribution along the inlet nozzle and the test section are shown in Figure 5.4 and Figure 5.5. The temperature is high where the respective parts are in contact with the co-flow conditioning system. For the flow conditioner, the maximum temperature is reached at the beginning of the droplet channel ($z = -60$ mm) and at the beginning of the quartz tube.

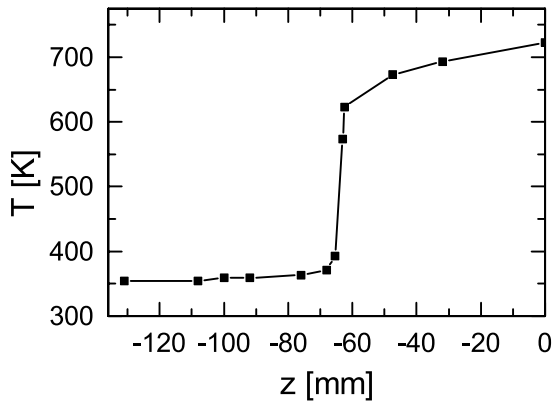


Figure 5.4: Hot flow: measured wall temperature profile of the inlet nozzle.

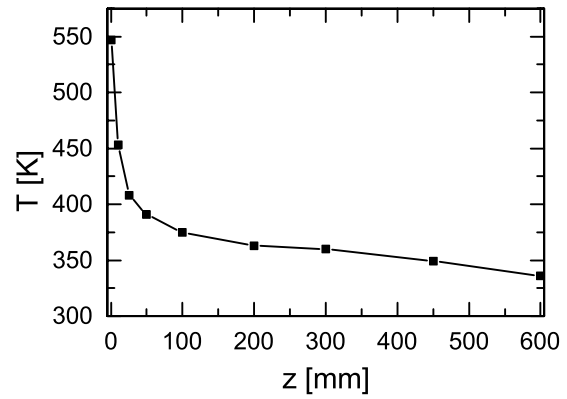


Figure 5.5: Hot flow: measured wall temperature profile of the test track.

Figure 5.6 and Figure 5.7 show the measured inlet temperature distributions. The temperature distribution at the co-flow inlet exhibits a certain degree of asymmetry. Measurements were taken with a thermocouple along the x- and y-axis with a distance of 1 mm. The 2D profiles are then interpolated from two cross-sectional measurements.

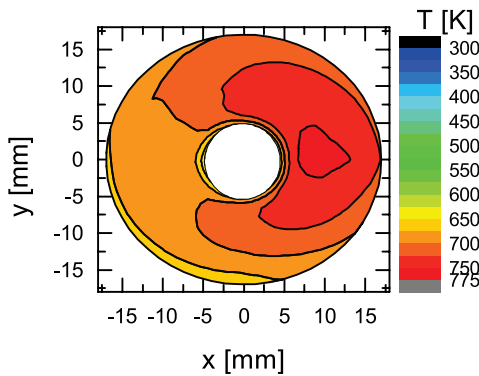


Figure 5.6: Hot flow: measured inlet temperature profile of the co-flow.

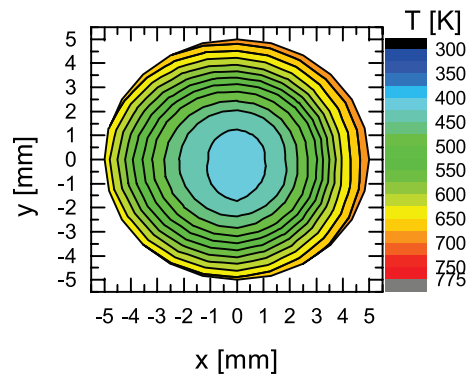


Figure 5.7: Hot flow: measured inlet temperature profile of the carrier jet.

5.2.2 Flow Field Validation

Experiments had been performed in two flow configurations, one in cold flow conditions, the other one in hot flow conditions. In the following, simulation results of the cold flow velocity field will be compared with the measurement data inferred from hot wire measurements first. Then, simulations of the hot flow temperature field will be compared with thermocouple measurement data.

Cold Flow

Figure 5.8 shows the center plane velocity field of the measured mean velocities in comparison with the simulation data. The length of the higher velocity carrier gas jet is predicted well by the simulation. As explained before, a block velocity profile was used as inlet condition for the co-

flow. For this reason, the irregular inflow is not captured by the simulation. However, the influence on the central region where the spray is transported into the test track $x = [-10,10]$ mm is limited. After $z = 75$ mm the predicted flow pattern agrees very well with the measurement data.

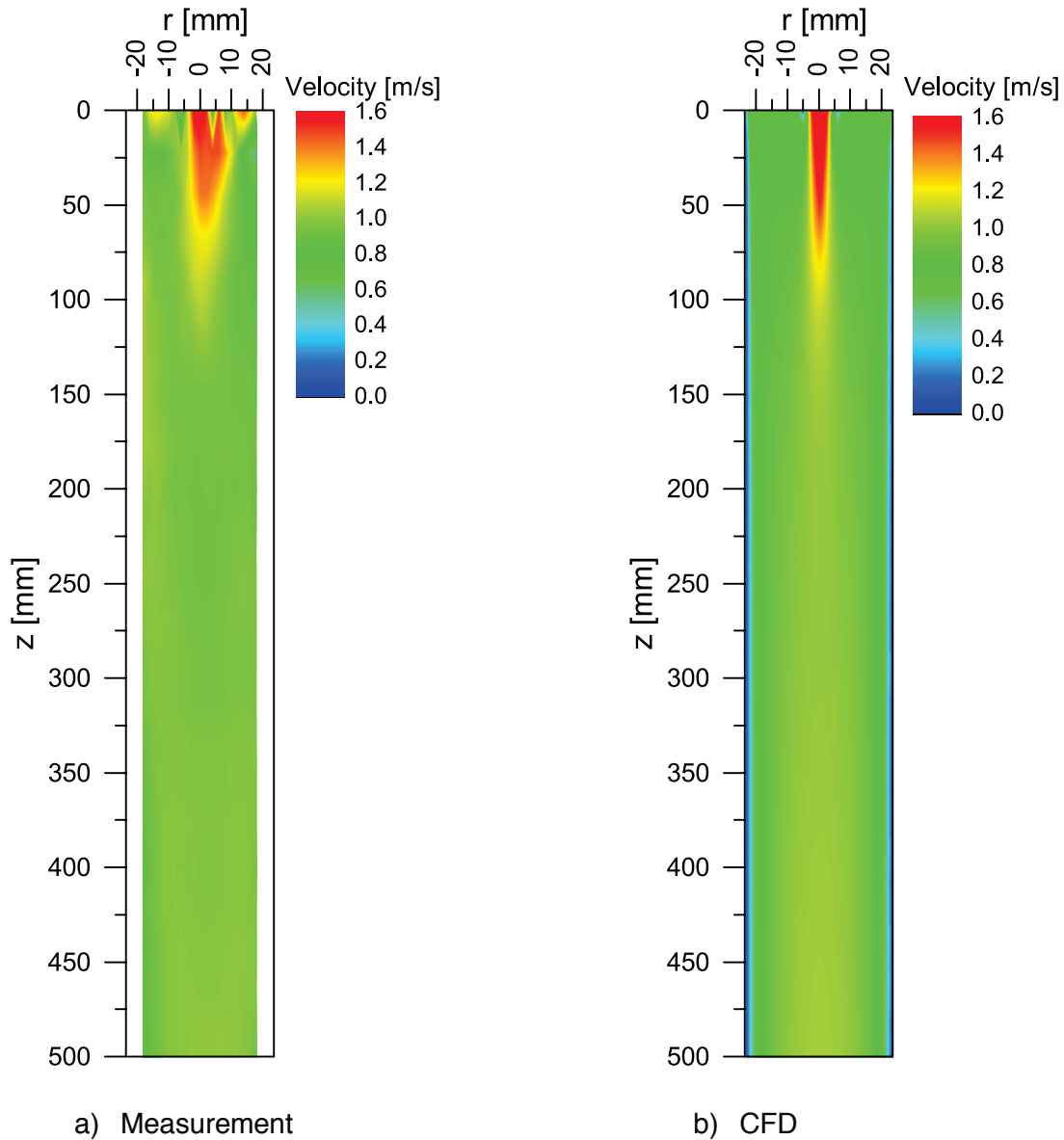


Figure 5.8: Cold flow: comparison of measured and predicted velocity fields.

The evolution of the mean velocity and the velocity fluctuations at the centerline of the test track is depicted in Figure 5.9. One can see that the mean velocity describing the carrier gas jet and the decay/mixing with the co-flow is predicted very well. After $z = 100$ mm the mean velocity is overpredicted with a maximum of 0.1 m/s at $z = 200$ mm. Afterwards, the measured velocity is increasing faster with respect to the predictions, and the prediction error becomes smaller than 0.05 m/s.

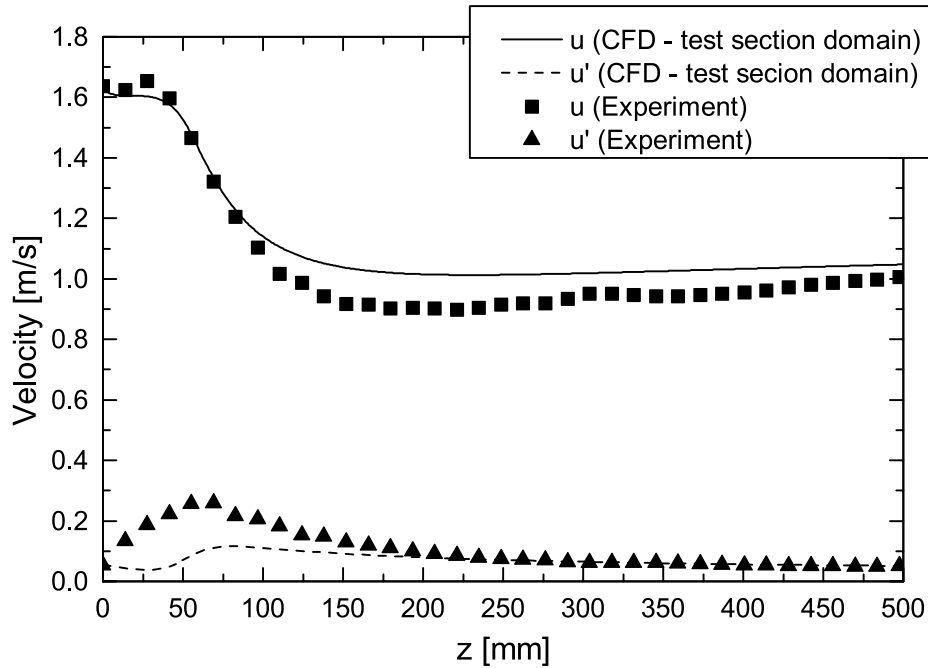


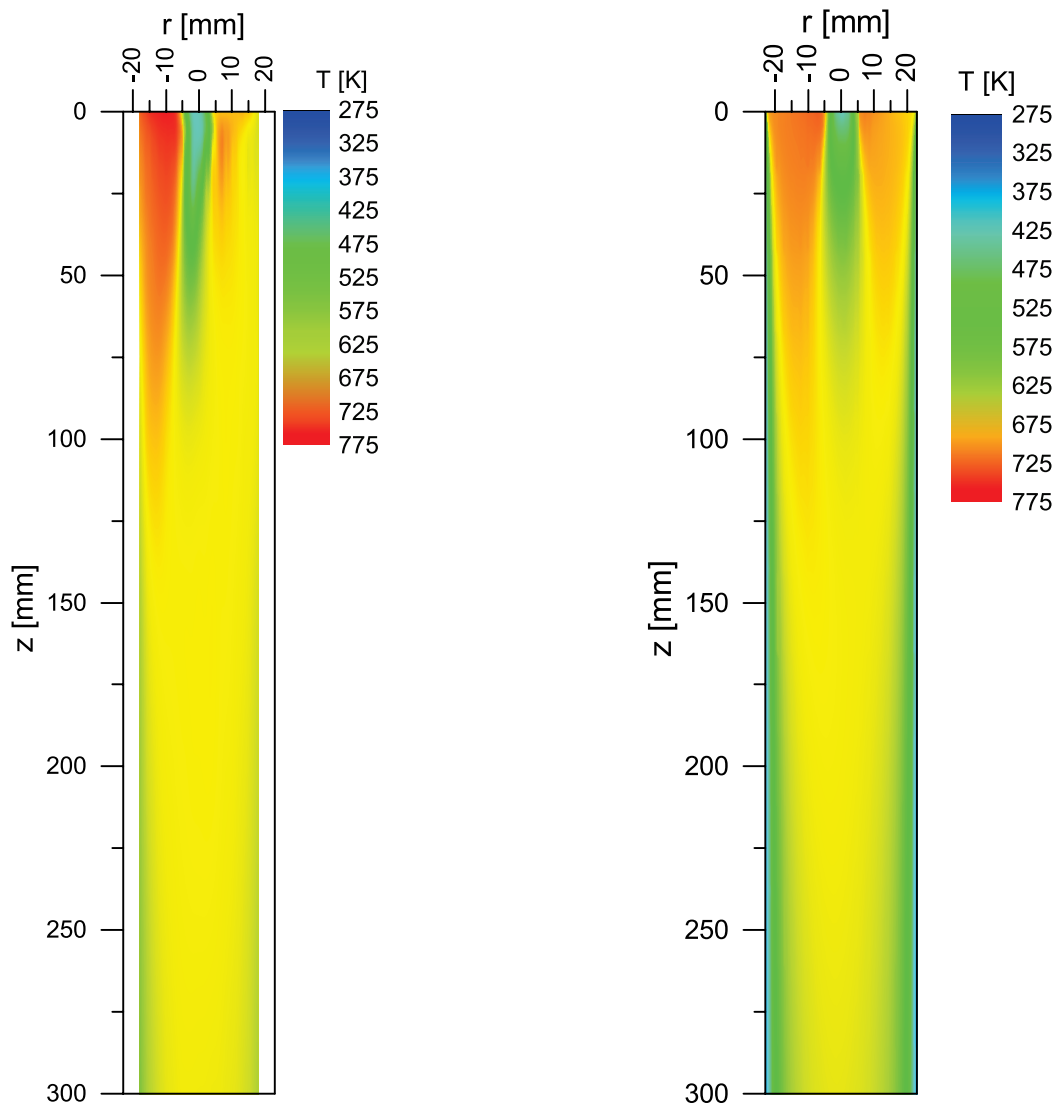
Figure 5.9: Cold flow centerline velocity and velocity fluctuations, comparison of CFD with measured data.

The velocity fluctuations of the carrier gas jet increase rapidly when being injected into the test section. The computed values contrarily decrease and first start increasing after $z = 50$ mm, at the same time when the mean velocity of the secondary flow starts decreasing.

Comparisons of the cross-section velocity profiles also show a good agreement with the experimental data. The agreement is well depicted by the centerline profile. The graphs with the comparisons of computed and experimental data can be found in Appendix C.1.1.

Hot Flow

Contour plots of the measured temperature field and the computed temperature are compared in Figure 5.10. Whereas the asymmetry of the co-flow and the length of the carrier jet are reproduced well by the simulation, the small inclination of the carrier gas is not captured. This can be explained by the boundary condition applied (as shown in Table 5.4). For the temperature inflow condition measurement data reflecting the asymmetry was used. However, due to the lack of data for the velocity inflow condition, a block velocity profile had to be assumed based on the mass flow rate. Thus any radial or tangential velocity components are neglected. In addition, the computed carrier jet shows a more diffusive behavior at $z = 30$ mm. Nevertheless, the qualitative agreement of the predicted temperature field with the measured field is good in the spray region. The general trend of the asymmetry is captured well.



a) Measurement

b) CFD

Figure 5.10: Hot flow: comparison of measured and predicted temperature fields.

The centerline temperature depicts the quantitative evolution of the temperature in the spray region. The comparison between measured and computed centerline temperatures is shown in Figure 5.11. A comparison of various cross-section temperature profiles with experimental data can be found in C.1.2. The predicted centerline profile generally agrees very well with experimental data. In the initial region, the measured temperature profile of the carrier gas jet shows a temperature plateau up to $z = 10$ mm, whereas the predicted temperature rises sharply. Differences in the turbulence boundary conditions for the carrier jet inlet might explain the differences shown here. Further refinement of the boundary conditions did not yield any improvement. To capture the dynamics of the laminar-turbulent transition precisely, more sophisticated computational methods like LES must be used. In addition, a detailed characterization of the inlet velocity and turbulence conditions is required to gain a more accurate flow field prediction.

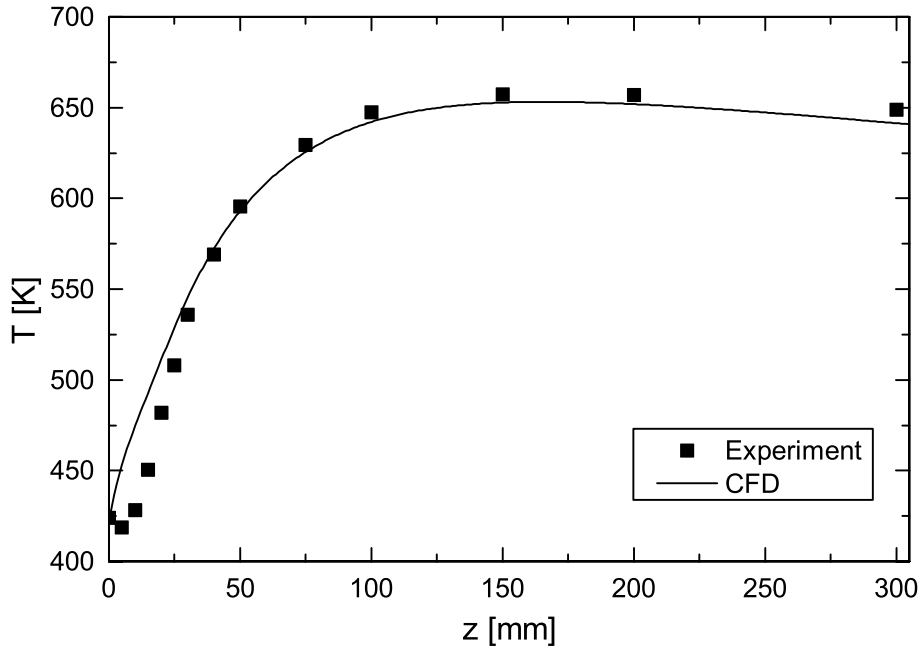


Figure 5.11: Hot flow centerline temperatures: Comparison of CFD with measured data.

5.3 Accuracy Assessment of *n*-Decane Droplet Evaporation Models

The primary goal of this study is the systematic accuracy assessment of alternative aviation fuel droplet evaporation models. In this section, the procedure to infer a validation metric for selected SRQ is derived for *n*-decane as a benchmark. To be useful for the adequacy assessment of future simulations, the SRQs need to be related to the application or represent input quantities for subsequent models.

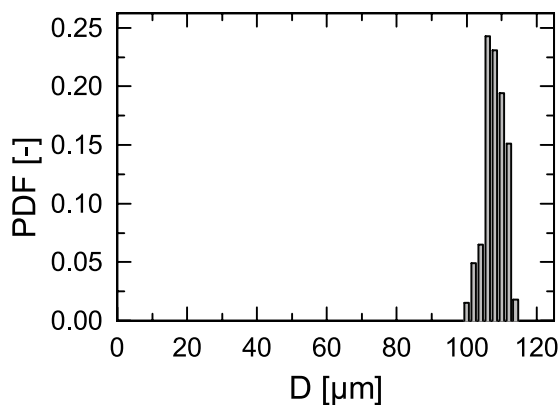
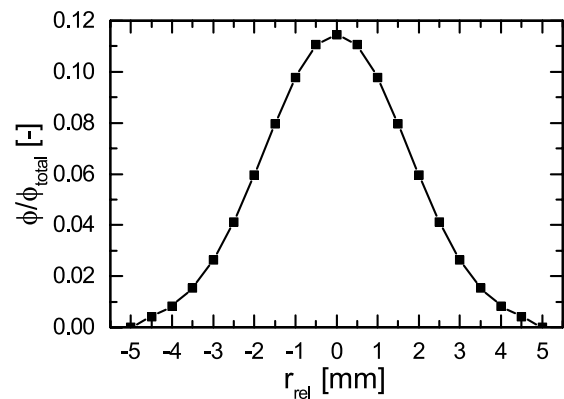
5.3.1 Parameter Estimation: Spray Injection Conditions

All injection conditions that could be determined by measurements were taken from the experimental data. Table 5.5 summarizes the spray initial conditions in the case of an *n*-decane measurement campaign. The measured injection conditions comprise the spatial distribution of the spray (spray center and radius), the diameter distribution, volume concentration profile, and the velocity distribution. For the analysis of the measurement data, it is assumed that the spray is axisymmetric and that the laser sheet is cutting the spray centrally. Since the possibilities for measuring the droplet temperature and composition are limited and prone to significant measurement uncertainties, these values were estimated by computing the spray heating in the carrier gas nozzle before the test section.

Injection condition	Value	
Diameter distribution	Figure 5.12	Measured
Spray velocity		
1. Mean value	2.6 m/s	Measured
2. Standard deviation	0.27 m/s	Measured
Volume concentration profile	Figure 5.13	Measured
Spray center	0.42 mm	Measured
Droplet temperature distribution	Figure 5.21	Estimated by num. sim.
Droplet composition	Required only for multicomponent-fuels	Estimated by num. sim.

Table 5.5 Spray injection conditions for the n-decane spray.

Droplets were injected at the first measurement position, $z = 5$ mm, in the experimentally observed off-center position 0.42 mm and with the measured spray radius of 5 mm. The droplet initial velocity distribution was computed by taking into account the measured mean velocity and its standard deviation. Sensitivity studies showed that the effect of the simplified injection velocity on the accuracy of the prediction results is negligible. The size distribution and volume concentration profiles at $z = 5$ mm, which represents the spatial distribution of the mass flow over the radius, were used as initial conditions for the SPRAYSIM code as presented in Figure 5.12 and Figure 5.13.


 Figure 5.12: Initial diameter distribution for n-decane injection at $z = 5$ mm.

 Figure 5.13: Volume concentration profile for n-decane injection at $z = 5$ mm.

Estimation of the Droplet Temperature Distribution

The spray temperature is an essential initial parameter strongly influencing the downstream evolution of the spray. To provide a consistent way of estimating this parameter for all fuels to be tested, numerical simulations of the heating of the spray in the inlet nozzle are performed. The flow field computations are validated with the measured velocity profiles (cold flow case) and temperature profiles (hot flow case.) The validation results of the nozzle flow field simulations are shown in Appendix C.1.3.

Although the flow field simulations are validated, when comparing predicted droplet velocities at the injection plane ($z = 5$ mm) with measurement data, the predicted droplet velocities always exhibit too small values (2.04 m/s in comparison to 2.6 m/s), as depicted in Figure 5.14. A plausible reason might be that the dilute spray assumption is not valid in the region before the test section. This assumption is supported by the observation of second order diameter peaks in the injection size distribution with a double volume diameter, which indicates the coalescence of droplets. In a dense spray region, the interaction of droplets is relevant and means that for short distances between the droplets the drag coefficient is lowered.

To estimate the influence of droplet-droplet interaction on the spray behavior, the corrections of (Atthasit et al. 2005) are used for the inlet nozzle computations. Atthasit et al. inferred this correlation for the case of evaporating streams of droplets. They found empirical correlations for the modification of the droplet drag coefficient C_D with respect to the case of a drag coefficient of the isolated droplet $C_{D,iso}$

$$\frac{C_D}{C_{D,iso}} = 1 - 0.86e^{-0.053C} \quad (4.19)$$

and for the modification of the vapor mass flow rate η :

$$\eta = 1 - 0.57 \left(1 - \frac{1 - e^{-0.13(C-6)}}{1 + e^{-0.13(C-6)}} \right) \quad (4.20)$$

The droplet spacing C is unknown and was calibrated such that the computed droplet mean velocities at the injection plane agree with measurement data (see Figure 5.14.) The resulting computed temperature distribution was then used as injection condition for the test section spray evaporation calculations. It has to be mentioned that these corrections had been developed for droplet streams and exhibited a certain uncertainty. The influence on the simulation results will be investigated in section 5.4.2.

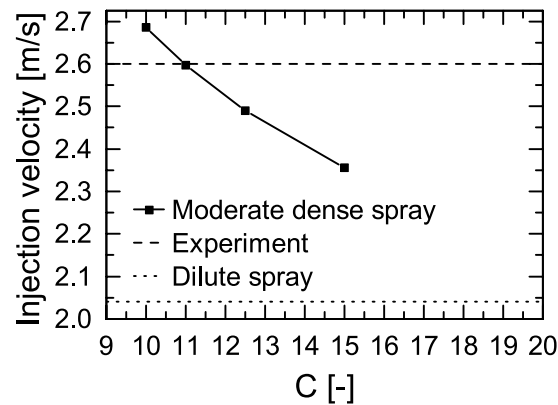


Figure 5.14: Computed injection velocities as a function of the droplet spacing in comparison to experimental mean injection velocity of 2.6 m/s and the computed dilute spray injection velocity of 2.04 m/s at $z = 5$ mm.

5.3.2 Definition of the Validation Metrics

For the user of the model, the validation metric is a means of evaluating the adequacy of the model for the intended application. When choosing the quantities for which the validation metric shall be deduced, the desired application has to be a guiding factor. The quantities that can be inferred depend on the design of the validation experiment, the capabilities, inherent limits and trade-offs, which had to be made. In the following, the spray measurement quantities and prediction results are analyzed in different ways to define the most useful validation metrics in the context of this work.

Definition of System Response Quantities of Interest for Spray Validation

Theoretically, validation metrics can be inferred for all model outputs. To be useful for the adequacy assessment in future applications of the model, the System Response Quantities (SRQ) need to be meaningful. This means that the SRQs can be of direct significance for (combustor) design questions. Alternatively, in case the model is used for coupled physics simulations, the SRQ should represent input quantities for subsequent models so that the validation metric results can be propagated to the simulation results of the coupled physics simulation. Furthermore, the nature of the chosen SRQs has implications on the quality of the validation and the difficulty to infer its metric (Oberkampf and Roy 2010).

When applying this context to the definition of SRQ for droplet evaporation models in GT combustors a range of quantities can be considered: starting from the integral quantities of total evaporation time or an empirically simplified evaporation rate constant, both can be used to support the definition of the size of the primary zone and total combustor length. The evaporated mass flow rate and the diameter distribution distributed in time and space is of intermediate difficulty. Most difficult is the prediction of the distribution of species concentration in time and space.

With the present configuration of the validation experiment and applied diagnostics, information about the diameter and velocity distribution is available. The distributions are described by their mean and the RMS values of the mean. In addition, the local volume flow rate (instead of the mass flow rate) can be computed from this information and used for further validation.

Derivation of the Validation Metrics

As shown in section 4.3.4, the spray is characterized by the evolution of the arithmetic mean and standard deviation of the diameter and velocity distributions in the spray versus the different axial positions. Figure 5.15 shows a comparison of the experimental spray mean diameter and standard deviation with predicted results for n-decane. The comparison of the velocity values is shown in Figure 5.16. As outlined in Oberkampff and Roy (2010), such a form of presenting validation results is focusing on qualitative aspects. The predicted values for diameter and velocity values are in excellent agreement with measurement data until $z = 100$ mm. Downstream the predicted mean values are underestimated with respect to the measurement values. The experimental data starting at $z = 125$ mm shows a stronger measurement error which is due to the lower diameter detection limit as explained in section 4.4. The deviation can be explained by the difference of the droplet velocity predictions and measurement data. These indicate a difference in the underlying flow field, yielding a smaller velocity of the spray droplets in the simulation and thus delayed evaporation with respect to the real droplet along the z -axis.

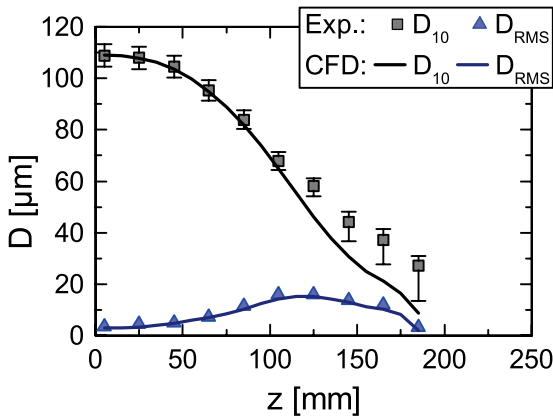


Figure 5.15: N-decane diameter validation.

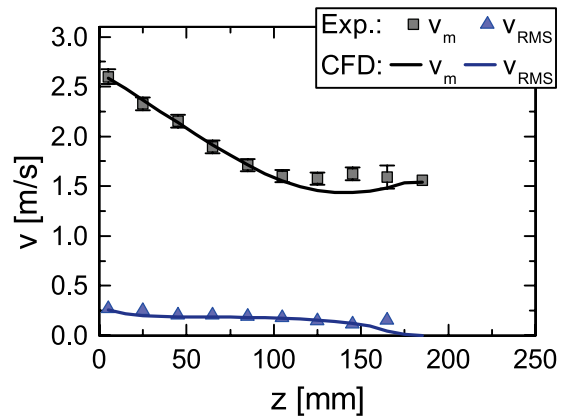


Figure 5.16: N-decane velocity validation.

Figure 5.17 and Figure 5.18 show the validation metric for droplet diameter and velocity prediction and put the focus on the validation information instead of describing the phenomena. The estimated errors are the differences between predicted and experimental values. Error bars are due to measurement uncertainties. It allows for a direct quantitative interpretation as a validation metric.

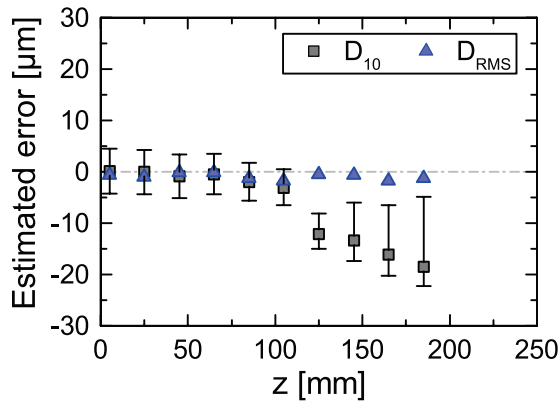


Figure 5.17: N-decane diameter validation metric.

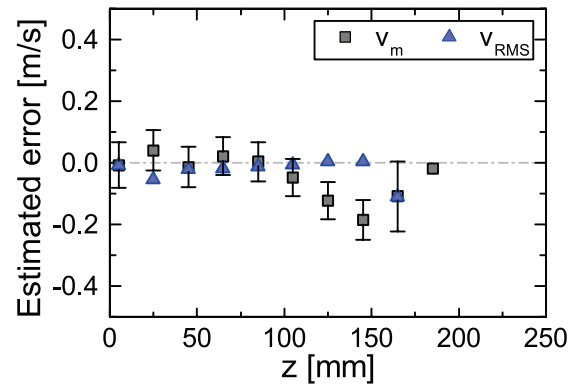


Figure 5.18: N-decane velocity validation metric.

The validation metric is based on the droplet mean diameter. It gives useful information about phenomena that depend on the droplet diameter and shows the capability of the model in dealing with them. For combustion related phenomena, the vapor mass flow rate is of high importance since it defines the fuel vapor mixture fraction at the different positions and thus defines the fuel placement. Since the droplet composition and droplet temperature cannot be easily measured, the evaporated vapor volume flow rate, which shows the same trend as the mass flow rate, is taken for further analysis. The validation graphs of normalized mean diameter and normalized volume flow rate are depicted in Figure 5.19. Since the volume flow rate is proportional to the cube of the diameter, the validation information is weighted differently. For the mean diameter, the first deviation of predicted values to measured values can be seen after a diameter reduction of 40% with respect to the initial diameter. The predicted volume flow values differ from measurement results, after around 80% of the liquid fuel has turned into vapor. The estimated relative errors shown in Figure 5.20 are around 3% until $z = 100$ mm, showing different trends downstream when approaching zero. This analysis shows the utility of both examination methods and that both are required to understand the meaning of the validation results comprehensively.

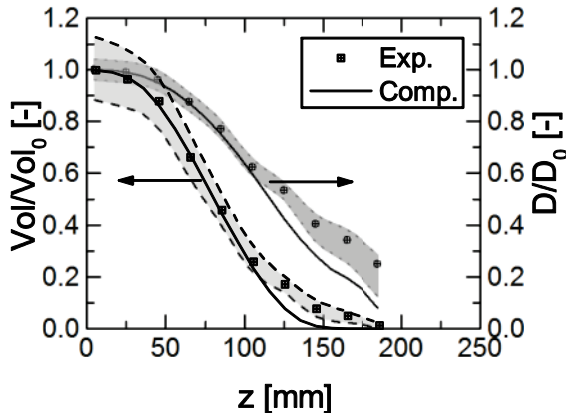


Figure 5.19: N-decane evaporated spray volume flow rate in comparison with mean diameter. Measurement errors are displayed as grey envelopes around the experimental data.

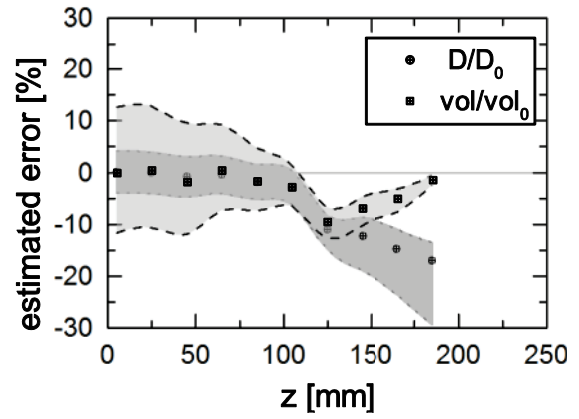


Figure 5.20: N-decane evaporated spray volume flow metric in comparison with mean diameter metric. Measurement errors are displayed as grey envelopes of the experimental data.

Global validation metrics are inferred by taking the arithmetic mean from the validation metric results over all z positions. In Table 5.6 the global metric results are shown in addition, the values of maximum deviation are summarized. This allows checking if the global validation is representative or if the averaging has smoothed the validation results (Oberkampff and Roy 2010). In addition, the information about the location of the maximum deviation provides useful information about the origin of the deviation. The global values allow the analyst to decide if the model is adequate for the application intended. For the modeler, the information about the difference between mean and maximum deviation and the position of the maximum deviation gives a first indication of the origin of the model form uncertainties.

	Mean	Uncert. of Mean	Max.	Uncert. of Max	Pos. of Max.
D	6.65 μm	-5.9/+3.9 μm	-18.47 μm	-13.5/+3.8 μm	185 mm
D_{RMS}	0.94 μm	--	-1.78 μm	--	165 mm
V	0.061 m/s	0.077 m/s	-0.185 m/s	0.114 m/s	165 mm
V_{RMS}	0.027 m/s	--	-0.109 m/s	--	165 mm
D/D_0	4.91 %	-4.6/+3.6%	-16.97 %	-12.4/+3.4 %	185 mm
Vol/Vol_0	2.91 %	-6.1/+6.2%	-9.45 %	-3.18/+2.62	125 mm

Table 5.6 N-decane global validation metrics for diameter, velocity, and volume flow rate.

The metrics presented here are based on deterministic computations. This means that stochastic variations of input quantities or the effects of uncertainties in the model inputs are ignored. To improve the reliability, the effect of uncertain inputs on the validation metrics has to be analyzed.

5.4 Evaluation of the Effect of Input Uncertainties

In the previous section, the validation metrics for different SRQs were determined. The metric is based on experimental data, measurement uncertainty, and deterministic simulation results. Deterministic computations mean that although input quantities are non-deterministic, as for example in the case of measurement data with measurement uncertainty specified on the basis of a confidence interval, only a single computation is performed based on the best estimate of the input quantity. In consequence, the validation metric based on deterministic computations could misleadingly indicate an error in the model form, which is only due to uncertainties in the model inputs. To infer representative validation metrics reflecting the stochastic nature of reality, input uncertainties need to be quantified and propagated through the non-linear models.

5.4.1 Identification and Characterization of Input Uncertainties

For spray evaporation models, input uncertainties are due to errors in the flow field simulation and uncertainties in the spray injection conditions. Uncertainties in the spray injection conditions, in turn, can originate from the method of determining them and simplifications in representing them.

Uncertainties in Spray Injection Conditions

The spray evolution is very sensitive to the spray injection conditions. This means that the spray injection parameters need to be determined accurately. However, there is a certain degree of uncertainty for each injection parameter depending on the method of determination. In Table 5.7 the injection conditions and their uncertainties are summarized. The diameter distribution, spray velocity distribution, the volume concentration profile, and the spray center can be determined from measurement data. Associated uncertainties are due to measurement uncertainties. The neglect of the injection velocity dependency on the radial position in the test track showed only negligible influence. The droplet temperature distribution and droplet composition have to be estimated by numerical simulations. To characterize associated uncertainties, the worst-case scenarios are computed.

Injection condition	Best Estimate	Uncertainty
Diameter distribution	Figure 5.12	$\pm 4.42 \mu\text{m}$
Spray velocity 1. Mean value 2. Standard deviation	2.6 m/s 0.27 m/s	$\pm 0.074 \text{ m/s}$ $\pm 0.05 \text{ m/s}$
Volume concentration profile	Figure 5.13	Unknown (estimated to $\pm 20\%$)
Spray center	0.42 mm	$\pm 0.1 \text{ mm}$
Droplet temperature distribution	Figure 5.21: C=11	Figure 5.21: range dilute to C = 11
Droplet composition	Required only for multicomponent-fuels	Estimated by num. sim.

Table 5.7 Summary of uncertainties in the spray injection conditions for the n-decane spray.

The two limiting cases of dilute spray and moderate dense spray heating in the nozzle are used to compute the maximum range of the droplet injection temperature at the test section. Figure 5.21 shows the resulting temperature profiles. One can see that the dilute spray has a temperature profile being 35 K hotter than for the moderate dense spray.

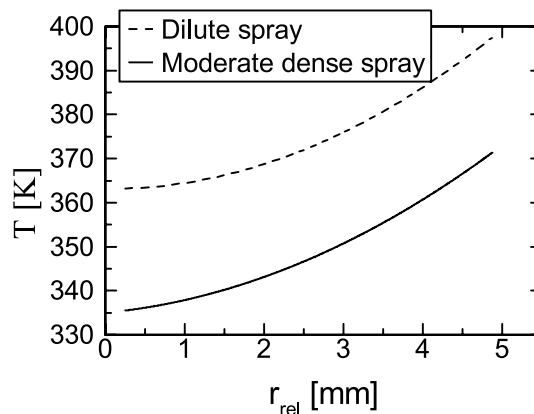


Figure 5.21: Uncertainty of initial temperature distribution for n-decane. Estimation was performed with numerical simulation of the spray heating in the carrier gas flow before the test section with dilute spray assumption and droplet interaction with a fitted droplet spacing $C = 11$.

Flow Field Uncertainties

Errors or uncertainties in the prediction of the flow field temperature, velocity, and turbulence characteristics are propagated to the spray simulation results. A quantification of these uncertainties was not performed as part of this study since the complexity due to the number of unknown inflow conditions - the laminar-turbulent transition (which is not well captured in numerical codes) in the freestream transporting the droplets - was too large and further information is required. In future studies, more advanced turbulence models can be used to investigate the sensitivity of the droplet evaporation on the flow field differences numerically. Detailed flow velocity measurements of the flow field with and without spray would further

reduce uncertainties and help to determine the quantitative flow velocity field error of the simulations.

Consequently, the error and uncertainties of the flow field cannot be distinguished from the spray validation metric results. By assuring a high repeatability of the flow field, the same flow field error is imposed on all validation studies. The good agreement of droplet velocity computations and measurement results, as shown in Figure 5.18, and the agreement in the temperature field prediction, depicted in Figure 5.11, indicate a limited influence of the flow field errors on the validation metric results.

5.4.2 Estimation of Uncertainties in the SRQs

To quantify the influence of input uncertainties on the spray predictions, the uncertainties are propagated through the spray evaporation models. The interval analysis method (Oberkampf and Roy 2010) is used, and input uncertainties are represented by block intervals. This means that all values between the lowest and highest value of the input variable have the same probability. The domain of input parameters is sampled by a stratified sampling technique called Latin Hypercube Sampling (LHS). The principles of LHS can be described as followed (Adams et al. 2013): First, each uncertain variable is divided into a specified number of segments of equal probability. Then, for each uncertain variable, a sample is selected randomly from each of these probability segments. The values for each of the individual parameters are then combined in a shuffling operation to create the set of parameter vectors. As an example, a subset of the injection parameter vector, containing the diameter and droplet temperature at injection for 500 samples is shown in Figure 5.22, this clearly illustrates the random nature of the LHS method. In consequence for each of the 500 combinations of injection parameter computations have been performed. The resulting evolutions of the mean diameter are depicted in Figure 5.23. Since all the input uncertainties are represented as block probability intervals, the area characterized by the envelope of the solution describes the interval of possible solutions, which have all the same probability.

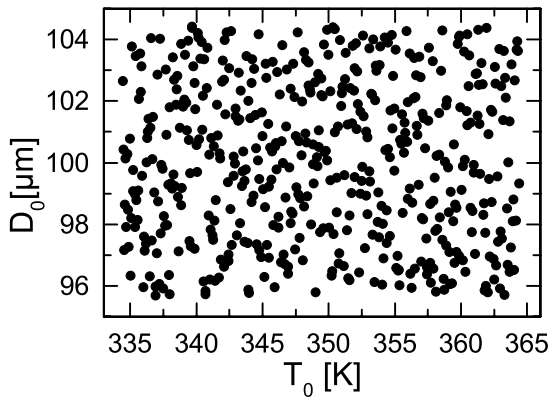


Figure 5.22: Injection parameter combinations of diameter and droplet temperature inferred by Latin Hypercube Sampling.

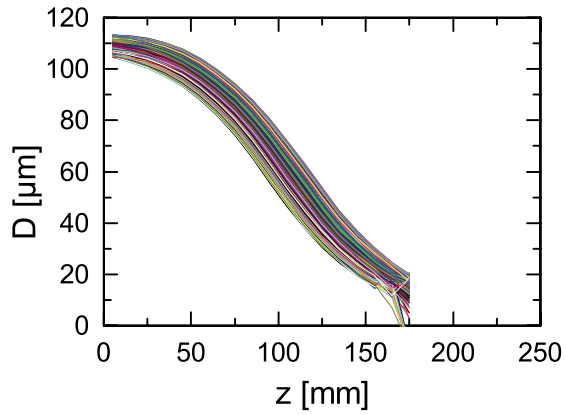
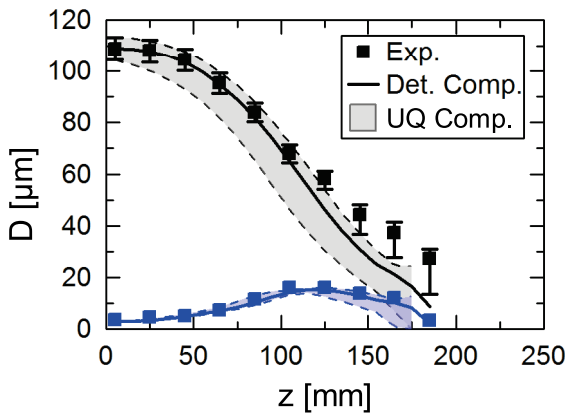
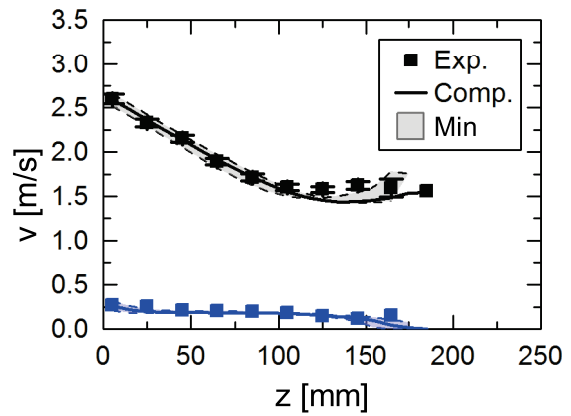


Figure 5.23: Non-deterministic simulation results of n-decane spray evaporation, each line represent the evolution of the mean diameter for one set of injection conditions.

Figure 5.24 shows the non-deterministic simulation results of the mean droplet diameter and velocity in comparison with the deterministic simulation results and with experimental data. The grey area represents the resulting domain where all values have the same probability.



a) Mean diameter evolution.



b) Mean velocity evolution.

Figure 5.24: Uncertainty quantification of n-decane evaporation: comparison of experimental data with deterministic computations that are based on a best estimate as spray injection input parameter and non-deterministic computations that take the variations and uncertainties in the injection parameter into account.

Up to $z = 100$ mm the experimental data is within the computational result for the droplet diameter evolution. This means that the prediction includes experimental data and is thus very accurate. Downstream a partial overlapping of experimental and simulation results can be seen. For the further interpretation, it must be considered that the measurement error is based on a 95% confidence interval stating that the true value is with 95% within the error range. The

definition of a quantitative validation metric in such a combination of probabilistic quantities is a recent topic of research (Roache 2009; Oberkampf and Roy 2010; Thacker and Paez 2013).

For the assessment of the validation approach, the concept of precision as a measure of the variability of the simulation results is introduced. One can say that the results of the diameter prediction are not precise enough to identify differences between predicted and experimental diameter evolutions. In contrary, the velocity prediction has a high precision allowing to identify differences downstream of $z = 100$ mm.

The advantage of non-deterministic simulations with respect to deterministic ones is that the precision is directly evaluated and can be analyzed. Since the precision of the simulation is a function of the input uncertainties, it can be reduced by characterizing the input quantities in detail and with methods that are more reliable. Deterministic computations instead weaken the validation metrics since an agreement between prediction and experiments indicates accurate models, but they can also be due to a combination of errors in the chosen values for the uncertain input condition that cancel each other.

5.4.3 Analysis of the Effect of Injection Parameter Uncertainties

The sensitivities of each boundary condition on the predicted mean diameter ($D_{1,0}$, D_{RMS} , v , v') are extracted from the computations performed for the uncertainty quantification and displayed in Figure 5.25. One can see that injection condition uncertainties of the droplet diameter distribution and droplet temperature have the half primary effect on the evolution of the droplet mean diameter. The effect of the other injection uncertainties is below $1 \mu\text{m}$.

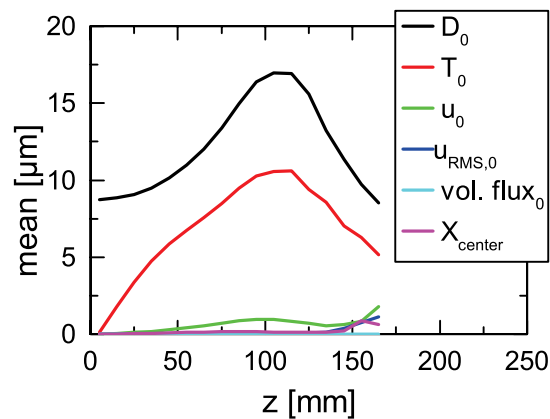


Figure 5.25: Main effect of the most dominant input uncertainties: initial mean diameter D_0 , initial droplet temperature T_0 , initial mean velocity u_0 , standard deviation of initial velocity $u_{RMS,0}$, volume concentration profile at injection vol. flux $_0$, and spray center position X_{center} on mean diameter evolution.

Figure 5.25 clearly demonstrates that it is very beneficial to put high effort in an accurate determination of the spray injection conditions. The precision can be directly influenced by improving the characterization of the boundary and injection conditions. Since the injection diameter D_0 and droplet injection velocity u_0 are systematic uncertainties, they can be reduced by

acquiring more knowledge. For the injection diameter, this would mean to reduce the uncertainty due to the neglect of the refractive index by considering the range of possible refractive indexes in the analysis of the GSI signals. To reduce the uncertainties of the droplet temperature is complicated and prone to large errors. For a single component mixture, the range of possible droplet temperatures can be reduced by applying a combined investigation using rainbow refractometry and numerical simulations (Rauch et al. 2010). More developments are required to apply this approach for multicomponent droplets. Another possibility to reduce the droplet injection temperature uncertainty is to modify the experimental system in a way that the heating of the spray before the test section is minimized.

5.5 Conclusions

The determination of validation metrics requires the combination of experimental data and numerical simulation results in the conceptual framework of validation. Validation approaches are in general a trade-off between what can experimentally be determined, what can be modeled, and the available resources. For the validation metric giving reliable information about model form uncertainty, the combination of validation experiment and numerical simulation has to be optimized to minimize uncertainties in the model inputs. For the numerical simulation, it would be beneficial if all boundary and injection conditions would be measured in detail, capturing variations in time and space. If this is not possible, assumptions and simplifications have to be made to be able to perform the computations. The method of determination of these parameters directly influences the trustworthiness of the validation metric. Parameters determined experimentally have the highest trustworthiness. Parameters that are determined by independent simulations, literature values or expert opinion have an intermediate trustworthiness, and parameters that are left adjustable and are used to calibrate the simulation results have the lowest trustworthiness.

The computational domain in the current study only includes the test track, which was demonstrated to show the best performance in modeling the flow field with RANS models. The resulting flow field has been validated against the temperature field and a cold flow velocity field. Although not considering the laminar-turbulent transition of droplet carrier gas flow and the asymmetric velocity inflow conditions the agreement is satisfactory with deviations smaller than 6.9 K for the temperature and 0.07 m/s for the velocity along the centerline. For the subsequent analysis, it has to be noted that these differences in the flow field modeling spuriously contribute to the validation metrics of the droplet evaporation model.

For the spray validation, n-decane is used as a benchmark. The injection conditions used are based on measurement values and a numerical parameter estimation to determine the droplet injection temperature and composition. To describe the accuracy of the spray evaporation simulations, the vapor volume flow and the evolution of the diameter and velocity distributions

along the centerline are chosen. These quantities have a strong physical meaning and represent input quantities for subsequent models in the combustor simulations.

To understand the effect of input parameter uncertainties on the simulation results, non-deterministic computations, a sampling of parameter input domain have been performed. To characterize the validation approach, the concept of precision was introduced. It defines the variability of non-deterministic simulation results, which is due to model input uncertainties. It can be used to describe for example how well differences between different validation runs can be resolved. It was shown that input uncertainties lower the precision of simulation results remarkably and that it is beneficial to reduce systematic uncertainties regarding injection conditions. The precision of the n-decane evaporation is most sensitive to uncertainties in the droplet diameter and droplet temperature injection conditions.

6 Accuracy Assessment of Alternative Aviation Fuel Droplet Evaporation Models

New or enhanced models can be used to facilitate the utilization of new fuels, the design of new combustion systems and also for the improvement or the optimization of fuel formulations. The demand for the model predictive capabilities is high; alternative aviation fuels have to be used in jet engines that were designed more than 50 years ago and in future engines. Several tiers of people are involved in such a process: modelers, who build or enhance the models, analysts and designers applying the model to design and understand the performance of new systems, and finally the decision makers, who decide about the results and the next steps to be performed. For all of them, the predictive capabilities of the models used are of crucial importance but from very different perspectives.

The modelers focus on the processes that have to be modeled. The quality of modeling depends on limitations of the models used and on the simplifications and the assumptions, which have to be made as trade-off during the model design. These factors are put together and build model form uncertainties (see chapter 3 for evaporation model uncertainties). The general intention of the modeler is to reduce the complexity of the mathematical description of the processes so that the problem can be solved in a reasonable time and with a reasonable accuracy.

The analysts/designers apply the models and need to know how “well” the models perform for the intended use. The accuracy of the models has to be within the constraints that are defined to be critical for the design of the system. To support the fidelity in the models, it is essential to know where and how the model accuracy has been inferred and if this metric can be used to assess the accuracy in the specific domain of application.

The responsible decision maker needs to be informed about the trustworthiness of the complete system simulation results. For this reason, the uncertainties for each model and the interactions of the different model uncertainties need to be taken into account. The comparison of the system simulation uncertainty with critical margins indicates whether further model improvements are required, or the results can be trusted.

For each of these roles, the model adequacy has a different meaning. This underlines the fact that the model adequacy evaluation should not depend on the person performing the validation, but on the person, who has to use the model or has to make a decision based on

information from simulation results. The best way to report validation results is a representation as objective quantitative measures of the agreement between model predictions and reality.

In this chapter, the modeling, simulation, and validation metric strategy derived in the last chapter is applied. No parameters are adjusted, and simulations of the evaporation of the different fuels were performed independently from their respective experimental results. The accuracy assessment is conducted on different scales, from global statements to detailed local assessments. This gives all information required for an overall assessment of the predictive capabilities of the used evaporation models for alternative aviation fuels.

6.1 Validation Domain for Droplet Evaporation Models

In chapter 2 the analysis of the evolution of alternative aviation fuels and the characteristics of the fuels were used to define a general validation domain. This general validation domain focuses on fuel variations that have a potential influence on combustor performance. Droplet evaporation is a sub-process with a certain influence on the combustor performance. The primary model form uncertainties of the droplet evaporation model, which are due to assumptions and simplifications made during model formulation, are reported in chapter 3. As the number of components of potential aviation fuels ranges from single to multicomponent fuels, the evaporation models have to cover the same range. In the following, a combination of fuels, which samples the validation domain is chosen to be able to infer the model form uncertainties of single component, discrete component, and multicomponent CTM droplet evaporation models.

6.1.1 Test Fuels

Since the evaporation models are built upon one another, the fuel validation domain is constructed to test the increasing complexity of the models stepwise:

- The fundamental droplet evaporation model is tested with single component fuels: n-heptane, n-decane, ethanol, and hexanol. These fuels are used as representatives for alternative aviation fuels like DSHC containing only farnesane.
- The discrete component droplet evaporation model is tested with binary mixtures of n-heptane and n-decane. They are used to represent the modeling of few component fuels like ATJ-SPKs.
- The discrete component droplet evaporation model with non-ideal mixtures is tested with mixtures of n-heptane and ethanol. The mixture of n-heptane and ethanol is highly non-linear. It is used to infer the droplet evaporation models' capabilities in representing the evaporation of potential long-term alternative fuels like Jet A-1 blended with hexanol.

6.1 Validation Domain for Droplet Evaporation Models

- The continuous thermodynamics model for fuels with a high number of components is tested with Jet A-1 and HEFA drop-in fuels. These two represent the multicomponent fuels like Jet A-1, HEFA, F-T, and CH.

The main properties of the fuels are summarized in Table 6.1 - Table 6.4.

Name	Carbon Number	Molar Mass [g/mol]	T _b [°C]
n-heptane	C7	100.21	98.42
n-decane	C10	142.29	174.1
ethanol	C3	46.07	78.37
hexanol	C6	102.18	157

Table 6.1: Validation domain: single component fuels.

Abbreviation	Name	Mass Fraction [-]	Name	Mass Fraction [-]
h(0.2)/d(0.8)	n-heptane	0.2	n-decane	0.8
h(0.5)/d(0.5)	n-heptane	0.5	n-decane	0.5
h(0.8)/d(0.2)	n-heptane	0.8	n-decane	0.2

Table 6.2: Validation domain: binary mixture fuels.

Abbreviation	Name	Mass Fraction [-]	Name	Mass Fraction [-]
h(0.2)/e(0.8)	n-heptane	0.2	ethanol	0.8
h(0.5)/e(0.5)	n-heptane	0.5	ethanol	0.5
h(0.8)/e(0.2)	n-heptane	0.8	ethanol	0.2

Table 6.3: Validation domain: non-ideal mixture fuels.

Name	Carbon Number	Molar Mass [g/mol]	T _b [°C]
Jet A-1	C6 - C17	153	150 - 244
HEFA	C8 - C18	156	152 - 257

Table 6.4: Validation domain: fuels with a high number of components.

6.1.2 CTM Description of Multicomponent Fuels

The CTM will be used to describe the evaporation of the multicomponent-fuel droplets with many components. Figure 6.1 shows a simplified Jet A-1 composition with gamma distribution functions describing the composition for the CTM evaporation model. For the fuel characterized by Wahl (2003), 86.6% of the components could be identified and were grouped into six hydrocarbon families. Due to the low amount of di-aromatics (1.2%) and alkenes (2.8%), these compounds are lumped into the mono-aromatics fuel family. The HEFA fuel utilized in this study was produced from tallow. The composition and the description with gamma distribution functions are shown in Figure 6.2. The main difference to the reference Jet A-1 is that in case of the HEFA blend, the iso-alkanes are the dominant fuel family and mono-aromatics are negligible (<0.3%). In conclusion, it can be stated, that the gamma distribution describes the composition of

6 Accuracy Assessment of Alternative Aviation Fuel Droplet Evaporation Models

the Jet A-1 very well. However, there are some discrepancies in the description of the iso-alkane fuel family in the HEFA fuel due to the asymmetric distribution of the fuel components. The parameters of the gamma distribution functions are summarized in Table 6.5 and Table 6.6.

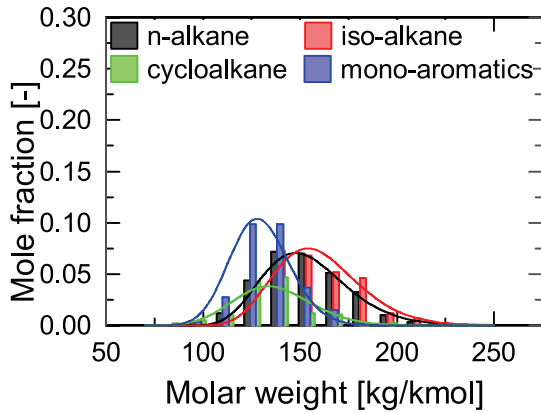


Figure 6.1: Jet A-1 composition and CTM description with Γ -PDF.

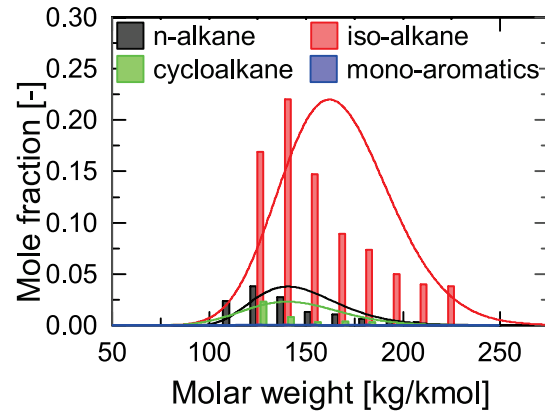


Figure 6.2: HEFA composition and CTM description with Γ -PDF.

Distribution parameters	N-alkane	Iso-alkane	Cycloalkane	Mono-aromatics
Mole fraction	0.3	0.29	0.13	0.28
Θ [kg/kmol]	154.12	160.03	136.67	129.66
σ [kg/kmol]	22.02	22.06	20.03	15.2
γ [kg/kmol]	78	80	0	0

Table 6.5: Parameter for the Γ -PDF representing Jet A-1 fuel families (mean Θ , standard deviation σ , origin γ).

Distribution parameters	N-alkane	Iso-alkane	Cycloalkane	Mono-aromatics
Mole fraction	0.127	0.827	0.044	0.003
Θ [kg/kmol]	148.15	166.73	244.49	--
σ [kg/kmol]	22.82	28.06	24.86	--
γ [kg/kmol]	80	0	0	--

Table 6.6: Parameter for the Γ -PDF representing HEFA fuel families (mean Θ , standard deviation σ , origin γ).

6.2 Global Statement of Model Accuracy

For the global statement, the accuracy assessment results are averaged into single values. Global metrics support the adequacy assessment of the prediction of global phenomena depending on the evaporation process, like for example the amount of unburned hydrocarbons and the flame front position under evaporation rate controlled conditions. Furthermore, global metrics enable a direct comparison of:

- the performance of different models and
- the effect of different validation domain parameters on the accuracy assessment of different SRQs.

The intended overview helps the analyst to decide which model to choose, by giving relevant background information. The modeler can decide which model has the highest improvement potential and what is the first step to take to improve the model.

6.2.1 Global Validation Metric for the Validation Domain

The global validation metric is inferred for the mean diameter, mean velocity, and volume flow rate as the average deviation of simulation results with respect to experimental data. It is then normalized by its initial value. For the diameter, velocity, and volume flow rate predictions, the average over the absolute differences between predictions and experimental results are reported. Additionally, the relative error, which represents the average of deviations including the compensating effects of opposed deviations, is reported for the evaporated volume flow. This integral value of the evaporated volume flow rate is of great importance for subsequent processes in a combustion chamber.

Global Metric for Fuel Models

To compare the performance of the respective droplet evaporation models, the metrics are averaged for each fuel in the respective model category of fuels. It has to be noted that the number of fuels per category is limited and not sufficient for a robust statistical analysis.

In Table 6.7 the groups of the different models are listed with rising complexity. The single component fuel evaporation models can be regarded as a reference. All subsequent models are based on the single component model formulation and thus have the model form uncertainties of the single component fuel models inherited. In consequence, expectations are that the prediction error will increase together with the complexity of the models. First, one can see a similar trend in the metrics for the three SRQs in the different fuel groups, which support the consistency in the validation procedure.

Comparing the best estimates of the different SRQs for each model, non-ideal mixture models have the smallest metrics, followed by single component fuels. This could be an indication of a compensating effect of errors in the corrected vapor pressure presented in section 3.4.4. Furthermore, it is remarkable that multicomponent-fuel models have a lower metric in diameter prediction than single component fuel models, but a higher error in the volume flow rate predictions. To understand this effect, the local variation of mean diameter and volume flow rate are investigated in section 6.3.

	Diameter [%]	Velocity [%]	Volume Flow Rate [%]		
	Abs. Error	Abs. Error	Abs. Error	Rel. Error	Uncert. range
Single Component Fuels	5.0 [-5.0/+3.6]	3.2 \pm 2.3	4.5	2.9	[-6.5/+6.8]
Binary Mixture Fuels	8.5 [-4.9/+4.1]	3.5 \pm 2.4	7.1	6.9	[-7.4/+7.9]
Non-Ideal Mixture Fuels	3.6 [-4.7/+3.7]	3.1 \pm 2.1	3.4	1.5	[-6.2/+6.6]
Multicomponent Fuels	4.6 [-4.9/+4.5]	4.7 \pm 2.7	5.4	4.1	[-8.2/+8.6]

Table 6.7 Comparison of global accuracy assessment results for the different fuel categories.

The average errors reported in Table 6.7 are comparable with the average confidence indicator, which is based on measurement uncertainties. Hence, when considering the span of possible errors for the overall assessment of the evaporation models, it can be stated that for the given boundary conditions with a 95% probability:

- the true error of the diameter predictions for all models is between 0% and 12.6%,
- the error for the velocity predictions for all models is between 0.9% and 7.4% and,
- the error for the volume flow rate predictions for all models is between 0% and 14.8%.

The confidence interval for the metrics includes zero for most models indicating a possible perfect agreement of the predicted value with the real value. Minimum errors in the predictions of the different SRQs can be identified for the binary fuel mixture diameter predictions (3.6%) and for the droplet velocity predictions of each fuel group (0.4%-2%). As shown in section 5.4.3, the measurement uncertainties form the precision of the validation metric. Since the precision of the metric is correlated with measurement uncertainties, assessments that are more precise can be made by reducing the measurement uncertainties.

Global Metric for Fuel Measurements

Within a fuel group, variations are due to the different thermodynamic properties of each fuel. The errors are related to the models describing the thermodynamic properties, but also to variations of the uncertainties in the experiment between the different measurement campaigns.

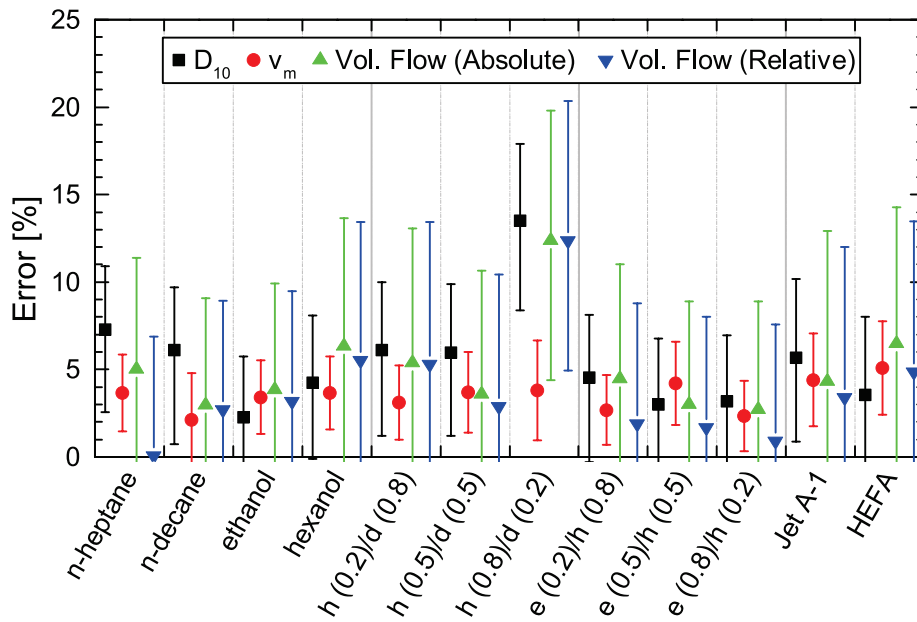


Figure 6.3: Global accuracy assessment for each fuel for the mean diameter predictions, mean velocity, and volume flow rate predictions.

Figure 6.3 summarizes the different errors for each fuel. In general, there are only small variations around the means for each fuel group reported in Table 6.7. This shows that long-term variations in the experiments over the course of two years and during different periods in the years played a minor role. For the binary mixture (h(0.8)/d(0.2)), an abnormality can be seen. The errors reported for the diameter and volume flow rate predictions are twice as high as for the other candidates of the group. To explore the origin of these deviations, information about the local evolution of the droplet mean diameter is required.

6.2.2 Analysis of the Maximum Error

Errors in the prediction of local or global trends are indicated by substantial differences between the averaged error and maximum error (Oberkampf and Roy 2010). In Figure 6.4, the ratio of the average error to the maximum error for the mean diameter, mean velocity, and evaporated volume flow rate predictions are plotted. It can be seen that the maximum errors are around two to four times higher than the mean error:

- Velocity predictions have the smallest difference,
- diameter predictions the highest, and
- evaporated volume flow rate predictions are in between.

For further analysis, the location of the maximum error and the spray penetration length are summarized in Figure 6.5. Different locations can be identified for each SRQ of interest, pointing to different causes of the error:

6 Accuracy Assessment of Alternative Aviation Fuel Droplet Evaporation Models

- the maximum error of the mean diameter predictions occurs close to the end of the spray lifetime,
- the maximum error of the volume flow predictions is in most of the cases in the first half of the spray lifetime, and
- the location of the maximum error of velocity predictions is split into one half occurring at the end of spray lifetime, the other half at the beginning of the spray lifetime.

Both, the diameter and evaporated volume flow metrics are based on the diameter, but with a different weighting. Since the evaporated volume flow rate depends on the diameter to the third power, the beginning of the spray is most relevant. The locations of the respective maximum error indicate errors in the modeling of the volume expansion of the droplets or errors in the estimation of the droplet injection temperature.

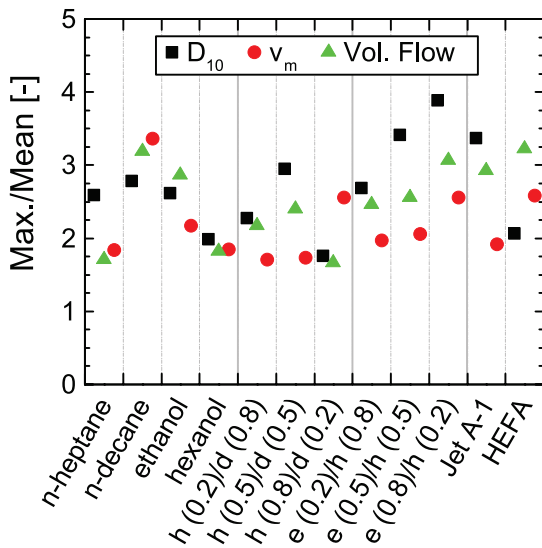


Figure 6.4: Ratio of maximum error and mean global error.

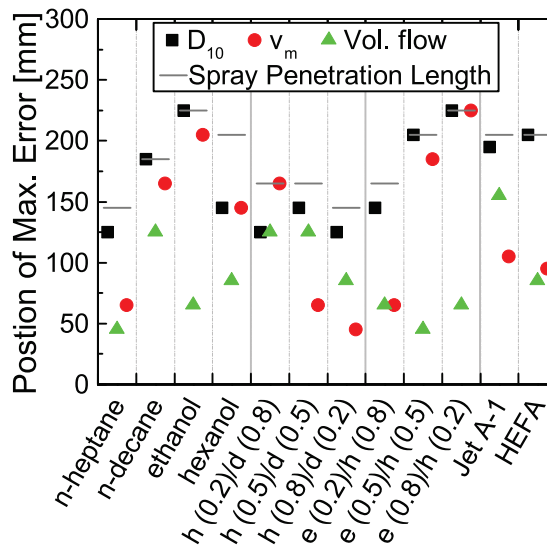


Figure 6.5: Position of maximum error for mean diameter, mean velocity, and volume flow rate predictions in comparison to the spray penetration length.

For the mean diameter metric, the location of the maximum error at the end of the spray lifetime can be explained by more substantial measurement uncertainties at the end of the spray lifetime and by model form uncertainties. Those errors accumulate during the spray lifetime. The location of the maximum error for the velocity predictions possibly has its origins in inaccuracies of the velocity field predictions or in the spray dispersion model. For further investigations, the evolution of the mean diameter and velocity metrics over the penetration length need to be considered.

6.3 Validation by the Evolution of the Mean Values

To investigate and assess the model performance in detail, the streamwise evolution of the diameters and velocity distributions are compared with experimental data. This gives underlying information about the physical processes and their interactions determining the evaporation process of the spray and thus the influence on local phenomena like hot spot formation, local blow out, or ignition. In the context of the model accuracy assessment, the identification of local differences between simulation results and experimental data, and if possible their origin, is the first step for improving the models.

6.3.1 Single Component Fuels

The single component fuels are used to infer the validation metric for the basic evaporation models. In the ideal case of infinite precision of the validation approach (as explained in section 5.4.3), the difference between simulation results and experimental data corresponds to the model form uncertainties. For the single component fuel, the model form uncertainties comprise the errors from the Lagrangian spray model formulation and the single component evaporation models. This part of the validation metric should be the same for all four fuels tested in this category. Consequently, relative variations of the metrics between the fuels can be explained by model form uncertainties in the thermodynamic models describing each fuel. However, with a finite precision of the validation approach, measurement uncertainties and model input uncertainties become part of the validation metric and increase the difficulty in identifying the origin of the differences.

In the following, the difference between numerical simulation results and experimental data is called the estimated error and serves as the validation metric. Whereas the evolution of the mean diameter and velocity puts the focus on the physical description of the phenomena, the validation metric centers on a critical examination of the model capabilities. For this reason, graphs with the validation metric are used in the following discussion. The comparison of mean diameter, diameter RMS, mean velocity, and velocity RMS with experimental data can be found in appendix C.2.

Discussion of the Validation Metric

Figure 6.6 shows the evolution of the diameter and velocity validation metric for single component fuels. Positive values denote an overprediction, negative values of the metric mean an underprediction. Data points represent the best estimate of the error. The grey areas represent the span of the 95%-confidence interval, which is due to measurement uncertainties.

Ethanol, shown in Figure 6.6 c), has the best metric for the diameter prediction. The metric is covering zero within its 95 % probability band in the whole spray evaporation history. Considering the best estimate of the measurement data only, the metric shows the difference of first an overprediction of the mean diameter with a maximum of 5 μm and then an

6 Accuracy Assessment of Alternative Aviation Fuel Droplet Evaporation Models

underprediction of 5 μm . For the other fuels, differences that are more significant can be observed. The pattern is similar for each: at the beginning of the spray lifetime, the diameter error confidence interval includes zero. At a certain point, the metric shows a significant decrease, especially in case of n-heptane, indicating an underprediction of the mean diameter.

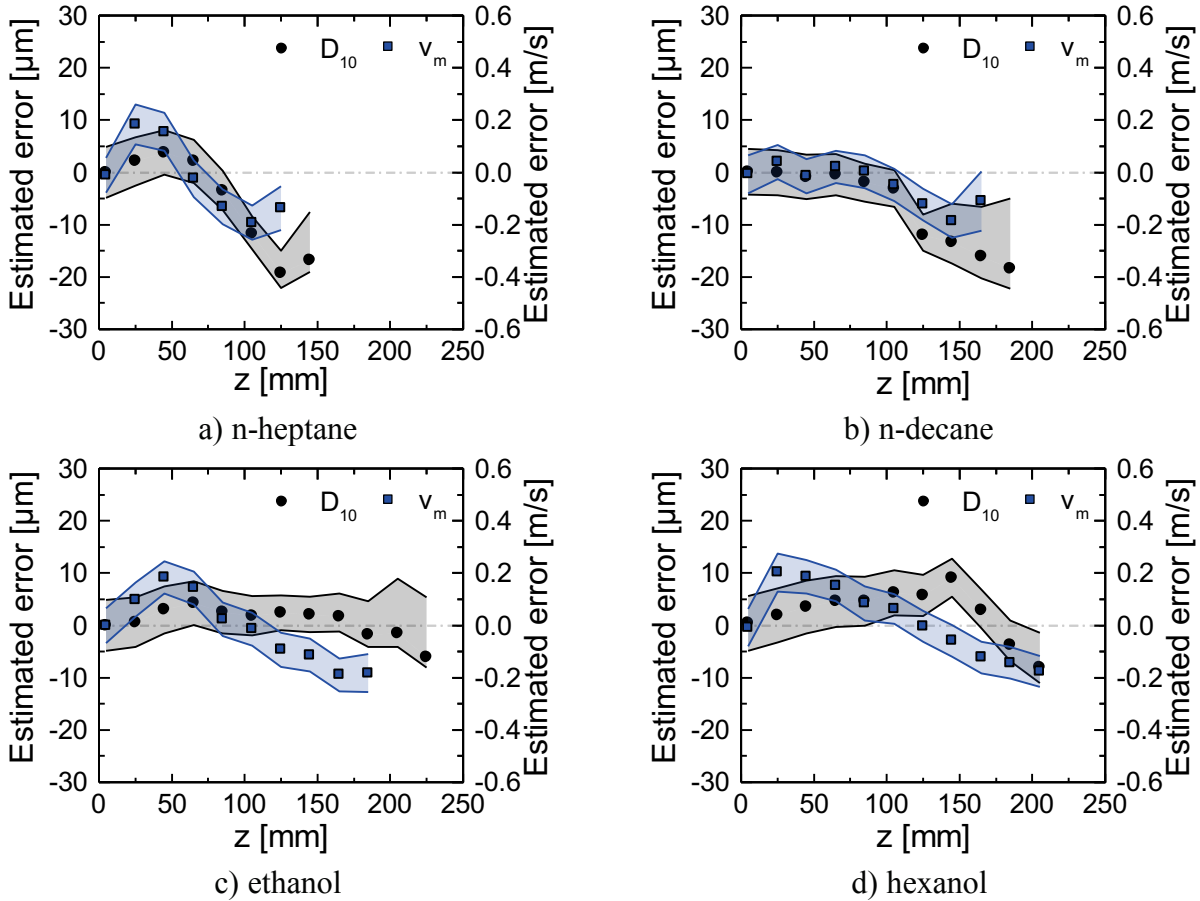


Figure 6.6: Evolution of the estimated mean diameter and velocity metric.

The velocity metric shows two maxima: at the beginning of the spray lifetime, the mean velocity is overpredicted, then, at the end of the spray lifetime, the mean velocity is underpredicted. An indication of this behavior was seen in the analysis of the position of the maximum velocity error in section 6.2.2. The error in the droplet velocity prediction is most probably due to inaccuracies in the prediction of the flow velocity field especially the mixing layer between the carrier jet and the co-flow. As described in section 5.2.2, the jet of the carrier flow entering the test section is bent slightly towards one side, causing a narrower spatial distribution of the jet velocity distribution in the experiment. Since this is not captured in the simulation, droplets stay in the higher velocity regions, which results in an overprediction of the spray velocity. The underprediction of the spray velocity towards the end of the spray lifetime is a direct result of the underprediction of the flow velocity field as depicted in Figure 5.9 in section 5.2.2.

Qualitative Discussion

When comparing the metric of the different fuels, the two hydrocarbons, and especially n-heptane show the highest decrease in the mean diameter metric. Sensitivity studies (Rauch, Calabria, Chiariello, Le Clercq, Massoli, and Rachner 2011) showed that the latent heat of vaporization is the dominant property influencing the evaporation process under the given experimental conditions. A higher latent heat of vaporization leads to a slower evaporation and an increased penetration of the spray into the test track. The vapor pressure is of second-order importance. Higher vapor pressures take effect especially in the beginning of the spray evaporation and furthermore correlate with a faster evaporation of the spray.

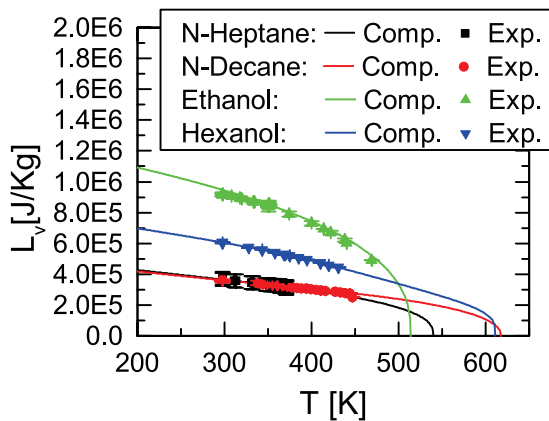


Figure 6.7: Comparison of thermodynamic property models with experimental data from (Frenkel et al. 2005) for latent heat of vaporization L_v .

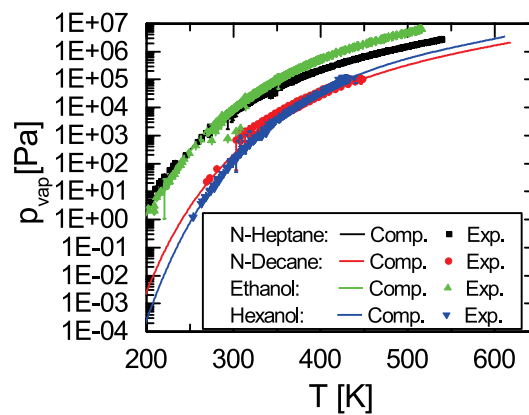


Figure 6.8: Comparison of thermodynamic property models with experimental data from (Frenkel et al. 2005) for vapor pressure p_{vap} .

Figure 6.7 and Figure 6.8 compare computed latent heat of vaporization and vapor pressure with experimental data. The computed values of n-heptane as well as for other fuels are in very good agreement with measurement data. Models for other properties that are relevant to the evaporation process show the same performance (see Appendix A). Consequently, the difference cannot be explained by errors in the thermodynamic property models.

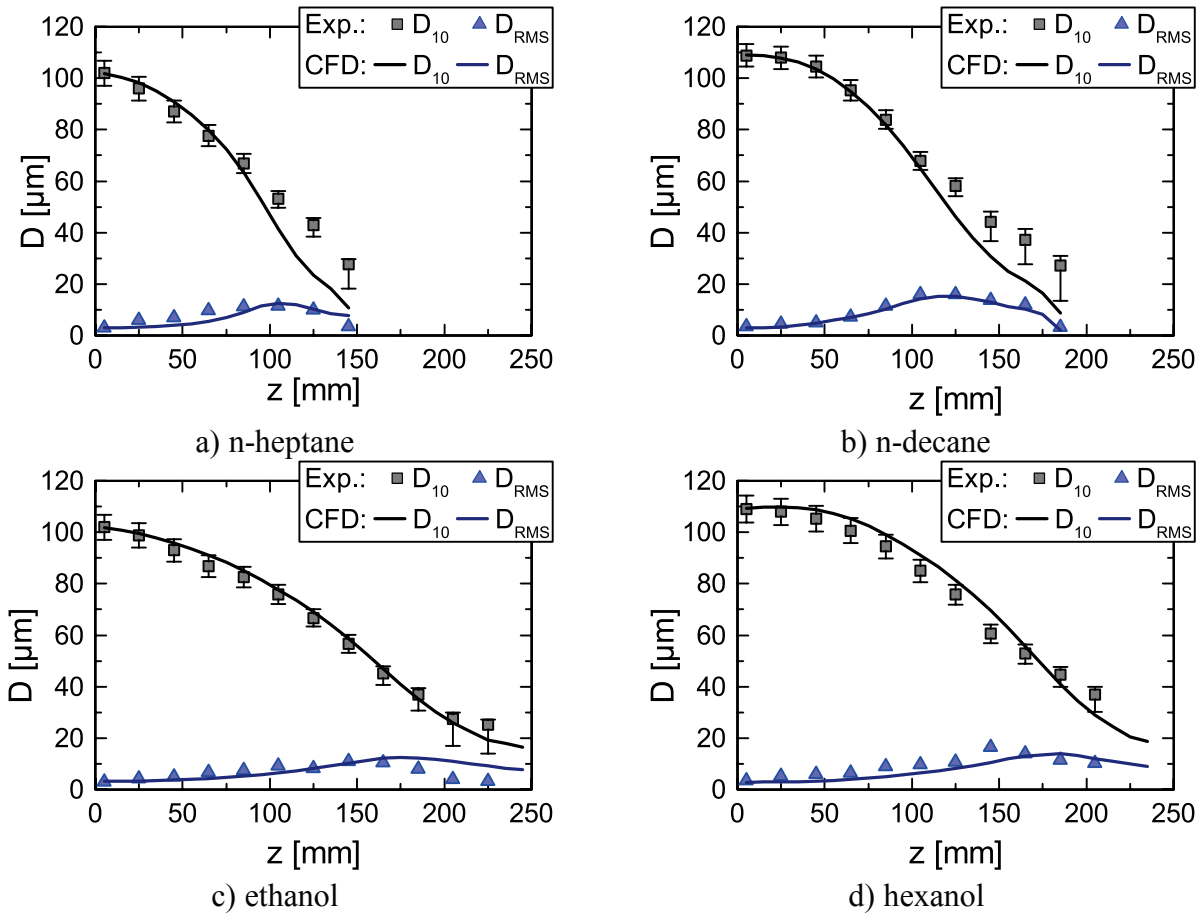


Figure 6.9: Validation graphs for the evolution of the diameter distribution.

The mean diameter evolution of the single component fuels is shown in Figure 6.9. As mentioned before, the higher latent heat of the two alcohols leads to stronger penetration of the spray into the test track. The higher vapor pressure of n-heptane and ethanol yield smaller mean diameters at the injection into the test track (102 μm for n-heptane and ethanol) with respect to 109 μm for n-decane and hexanol. Until $z = 100$ mm, the n-heptane and n-decane mean diameter evolution is described very well by numerical simulation results. Afterwards, the gradient of the experimental results changes to lower values delaying the evaporation.

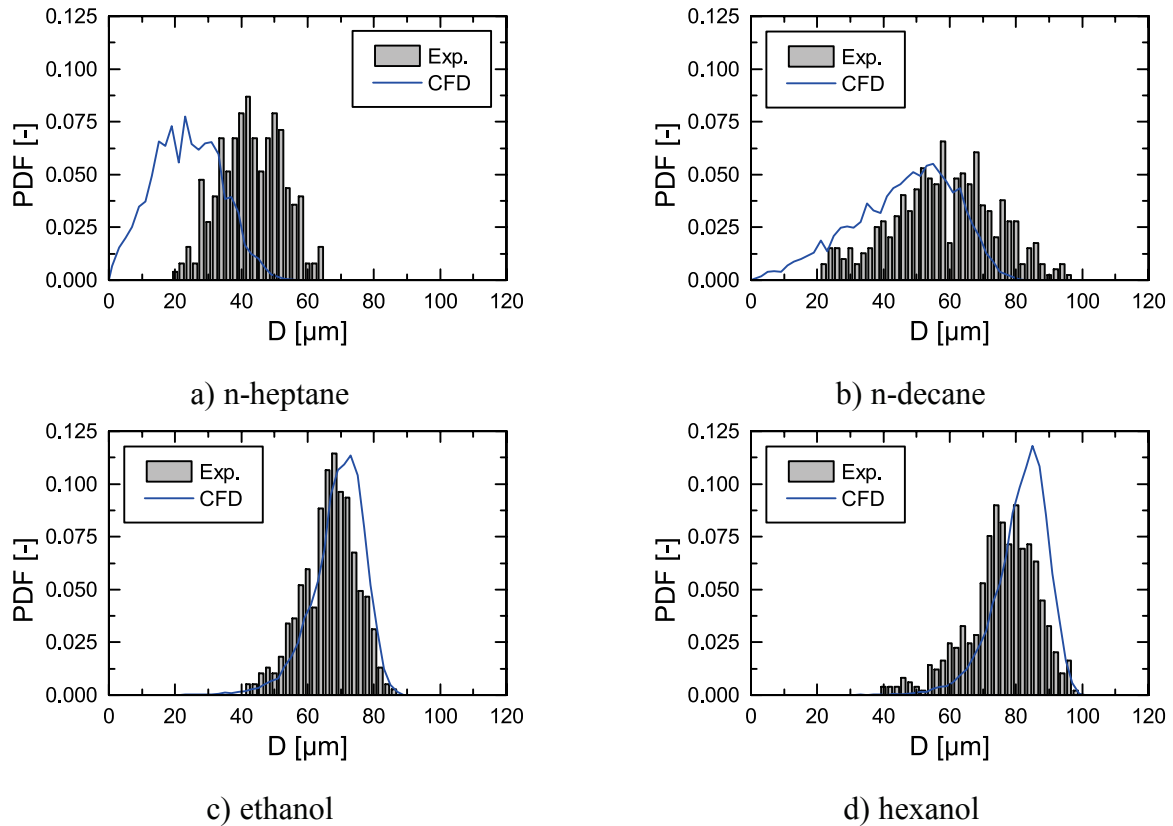


Figure 6.10: Comparison of experimental and predicted diameter histograms at $z = 125$ mm for: a) n-Heptane b) n-Decane c) Ethanol d) Hexanol.

Two possible explanations can be found when considering the diameter distributions at $z = 125$ mm, as displayed in Figure 6.10. First, with the chosen sections of the GSI setup, droplets under $20 \mu\text{m}$ cannot be detected. The influence on the measurement uncertainty δD_{range} was estimated by numerical simulations as described in section 4.4.2, but the procedure itself introduces uncertainties in the evaluation of the measurement uncertainty. Second, the decaying zone of the carrier jet starts after $z = 80$ mm. The influence of the higher turbulent co-flow becomes higher and small droplets might be ejected from the measurement volume thus shifting the mean droplet diameter to higher values. In future works, this fact needs to be verified with combined PIV and GSI measurements.

6.3.2 Binary Mixtures

The model form uncertainties of the binary mixtures consist of the model form uncertainty of single component fuels and additional model form uncertainties from thermodynamic mixing models and the droplet interior mixing models, which is assumed to be a rapid mixing model as described in section 3.2.3. The evolution of the mean diameter and mean velocity validation metric is shown in Figure 6.11 a)-c). A comparison of the binary mixture metrics with the pure compound metric is shown in Figure 6.11 d). The qualitative trends for the estimated errors of the mixtures are similar as for its pure constituents: in the beginning, the estimated errors are around zero and downstream of $z = 80$ mm, the mean diameter is increasingly underpredicted. However,

in case of the h(0.8)/d(0.2) mixture, the simulation result strongly underpredicts the evaporation of the spray. When comparing the mean diameter at injection, the diameter for the h(0.8)/d(0.2) is 10% smaller. It is 94 μm compared to a range of 104 to 110 μm for the other fuels (see Appendix C, Figure C.8.) This indicates a strong pre-evaporation of the spray before the test section, resulting in a composition with a lower content of n-heptane as specified (80% n-heptane) and used as injection condition for the simulation.

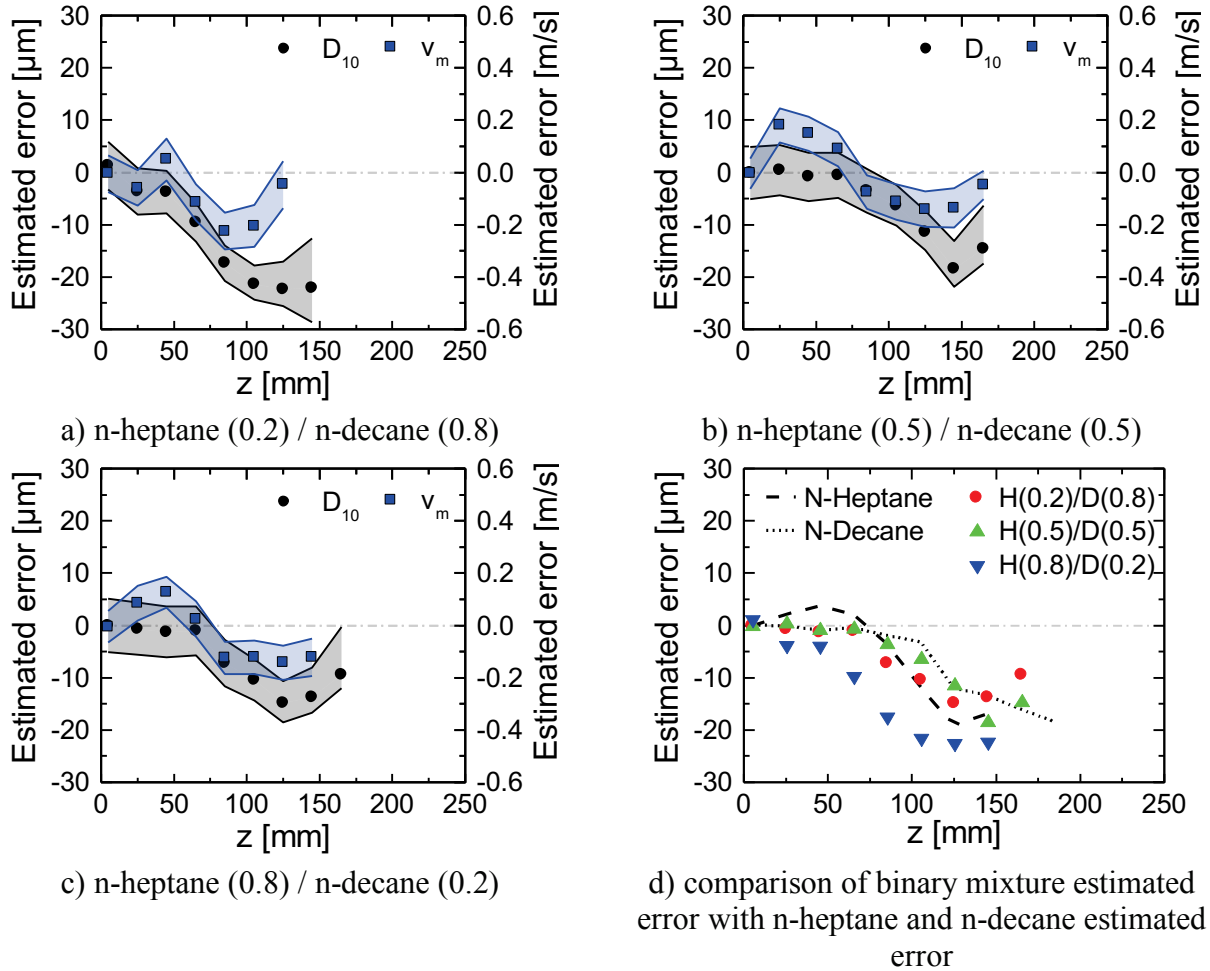


Figure 6.11: Evolution of the estimated mean diameter and velocity.

6.3.3 Non-Ideal Mixtures

The model form uncertainty of non-ideal binary mixtures models consists of that of binary mixtures and the potential uncertainties introduced by the non-linear mixing model for the thermodynamic properties, as described in section 3.4.4. The validation metrics for the mean diameter and velocity are depicted in Figure 6.12 a) – c). A comparison of the estimated non-ideal mixture model errors with the pure compound errors is shown in Figure 6.12 d). The validation metric for the mean velocity and mean diameter consistently shows the same qualitative trend as for the pure compounds. The diameter error confidence interval comprises zero most of the time. The estimated error lies within the range of its pure components showing the compensating

effects of overpredicted ethanol diameter evolution and an underpredicted n-heptane evaporation.

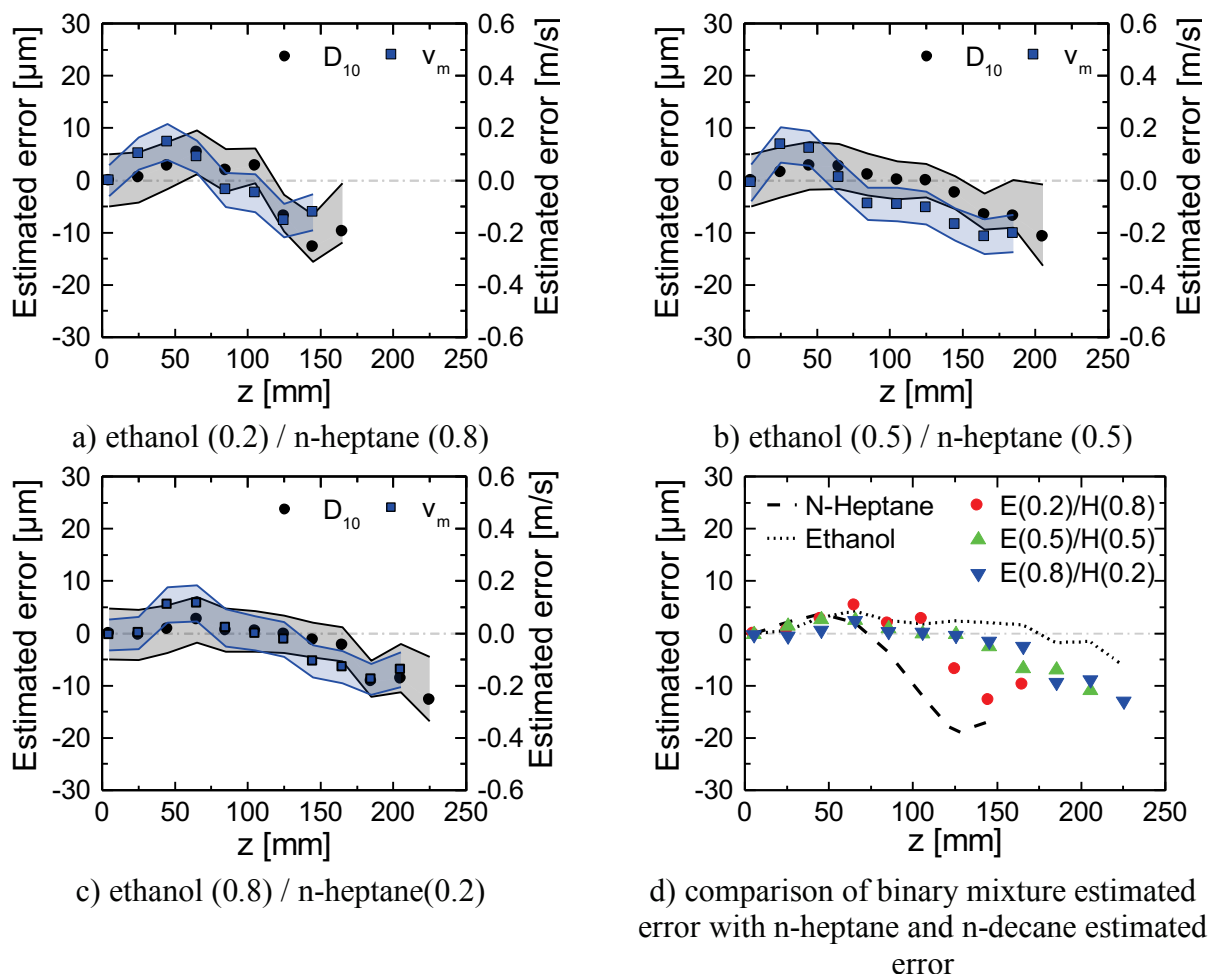


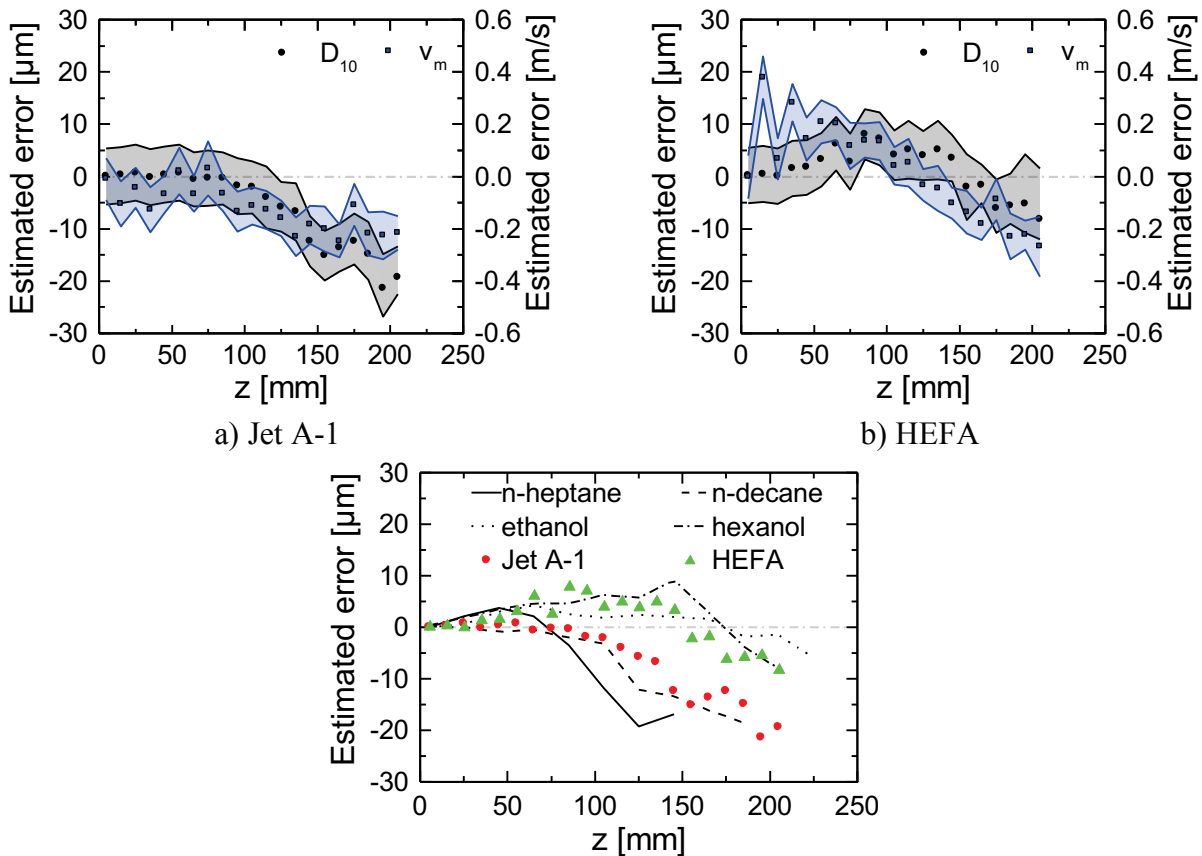
Figure 6.12: Evolution of the estimated mean diameter and velocity metric.

6.3.4 Multicomponent Mixtures

As described in section 3.3.2, CTM describes the complex composition of real fuels with distribution functions. In addition to model form uncertainties from single component evaporation models, uncertainties arise from the simplified thermodynamic properties (see section 3.4) and input uncertainties due to the fitting of the distribution functions to the simplified compositions (see section 6.1.2.)

Figure 6.13 a) and b) show the evolution of the diameter and velocity metric for Jet A-1 and HEFA. Measurement capabilities with an increased framerate have been implemented to enable a high resolution in the characterization of the spray along the z-axis and thus maximize the number of validation points. Fluctuations between subsequent data points in the velocity metrics are due to variations in the spray injection conditions during the experimental procedure. Within the maximized measurement time required to characterize the full spray, the pressure in the fuel reservoir changed slightly causing small differences in the injection velocity. Nevertheless, the

effect on the diameter evolution was negligible. In Figure 6.13 c), the best estimates of the diameter metrics are compared with the metrics for the single component fuels. The Jet A-1 evaporation follows the same qualitative behavior as described before. For HEFA there is an overprediction of the droplet mean diameter of $8 \mu\text{m}$ at $z = 85 \text{ mm}$. This might be due to input errors when describing the HEFA composition. Especially for iso-alkanes, the describing distribution function is shifted to higher molar weights or boiling points respectively. For a final explanation, additional experiments with systematic variation of the distribution of fuel components are required to quantify the sensitivities. Overall, the diameter metric results are within the range of hexanol and n-decane metrics. In consequence, compared to the less complex fuels, no additional errors can be identified.



c) comparison of the CTM estimated errors with single component estimated errors
 Figure 6.13: Evolution of the estimated mean diameter and velocity metric.

6.4 Conclusions

Different metrics required for the judgment of the droplet evaporation model adequacy for their later application are inferred. The fuels are systematically selected to fill the validation domain developed in section 2.2. Validation metrics were inferred for:

- single component fuels (n-heptane, n-decane, ethanol, hexanol), to test the basic single component evaporation equations,

- binary mixtures of n-heptane, and n-decane to test the discrete multicomponent-fuel droplet evaporation model,
- non-ideal binary mixtures of n-heptane and ethanol, to test the phase equilibrium equations for non-ideal mixtures, and
- the two multicomponent-fuels Jet A-1 and HEFA to evaluate the accuracy of the CTM droplet evaporation models.

The discussion of the validation results emphasizes the importance of the intended user: modeler, analyst, and decision maker. Global metrics with maximum error and position of the maximum error were inferred. These metrics were shown to be in the range of 3% and 8% for all fuels, and SRQs tested. The results are consistent except for the binary mixture h(0.8)/d(0.2), where larger errors can be seen. These were explained by the pre-vaporization prior to the experimental domain causing errors in the initial composition of the spray. The position of the maximum errors for mean diameter and velocity predictions were found to be at the end of the spray evaporation. It is on the one hand due to large measurement uncertainties in this region and on the other hand due to inaccuracies in the flow field predictions. For the spray volume flow evaporation rate, maximum errors were identified at the beginning of the spray evaporation. Possible reasons are model form uncertainties or uncertainties due to droplet injection temperature estimations.

In the local metric, the mean diameter and velocity evolution were compared with experimental data. The prediction of local quantities is of importance for local effects like ignition, flame propagation, and hot spots. The evaluation showed that for each fuel tested, up to $z = 100$ mm the metrics are around zero. Stronger differences arise downstream, up to an underprediction resulting in differences of $20 \mu\text{m}$ and 0.2 m/s . In the comparison of the CTM model form uncertainties with single component model form uncertainties, the CTM metrics are positioned in-between the values of the single component fuels. This indicates a limited additional model form uncertainty due to the CTM extensions. It can be concluded that the major parts of the model form uncertainty are already present in the formulation of the discrete component model or is due to uncertainties in the input parameters.

7 Summary

The usage of alternative aviation fuels comes along with changes in fuel composition and related properties. These can affect the complex processes in combustion chambers to the positive and negative. Since failures come with a high price, enormous effort in the development of combustion chambers and fuels is put in safety-related issues. The design of such risk-related applications comes with high costs. The numerical simulation could be a beneficial tool to support the robust design by methods of virtual prototyping. Detailed and computationally efficient models as CTM for the fuel evaporation could be part of such a numerical simulation model. Systematic quantitative accuracy assessments of models describing the evaporation of actual and future fuels are fundamentally required to support the use of these models for risk-related applications.

Up to now, validation activities have been performed mainly by comparing numerical simulation results with experimental data from suspended droplet experiments but without knowing the fuel composition used. These tests successfully proofed the functionality of the concepts, but due to substantial intrusive effects of the droplet suspension and the high number of unknowns, the validations are limited to qualitative statements. For risk-related applications, new standards and methods have been developed to infer quantitative metrics and characterize the effect of uncertainties on simulation results. In this study, systematic studies have been performed to assess the accuracy of evaporation models for existing and potential alternative aviation fuels.

To understand the origin of differences between simulation results and experimental data, the uncertainties present in the model form of different relevant evaporation models are discussed. Model form uncertainties are due to assumptions and simplifications made during the model formulation process. Listed in rising complexity, the models tested in this study were: single component fuel models, discrete component models for ideal and non-ideal mixtures, and Continuous Thermodynamics Models (CTM). Models with higher complexity are based on models of low complexity and thus include their model form uncertainties.

The data delivered in this work enables testing different features of the evaporation model by providing data of the evaporation of different fuels with rising complexity: from a single component, binary mixtures, non-ideal mixtures, up to real multicomponent-fuels. The developed fuel validation domain is based on a review of the evolution jet fuel processing technology to determine the main features of actual and future aviation fuels. As shown, alternative aviation fuels consist of hydrocarbon components from different fuel families. The

7 Summary

number of components varies from a single component (like farnesane) to multicomponent fuels with several hundreds of components like Jet A-1 or HEFA.

An experimental system has been built to investigate in a non-intrusive way the evaporation of the different sprays under well-controlled conditions and obtain experimental data for the model validation. The Generalized Scattering Imaging (GSI), a robust measurement technique insensitive to changes in the fuel properties, has been applied. Boundary conditions and injection conditions of the spray are characterized in detail to be able to setup accurate simulations. The cold flow velocity field and hot flow temperature field are used for the validation of the flow field simulations. The spray position, droplet diameters, and velocities are inferred to determine the Systems Response Quantities (SRQ) for the validation of spray evaporation models: evaporated volume flow rate, diameter, and velocity distribution (characterized by the arithmetic mean and RMS of the mean.)

A systematic study with n-decane as a benchmark was performed to assess the capabilities and limitations of the validation approach. The details of the conceptualization of the validation domain are discussed showing the implications on quality of the simulation results. The simulation input parameters were identified, and procedures for the determination were shown. Whenever possible, experimental data were used to determine the parameters, otherwise applicable numerical simulations were used for the parameter estimation. For the validation studies, this procedure has been applied without modifications to the other fuels. To infer the validation metrics, first predictions of the fuels of the validation domain have been performed independently from experimental results. The simulation results are compared with experimental data to infer the quantitative metric for selected SRQs.

Different uncertainties in the spray simulation input uncertainties are identified and characterized. Series of computations have been performed sampling the model input domain with Latin Hypercube Sampling. For the interpretation of the non-deterministic simulation results, the concept of precision as a measure of the variability in the SRQ was introduced. With regard to validation studies, the precision shows the capability of the validation approach to distinguish between two simulation result computations. Additionally, it quantifies the effect of input uncertainties on the SRQ, which is vital for the interpretation of the validation metric. A validation metric might indicate very accurate models as no difference between simulation results and experimental data are shown. However, this might just be due to low precision. A low precision means that SRQs resulting from the non-deterministic computation have a high variability/uncertainty at each given position. Only due to the wide range of SRQs at a given position, simulation results cover the experimental data.

Different validation metrics have been inferred: global metrics, local metrics, and maximum deviation for spray evaporation volume rate, mean diameter evolution, and mean

velocity evolution of the spray. This information is prepared for and arranged for different groups of model users: modelers, which are concerned with the model development; analysts and designers, who need the models to design and analyze systems; and finally decision-makers, who are facing the task of simulation-informed decision making. The adequacy judgment of the models is part of the tasks of the user of the model. The validation metrics for the models tested in this study are provided in detail so that decision-makers can decide about the appropriateness of the models for the intended use.

When comparing the metric for the different models, similar metrics can be inferred for each class of models. These metrics have been shown to be in the range of 3% and 8% for all fuels, and SRQs tested. The results are consistent except for the binary mixture h(0.8)/d(0.2). Larger errors can be seen, which are explained by the pre-vaporization prior to the experimental domain and causing errors in the initial composition of the spray. The best metrics can be reported for a single component and non-ideal mixtures. In the comparison metrics of the CTM with the metrics of single component fuels, the CTM metrics are positioned in-between the values of the single component fuels. This indicates a limited additional model form uncertainty due to the CTM extensions. It can be concluded that major parts of the model form uncertainty is already present in the formulation of the discrete component model or is due to uncertainties in the input parameters.

For the evaluation of accuracy in predicting local effects, the mean diameter prediction is analyzed at each measurement position. For the first half of the spray evaporation, until $z = 100$ mm, the metrics display that the difference between simulation results and experimental data is around zero. Downstream close to the spray end, differences up to $20 \mu\text{m}$ can be identified indicating an underprediction of the models. It has to be pointed out that at this position the measurement uncertainties become dominating. Additionally, inaccuracies in the flow field predictions add to the uncertainty of the spray prediction. For an identification of a possible origin of the deviations in the model form uncertainty, the precision of the validation approach must be increased by inferring detailed flow field characteristics during the evaporation process.

7.1 Outlook

7.1.1 General

Validation is an ongoing activity. As described in this work, to set up a validation study requires a multidisciplinary approach. Firstly, an understanding of the potential uses of the model is required to set up the validation experiment and the validation metrics. Secondly, the definition of the boundary and initial conditions and the degree of detail that are needed, requires a strong interaction between the experimenter and the analyst performing the computations. This interaction can be simplified by using the concept of precision characterizing the validation approach. The precision quantifies the difficulty in defining the origin of model form

uncertainties. In other words, it is a metric to show the difficulty in understanding if a difference between experiment and simulation results is due to a model form uncertainty or it is an effect of input uncertainties (boundary conditions, injection uncertainties). It thus becomes manageable for all stakeholders. Furthermore, it shows the strong interdependence between numerical simulation and the experimenter directly. In an ideal case for a systematic evaluation of the model adequacy for the intended application, experienced decision makers define the required precision and accuracy margins before performing the validation studies. Collaborations are required to identify most relevant input parameter by numerical simulation studies and to optimize the validation experiment by inferring the most sensitive input parameters in detail.

Uncertainty quantification has proven to be very useful in supporting the evaluation of the validation approach and the reliability of the validation metric. Different methods to propagate uncertainties through the models exist. However, these methods lack of validation themselves. Particular designed experiments for the accuracy assessment of uncertainty propagation methods are required with well-characterized variations in model inputs.

To reduce uncertainties in the extrapolation of the inferred model metric to the application domain, systematic validation studies of droplet evaporation in regimes of higher pressure and velocities closer to the thermodynamical operational conditions in gas turbine combustion chambers should be performed. Furthermore, to strengthen the validation results and the comparison between the different evaporation models, repeated studies of fuel evaporation would support the statistics for validation metric results. This is even more important for metrics concerning the prediction of high sensitive local quantities like gas phase composition.

7.1.2 Validation and Uncertainty Quantification for Reacting Multiphase Flow Models

To build the predictive capabilities for simulating the combustion performance of alternative fuels with high reliability, verification, validation and uncertainty quantification studies for models describing reacting multiphase flows have to be performed. Figure 7.1 gives an overview of the phenomena and interactions in a reacting multiphase flow. The left-hand side can be seen as a representation of a reacting gas flow. When adding the multiphase flows, on the right-hand side, the complexity is greatly enhanced by a high number of interactions between the models describing the different phenomena. The high interdependence between the models can be exemplified by the propagation of model form errors in the evaporation models to uncertainties in the local species mixture rates, which have a high influence on combustion consequently. Vice versa uncertainties in the chemical reaction rates significantly influence the gas phase temperature and composition and thus the evaporation process.

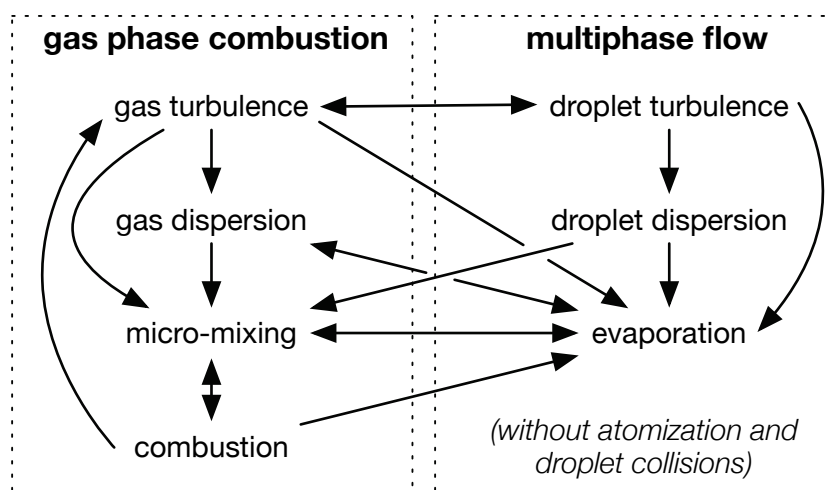


Figure 7.1: Phenomena and interactions in reacting multiphase flows, adopted from Jenny, Roekaerts, and Beishuizen (2012).

Different system response quantities can be used for validating reacting multiphase flows. These depend strongly on the phenomena of interest, like soot or emissions characteristics at the combustion chamber exit or the combustor fuel/air ratio leading to lean blow out. Prior to this, the prediction of the local species mixture fraction, as an essential linking element between the different multiphase flow models and combustion models, still requires extensive validation (Jenny, Roekaerts, and Beishuizen 2012). However, as discussed in the overview about existing validation experiments for reaction multiphase flows in Jenny, Roekaerts, and Beishuizen (2012), the characterization of gas phase composition in multiphase flows is difficult and often missing.

While high numbers of validation activities exist for reacting multiphase flows, uncertainty quantification of reacting multiphase flow simulations have not been performed to the best of the authors' knowledge. However, especially uncertainties in reaction rates are still remarkably high and often prevent the chemical reaction models from being predictive (Wang and Sheen 2015). The high computational load of combustion computations impedes with traditional methods for uncertainty quantification, which require hundreds to thousands of computations. This approach is only feasible for simple combustion problems, like homogeneous reactors and one-dimensional laminar flames. For more complex cases, strategies to minimize the number of runs are required. To compute the effect of uncertainties in chemical reaction rates on LES computations of the Sandia D flame, Mueller et al. (2013) took advantage of the steady flamelet model. With a steady flamelet model, only three quantities are required to evolve the LES equations: density, molecular viscosity, and molecular diffusivity (Mueller, Iaccarino, and Pitsch 2013). First uncertainties in chemical reaction rates are propagated through the flamelet equations resulting in a stochastic equation of state. Then non-intrusive stochastic collocation (Le Maitre and Knio 2010) is used to propagate the uncertainty in density, requiring only a few LES runs (uncertainties in molecular viscosity and molecular diffusivity have been neglected in this study.) Uncertainties in quantities like temperature and species mass fraction were computed with random sampling during the LES

runs. Results showed that the uncertainties in the chemical reaction rates are large enough to explain the difference with respect to experimental data and underlined the need to infer and reduce the uncertainties in chemical reaction rates systematically.

In consequence, to move in the direction of reliable predictive simulations of reacting multiphase flows, progress in different fields is required:

- Advances in optical diagnostic techniques to enable the quantification of species mixture fraction of complex fuels in reacting multiphase flows.
- Development and testing of methods to reduce computational costs for uncertainty quantification in complex simulations.
- Development and testing of reaction mechanisms with systematic uncertainty quantification of reaction rates (Sheen et al. 2009; Wang and Sheen 2015).

8 Bibliography

- Abdel-Qader, Z., & Hallett, W. L. H. (2005). The role of liquid mixing in evaporation of complex multicomponent mixtures: modelling using continuous thermodynamics. *Chemical Engineering Science*, 60(6), 1629–1640. <http://doi.org/10.1016/j.ces.2004.10.015>
- Abianeh, O. S., & Chen, C. P. (2012). Multi-component turbulent droplet evaporation of kerosene fuel in hot gas environment (pp. 2012–0345). Presented at the 50th AIAA Aerospace Sciences Meeting including the New Horizons Forum and Aerospace Exposition. <http://doi.org/10.2514/6.2012-345>
- Abramzon, B., & Sirignano, W. A. (1988). Droplet vaporization model for spray combustion calculations. Presented at the AIAA 26th Aerospace Sciences Meeting, Reno, Nevada: American Institute of Aeronautics and Astronautics. <http://doi.org/10.2514/6.1988-636>
- Abramzon, B., & Sirignano, W. A. (1989). Droplet vaporization model for spray combustion calculations. *International Journal of Heat and Mass Transfer*, 32(9), 1605–1618.
- Adams, B. M., Ebeida, M. S., Eldred, M. S., Jakeman, J. D., Swiler, L. P., Bohnhoff, W. J., et al. (2013). Dakota, A Multilevel Parallel Object-Oriented Framework for Design Optimization, Parameter Estimation, Uncertainty Quantification, and Sensitivity Analysis Version 5.4 User's Manual (5 ed.) (pp. 1–333). Albuquerque, New Mexico.
- AIAA. (1998). Aiaa Guide for the Verification and Validation of Computational Fluid Dynamics Simulations. Amer Inst of Aeronautics .
- Aitani, A. M. (2004). Oil Refining and Products. In *Encyclopedia of Energy* (pp. 715–729). Elsevier. <http://doi.org/10.1016/B0-12-176480-X/00259-X>
- Albrecht, H. E., Damaschke, N., Borys, M., & Tropea, C. (2002). Laser Doppler and Phase Doppler Measurement Techniques. Springer.
- Allouche, Y., Fabre, C., Salvi, O., Caillard, B., Braun-Unkhoff, M., Le Clercq, P., et al. (2012). *Alfa-Bird Alternative Fuels and Biofuels for Aircraft Development* (pp. 1–33). EU-VRI. Retrieved from <http://www.alfabird.eu-vri.eu>
- Arias-Zugasti, M., & Rosner, D. E. (2003). Multicomponent fuel droplet vaporization and combustion using spectral theory for a continuous mixture. *Combustion and Flame*, 135(3), 271–284. [http://doi.org/10.1016/S0010-2180\(03\)00166-4](http://doi.org/10.1016/S0010-2180(03)00166-4)
- ASME. (2006). Guide for Verification and Validation in Computational Solid Mechanics (p. 36). New York, NY.
- ASME. (2009). *Standard for Verification and Validation in Computational Fluid Dynamics and Heat Transfer* (No. ASME V&V 20-2009) (p. 88). New York, NY: ASME International.

Bibliography

- ASTM. (2012). Standard Test Method for Distillation of Petroleum Products at Atmospheric Pressure (No. ASTM D86 - 12) (pp. 1–24).
- ASTM. (2013). Standard Test Method for Distillation of Heavy Hydrocarbon Mixtures (Vacuum Potstill Method) (No. ASTM D5236 - 13).
- ASTM International. (2013). *Standard Specification for Aviation Turbine Fuels* (No. D1655, 13 ed.). West Conshohocken, PA: ASTM International.
- ASTM International. (2014a). Standard Practice for Qualification and Approval of New Aviation Turbine Fuels and Fuel Additives (No. D4054, 14 ed.). West Conshohocken, PA: ASTM International.
- ASTM International. (2014b). *Standard Specification for Aviation Turbine Fuel Containing Synthesized Hydrocarbons* (No. D7566, 14 ed.). West Conshohocken, PA: ASTM International.
- Atthasit, A., Doué, N., Rosa, N. G., Biscos, Y., & Lavergne, G. (2005). Influence of droplet concentration on the dynamics and evaporation of a monodisperse stream of droplets in evaporation regime. *Advances in Combustion and Atmospheric Pollution, Torus Press, Russia*, 19–36.
- Bardon, M. F., & Rao, V. K. (1984). Calculation Of Gasoline Volatility. *Journal of the Institute of Energy*, 57(432), 343–348.
- Bardon, M. F., Gauthier, J. E. D., & Rao, V. K. (1990). Flame propagation through sprays of multi-component fuel. *Journal of the Institute of Energy*, 63(455), 53–60.
- Bartholdi, M., Salzman, G. C., Hiebert, R. D., & Kerker, M. (1980). Differential light scattering photometer for rapid analysis of single particles in flow. *Applied Optics*, 19(10), 1573–1581. <http://doi.org/10.1364/AO.19.001573>
- Bellan, J., & Selle, L. C. (2009). Large Eddy Simulation composition equations for single-phase and two-phase fully multicomponent flows. *31st International Symposium on Combustion*, 32 II, 2239–2246.
- Blakey, S., Novelli, P., Brington, S., Costes, P., Christensen, D., Sakintuna, B., et al. (2011). *SWAFEA: State of the Art for Alternative Fuels and Energy Carriers in Aviation* (No. D.2.1 v2) (pp. 1–317). European Commission.
- Bluemcke, E., Brandt, M., Eickhoff, H., & Hassa, C. (1991). Particle dispersion in highly swirling, turbulent flows. *IN: Symposium on Turbulent Shear Flows*, 1, 10–5.
- Bowman, J. R. (1949). Distillation of an Indefinite Number of Components. *Industrial & Engineering Chemistry*, 41(9), 2004–2007. <http://doi.org/10.1021/ie50477a039>
- Brandt, M., Rachner, M., & Schmitz, G. (1998). An Experimental and Numerical Study of Kerosine Spray Evaporation in a Premix Duct for Gas Turbine Combustors at High Pressure. *Combustion Science and Technology*, 138(1-6), 313–348. <http://doi.org/10.1080/00102209808952074>
- Bruno, T. J. (2006). Improvements in the Measurement of Distillation Curves. 1. A Composition-Explicit Approach †. *Industrial & Engineering Chemistry Research*, 45(12), 4371–4380. <http://doi.org/10.1021/ie051393j>

- Bruno, T. J., & Huber, M. L. (2010). Evaluation of the Physicochemical Authenticity of Aviation Kerosene Surrogate Mixtures. Part 2: Analysis and Prediction of Thermophysical Properties. *Energy & Fuels*, 24(8), 4277–4284. <http://doi.org/10.1021/ef1004978>
- Bruno, T. J., & Smith, B. L. (2006). Improvements in the Measurement of Distillation Curves. 2. Application to Aerospace/Aviation Fuels RP-1 and S-8 †. *Industrial & Engineering Chemistry Research*, 45(12), 4381–4388. <http://doi.org/10.1021/ie051394b>
- Bruno, T. J., & Smith, B. L. (2010). Evaluation of the Physicochemical Authenticity of Aviation Kerosene Surrogate Mixtures. Part 1: Analysis of Volatility with the Advanced Distillation Curve. *Energy & Fuels*, 24(8), 4266–4276. <http://doi.org/10.1021/ef100496j>
- Burger, M., Schmehl, R., Prommersberger, K., Schäfer, O., Koch, R., & Wittig, S. (2003). Droplet evaporation modeling by the distillation curve model: accounting for kerosene fuel and elevated pressures. *Fuel*, 46(23), 4403–4412. [http://doi.org/10.1016/S0017-9310\(03\)00286-2](http://doi.org/10.1016/S0017-9310(03)00286-2)
- Calabria, R., & Massoli, P. (2000). Experimental study of droplets in evaporating regime by 2D scattering analysis. Presented at the 10th International Symposium on Applications of laser techniques, Lisbon, Portugal.
- Calabria, R., & Massoli, P. (2004). Scattering imaging to measure size and velocity of small particles in dense particle systems (pp. 12–15). Presented at the 12th international symposium on applications of laser techniques to fluids mechanics, Lisbon, Portugal.
- Calabria, R., & Massoli, P. (2007). Generalised scattering imaging laser technique for 2-D characterization of non-isothermal sprays. *Experimental Thermal and Fluid Science*, 31(5), 445–451. <http://doi.org/10.1016/j.exptthermflusci.2006.04.013>
- Calabria, R., Casaburi, A., & Massoli, P. (2003). Improved GSI out-of-focus technique for application to dense sprays and PIV measurements (pp. 10–16). Presented at the 9th Int Conf on Liquid Atomization and Spray Systems-ICLASS 2003, Sorrento, Italy.
- Chin, J. S. (1994). Engineering calculation method for multi-component stagnant droplet evaporation with finite diffusivity (pp. 1–13). Presented at the International Gas Turbine and Aeroengine Congress and Exposition, Hague, Neth: Publ by ASME.
- Chiu, H. H. (2000). Advances and challenges in droplet and spray combustion. I. Toward a unified theory of droplet aerothermochemistry. *Progress in Energy and Combustion Science*, 26(4), 381–416.
- Cleveland, C. J., & Ayres, R. U. (2004). Appendix 1. Chronology of Energy-Related Developments. In C. J. Cleveland (Ed.), *Encyclopedia of Energy* (pp. 641–707). Elsevier. <http://doi.org/10.1016/B0-12-176480-X/00807-X>
- Clift, R. R., Grace, J. R. J. A., & Weber, M. E. J. A. (1978). Bubbles, drops, and particles. New York : Academic Press.
- Cotterman, R. L., Bender, R., & Prausnitz, J. M. (1985). Phase equilibria for mixtures containing very many components. Development and application of continuous thermodynamics for chemical process design. *Industrial & Engineering Chemistry Process Design and Development*, 24(1), 194–203.

Bibliography

- Crowe, C. T. (Ed.). (2005). *Multiphase flow handbook*. CRC Press.
- D'Alessio, J., Lazzaro, M., Massoli, P., & Moccia, V. (1998). Thermo-optical investigation of burning biomass pyrolysis oil droplets (Vol. 27, pp. 1915–1922). Presented at the 27th Symposium (International) on Combustion. [http://doi.org/10.1016/S0082-0784\(98\)80035-0](http://doi.org/10.1016/S0082-0784(98)80035-0)
- de Klerk, A. (2012). *Fischer-Tropsch Refining*. Weinheim, Germany: John Wiley & Sons. <http://doi.org/10.1002/9783527635603>
- Dehaeck, S., & van Beeck, J. P. A. J. (2007). Designing a maximum precision interferometric particle imaging set-up. *Experiments in Fluids*, 42(5), 767–781. <http://doi.org/10.1007/s00348-007-0286-2>
- DoD. (1994). DoD Directive No. 5000.59: Modeling and Simulation (M&S) Management. Retrieved from www.msco.mil
- Doué, N. (2005, November 10). Modélisation de l'évaporation de gouttes multi-composants. (G. Lavergne, Ed.) *L'école nationale supérieure de l'aéronautique et de l'espace*. L'école nationale supérieure de l'aéronautique et de l'espace.
- Doué, N., Le Clercq, P., & Aigner, M. (2006). Validation Of A Multicomponent-Fuel Droplet Evaporation Modelbased On Continuous Thermodynamics (pp. 1–7). Presented at the ICLASS-2006, Kyoto, Japan.
- Doué, N., Le Clercq, P., & Aigner, M. (2007). A New Multicomponent-Fuel Droplet Vaporization Model Based on Continuous Thermodynamics Theory Using Fourier Series. Presented at the THIRD EUROPEAN COMBUSTION MEETING ECM 2007, Chania, Crete.
- Edmister, W. C. (1955). Improved integral technique for petroleum distillation calculations. *Industrial & Engineering Chemistry*, 47(9), 1685–1690.
- Edwards, T. (2003). Liquid fuels and propellants for aerospace propulsion: 1903-2003. *Journal of Propulsion and Power*, 19(6), 1089–1107.
- Edwards, T. (2007). Advancements in Gas Turbine Fuels From 1943 to 2005. *Journal of Engineering for Gas Turbines and Power*, 129(1), 13. <http://doi.org/10.1115/1.2364007>
- Edwards, T., Moses, C. A., & Dryer, F. L. (2010). Evaluation of Combustion Performance of Alternative Aviation Fuels - Panel Discussion (pp. 1–21). Presented at the 46th AIAA/ASME/SAE/ASEE Joint Propulsion Conference & Exhibit, Nashville, TN.
- Elwardany, A. E., & Sazhin, S. S. (2012). A quasi-discrete model for droplet heating and evaporation: Application to Diesel and gasoline fuels. *Fuel*, 97(C), 685–694. <http://doi.org/10.1016/j.fuel.2012.01.068>
- Elwardany, A. E., Sazhin, S. S., & Farooq, A. (2013). Modelling of heating and evaporation of gasoline fuel droplets: A comparative analysis of approximations. *Fuel*, 111(C), 643–647. <http://doi.org/10.1016/j.fuel.2013.03.030>
- Frenkel, M., Chirico, R. D., Diky, V., Muzny, C. D., Lemmon, E. W., Yan, X., & Dong, Q. (2005). NIST standard reference database 103a, NIST ThermoData engine, version 2.1; standard reference data. Gaithersburg, MD: National Institute of Standards and Technology.

- Frössling, N. (1938). Über die Verdunstung fallender Tropfen. *Gerlands Beitr. Geophys.*, 170–216.
- Glantschnig, W. J., & Chen, S.-H. (1981). Light scattering from water droplets in the geometrical optics approximation. *Applied Optics*, 20(14), 2499. <http://doi.org/10.1364/AO.20.002499>
- Glover, A. R., Skippon, S. M., & Boyle, R. D. (1995). Interferometric laser imaging for droplet sizing: a method for droplet-size measurement in sparse spray systems. *Applied Optics*, 34(3), 8409. <http://doi.org/10.1364/AO.34.008409>
- Godsave, G. A. E. (1953). Studies of the combustion of drops in a fuel spray—the burning of single drops of fuel. *Multiple Values Selected*, 4(1), 818–830.
- Goos, E., Burcat, A., & Ruscic, B. (n.d.). Extended Third Millennium Ideal Gas and Condensed Phase Thermochemical Database for Combustion with updates from Active Thermochemical Tables. Elke Goos. Retrieved from <http://burcat.technion.ac.il/dir>
- Gökalp, I., Chauveau, C., Berrekam, H., & Ramos-Arroyo, N. A. (1994). Vaporization of Miscible Binary Fuel Droplets Under Laminar and Turbulent Convective Conditions. *Atomization and Sprays*, 4, 661–676.
- Great Britain Ministry of Defence. (2008). Ministry of Defence Defence Standard 91/91. GLASGOW, UK: Defence Equipment and Support UK Defence Standardization. Retrieved from <http://www.dstan.mod.uk>
- Gupta, M. L., Roquemore, M., & Edwards, T. (2014). National Jet Fuels Combustion Program. Presented at the 7th Annual Fuel and Combustion Research Review, Boulder, Colorado, USA.
- Hallett, W. L. H. (2000). A simple model for the vaporization of droplets with large numbers of components. *Combustion and Flame*, 121(1), 334–344.
- Hallett, W. L. H., & Beauchamp-Kiss, S. (2010). Evaporation of single droplets of ethanol–fuel oil mixtures. *Fuel*, 89(9), 2496–2504. <http://doi.org/10.1016/j.fuel.2010.03.007>
- Hallett, W. L. H., & Clark, N. A. (2006). A model for the evaporation of biomass pyrolysis oil droplets. *Fuel*, 85(4), 532–544. <http://doi.org/10.1016/j.fuel.2005.08.006>
- Hallett, W. L. H., & Legault, N. V. (2011). Modelling biodiesel droplet evaporation using continuous thermodynamics. *Fuel*, 90(3), 1221–1228. <http://doi.org/10.1016/j.fuel.2010.11.035>
- Harstad, K. G., & Bellan, J. (2004a). Modeling evaporation of Jet A, JP-7, and RP-1 drops at 1 to 15 bars. *Combustion and Flame*, 137(1-2), 163–177. <http://doi.org/10.1016/j.combustflame.2004.01.012>
- Harstad, K. G., & Bellan, J. (2004b). Modeling of multicomponent homogeneous nucleation using continuous thermodynamics. *Combustion and Flame*, 139(3), 252–262.
- Harstad, K. G., Bellan, J., & Le Clercq, P. (2003a). Statistical Model of Multicomponent-Fuel Drop Evaporation for Many-Drop Flow Simulations. *AIAA Journal*, 41, 1858–1874. <http://doi.org/10.2514/2.1894>

- Harstad, K. G., Le Clercq, P., & Bellan, J. (2003b). A robust statistical model for the evaporation of multicomponent-fuel drops containing a multitude of chemical species (pp. 1–1). Presented at the 41st Aerospace Sciences Meeting and Exhibit, Reno, Nevada.
- Hesselbacher, K. H., Anders, K., & Frohn, A. (1991). Experimental investigation of Gaussian beam effects on the accuracy of a droplet sizing method. *Appl Opt*, *30*(33), 4930. <http://doi.org/10.1364/AO.30.004930>
- Höfler, C. (2013). Entwicklung Eines Smoothed Particle Hydrodynamics (SPH) Codes Zur Numerischen Vorhersage Des Primärzerfalls an Brennstoffeinspritzdüsen. Edited by Hans-Jörg Bauer. Karlsruhe Institut für Technologie (KIT).
- Höök, M., & Aleklett, K. (2009). A review on coal-to-liquid fuels and its coal consumption. *International Journal of Energy Research*, *34*(10), 848–864. <http://doi.org/10.1002/er.1596>
- Hubbard, G. L., Denny, V. E., & Mills, A. F. (1975). Droplet evaporation: Effects of transients and variable properties. *International Journal of Heat and Mass Transfer*, *18*(9), 1003–1008. [http://doi.org/10.1016/0017-9310\(75\)90217-3](http://doi.org/10.1016/0017-9310(75)90217-3)
- IATA. (2012). *IATA 2012 Report on Alternative Fuels* (Vol. 7, pp. 1–54). Montreal, Quebec: International Air Transport Association.
- IPCC. (2007). Intergovernmental panel on climate change (IPCC), fourth assessment report.
- ISO Guide. (1995). Guide to the expression of uncertainty in measurement (GUM). Geneva, Switzerland: International Organization for Standardization.
- Jenny, P., Roekaerts, D., & Beishuizen, N. (2012). Modeling of turbulent dilute spray combustion. *Progress in Energy and Combustion Science*, *38*(6), 846–887. <http://doi.org/10.1016/j.pecs.2012.07.001>
- Johnson, J. M., & Hadaller, O. J. (2006). *World Fuel Sampling Program* (No. CRC Report No. 647) (pp. 1–138). ALPHARETTA, GA: COORDINATING RESEARCH COUNCIL, INC.
- Kadota, T., & Hiroyasu, H. (1976). Evaporation Of A Single Droplet At Elevated Pressures And Temperatures - 2. Theoretical Study. *Bull JSME*, *19*(138), 1515–1521.
- Katz, D. L., & Brown, G. G. (1933). Vapor Pressure and Vaporization of Petroleum Fractions. *Industrial & Engineering Chemistry*, *25*(12), 1373–1384. <http://doi.org/10.1021/ie50288a018>
- Kehlen, H., Rätzsch, M. T., & Bergmann, J. (1985). Continuous thermodynamics of multicomponent systems. *AIChE Journal*, *31*(7), 1136–1148.
- Kerker, M. (1969). *The Scattering of Light and Other Electromagnetic Radiation*. New York: Academic Press.
- Kick, T., Herbst, J., Kathrotia, T., Marquetand, J., Braun-Unkhoff, M., Naumann, C., & Riedel, U. (2012). An experimental and modeling study of burning velocities of possible future synthetic jet fuels. *Energy*, *43*(1), 111–123. <http://doi.org/10.1016/j.energy.2012.01.035>
- Knothe, G. (2012). *Comprehensive Renewable Energy*. *sciencedirect.com* (pp. 11–14). Elsevier. <http://doi.org/10.1016/B978-0-08-087872-0.00502-3>

- Kovarik, B. (1998). Henry Ford, Charles F. Kettering and the Fuel of the Future. *Automotive History Review*, 32, 7–27.
- König, G., Anders, K., & Frohn, A. (1986). A new light-scattering technique to measure the diameter of periodically generated moving droplets. *Fuel*, 17(2), 157–167. [http://doi.org/10.1016/0021-8502\(86\)90063-7](http://doi.org/10.1016/0021-8502(86)90063-7)
- Langtry, R. B., & Menter, F. R. (2005). Transition Modeling for General CFD Applications in Aeronautics. *AIAA Paper*.
- Laurent, C., Lavergne, G., & Villedieu, P. (2009). Continuous thermodynamics for droplet vaporization: Comparison between Gamma-PDF model and QMoM. *C. R. Mecanique*, 337(6-7), 449–457. <http://doi.org/10.1016/j.crme.2009.06.004>
- Laurent, C., Lavergne, G., & Villedieu, P. (2010). Quadrature method of moments for modeling multi-component spray vaporization. *International Journal of Multiphase Flow*, 36(1), 51–59. <http://doi.org/10.1016/j.ijmultiphaseflow.2009.08.005>
- Law, C. K. (1982). Recent advances in droplet vaporization and combustion. *Progress in Energy and Combustion Science*, 8(3), 171–201. [http://doi.org/doi:10.1016/0360-1285\(82\)90011-9](http://doi.org/doi:10.1016/0360-1285(82)90011-9)
- Law, C. K. (2011). Dryden Lecture: Fuel Options for Next Generation Chemical Propulsion (pp. 1–30). Presented at the 49th AIAA Aerospace Sciences Meeting, Orlando, Florida.
- Le Clercq, P., & Bellan, J. (2004a). Direct numerical simulation of a temporal mixing layer laden with multicomponent evaporating drops. Presented at the 42nd AIAA Aerospace Sciences Meeting and Exhibit, Reno, NV.
- Le Clercq, P., & Bellan, J. (2004b). Direct numerical simulation of a transitional temporal mixing layer laden with multicomponent-fuel evaporating drops using continuous thermodynamics. *Physics of Fluids*, 16(6), 1884–1907. <http://doi.org/10.1063/1.1688327>
- Le Clercq, P., & Bellan, J. (2005a). Direct numerical simulation of gaseous mixing layers laden with multicomponent-liquid drops: liquid-specific effects. *Journal of Fluid Mechanics*, 533. <http://doi.org/10.1017/S0022112005003940>
- Le Clercq, P., & Bellan, J. (2005b). Modeling of multicomponent-fuel drop-laden mixing layers having a multitude of species. *Proceedings of the Combustion Institute*, 30(2), 2011–2019. <http://doi.org/10.1016/j.proci.2004.07.023>
- Le Clercq, P., Di Domenico, M., Rachner, M., Ivanova, E., & Aigner, M. (2010). Impact of fischer-tropsch fuels on aero-engine combustion performance. Presented at the 48th AIAA Aerospace Sciences Meeting, Orlando, Florida.
- Le Clercq, P., Doué, N., Rachner, M., & Aigner, M. (2009). Validation of a multicomponent-fuel model for spray computations. Presented at the 47th AIAA Aerospace Sciences Meeting, Orlando, Florida.
- Le Maitre, O., & Knio, O. M. (2010). Spectral Methods for Uncertainty Quantification. Dordrecht: Springer Science & Business Media. <http://doi.org/10.1007/978-90-481-3520-2>
- Lefebvre, A. H., & Ballal, D. R. (2010). Gas Turbine Combustion: Alternative Fuels and Emissions. *CRC PressINC*. CRC PressINC.

- Lemmon, E. W., Huber, M. L., & Mc Linden, M. O. (2007). NIST standard reference database 23, NIST reference fluid thermodynamic and transport properties database (REFPROP), version 8.0; standard reference data. Gaithersburg, MD: National Institute of Standards and Technology.
- Lewis, C. (2011). SWAFEA: Technical feasibility and performance of biofuels in aviation - Aero engine analysis (No. D.3.2) (pp. 1–44). European Commission.
- Lippert, A. M., & Reitz, R. D. (1997). Modeling of Multicomponent Fuels Using Continuous Distributions with Application to Droplet Evaporation and Sprays. *Papersaerorg*, 972882. <http://doi.org/10.4271/972882>
- Lippert, A. M., Stanton, D. W., Rutland, C. J., Hallett, W. L. H., & Reitz, R. D. (2000). Multidimensional simulation of diesel engine cold start with advanced physical submodels. *International Journal of Engine Research*, 1(1), 1–27. <http://doi.org/10.1177/146808740000100101>
- Llamas, A., Al-Lal, A.-M., Hernandez, M., Lapuerta, M., & Canoira, L. (2012). Biokerosene from Babassu and Camelina Oils: Production and Properties of Their Blends with Fossil Kerosene. *Energy & Fuels*, 26(9), 5968–5976. <http://doi.org/10.1021/ef300927q>
- Lucier, P. (2010). *Scientists and Swindlers: Consulting on Coal and Oil in America, 1820–1890*. Johns Hopkins University Press.
- Maeda, M., Kawaguchi, T., & Hishida, K. (2000). Novel interferometric measurement of size and velocity distributions of spherical particles in fluid flows. *Meas Sci Technol*, 11(12), L13–L18. <http://doi.org/10.1088/0957-0233/11/12/101>
- Martin, M. J., Scavazze, K. J., Boyd, I. D., & Bernal, L. P. (2006). Design of a Low-Turbulence, Low-Pressure Wind-Tunnel for Micro-Aerodynamics. *Journal of Fluids Engineering*, 128(5), 1045. <http://doi.org/10.1115/1.2236128>
- Massoli, P. (1998). Rainbow refractometry applied to radially inhomogeneous spheres: the critical case of evaporating droplets. *Applied Optics*, 37(15), 3227–3235.
- Massoli, P., & Calabria, R. (1999). Sizing of droplets in reactive sprays by mie scattering imaging (pp. 1–6). Presented at the ILASS-Europe, Toulouse, France.
- Massoli, P., Beretta, F., & D'Alessio, A. (1990). Pyrolysis in the Liquid Phase Inside Single Droplets of Light Oil Studied with Laser Light Scattering Methods. *Combustion Science and Technology*, 72(4-6), 271–282. <http://doi.org/10.1080/00102209008951651>
- Massoli, P., Beretta, F., D'Alessio, A., & Lazzaro, M. (1993). Temperature and size of single transparent droplets by light scattering in the forward and rainbow regions. *Applied Optics*, 32, 3295–3301. <http://doi.org/10.1364/AO.32.003295>
- Maurice, L. Q., Lander, H., Edwards, T., & Harrison, W. E., III. (2001). Advanced aviation fuels: a look ahead via a historical perspective. *Fuel*, 80(5), 747–756. [http://doi.org/10.1016/S0016-2361\(00\)00142-3](http://doi.org/10.1016/S0016-2361(00)00142-3)
- Menter, F. R. (1994). Two-equation eddy-viscosity turbulence models for engineering applications. *AIAA Journal*, 32, 1598–1605. <http://doi.org/10.2514/3.12149>

- Miller, R. S., Harstad, K. G., & Bellan, J. (1998). Evaluation of equilibrium and non-equilibrium evaporation models for many-droplet gas-liquid flow simulations. *International Journal of Multiphase Flow*, 24(6), 1025–1055.
- Miranda, A. L. (2011, October). *Validation Of Multi-Component Evaporation Models For Alternative Fuels*. (B. Rauch & M. Aigner, Eds.). Universität Stuttgart, Stuttgart, Germany.
- Morin, C., Chauveau, C., & Gökalp, I. (2000). Droplet vaporisation characteristics of vegetable oil derived biofuels at high temperatures. *Experimental Thermal and Fluid Science*, 21, 41–50.
- Moses, C. A. (2007). Development of the protocol for acceptance of synthetic fuels under commercial specification (No. CRC Contract No. AV-2-04, Final Report) (pp. 1–40). Alpharetta, GA: Coordinating Research Council, Inc.
- Moses, C. A. (2008). *Comparison of Semi-Synthetic Jet Fuels* (No. CRC Project No. AV-2-04a). *Contract* (pp. 1–49). Coordinating Research Council, Inc.
- Moses, C. A. (2012). Jet fuel “aromatics effects” and ‘distillation slope’ research survey (No. CRC Report AV-10-09, Final Report) (pp. 1–21). Alpharetta: COORDINATING RESEARCH COUNCIL, INC.
- Moses, C. A., & Roets, P. N. J. (2009). Properties, Characteristics, and Combustion Performance of Sasol Fully Synthetic Jet Fuel. *Journal of Engineering for Gas Turbines and Power*, 131(4), 041502. <http://doi.org/10.1115/1.3028234>
- Mueller, M. E., Iaccarino, G., & Pitsch, H. (2013). Chemical kinetic uncertainty quantification for Large Eddy Simulation of turbulent nonpremixed combustion. *Proceedings of the Combustion Institute*, 34(1), 1299–1306. <http://doi.org/10.1016/j.proci.2012.07.054>
- Nomura, H., Ujiie, Y., Rath, H. J., Sato, J., & Kono, M. (1997). Experimental Study On High-Pressure Droplet Evaporation Using Microgravity Conditions. *Twenty-Sixth Symposium (International) on Combustion/the Combustion Institute*, 1267–1273.
- Oberkampf, W. L., & Roy, C. J. (2010). *Verification and Validation in Scientific Computing*. Cambridge University Press (1st ed.). Cambridge University Press.
- Oberkampf, W. L., & Trucano, T. G. (2008). Verification and validation benchmarks. *Benchmarking of CFD Codes for Application to Nuclear Reactor Safety*, 238(3), 716–743.
- Ochs, M. (1999, June). Verdunstung monodisperser, frei beweglicher Brennstoff-Tropfen in einer turbulenten Heissluftströmung. (L. Reh, Ed.)ETH Zürich. ETH Zürich, Zürich.
- Ochs, M., Gass, J., & Reh, L. (2001). Convective vaporization of freely moving fuel droplets in a hot air flow. Presented at the ILASS-Europe, Zurich.
- Pan, G., Shakal, J., Lai, W., Calabria, R., & Massoli, P. (2006). Spray Features Investigated by GSV: A New Planar Laser Technique. Presented at the 10th Int Conf on Liquid Atomization and Spray Systems-ICLASS 2006.
- Panão, M. R. O., & Moreira, A. L. N. (2008). A real-time assessment of measurement uncertainty in the experimental characterization of sprays. *Measurement Science and Technology*, 19(9), 095402. <http://doi.org/10.1088/0957-0233/19/9/095402>

Bibliography

- Pedersen, K. S., Fredenslund, A., & Thomassen, P. (1989). Properties of Oils and Natural Gases (Contributions in Petroleum Geology and Engineering) (v. 5). *Gulf Publishing Co.* Gulf Publishing Co.
- Pegden, C. D., Shannon, R. E., & Sadowski, R. P. (1995). Introduction to Simulation Using SIMAN.
- Poling, B. E., Prausnitz, J. M., & O'Connell, J. P. (2000). The Properties of Gases and Liquids (5 ed.). McGraw-Hill Professional.
- Ra, Y., & Reitz, R. D. (2005). The application of a multicomponent droplet vaporization model to gasoline direct injection engines. *International Journal of Engine Research*, 4(3), 193–218. <http://doi.org/10.1243/146808703322223388>
- Ra, Y., & Reitz, R. D. (2009). A vaporization model for discrete multi-component fuel sprays. *International Journal of Multiphase Flow*, 35(2), 101–117. <http://doi.org/10.1016/j.ijmultiphaseflow.2008.10.006>
- Rachner, M. (1998). *Die Stoffeigenschaften von Kerosin Jet A-1* (No. 98-01) (p. 119). Köln: DLR.
- Rachner, M. (2014). *SPRAYSIM Manual* (4 ed.). Köln, Germany.
- Rachner, M., Becker, J., Hassa, C., & Doerr, T. (2002). Modelling of the Atomization of a Plain Liquid Fuel Jet in Crossflow at Gas Turbine Conditions. *Aerospace Science and Technology*, 6, 495–506.
- Rachner, M., Brandt, M., Eickhoff, H., Hassa, C., Bräumer, A., Krämer, H., et al. (1996). A numerical and experimental study of fuel evaporation and mixing for lean premixed combustion at high pressure. *Twenty-Sixth Symposium (International) on Combustion/the Combustion Institute*, 26(2), 2741–2748.
- Ragucci, R., Cavaliere, A., & Massoli, P. (1990). Drop Sizing by Laser Light Scattering Exploiting Intensity Angular Oscillation in the mie regime. *Part Part Syst Charact*, 7(1-4), 221–225. <http://doi.org/10.1002/ppsc.19900070136>
- Rauch, B., Calabria, R., Chiariello, F., Le Clercq, P., Massoli, P., & Rachner, M. (2011). Accurate analysis of multicomponent fuel spray evaporation in turbulent flow. *Experiments in Fluids*, 52(4), 935–948. <http://doi.org/10.1007/s00348-011-1169-0>
- Rauch, B., Chiariello, F., Calabria, R., Le Clercq, P., & Massoli, P. (2010). Prediction of refractive index profiles within evaporating droplets (pp. 1–13). Presented at the 12th Workshop on Two-Phase Flow Predictions, Halle (Saale).
- Riazi, M. R. (2005). Characterization And Properties Of Petroleum Fractions. Astm International.
- Riazi, M. R., & Al-Sahhaf, T. A. (1996). Physical properties of heavy petroleum fractions and crude oils. *Fluid Phase Equilibria*, 117(1), 217–224.
- Roache, P. J. (2009). Fundamentals of Verification and Validation. Socorro, New Mexico, USA: hermosa publishers.

- Satyro, M. A., & Yarranton, H. (2009). Oil Characterization from Simulation of Experimental Distillation Data. *Energy & Fuels*, 23(8), 3960–3970. <http://doi.org/10.1021/ef9000242>
- Sazhin, S. S., Elwardany, A. E., Sazhina, E. M., & Heikal, M. R. (2011). A quasi-discrete model for heating and evaporation of complex multicomponent hydrocarbon fuel droplets. *International Journal of Heat and Mass Transfer*, 54(19-20), 4325–4332. <http://doi.org/10.1016/j.ijheatmasstransfer.2011.05.012>
- Sazhin, S. S., Qubeissi, Al, M., Kolodnytska, R., Elwardany, A. E., Nasiri, R., & Heikal, M. R. (2014a). Modelling of biodiesel fuel droplet heating and evaporation. *Fuel*, 115(C), 559–572. <http://doi.org/10.1016/j.fuel.2013.07.031>
- Sazhin, S. S., Qubeissi, Al, M., Nasiri, R., Gun'ko, V. M., Elwardany, A. E., Lemoine, F., et al. (2014b). A multi-dimensional quasi-discrete model for the analysis of Diesel fuel droplet heating and evaporation. *Fuel*, 129(C), 238–266. <http://doi.org/10.1016/j.fuel.2014.03.028>
- Selle, L. C., & Bellan, J. (2006). Direct numerical simulation of multicomponent-species transitional mixing layers (Vol. 3, pp. 1961–1985). Presented at the 44th AIAA Aerospace Sciences Meeting 2006, Reno, NV.
- Selle, L. C., & Bellan, J. (2007a). Characteristics of transitional multicomponent gaseous and drop-laden mixing layers from direct numerical simulation: Composition effects. *Physics of Fluids*, 19(6).
- Selle, L. C., & Bellan, J. (2007b). Evaluation of assumed-PDF methods in two-phase flows using direct numerical simulation. *31st International Symposium on Combustion*, 31 II, 2273–2281.
- Selle, L. C., & Bellan, J. (2007c). Scalar-dissipation modeling for passive and active scalars: A priori study using direct numerical simulation. *31st International Symposium on Combustion*, 31 I, 1665–1673.
- Selle, L. C., & Bellan, J. (2008). Modeling requirements for large eddy simulation of multi-component fuel flows. Presented at the 46th AIAA Aerospace Sciences Meeting and Exhibit, Reno, NV.
- Sheen, D. A., You, X., Wang, H., & Løvås, T. (2009). Spectral uncertainty quantification, propagation and optimization of a detailed kinetic model for ethylene combustion. *Proceedings of the Combustion Institute*, 32(1), 535–542. <http://doi.org/10.1016/j.proci.2008.05.042>
- Shringi, D., Dwyer, H. A., & Shaw, B. D. (2013). Computers & Fluids. *Computers and Fluids*, 77(C), 66–75. <http://doi.org/10.1016/j.compfluid.2013.02.005>
- Sirignano, W. A. (1983). Fuel droplet vaporization and spray combustion theory. *Progress in Energy and Combustion Science*, 9(4), 291–322. [http://doi.org/10.1016/0360-1285\(83\)90011-4](http://doi.org/10.1016/0360-1285(83)90011-4)
- Sirignano, W. A. (1999). Fluid Dynamics and Transport of Droplets and Sprays. *Cambridge University Press*. Cambridge University Press.
- Smith, B. L., & Bruno, T. J. (2007a). Improvements in the Measurement of Distillation Curves. 3. Application to Gasoline and Gasoline + Methanol Mixtures. *Industrial & Engineering Chemistry Research*, 46(1), 297–309. <http://doi.org/10.1021/ie060937u>

Bibliography

- Smith, B. L., & Bruno, T. J. (2007b). Improvements in the Measurement of Distillation Curves. 4. Application to the Aviation Turbine Fuel Jet-A. *Industrial & Engineering Chemistry Research*, 46(1), 310–320. <http://doi.org/10.1021/ie060938m>
- Spalding, D. B. (1953). The combustion of liquid fuels. *Fourth Symposium (International) on Combustion*, 4(1), 847–864.
- Stengele, Jörg Ferdinand. (1997). “Tropfenverdunstung in Hochdruckatmosphäre.” Edited by Sigmar Wittig. Universität Karlsruhe.
- Tamim, J. (1996, December). *A continuous thermodynamics model for multicomponent droplet vaporization*. (W. L. H. Hallett, Ed.). University of Ottawa, Ottawa, Canada.
- Tamim, J., & Hallett, W. L. H. (1995). A continuous thermodynamics model for multicomponent droplet vaporization. *Chemical Engineering Science*, 50(18), 2933–2942.
- Tanner, F. X. (2004). Development and Validation of a Cascade Atomization and Drop Breakup Model for High-Velocity Dense Sprays. *Atomization and Sprays*, 14, 211–242.
- Thacker, B. H., & Paez, T. L. (2013). A Simple Probabilistic Validation Metric for the Comparison of Uncertain Model and Test Results. Presented at the ASME 2013 Verification and Validation Symposium - V&V2013, Las Vegas, USA.
- Wahl, C. (2003). *EU FP5 GARD-CT-00075 final report*. Stuttgart, Germany.
- Wang, H., & Sheen, D. A. (2015). Combustion kinetic model uncertainty quantification, propagation and minimization. *Progress in Energy and Combustion Science*, 47(c), 1–31. <http://doi.org/10.1016/j.pecs.2014.10.002>
- Wilson, G. R., III, Edwards, T., Corporan, E., & Freerks, R. L. (2013). Certification of Alternative Aviation Fuels and Blend Components. *Energy & Fuels*, 27(2), 962–966. <http://doi.org/10.1021/ef301888b>
- Yang, J.-R., & Wong, S.-C. (2001). On the discrepancies between theoretical and experimental results for microgravity droplet evaporation. *International Journal of Heat and Mass Transfer*, 44, 4433–4443.
- Yang, S., & Reitz, R. D. (2009). Integration Of A Continuous Multi-Component Fuel Evaporation Model With An Improved G-Equation Combustion And Detailed Chemical Kinetics Model With Application To Gdi Engines (0 ed.). papers.sae.org (pp. 2009–01–0722). Warrendale, PA: SAE International.
- Yang, S., & Reitz, R. D. (2010). A Continuous Multicomponent Fuel Flame Propagation and Chemical Kinetics Model. *Journal of Engineering for Gas Turbines and Power*, 132(7), 072802. <http://doi.org/10.1115/1.4000267>
- Yang, S., Ra, Y., Reitz, R. D., VanDerWege, B., & Yi, J. (2010). Development Of A Realistic Multicomponent Fuel Evaporation Model. *Atomization and Sprays*, 20(11), 965–981. <http://doi.org/10.1615/AtomizSpr.v20.i11.40>

- Zhang, L., & Kong, S.-C. (2009). Modeling of multi-component fuel vaporization and combustion for gasoline and diesel spray. *Chemical Engineering Science*, 64(16), 3688–3696. <http://doi.org/10.1016/j.ces.2009.05.013>
- Zhang, L., & Kong, S.-C. (2010). Vaporization modeling of petroleum biofuel drops using a hybrid multi-component approach. *Combustion and Flame*, 157(11), 2165–2174. <http://doi.org/10.1016/j.combustflame.2010.05.011>
- Zhang, L., & Kong, S.-C. (2011). High-pressure vaporization modeling of multi-component petroleum-biofuel mixtures under engine conditions. *Combustion and Flame*, 158(9), 1705–1717. <http://doi.org/10.1016/j.combustflame.2011.01.002>
- Zhang, L., & Kong, S.-C. (2012). Multicomponent vaporization modeling of bio-oil and its mixtures with other fuels. *Fuel*, 95(C), 471–480. <http://doi.org/10.1016/j.fuel.2011.12.009>
- Zhu, G. S., & Reitz, R. D. (2001). Engine Fuel Droplet High-Pressure Vaporization Modeling. *Journal of Engineering for Gas Turbines and Power*, 123(2), 412–418. <http://doi.org/10.1115/1.1361058>
- Zhu, G. S., & Reitz, R. D. (2002). A model for high-pressure vaporization of droplets of complex liquid mixtures using continuous thermodynamics. *International Journal of Heat and Mass Transfer*, 45(3), 495–507.
- Zschocke, A. (2013). Blending issues (pp. 1–24). Presented at the European Advanced Biofuels Flight path Initiative Meeting, Brussels.
- Zschocke, A., Scheuermann, S., & Ortner, J. (2015). *High Biofuel Blends in Aviation (HBBA)* (pp. 1–156). Retrieved from www.hbba.eu

A Validation of Single Component Fuel Property Models

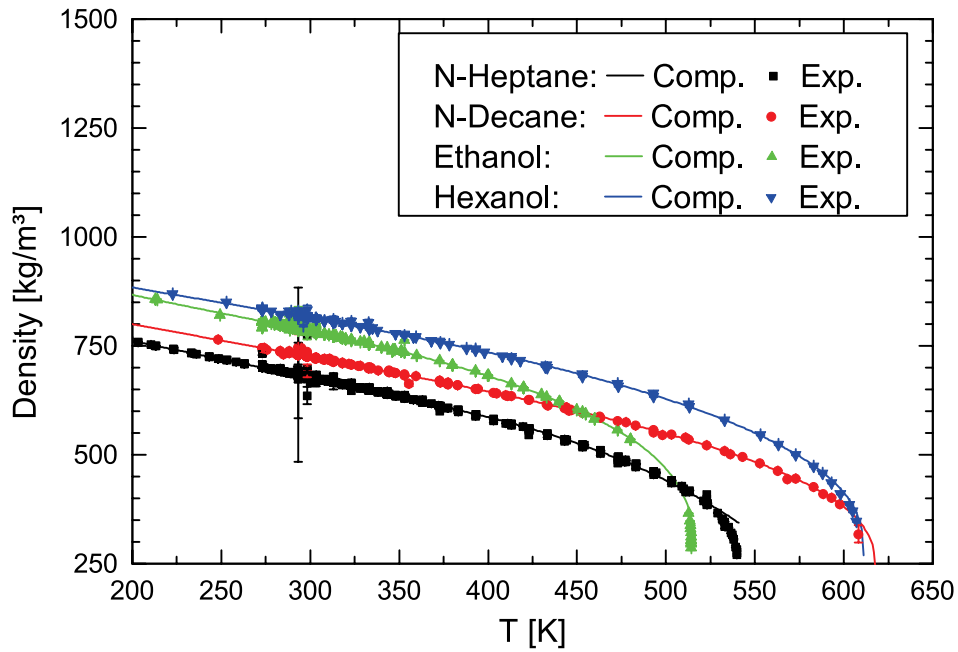


Figure A.1: Comparison of thermodynamic property models with experimental data for liquid density.

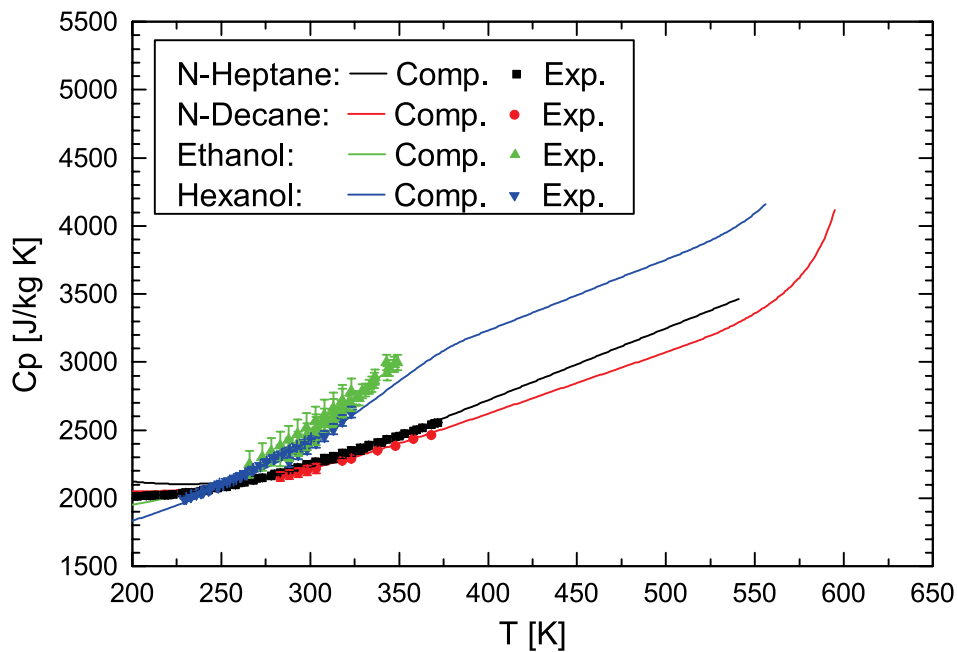


Figure A.2: Comparison of thermodynamic property models with experimental data for liquid heat capacity.

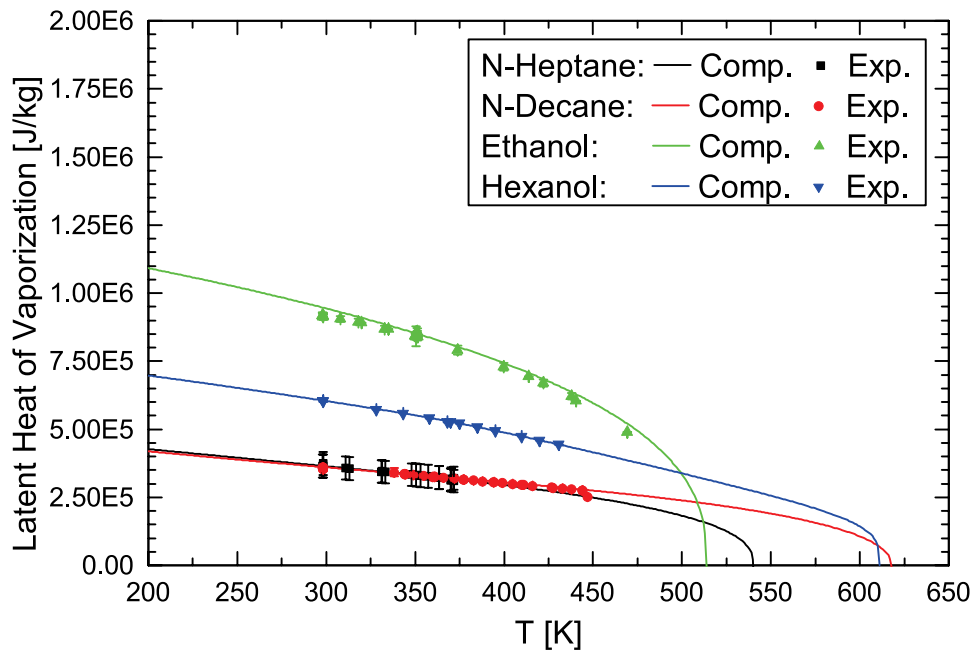


Figure A.3: Comparison of thermodynamic property models with experimental data for latent heat of vaporization.

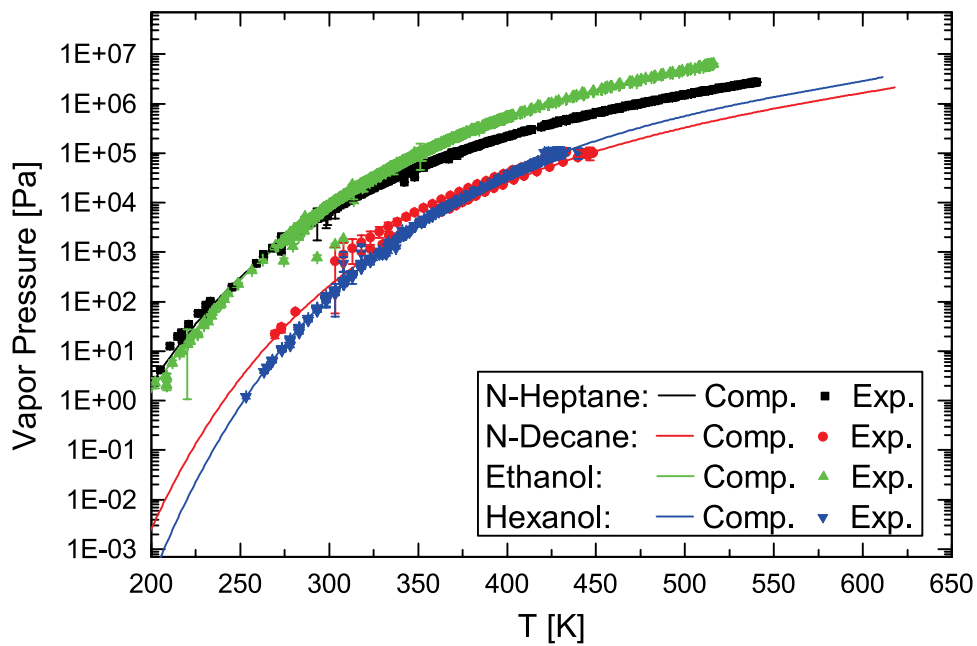


Figure A.4: Comparison of thermodynamic property models with experimental data for vapor pressure.

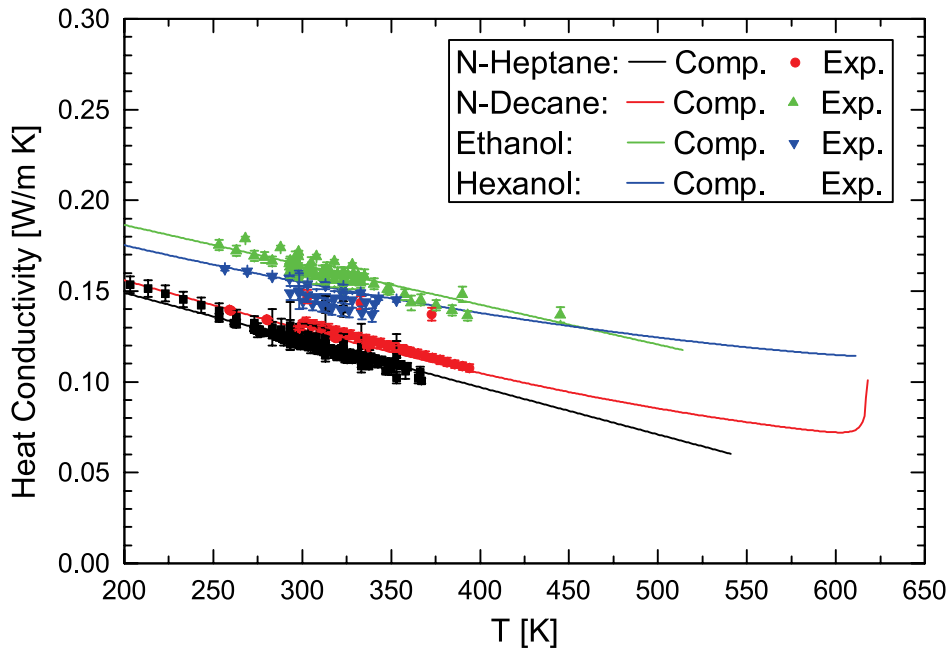


Figure A.5: Comparison of thermodynamic property models with experimental data for liquid heat conductivity.

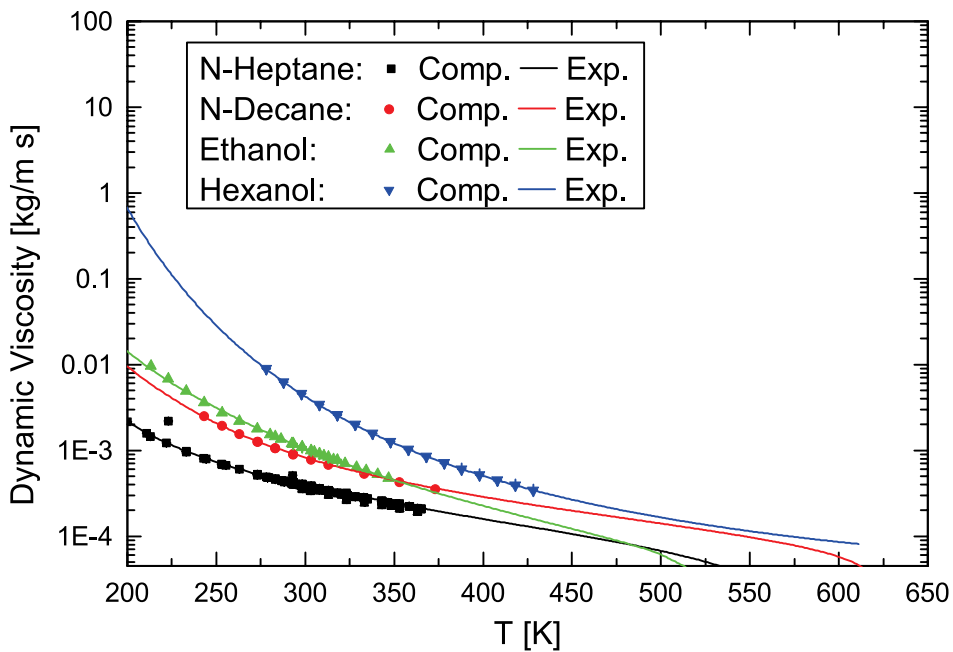


Figure A.6: Comparison of thermodynamic property models with experimental data for liquid dynamic viscosity.

B Boundary Conditions

B.1 Cold flow Carrier Jet Inflow Conditions

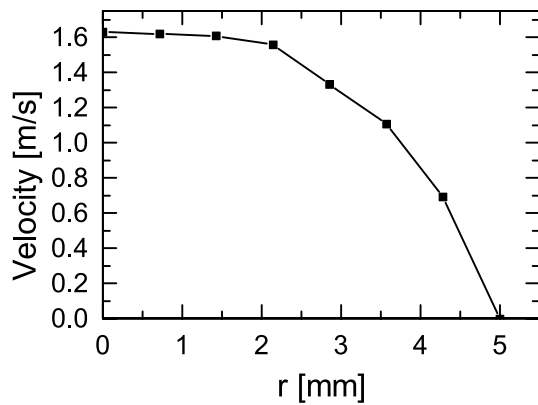


Figure B.1: Cold flow, measured carrier jet velocity profile.

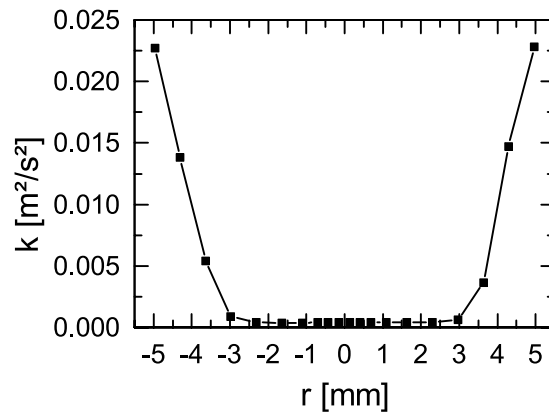


Figure B.2: Cold flow, measured carrier turbulence kinetic energy.

B.2 Hot Flow Carrier Jet Inflow Conditions

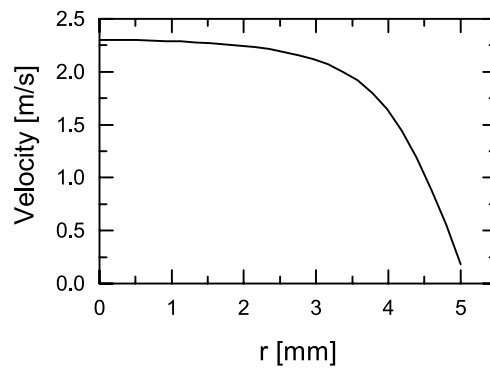


Figure B.3: Hot flow: velocity profile of the carrier jet, estimated by computations of the inlet nozzle system .

C Validation Results

C.1 Flow Field Validation

C.1.1 Cold Flow Velocity Field

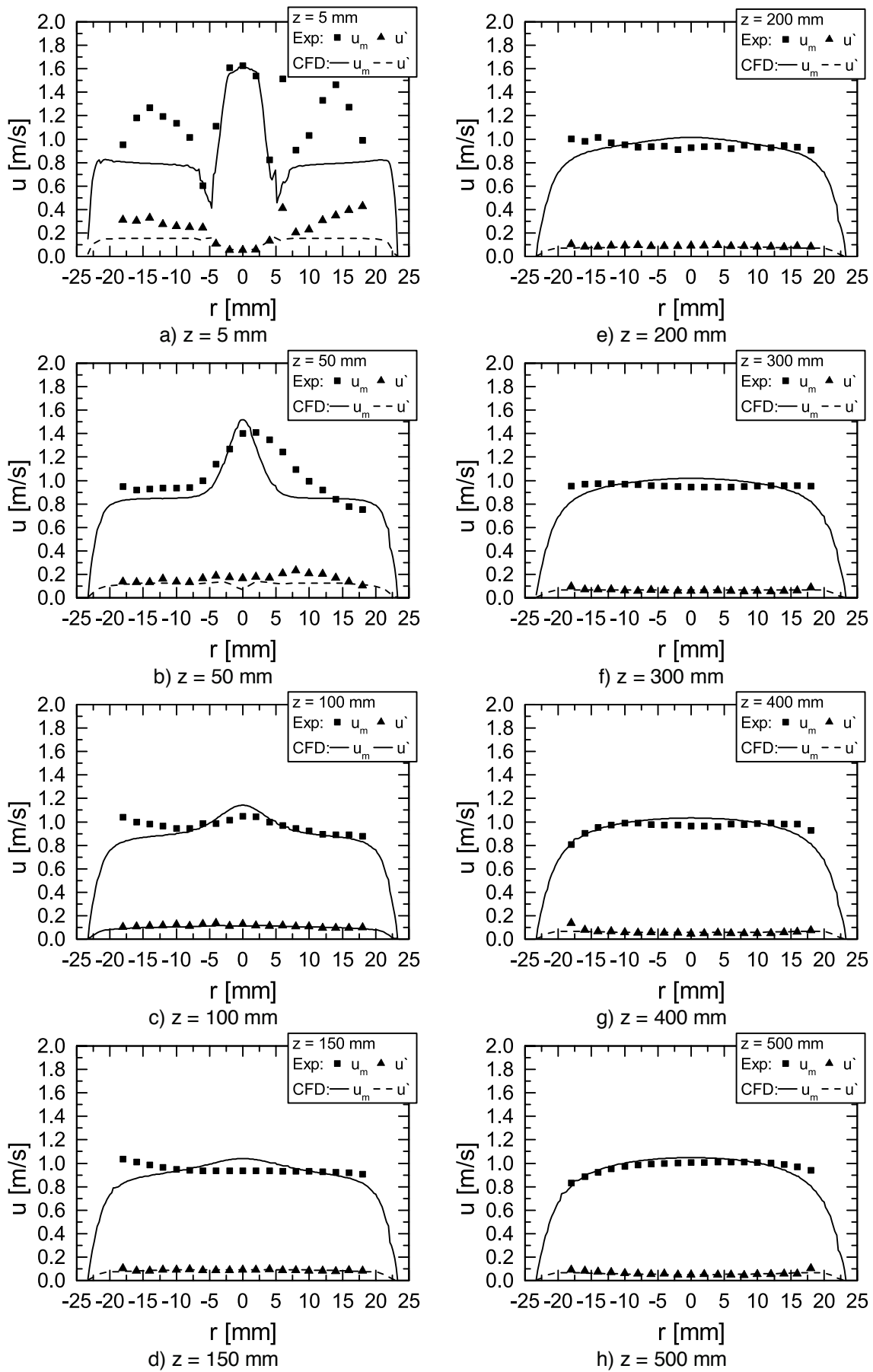


Figure C.1: Cross section velocity profiles: Comparison of CFD with measured data.

C.1.2 Hot Flow Temperature Field

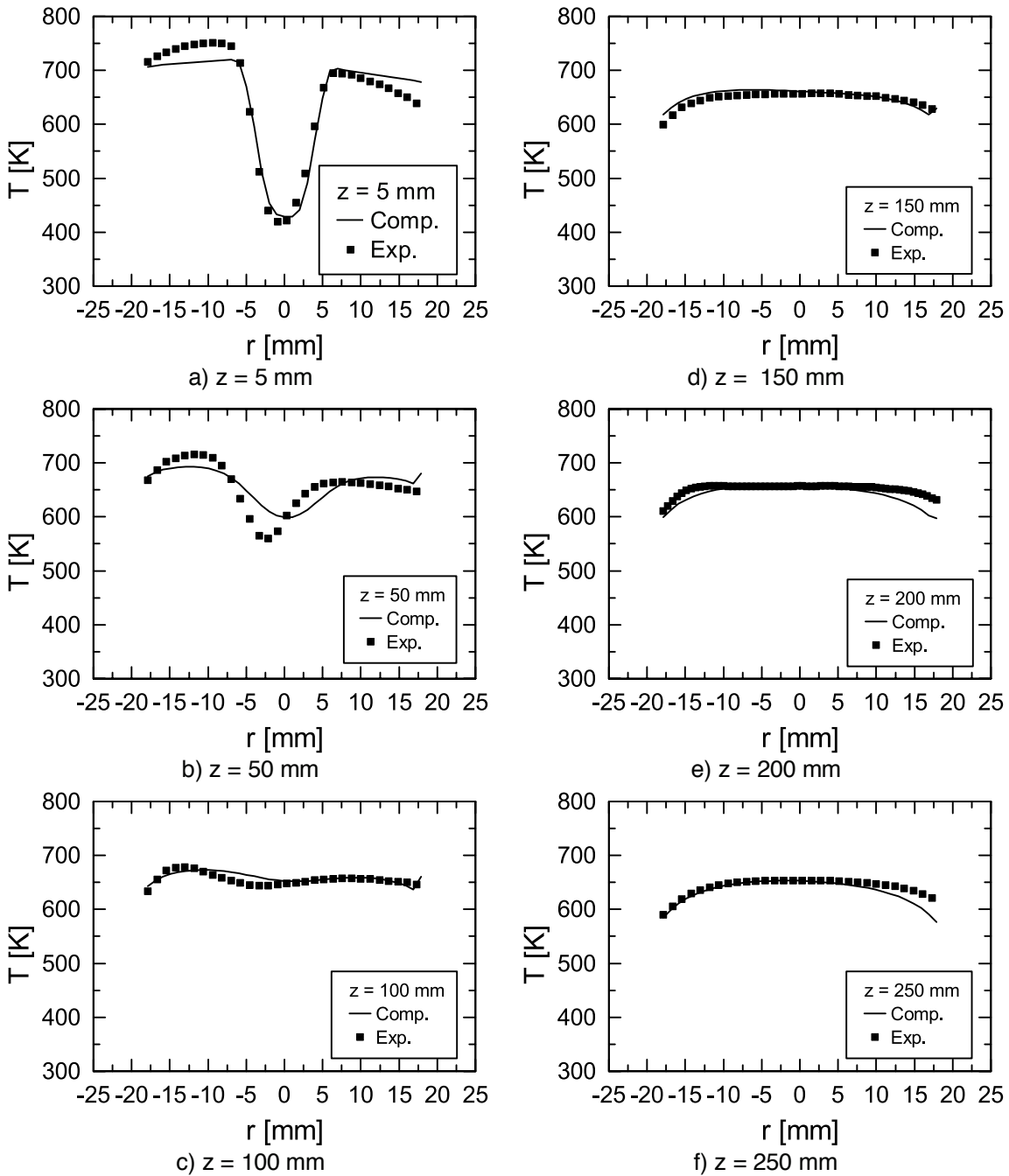


Figure C.2: Cross section velocity profiles: Comparison of CFD with measured data.

C.1.3 Heating Up Computations

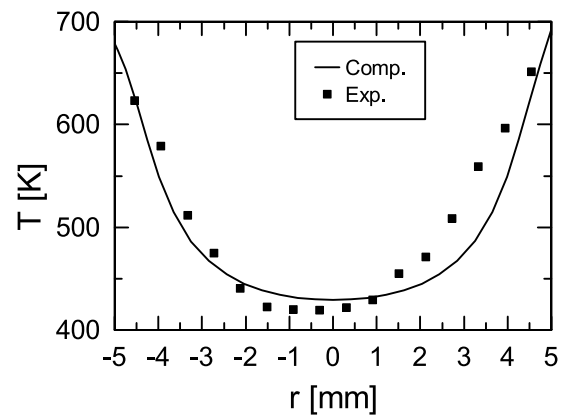


Figure C.3: Heating up simulation for carrier jet flow heating up computation, comparison with measured temperature profile at $z = 5$ mm.

C.2 Spray Validation Results

C.2.1 Single Component Fuels

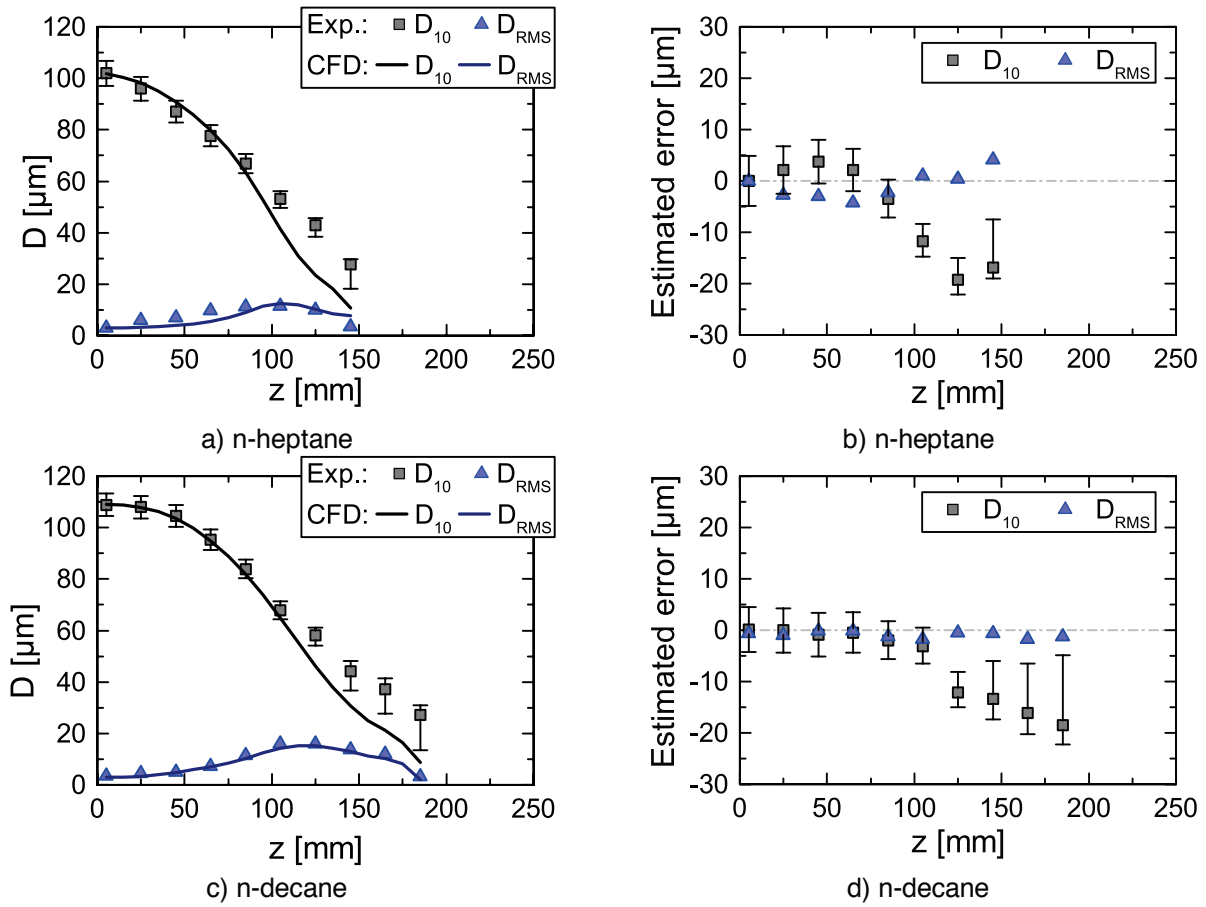
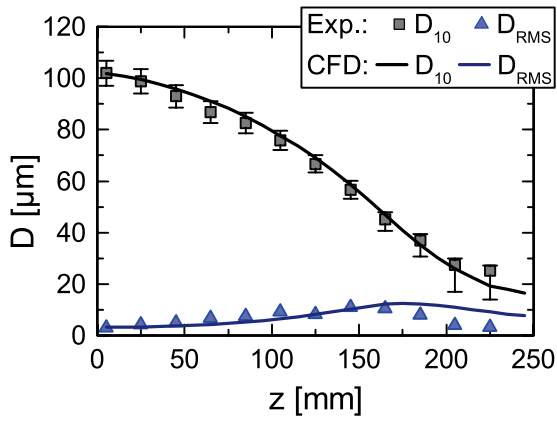
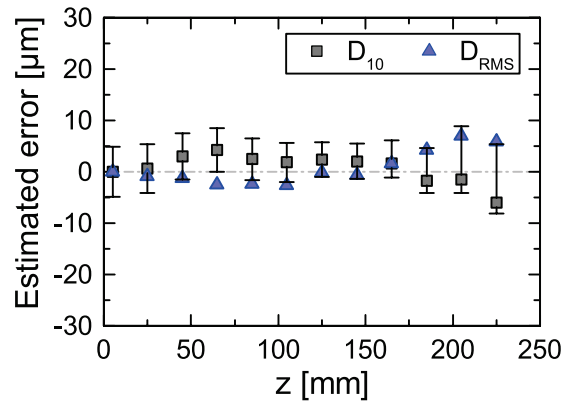


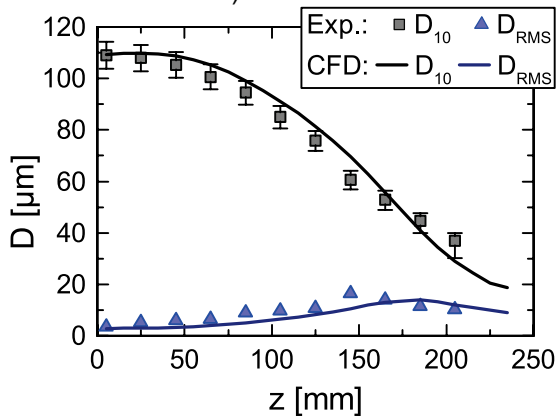
Figure C.4: Diameter validation for n-heptane and n-decane. Left column: comparison of computed with experimental data for diameter evolution. Right column: corresponding validation metrics.



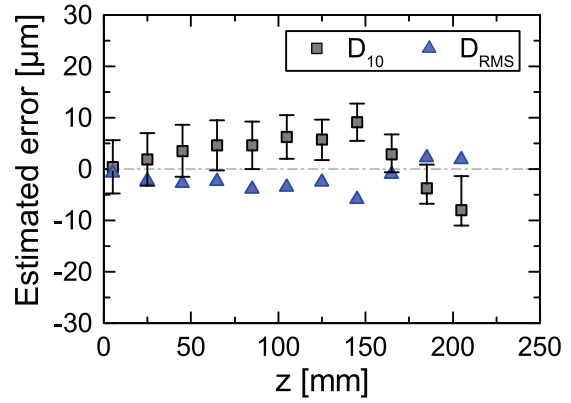
a) ethanol



a) ethanol

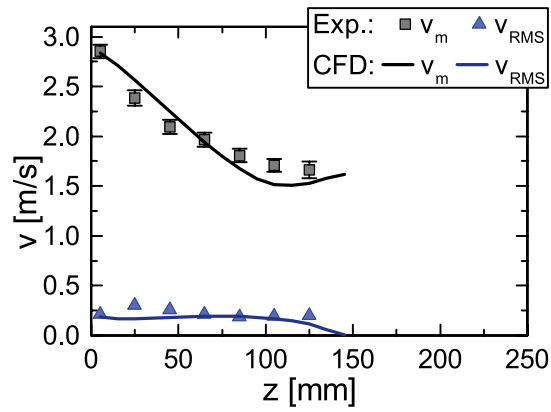


c) hexanol

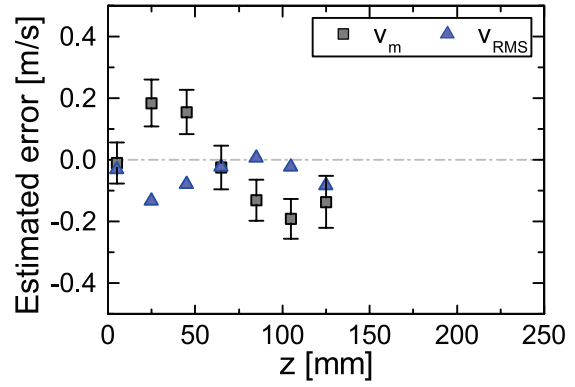


d) hexanol

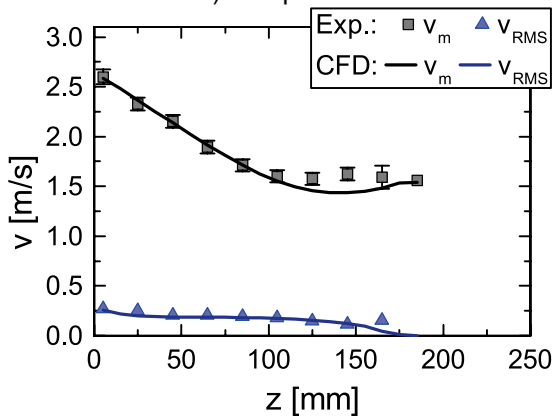
Figure C.5: Diameter validation for ethanol and hexanol. Left column: comparison of computed with experimental data for diameter evolution. Right column: corresponding validation metrics.



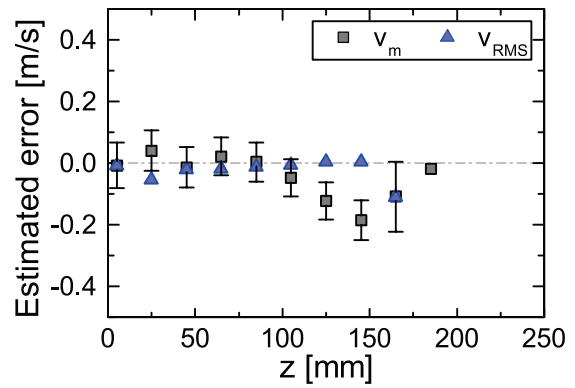
a) n-heptane



b) n-heptane

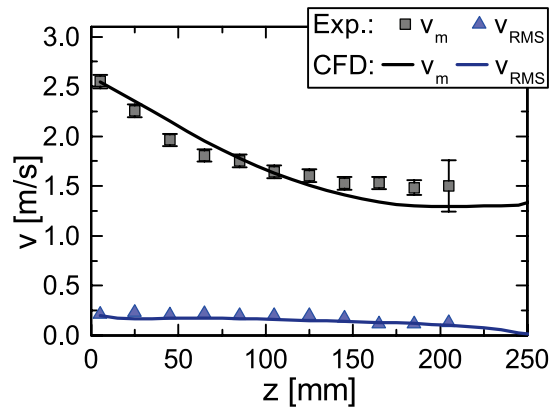


c) n-decane

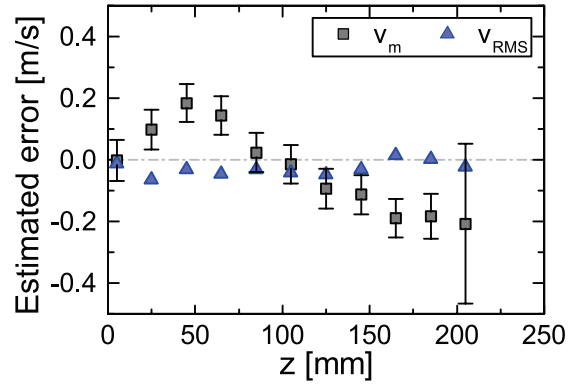


d) n-decane

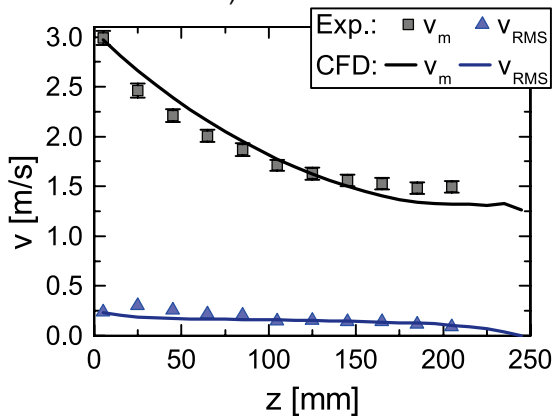
Figure C.6: Velocity validation for n-heptane and n-decane. Left column: comparison of computed with experimental data for velocity evolution. Right column: corresponding validation metrics.



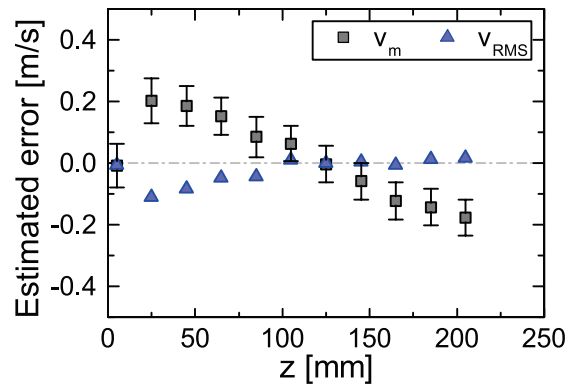
a) ethanol



b) ethanol



c) hexanol



d) hexanol

Figure C.7: Velocity validation for ethanol and hexanol. Left column: comparison of computed with experimental data for velocity evolution. Right column: corresponding validation metrics.

C.2.2 Binary Mixtures

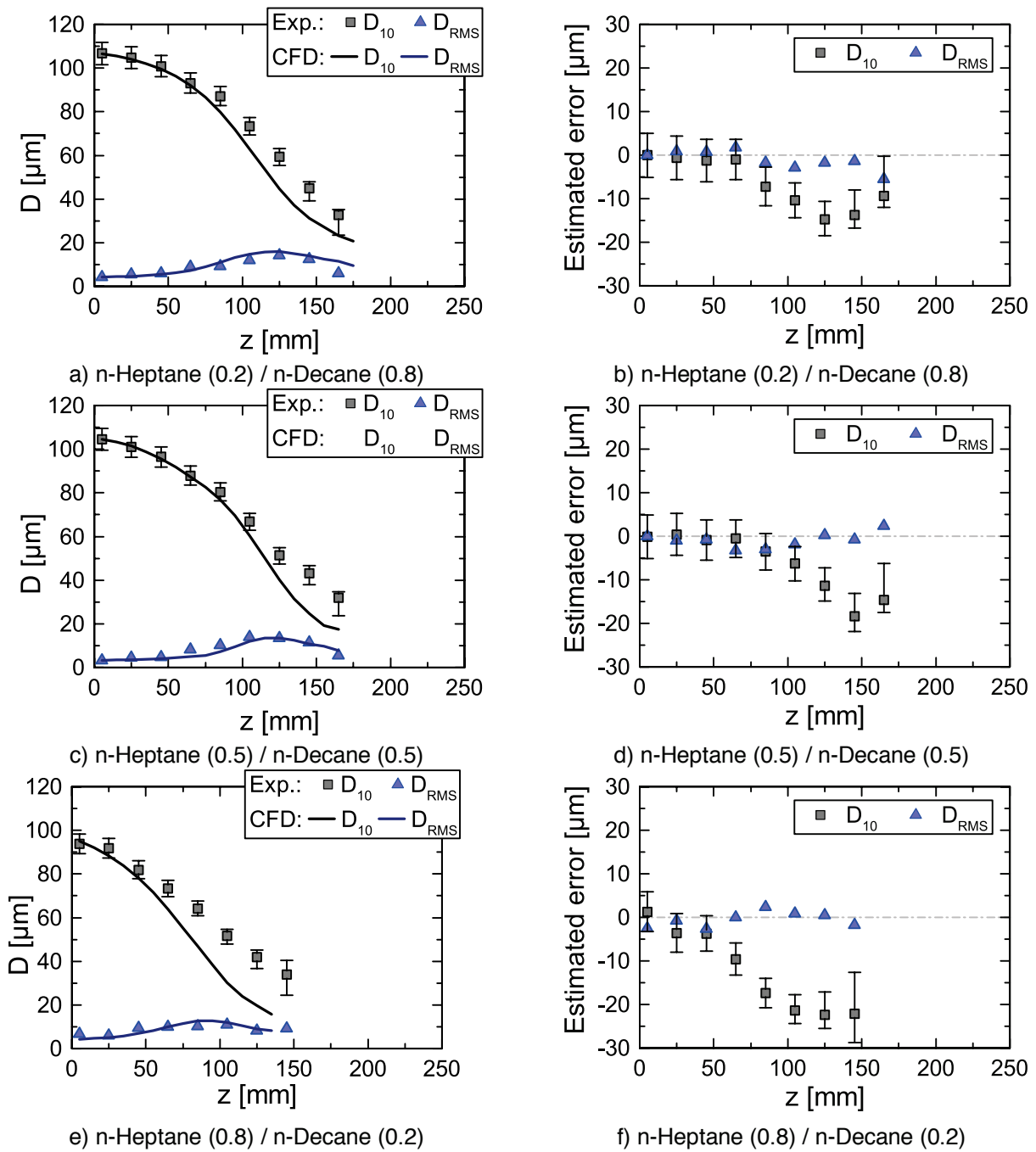
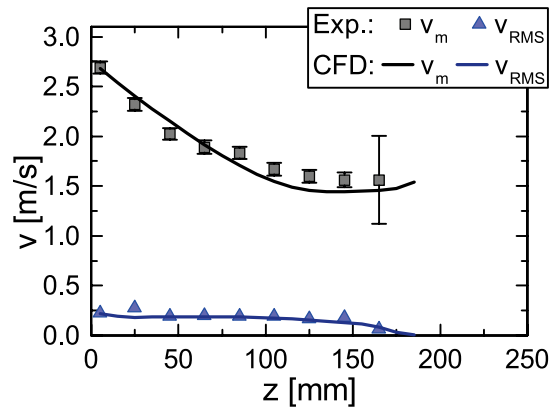
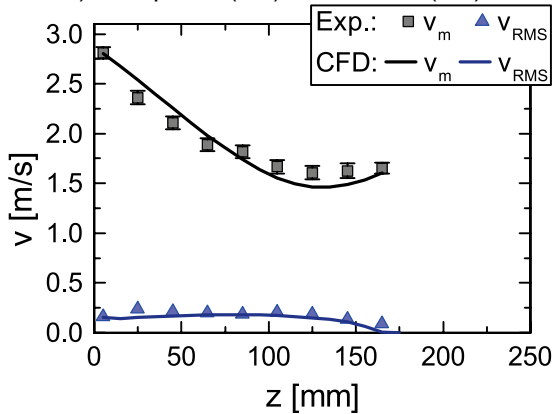


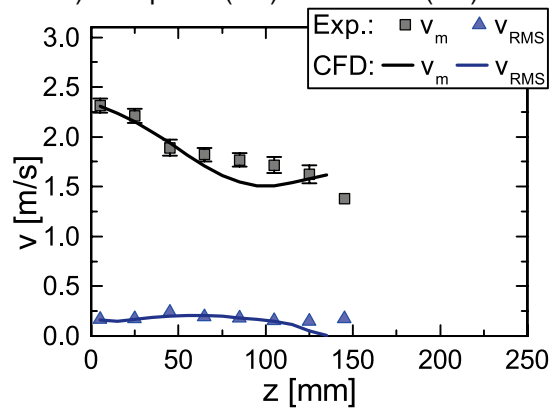
Figure C.8: Diameter validation for the binary mixtures of n-heptane and n-decane. Left column: comparison of computed with experimental data for diameter evolution. Right column: corresponding validation metrics.



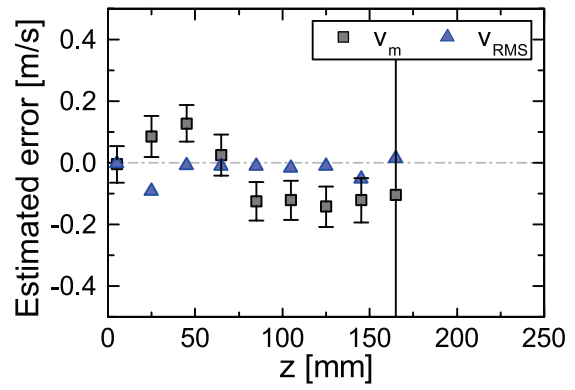
a) n-Heptane (0.2) / n-Decane (0.8)



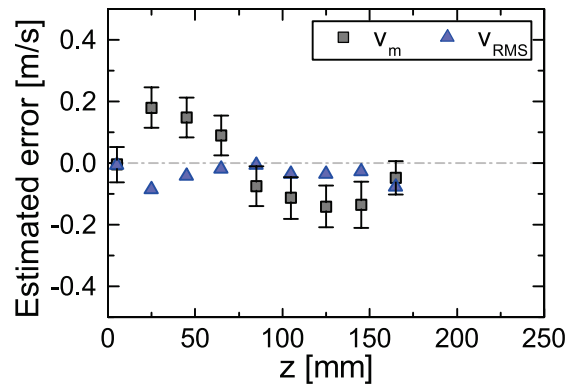
c) n-Heptane (0.5) / n-Decane (0.5)



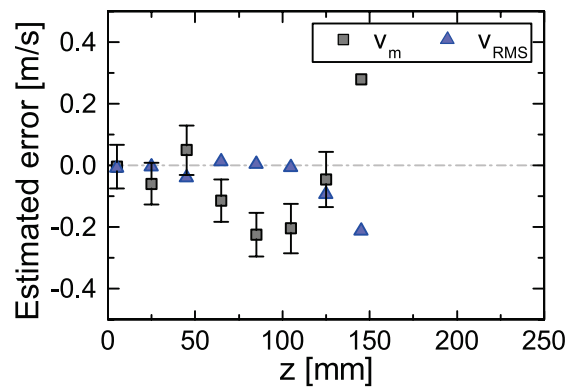
e) n-Heptane (0.8) / n-Decane (0.2)



b) n-Heptane (0.2) / n-Decane (0.8)



d) n-Heptane (0.5) / n-Decane (0.5)



f) n-Heptane (0.8) / n-Decane (0.2)

Figure C.9: Velocity validation for the binary mixtures of n-heptane and n-decane. Left column: comparison of computed with experimental data for velocity evolution. Right column: corresponding validation metrics.

C.2.3 Non-Ideal Mixtures

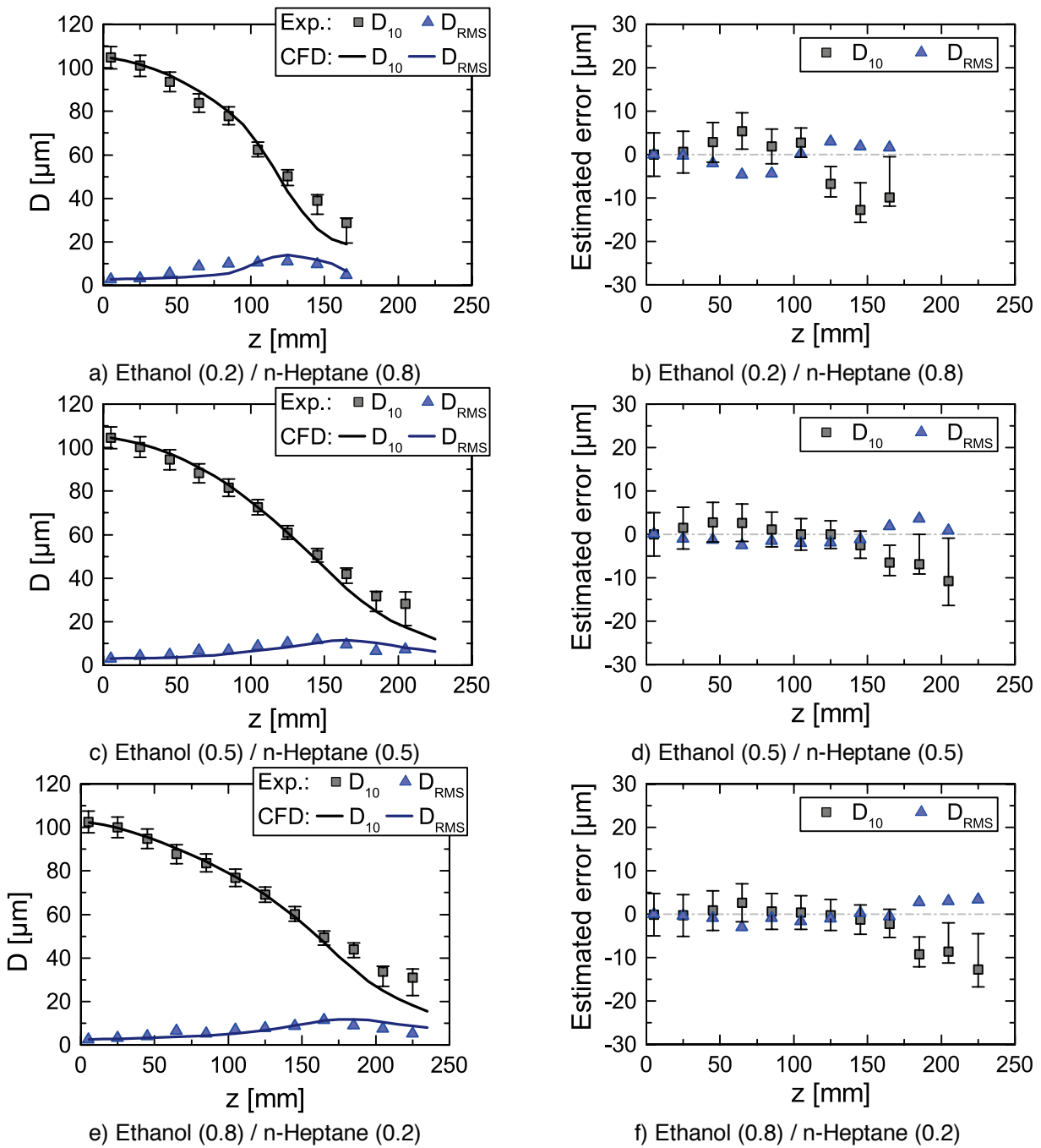
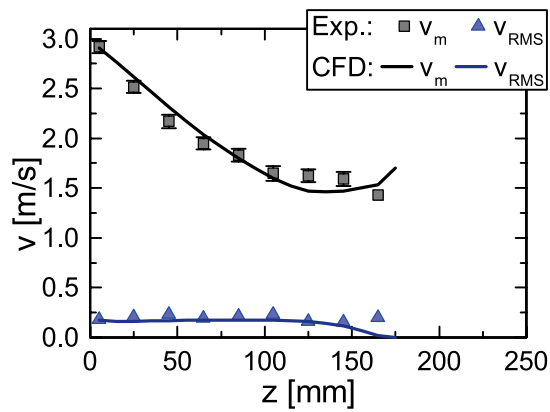
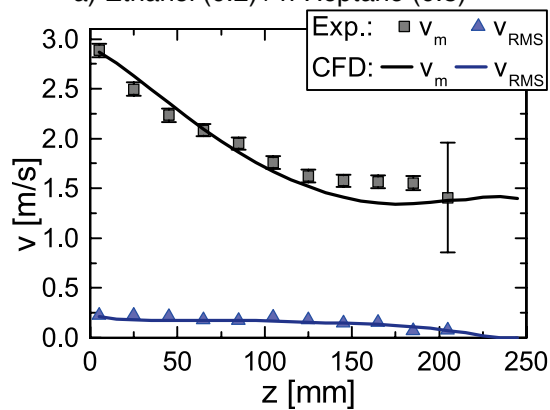


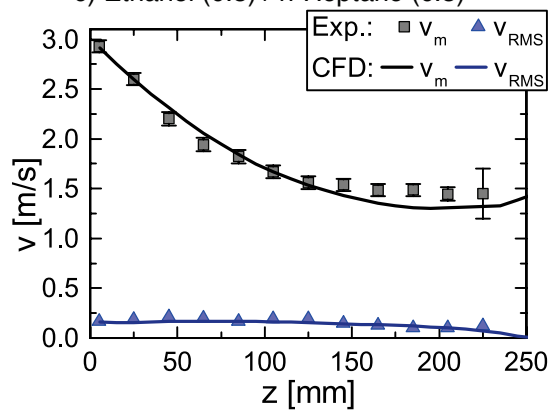
Figure C.10: Diameter validation for the non-ideal mixtures of ethanol and n-heptane. Left column: comparison of computed with experimental data for diameter evolution. Right column: corresponding validation metrics.



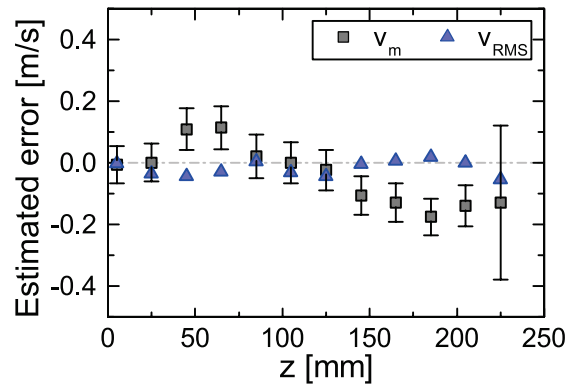
a) Ethanol (0.2) / n-Heptane (0.8)



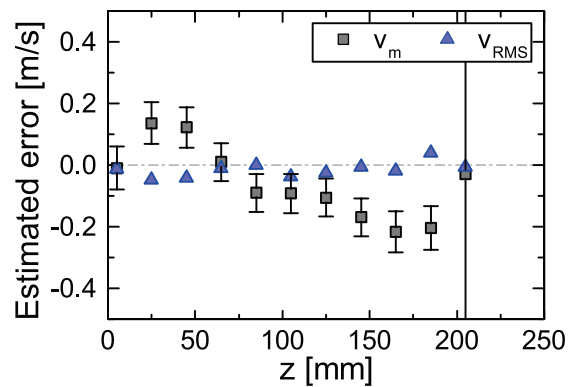
c) Ethanol (0.5) / n-Heptane (0.5)



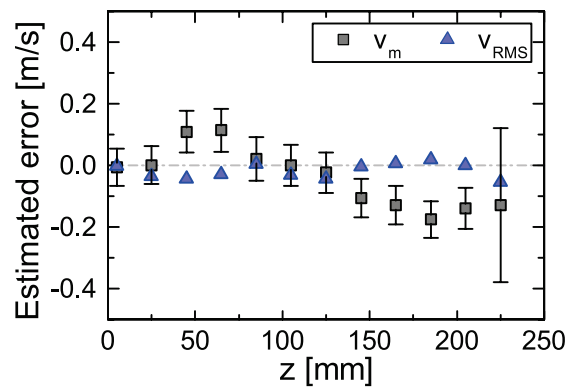
e) Ethanol (0.8) / n-Heptane (0.2)



b) Ethanol (0.2) / n-Heptane (0.8)



d) Ethanol (0.5) / n-Heptane (0.5)



f) Ethanol (0.8) / n-Heptane (0.2)

Figure C.11: Velocity validation for the non-ideal mixtures of ethanol and n-heptane. Left column: comparison of computed with experimental data for diameter evolution. Right column: corresponding validation metrics.

C.2.4 Multicomponent Mixtures

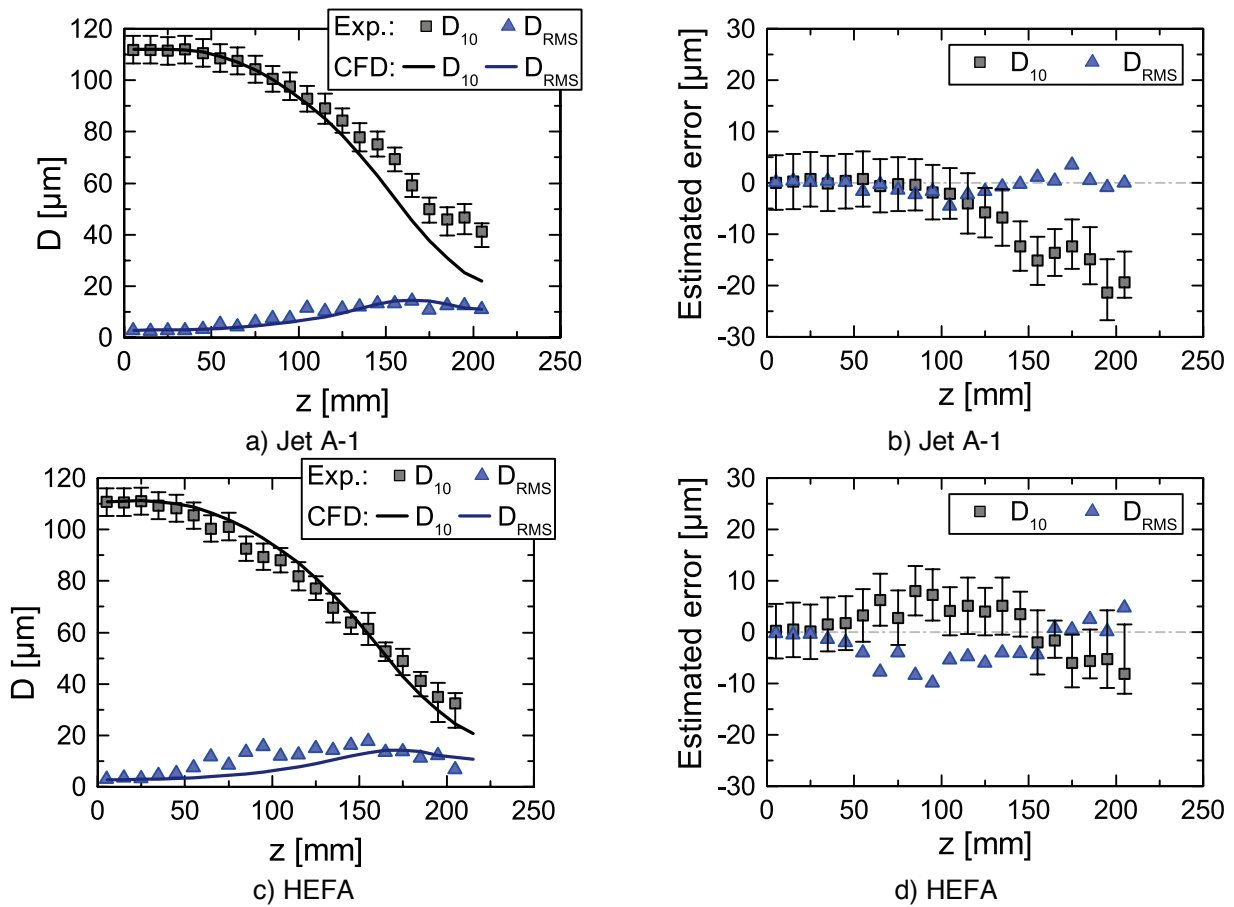


Figure C.12: Diameter validation for Jet A-1 and HEFA.
Left column: comparison of computed with experimental data for diameter evolution.
Right column: corresponding validation metrics.

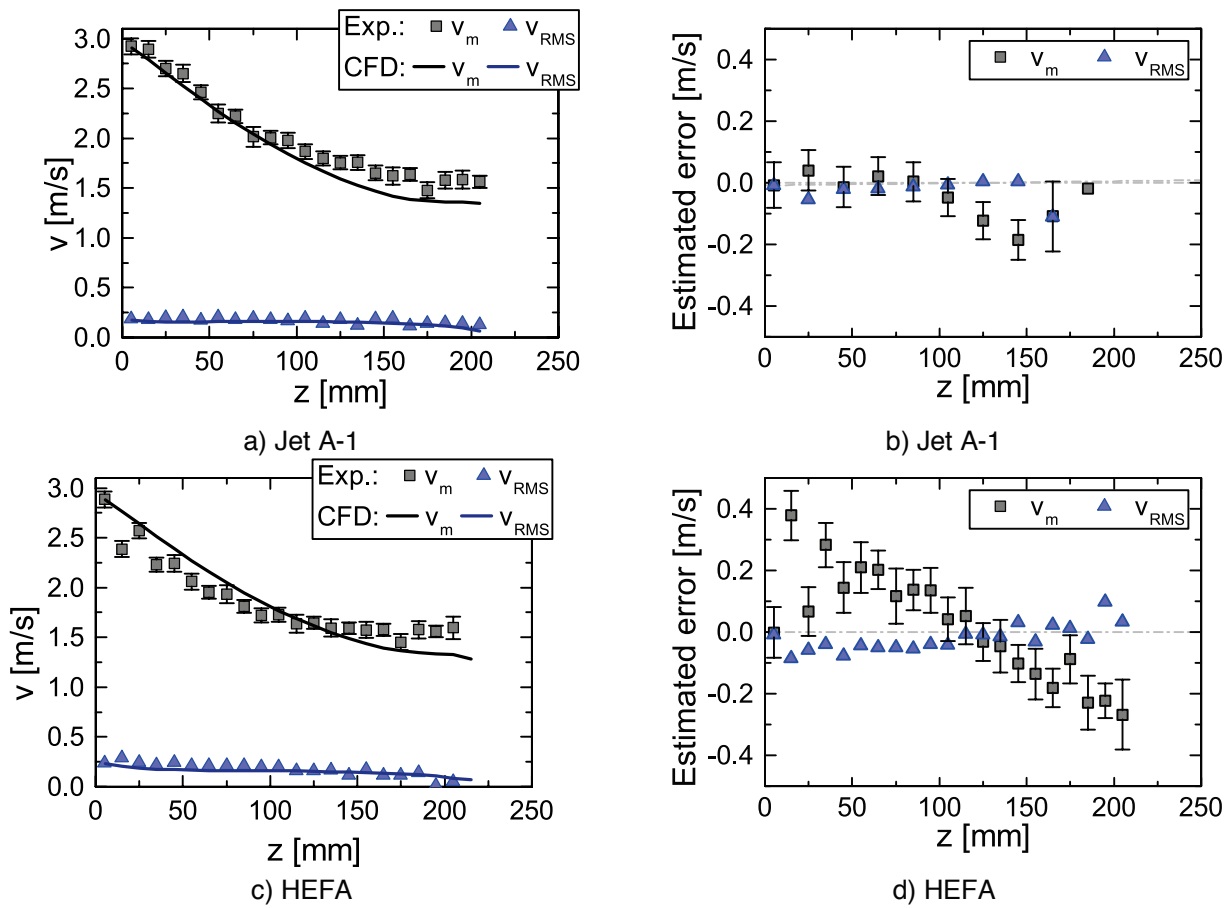


Figure C.13: Validation validation for Jet A-1 and HEFA.
 Left column: comparison of computed with experimental data for diameter evolution.
 Right column: corresponding validation metrics.

Curriculum Vitae

Name Bastian Rauch
Email bastian.rauch@dlr.de
Date of birth: 22.04.1980
Place of birth: Bruchsal, Germany
Nationality: German

Education

1990 - 1999 Justus-Knecht Gymnasium Bruchsal, Abitur (High school diploma)
2000 - 2006 University of Stuttgart, Germany: Studies of Aerospace Engineering.
Graduation Degree Dipl.-Ing.

Student Theses

2005 Institute of Space Systems, University of Stuttgart,
First Thesis: „Numerical simulation of magnetoplasmadynamic self-field thrusters
at high discharge currents“
2006 Istituto Motori, Consiglio Nazionale delle Ricerche, Naples, Italy:
Final Thesis: "Optical characterization of microemulsion droplets in controlled
turbine-like conditions"

Work Experience

2003 – 2004 Daimler Chrysler AG, Engine Development Department:
Internship
2006 - 2012 Istituto Motori, Consiglio Nazionale delle Ricerche, Naples, Italy:
Research Associate
2014 - 2016 Institute of Combustion Technology for Aerospace Engineering, University of
Stuttgart:
Research Associate
2006 - today Institute of Combustion Technology, German Aerospace Center (DLR):
Research Associate